



**HAL**  
open science

# MOF-based nanomaterials for photocatalytic CO<sub>2</sub> reduction and H<sub>2</sub> production

Maria Anagnostopoulou

► **To cite this version:**

Maria Anagnostopoulou. MOF-based nanomaterials for photocatalytic CO<sub>2</sub> reduction and H<sub>2</sub> production. Theoretical and/or physical chemistry. Université de Strasbourg, 2023. English. NNT : 2023STRAF018 . tel-04216877

**HAL Id: tel-04216877**

**<https://theses.hal.science/tel-04216877>**

Submitted on 25 Sep 2023

**HAL** is a multi-disciplinary open access archive for the deposit and dissemination of scientific research documents, whether they are published or not. The documents may come from teaching and research institutions in France or abroad, or from public or private research centers.

L'archive ouverte pluridisciplinaire **HAL**, est destinée au dépôt et à la diffusion de documents scientifiques de niveau recherche, publiés ou non, émanant des établissements d'enseignement et de recherche français ou étrangers, des laboratoires publics ou privés.

**ÉCOLE DOCTORALE DES SCIENCES CHIMIQUES**

Institut de Chimie et Procédés pour l'Énergie, l'Environnement et la Santé-  
ICPEES/CNRS/UNISTRA UMR-7515

**THÈSE** présentée par :

**Maria ANAGNOSTOPOULOU**

soutenue le : 16 Juin 2023

pour obtenir le grade de : **Docteur de l'université de Strasbourg**

Discipline/ Spécialité : Chimie/Chimie Physique

**Nanomatériaux à base de MOF pour la  
réduction photocatalytique de CO<sub>2</sub> et la  
production de l'hydrogène**

**THÈSE dirigée par :**

**Mme. KELLER Valérie**

Directrice de Recherche, CNRS, (ICPEES UMR-7515)

**THÈSE co-encadrée par :**

**M. CHRISTOFORIDIS Konstantinos**

Maitre de conférences, Democritus Université de Thrace

**RAPPORTEURS :**

**M. ARMATAS Gerasimos**

Professeur, Université de Crète, Grèce

**M. FORNASIERO Paolo**

Professeur, Université de Trieste, Italie

**EXAMINATRICE :**

**Mme. BEGIN Sylvie**

Professeure, Université de Strasbourg, (IPCMS UMR-7504)



## Acknowledgments

The present thesis would have never been realized without the support, the contribution and the advice of the people that have been by my side during the last 3 years.

First and foremost, I would like to express my acknowledgment to the director of my thesis, Dr. Valerie Keller, for her expertise and her support throughout the course of my research. A sincere thank you to my co-supervisor, Dr. Konstantinos Christoforidis for his constructive feedback, continuous encouragement and trust that helped me grow scientifically. I would also like to thank the French national Agency for Research (ANR) in the framework of Make Our Planet Great Again-MOPGA project, for funding my PhD studies.

I am also deeply thankful to Pr. Gerasimos Armatas (University of Crete, Greece), Pr. Paolo Fornasiero (University of Trieste, Italy) and Pr. Sylvie Begin (University of Strasbourg, France) for accepting being members of the jury committee of my PhD.

This journey would have never started without the people that inspired me to pursue PhD studies during my Master's Internship, a special thanks to Dr. Loic Charbonnier, Dr. Aline Nonat and Alexandre Lecointre. I would also like to express my deepest appreciation to Dr. Nicolas Keller and Dr. Valerie Caps for their scientific advice. Moreover, I am extremely thankful to Dr. Thomas Cottineau for giving my access to his experimental set up and for his scientific guidance resulting in a fruitful collaboration.

Except for the scientific support, I would also like to recognize the support provided by the administrative and technical departments of ICPEES. In particular, I would like to thank Julien Bertrand for his help with administration. I would also like to express my gratitude to Sylviane Bronner, not only because she was in charge of my order demands, ensuring the availability of chemicals to manipulate with. But most importantly, for her unconditional support. I would never find enough words to thank Alain Rach, not only for repairing the experimental set-ups, but also my bike. He has always been willing to do it with a big smile. I would also like to thank Michel Wolf, Dr. Jean-Mario Nhut, and Christophe Shutter for making sure that we have reactors, experimental set-ups and functional software to work with.

Thanks should also go to the people that helped me carry out experiments during my PhD studies. I would like to thank Thierry Dintzer and Dris Ihiwakrim (IPCMS) for SEM and TEM images, respectively. My acknowledgment is also addressing to Dr. Julien Massue, for providing access to his laboratory for the Photoluminescence measurements. I would also like to acknowledge Fabrice Vigneron, Christophe Melart and Secou Sall for providing their technical support and their good mood. Special thanks to Dr. Vasiliki Papaefthymiou for the XPS measurements and Dr. Spyros

Zafeiratos. They were always there replying to my questions concerning peaks deconvolutions and sharing with me tips for pottery.

A shout out to my wonderful colleagues for all those lovely moments throughout the last three years. I had the pleasure working with post-doctoral researcher Clement Marchal, who has always been willing to reply to my questions, listen to my ideas when I was inspired and offer me a glass of beer when I was discouraged. A special thanks to my PhD brother, Javi for listening to my complains and teaching me SUDOKU. Thanks to Hamza for sharing the same office and also sharing the same taste in music (loud in the office). Thanks to Jean Philippe and Nina for helping me integrate in the city and in the lab once I arrived. A big thank you to Marie and Leila, my partners in crime, because they render my PhD journey funnier and adventurous. I would also like to thank Mael, Justine, XI, Caro, Eliane, Mathias, Florian and Steven for their good mood and support in the lab and the moments we shared together outside of the lab. I would also like to express my gratitude to Laura, Marta, Ricardo and Maria for the pleasant lunch breaks we shared, the Spanish courses and the geography knowledge I obtained.

This journey wouldn't have been the same without the people that made me feel home, while being away from home. For their support and their advice, I would always appreciate and admire them. Thank you Camila, Franck, Calogera, Katerina, Ourania, Argyro, Ioanna, Irene and Georgia.

Last but not least, I would have been here without the encouragement of my family, especially my parents and my sisters. Their unconditional support, belief in me and my potential were a motivation to achieve what I have done so far. **Ευχαριστώ.**





## Abbreviations:

**ADP:** Adenosine Diphosphate

**ATP:** Adenosine Triphosphate.

**ATR:** Attenuated Total Reflectance

**BET:** Brunauer-Emmett-Teller

**Bk:** bulk

**CB:** Conduction band

**CCS:** Carbon capture and storage

**CCUS:** Carbon capture, utilization, and storage

**CN:** Carbon Nitride

**CO<sub>2</sub>RR:** CO<sub>2</sub> reduction reaction

**CV:** Cyclic Voltammetry

**DRIFTS:** Diffuse Reflectance Infrared Fourier Transform Spectroscopy

**DRS:** Diffuse Reflectance Spectroscopy

**EDS:** Electron Diffraction Spectroscopy

**EOR:** enhanced oil recovery

**EPR:** Electron Paramagnetic Resonance

**FWHM:** Full Width Half Maximum

**FTIR:** Fourier Transform infrared spectroscopy

**FID:** Flame Ignition Detector

**GC:** Gas Chromatography

**GHG:** Greenhouse gas

**H<sub>2</sub>TCP:** mesotetracarboxyl phenyl porphyrin

**IEA:** International Energy Agency

**IPCC:** Intergovernmental Panel for Climate Change

**IR:** Infrared

**LSPR:** Localized Surface Plasmon Resonance

**Me:** Metal

**MeOH:** Methanol

**MOF:** Metal-Organic Framework

**NADP:** Nicotinamide Adenine Dinucleotide Phosphate

**NHE:** Normal Hydrogen electrode

**NIR:** Near Infrared

**NPs:** Nanoparticles

**NSs:** Nanosheets

**PCN:** Porous Coordination Network

**PEC:** Photoelectrochemical

**PL:** Photoluminescence

**POX:** Partial Oxidation

**PSA:** Pressure Swing Adsorption

**RHE:** Reference hydrogen electrode

**RWGS:** reverse water-gas shift

**SC:** Semiconductor

**sc-CO<sub>2</sub>:** supercritical CO<sub>2</sub>

**SEM:** Scanning Electron Microscopy

**SSA:** Specific Surface Area

**STM:** Scanning Tunnel Microscopy

**STM:** Steam Methane Reforming

**TAS:** Transient Adsorption Spectroscopy

**TCD:** Thermal Conductivity Detector

**TEM:** Transmission Electron Microscopy

**TGA:** Thermo gravimetric Analysis

**TMO:** Transition Metal Oxides

**TRMC:** Time-resolved microwave conductivity

**TSA:** Temperature Swing Adsorption

**UV/VIS:** Ultraviolet/visible

**VB:** Valence band

**XPS:** X-ray Photoelectron Spectroscopy

**XO:** Xylenol Orange

**XRD:** X-ray powder Diffraction

**ZIF:** Zeolitic Imidazolate Framework



# Table of Contents

<b>CHAPTER 1: STATE OF THE ART</b>	<b>1</b>
INTRODUCTION	3
I. RENEWABLE ENERGY RESOURCES	6
<i>I.1. H<sub>2</sub> as energy carrier</i>	7
<i>I.2. Carbon Capture Utilization and Storage Technology (CCUS)</i>	11
II. PHOTOCATALYSIS	14
<i>II.1. Natural Photosynthesis</i>	14
<i>II.2. Principles of photocatalysis</i>	15
<i>II.3. Mechanism of Photocatalysis</i>	15
<i>II.4. Photocatalysts</i>	16
<i>II.5. Artificial Photosynthesis</i>	22
III. CARBON NITRIDE	29
<i>III.1. Generalities</i>	29
<i>III.2. Properties</i>	29
<i>III.3. Methods of Synthesis</i>	30
IV. TITANIUM DIOXIDE	33
<i>IV.1. Generalities</i>	33
<i>IV.2. Properties</i>	33
<i>IV.3. Methods of synthesis</i>	35
V. MOFs	36
<i>V.1. Generalities</i>	36
<i>V.2. Methods of synthesis</i>	37
<i>V.3. MOFs applications</i>	39
VI. CONCLUSIONS	46
VII. REFERENCES	48
<b>CHAPTER 2: MATERIALS AND METHODS</b>	<b>69</b>
INTRODUCTION	71
I. SYNTHESIS PROTOCOLS	72
<i>I.1. Carbon nitride</i>	72
<i>I.2. Titanium dioxide</i>	73
<i>I.3. MOFs</i>	74
<i>I.4. Platinum Deposition</i>	79
II. CHARACTERIZATION TECHNIQUES	80
<i>II.1. Thermogravimetric Analysis (TGA)</i>	80
<i>II.2. X-Ray Diffraction (XRD)</i>	80
<i>II.3. BET</i>	81
<i>II.4. X-Ray Photoelectron Spectroscopy (XPS)</i>	81
<i>II.5. Scanning Electron Microscopy (SEM)</i>	83
<i>II.6. Transmission Electron Microscopy (TEM)</i>	84
<i>II.7. UV-Visible Spectroscopy (UV/Vis)</i>	84
<i>II.8. Infrared Spectroscopy (IR)</i>	85
<i>II.9. Photoelectrochemical analysis</i>	86
<i>II.10. Transient absorption spectroscopy (TAS)</i>	87
<i>II.11. Electron paramagnetic resonance (EPR)</i>	88
<i>II.12. Photoluminescence Measurements (PL)</i>	90
<i>II.13. Temperature-programmed Desorption (TPD)</i>	91

III. PHOTOCATALYTIC SET-UPS	92
<i>III.1. Set up for photocatalytic H<sub>2</sub>O splitting</i>	92
<i>III.2. Set up for Photocatalytic CO<sub>2</sub> reduction</i>	93
IV. REFERENCES	98
<b>CHAPTER 3: MOF-DERIVED CO<sub>3</sub>O<sub>4</sub>-CN COMPOSITES</b>	<b>101</b>
INTRODUCTION	105
I. CHARACTERIZATION OF CO <sub>3</sub> O <sub>4</sub> -CN NANOCOMPOSITES	106
<i>I.1. Structural and compositional characterization</i>	106
<i>I.2. Characterization of optical properties</i>	118
<i>I.3. Morphological Characterization</i>	119
<i>I.4. Characterization of electronic properties-Studies of Charge carriers' behavior</i>	123
II. PHOTOCATALYTIC ACTIVITY OF CO <sub>3</sub> O <sub>4</sub> -CN NANOCOMPOSITES	131
<i>II.1. CO<sub>2</sub> photoreduction results</i>	131
<i>II.2. Photocatalytic H<sub>2</sub>O splitting results</i>	135
<i>II.3. Proposed mechanism</i>	136
<i>II.4. Photocatalyst stability test</i>	138
III. CONCLUSIONS	140
IV. REFERENCES	142
<b>CHAPTER 4: COMPOSITES OF (M)-PCN-224/ TiO<sub>2</sub></b>	<b>147</b>
INTRODUCTION	149
I. CHARACTERIZATION OF (ME-PCN-224)/TiO <sub>2</sub> COMPOSITES	150
<i>I.1. Characterization of structural properties</i>	150
<i>I.2. Characterization of electronic and morphological properties</i>	158
II. PHOTOCATALYTIC ACTIVITY OF (ME)-PCN-224/TiO <sub>2</sub> (UV-100) NANOCOMPOSITES	166
<i>II.1. Photocatalytic CO<sub>2</sub> reduction results</i>	166
<i>II.2. Photocatalytic H<sub>2</sub>O Splitting results</i>	169
III. CONCLUSIONS	170
IV. REFERENCES	172
<b>CHAPTER 5: NANOCOMPOSITES OF BIMETALLIC ZIFS/TiO<sub>2</sub></b>	<b>177</b>
INTRODUCTION	179
I. CHARACTERIZATION OF MULTI-LAYER ZIFS/TiO <sub>2</sub> (UV-100) COMPOSITES	180
<i>I.1. Characterization of structural properties</i>	180
<i>I.2. Characterization of chemical and morphological properties</i>	185
<i>I.3. Characterization of optical and electronic properties</i>	189
II. PHOTOCATALYTIC ACTIVITY OF BIMETALLIC ZIFS/TiO <sub>2</sub> (UV-100) COMPOSITES	192
III. CONCLUSIONS	194
IV. REFERENCES	196
<b>GENERAL CONCLUSIONS AND PERSPECTIVES</b>	<b>199</b>

Chapter 1:  
State of the art

## Table of Figures

FIGURE 1.1: YEARLY CARBON DIOXIDE EMISSIONS (IN GIGATONS), FROM 1959 TO 2019 <sup>6</sup> .....	3
FIGURE 1.2: NITROGEN DIOXIDE CONCENTRATION OVER FRANCE AS RECORDED BY EUROPEAN SPACE AGENCY SATELLITES IN MARCH 2019 (LEFT) AND MARCH 2020 (RIGHT).....	4
FIGURE 1.3: HYDROGEN PRODUCTION APPROACHES <sup>40</sup> .....	9
FIGURE 1. 4: CCUS SCHEMATIC ILLUSTRATION .....	13
FIGURE 1. 5: (A) THE MOLECULE OF CHLOROPHYLL, WHERE NATURAL PHOTOSYNTHESIS IS TAKING PLACE, (B) THE SCHEMATIC DIAGRAM OF A DOUBLE EXCITATION PROCESS IN NATURAL PHOTOSYNTHESIS .....	15
FIGURE 1. 6: SCHEMATIC ILLUSTRATION OF THE DIFFERENT PATHWAYS OF PHOTOGENERATED CHARGE CARRIERS IN PHOTOCATALYST UPON LIGHT IRRADIATION .....	16
FIGURE 1. 7: BANDS POSITION OF DIFFERENT SEMICONDUCTORS, REGARDING TO THE REDOX POTENTIAL OF WATER SPLITTING REACTION .....	17
FIGURE 1. 8: CHARGE TRANSFER IN A TYPE-II (LEFT SIDE) AND A Z-SCHEME (RIGHT SIDE) HETEROJUNCTION:.....	19
FIGURE 1. 9: SCHEMATIC ILLUSTRATION OF THE ADVANTAGEOUS CONTACT BETWEEN BOTH COMPONENTS IN 2D–2D COMPOSITE PHOTOCATALYSTS IN COMPARISON TO 0D–2D AND 0D-1D COMPOSITES LAYERED COMPOSITE PHOTOCATALYSTS.....	20
FIGURE 1. 10: SCHOTTKY BARRIER IN THE INTERFACE OF SC/METAL NANOPARTICLE: (A) BEFORE CONTACT, (B) AFTER CONTACT .....	21
FIGURE 1. 11: SCHEME OF THE OVERALL PHOTOCATALYTIC WATER SPLITTING WITH ITS REDOX POTENTIALS.....	23
FIGURE 1. 12: SCHEMA OF THE PHOTOCATALYTIC CO <sub>2</sub> REDUCTION WITH ITS REDOX POTENTIALS .....	25
FIGURE 1. 13: CO <sub>2</sub> ADSORPTION MODE ON PHOTOCATALYSTS SURFACE BY : (A) OXYGEN COORDINATION, (B) CARBON COORDINATION, (C) MIXED COORDINATION.....	26
FIGURE 1. 14: SCHEMATIC ILLUSTRATION OF THE SYNTHESIS PROCESS OF G-C <sub>3</sub> N <sub>4</sub> BY THERMAL POLYCONDENSATION FROM DIFFERENT PRECURSORS. <sup>162</sup> .....	31
FIGURE 1. 15: CRYSTALLINE STRUCTURES OF: (A) ANATASE, (B) RUTILE, (C) BROOKITE .....	34
FIGURE 1. 16: VARIOUS APPLICATIONS OF MOF MATERIALS .....	36
FIGURE 1. 17: SURFACE TENSION OF SOME COMMON ORGANIC SOLVENTS COMPARED TO LIQUID CO <sub>2</sub> . DCM: DICHLOROMETHANE; DMF: N,N-DIMETHYLFORMAMIDE; DMSO: DIMETHYL SULFOXIDE <sup>213</sup> .....	38
FIGURE 1. 18: KEY PARAMETERS OF MOF-BASED OR MOF-DERIVED MATERIALS <sup>226</sup> .....	41
FIGURE 1. 19: SCHEMATIC ILLUSTRATION OF THE SYNTHETIC CONDITIONS USED TO CONSTRUCT THE DIFFERENT ZIF-8-ON-ZIF-67 PARTICLES ACCORDING TO THE SEQUENTIAL DECONSTRUCTION-RECONSTRUCTION STRATEGY <sup>251</sup> .....	45

## Introduction

The presence of primary greenhouse gases (GHGs) in Earth's atmosphere ( $\text{H}_2\text{O}$ ,  $\text{CO}_2$ ,  $\text{CH}_4$ ,  $\text{N}_2\text{O}$ ,  $\text{O}_3$ ) is necessary maintaining a temperature favorable for human and animal beings <sup>1</sup>. Namely, greenhouse gases absorb and radiate thermal infrared energy (i.e., heat), warming Earth's land and ocean surfaces. Without them, the average temperature of Earth's surface would be approximately  $-18^\circ\text{C}$ , rather than the present average of  $15^\circ\text{C}$  <sup>2</sup>.

Among greenhouse gases,  $\text{CO}_2$  is the one with the highest concentration. Normally, to maintain the carbon balance in the planet, carbon flows between atmosphere, land and oceans through physicochemical and biological processes. In this direction, plants play an important role in the carbon cycle, through the process of photosynthesis where solar energy is essential for the process <sup>3</sup>. Specifically, plants are uptaking  $\text{CO}_2$  from the atmosphere and converting it into carbohydrates (i.e., glucose), which are useful for their growth, thus producing oxygen at the same time. On the other hand, through the process of cellular respiration, glucose and oxygen are used to produce carbon dioxide and water, in this way the carbon cycle is completed <sup>4</sup>. However, over the last 150 years, due to industrialization, carbon equilibrium is destabilized resulting to an excess of greenhouse gases found in the atmosphere, as seen in Figure 1.1 <sup>5</sup>. The main anthropogenic emission source sectors include electricity production (fuel combustion and fugitive emissions from fuels), transportation, industrial processes, product use and finally agriculture.

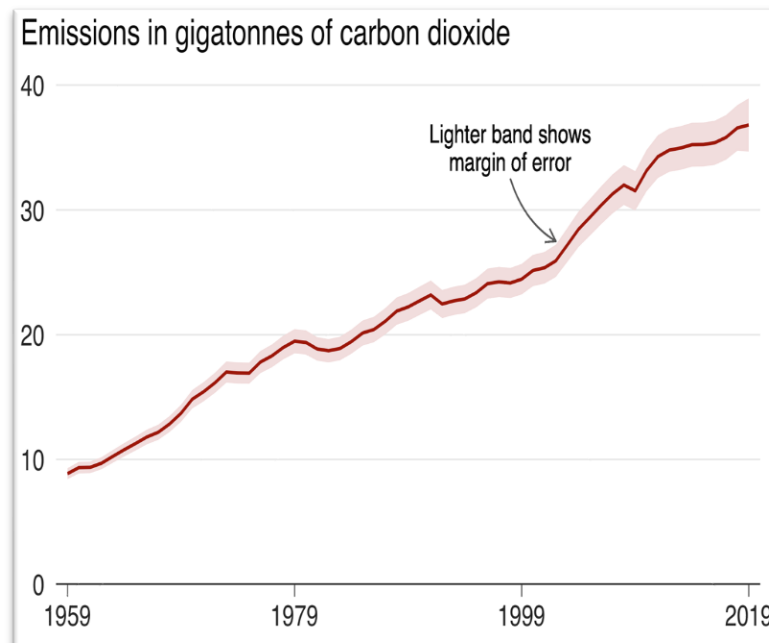
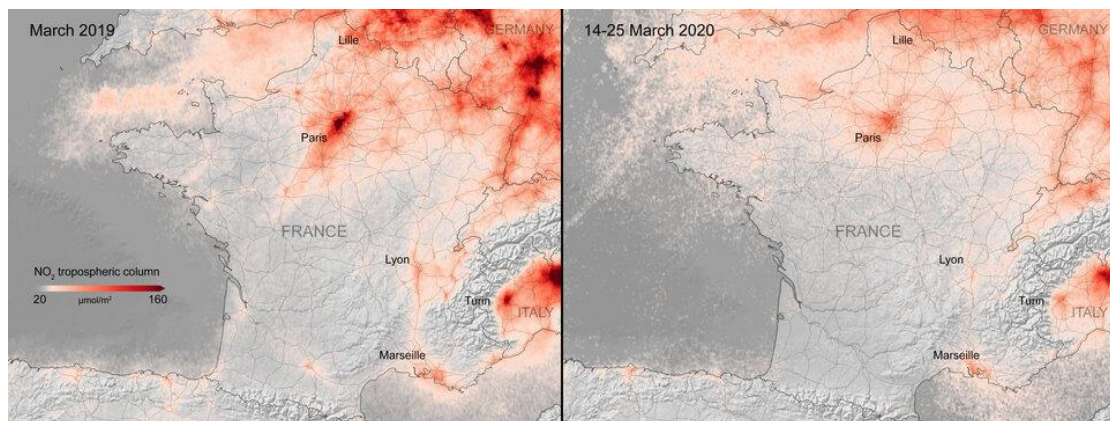


Figure 1.1: Yearly Carbon Dioxide emissions (in gigatons), from 1959 to 2019 <sup>6</sup>

## CHAPTER 1

Along with the industrialization, deforestation and forest wildfires are deteriorating this situation. A tremendous case is the Amazon's rainforest wildfires in 2019. More than 906,000 hectares of forest were burnt and caused important impacts on the biodiversity of the Amazon, and threats to indigenous tribes that live within the forest. In addition to that, an excess of carbon dioxide and carbon monoxide within the wildfires' emissions was detected. Amazon is the world's largest terrestrial carbon dioxide sink and plays a significant role in mitigating global warming. Therefore, the extent of this natural disaster raised international concerns.

Yet, the increasing demands of modern lifestyle are also inducing a drastic rise in CO<sub>2</sub> emissions. This assumption has been confirmed due to Coronavirus pandemic in 2020. Specifically, the spread of this lethal virus led to the lockdown of almost two thirds of the global population. As a result, human activities decreased- as motorways cleared, and factories closed- and nature bounced back. Figure 1.2 shows a sharp reduction of nitrogen dioxide pollution, deriving from fuel combustion processes, between March 2019 and March 2020 <sup>7</sup>.



*Figure 1.2: Nitrogen dioxide concentration over France as recorded by European Space Agency satellites in March 2019 (left) and March 2020 (right)*

As stated by the Intergovernmental Panel for Climate Change (IPCC), if mitigation actions are not taken, it is predicted that the CO<sub>2</sub>-equivalent concentrations in the atmosphere will attain 600-1500 ppm in 2030 <sup>8</sup>. All these facts raised human's and government's awareness with focus on taking actions towards climate change. Over the last few years, legislation for climate change mitigation has been introduced and are summarized in Table 1.1. The world's first greenhouse gas emissions reduction treaty is the Kyoto protocol <sup>9</sup>. Later, in 2016 the Paris Agreement was signed with the objective to maintain the increase in global temperatures well below two degrees Celsius above pre-industrial levels, whilst making efforts to limit the increase to 1.5 degrees. More recently, at the COP26 conference that took place in Glasgow in 2021, countries agreed to the goal of climate neutrality. It included an increase of the

## CHAPTER 1

funding for vulnerable developing countries and reduced the investment for new fossil fuel projects. Albeit the different members did not reach a common response regarding phasing out the use of coal.

*Table 1. 1: Historical overview of environmental treaties*

<i>Montreal Protocol</i> <sup>10</sup>	<b>1987</b>	Aimed at stop producing substances that damage the ozone layer (i.e., CFCs)	Succeeded in eliminating nearly 99% of these ozone-depleting substances
<i>UN Framework Convention on climate change (UNFCCC)</i> <sup>11</sup>	<b>1992</b>	Aimed at stabilizing the concentration of greenhouse gases in the atmosphere	Established an annual forum, known as the Conference of the Parties (COP), for international discussions
<i>Kyoto Protocol</i> <sup>9</sup>	<b>2005</b>	Required developed countries to reduce emissions by an average of 5% below 1990 levels Established a system to monitor countries' progress	Did not compel developing countries to take action
<i>Paris Agreement</i> <sup>12</sup>	<b>2015</b>	Required all countries to set emissions-reduction pledges Governments set targets, known as nationally determined contributions (NDCs) Aimed to reach global net-zero emissions in the second half of the century	

It is worth mentioning that the transition from fossil fuels to renewable energy is not only a solution towards the decrease of greenhouse gas emissions but also towards the depletion of fossil fuels <sup>13,14,15</sup>. Along with the environmental crisis that hits the globe, energy crisis has been intensified in Europe. Since the beginning of 2022, there is a severe energy shortage and global inflation not only to oil industry but in the total market <sup>16</sup>. This fact indicated that there is a need for rapid acceleration of other alternative to fossil fuels that are geographically independent, easily found using abundant resources. In this direction, the use of renewable energy is highly recommended.

Renewable energy, also referred to as clean energy, comes from natural sources or processes that are constantly replenished. More precisely, in its various forms, it

derives directly from the sun, or from heat generated deep within the earth, or from fluid movements like the winds, waterfall, waves <sup>17</sup>. Included in the definition is electricity and heat generated from solar, wind, ocean, hydropower, biomass, geothermal resources, as well as biofuels and hydrogen derived from renewable resources.

In the context of harnessing solar power, various technologies have been introduced, among them, photovoltaic effect allows the conversion of solar energy into electrical energy <sup>18</sup>. However, a major inconvenience of these techniques is that the sun irradiation is intermittent, and they are directly dependent on the power of solar irradiation. Storing solar energy by converting it into chemical energy is a way to address these limitations, by utilizing photocatalytic pathways <sup>19</sup>. Namely, storing this energy in chemical compounds in the form of chemical bonds is more attractive thanks to their easy storage and transport.

Up to now, several different applications of photocatalytic conversion have been studied <sup>20,21</sup>, but a major interest lies in the artificial photosynthesis <sup>22,23</sup>. Even though, the reported yields of photocatalytic CO<sub>2</sub> conversion are relatively low, research studies are carried out in order to improve the efficiency of the process.

### I. Renewable energy resources

The mitigation strategies that have already been suggested focus, firstly, on the diminution of the utilization of fossil fuels and their replacement with environmental-friendly fuels and secondly, on the sequestration of the GHGs. The suggested key strategies to reach the decrease of CO<sub>2</sub> emissions include measures such as:

1. Improving efficiency on both the demand side (efficient energy use) and the supply side (efficient electricity generation)
2. Using low-carbon energy sources (e.g., nuclear and renewable energy) as an alternative to fossil fuel sources
3. Capturing CO<sub>2</sub> from fossil fuel combustion <sup>24</sup>

The first step towards the reduction of GHG emissions is the replacement with other energy sources that are not harmful for the environment. As International Energy Agency (IEA) mentions, it is considered that cumulative contributions of low-carbon technologies can result in a 39% reduction in annual CO<sub>2</sub> emissions by 2035 <sup>25</sup>. In that regard, hydrogen gas (H<sub>2</sub>) is considered a promising energy vector, thanks to its high energy density and zero GHG emission after combustion <sup>26</sup>.

However, despite the efforts for transition towards environmentally friendly energy sources, CO<sub>2</sub> emissions are still hitting new records implying that the transition is not

sufficient to tackle the excess of GHGs in the atmosphere. For this reason, CCS technology has recently been studied as a simple approach to mitigation and involves capturing, transporting, and storing CO<sub>2</sub><sup>27</sup>. According to IEA, Carbon Capture and Storage (CCS) technology should be able to reduce CO<sub>2</sub> emissions by 19% by 2050<sup>28</sup>.

### I.1.H<sub>2</sub> as energy carrier

#### *I.1.A. H<sub>2</sub> properties and utilization*

Hydrogen (H<sub>2</sub>) is the most abundant element in the universe, constituting about 75% of all baryonic mass, and is found on planet earth mainly in water and organic compounds<sup>29</sup>. The Sun and other stars are mainly composed of hydrogen in the plasma state<sup>30</sup>. Hydrogen is an important raw material for synthesizing chemical compounds and in metallurgical reduction reactions<sup>31</sup>. In chemical industry, H<sub>2</sub> is a fundamental building block for the manufacture of ammonia, and hence fertilizers. It is also used for the production of methanol, many polymers, and other pharmaceutical products, such as vitamins<sup>32</sup>. Furthermore, H<sub>2</sub> is also required in the food and beverages industry to hydrogenate unsaturated fatty acids in animal and vegetable oils, producing solid fats for margarine and other food products.

Another important application of H<sub>2</sub> is the hydrogenating method of crude oil processing, in the refinery sector and the sulfur removal from fuels during the oil-refining process. Thus, about 55 % of the H<sub>2</sub> produced around the world is used for ammonia synthesis, 25 % in refineries and about 10 % for methanol production. The other applications worldwide account for only about 10 % of global hydrogen production<sup>33</sup>. It is evident that H<sub>2</sub> is essential for the food and oil industry, which both hold the biggest share of profits. This necessity has profoundly influenced the development of hydrogen technology. Therefore, the experience gained in production and safe usage of large amounts of H<sub>2</sub> will be important in the future utilization of hydrogen as an energy carrier.

By investigating the historical overview of H<sub>2</sub> as energy carrier, it is reported that in 1839 a British scientist, Sir William Robert Grove, developed the first hydrogen-powered fuel cell<sup>34</sup>. Later in 1900, Count Ferdinand von Zeppelin of Germany invented the first balloon using hydrogen to maintain the buoyancy of an airframe. In the U.S., NASA made great historical contributions to hydrogen utilization by realizing space explorations, they specifically employed hydrogen as a fuel, becoming the world's largest liquid hydrogen user by 1961<sup>35</sup>. Thereafter in 1988, the Soviet Union completed a flight with space shuttle, the world's first jet engine aircraft using liquid hydrogen fuel.

## CHAPTER 1

H<sub>2</sub> has played an important role as a rocket fuel because out of all fuels it is the one which concentrates the most energy. Specifically, 1 kg of hydrogen contains 3 times more energy than 1 kg of gasoline <sup>36</sup>. This is a critical criterion considering that a launcher must be as light as possible. As seen in Table 1.2, hydrogen energy content at the higher heating value is 141.8 MJ/kg at 298 K and the lower heating value of hydrogen is 120 MJ/kg at 298 K <sup>37</sup>, whereas the gravimetric energy density of gasoline is 45 MJ/kg at 298 K <sup>29</sup>.

*Table 1.2: Lower Heating Value of different fuels <sup>36</sup>*

Fuel	Lower Heating value (MJ/kg)
Hydrogen	119.7
Natural Gas	45.8
Petrol	44.8
Diesel	42.5

Apart from its high energy density, hydrogen has zero greenhouse gas emission after combustion, in contrast to the use of traditional fossil fuels that emit significant amounts of CO<sub>2</sub> and CO. In particular, the only combustion product of H<sub>2</sub> (Equation 1.1) is water vapor without any trace of noxious carbon emissions in the form of CO<sub>2</sub>, CO, or unburned hydrocarbons <sup>38</sup>.



As a result of a growing interest, hydrogen has been introduced as energy carriers by several EU policies and legislations in the past few years. Indeed, with the European Commission's Clean Energy and Mobility Plans, the EU is aiming for decarbonized energy and transport systems where hydrogen will have a key role. For example, employing renewably produced hydrogen & hydrogen-based fuels in the mobility sector (i.e., for maritime and aviation), will lead to two major impacts: increase the share of renewable energy in our current fuel infrastructure while enabling the deployment of zero-emission vehicles throughout Europe <sup>39</sup>.

### *1.2.B. H<sub>2</sub> production technologies*

Due to the promising properties of hydrogen and the legislative acts that are imposed, hydrogen production technologies have been extensively studied by the scientific community. The different approaches of H<sub>2</sub> production can be sorted by the origin of raw materials and are depicted in Figure 1.3.

## CHAPTER 1

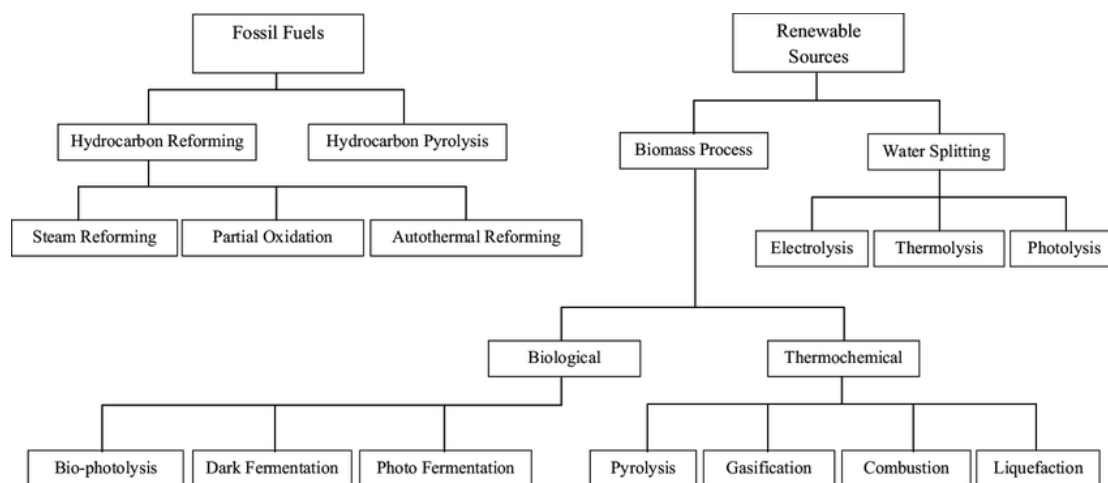


Figure 1.3: Hydrogen production approaches <sup>40</sup>

Originated from fossil fuels, H<sub>2</sub> can be produced either by hydrocarbons reforming or by hydrocarbon pyrolysis <sup>41</sup>. The former is carried out by techniques like Steam Reforming, Partial oxidation, and Auto-thermal Reaction.

**Steam reforming:** Hydrogen and steam are converted to H<sub>2</sub> and CO<sub>2</sub> with the assistance of catalysts, such as Nickel based catalysts. Hydrogen steam reforming is a highly endothermic process. As a result, it demands high temperature conditions, i.e., 850-900 °C. Steam Methane reforming (SMR) process is the most developed, efficient (up to 85%) and widely used for large-scale H<sub>2</sub> production <sup>42</sup>.

**Partial oxidation (POX):** This is the most preferable process to produce H<sub>2</sub> from heavier feedstock such as heavy oil residues and coal <sup>43</sup>. Hydrocarbon feedstock reacts with steam and is converted to H<sub>2</sub> and CO<sub>2</sub> in the presence of O<sub>2</sub> gas. The POX process requires high temperatures, i.e., ~950 °C or ~1300 °C, in the presence or absence of catalyst, respectively <sup>37</sup>. Nevertheless, this technique is cost-demanding, due to O<sub>2</sub> recirculation and desulphurization steps.

**Auto thermal reforming:** In this process, partial exothermic oxidation provides the heat during endothermic steam reforming, which increases the H<sub>2</sub> production. Typically, steam and O<sub>2</sub> or air are injected in the reforming chamber and the oxidation step and reforming step are realized simultaneously <sup>44</sup>.

**Hydrocarbon pyrolysis:** Thermocatalytic decomposition of light liquid hydrocarbons (boiling point: 50-200 °C) produces elemental carbon and H<sub>2</sub> <sup>45</sup>. The important advantage of this method over SMT technique is that the required energy for H<sub>2</sub> production by methane decomposition is significantly lower. In addition, there is no waste gas sequestration needed, and pyrolysis does not require CO<sub>2</sub> removal steps.

Despite H<sub>2</sub> being a zero-carbon emission fuel, its truly environmental friendly character depends on the type of the production pathway <sup>29</sup>. As it is stated at IEA

report for the G20 in Japan at 2019, an overwhelming majority of produced H<sub>2</sub> comes from the conversion of fossil fuels, while only less than 1% of H<sub>2</sub> is produced from renewable sources <sup>46</sup>. Focusing on H<sub>2</sub> production from renewable sources, biomass processes and water splitting processes can be used. The former one can be classified into thermochemical and biological.

**Thermochemical:** Pyrolysis or gasification are the two main thermochemical processes for H<sub>2</sub> rich gases. In these processes, CH<sub>4</sub> and CO, with other gaseous products, can be processed for more H<sub>2</sub> production through steam reforming and water-gas-shift reactions <sup>47</sup>. Syngas (a mixture of CO and H<sub>2</sub>) and biofuels are the main products of gasification and pyrolysis, respectively. Consequently, the biofuels are then converted into syngas by other techniques such as bio-oil reforming or bio-oil gasification <sup>48</sup>.

**Biological:** The major biological processes employed for H<sub>2</sub> production are direct and indirect bio-photolysis, photo- and dark fermentation. This kind of methods have some drawbacks, like the low hydrogen production and slower kinetics compared to the thermochemical methods <sup>49</sup>.

Hydrogen Production based on water splitting processes can be classified into three categories based on the origin of the energy input.

**Electrolysis:** Water dissociation is an endothermic reaction, therefore, an energy input is required to produce H<sub>2</sub> <sup>50</sup>. Different electrolysis techniques have been developed over the past few years. These include alkaline water electrolysis (AWE), proton exchange membranes (PEM), and solid oxide water electrolysis (SOE) <sup>51</sup>. Nevertheless, considerable amounts of electric energy input are needed for the electrolysis processes, specifically ~40 kWh per kg of H<sub>2</sub> <sup>37</sup>. Therefore, the scale-up of the process is not feasible.

**Thermolysis:** Water splitting can be also carried out by thermochemical processes. High temperature ~2500 °C are required, due to its high Gibbs Free Energy <sup>37</sup>. High temperatures can be generated in the following ways: solar- and nuclear-driven high-temperature thermochemical water-splitting cycles producing hydrogen using water, catalysts and either sunlight or nuclear energy <sup>52</sup>. This is a carbon-zero process.

**Photo-electrolysis:** This process uses light irradiation to produce electrical charges from a semiconductor<sup>53</sup>. The photocatalysts are semiconductor-based materials which generate charge carriers (electrons and holes pairs, e<sup>-</sup>/h<sup>+</sup>) by absorbing photons with sufficient energy (of energies higher than their bandgap energy, E<sub>g</sub>). The application of external bias allows the charges to be separated. The electrons are collected by the cathode, where H<sup>+</sup> ions are reduced into H<sub>2</sub>. The holes are collected by the anode, and oxidize the water to generate H<sup>+</sup> and O<sub>2</sub>. We note that an

electrical circuit is needed for this method to operate. However, this process is mainly limited by the charge transport and light absorption efficiency of the semiconductor electrode<sup>54</sup>. A similar process is photocatalysis which also uses visible light in order to dissociate water by using photoactive materials. In this case, no electrical circuit is required. Photocatalysis and its principles will be discussed in the following chapters.

Currently, SMR and electrolysis are the major H<sub>2</sub> production methods. Regarding to electrochemical water splitting, the electricity cost is one of the biggest barrier for sustainable energy systems. The emerging technologies include various biogas production options: biomass fermentation with microorganisms, and newly developed photo-electrochemical H<sub>2</sub>O splitting into H<sub>2</sub> and O<sub>2</sub> with lower energy demands compared to conventional electrolysis. In the long run, production pathways with almost zero carbon emissions, such as those based on solar energy are expected to become more viable<sup>37</sup>.

### 1.2. Carbon Capture Utilization and Storage Technology (CCUS)

Carbon Capture and Storage technology is recognized as a key-proven strategy in reducing greenhouse gas emissions. Specifically, it has been applied since 1972 in a wide range of industries, when several natural-gas processing plants in the Val Verde area of Texas began using carbon capture to supply CO<sub>2</sub> for EOR operations<sup>55</sup>. However, the high cost of capture and transportation of CO<sub>2</sub> discourages its application. The captured CO<sub>2</sub> has a negative economic value, rendering the overall process less profitable. In order to overcome this barrier, an alternative strategy, called CCUS is introduced and includes carbon utilization, in the framework of circular economy. These technologies recently have started to attract worldwide interest thanks to their wide variety of positive value applications<sup>56</sup>.

#### 1.2.A. CO<sub>2</sub> Capture

Carbon capture is the first step of the CCUS technology. Three main approaches have been used, involving the removal of CO<sub>2</sub> from flue gases by a capture process prior to their release to the atmosphere<sup>57</sup>. Namely, the pre-combustion capture, the post-combustion and the oxy-fuel combustion<sup>58</sup>. Amongst them post-combustion is the most mature process.

In order to capture CO<sub>2</sub>, adsorption processes have been employed using different kind of materials, such as solid adsorbents<sup>59</sup>, amine-based absorbent solutions<sup>60</sup> or membranes<sup>61</sup>. In processes that are executed at temperatures below 200 °C, porous organic frameworks and carbon-based adsorbents are the most commonly used materials. Notably activated carbon, zeolites, metal organic frameworks (MOFs), nitrogen enriched microporous polymers are some examples of solid sorbents<sup>62</sup>. In

particular, porous organic frameworks exhibit high CO<sub>2</sub> selectivity and uptake and have been used for CO<sub>2</sub> capture. Then, the adsorbed CO<sub>2</sub> can be recovered by Pressure Swing Adsorption (PSA) or Temperature Swing Adsorption (TSA) of the CO<sub>2</sub>-saturated sorbent.

In addition, the gas components can be dissolved physically or bound chemically to the amine-based solvent. The former case is related to weak Van der Waals forces, while the latter entail covalent bonding due to electrostatic attraction<sup>63</sup>. However, the main drawbacks of chemical absorption are the high equipment corrosion rate, amine degradation, low CO<sub>2</sub> loading capacity and high energy consumption (during regeneration) compared to physical sorbents (i.e., carbonaceous materials, zeolites)<sup>64</sup>.

Membrane technology is a recent method involving the use of polymer or ceramic-based materials in order to separate CO<sub>2</sub><sup>62</sup>. The main drawback of this method is the need for high-cost modules. The approach of cryogenic CO<sub>2</sub> separation is applied commercially for high concentration and high-pressure gases. But due to its high energy consumption, it is not an attractive approach<sup>28</sup>.

As mentioned above, the methods employed for CO<sub>2</sub> capture are cost demanding, due to the energy requirements (i.e., high temperature and pressure) and the equipment installations needed. More precisely, as mentioned by Dubey and Arora, the CO<sub>2</sub> capture technologies that are available in market are comprising the 70-80% of the total cost of capture, transport, and storage<sup>65</sup>. Therefore, alternative technologies involving advanced processes and materials, such as Metal Organic Frameworks (MOFs) are emerging. In this context, the approach of combining capture and conversion process by using multifunctional materials appears more attractive.

### *1.2.B. CO<sub>2</sub> storage*

Towards the achievement of CO<sub>2</sub> sequestration, carbon storage is a requisite step. Notably, this process concerns securely storing the carbon dioxide emissions, underground in depleted oil and gas fields or deep saline aquifer formations<sup>66</sup>. But the cost renders this approach economically non-profitable and obsolete. Another issue which raised concerns is that CO<sub>2</sub> could leak out of these underground reservoirs into the surrounding air or contaminate nearby water supplies. Also, this kind of human intervention can induce a pressure increase underground, resulting to seismicity<sup>67</sup>. In the contrary, carbon conversion is a more appealing and viable approach, minimizing these concerns.

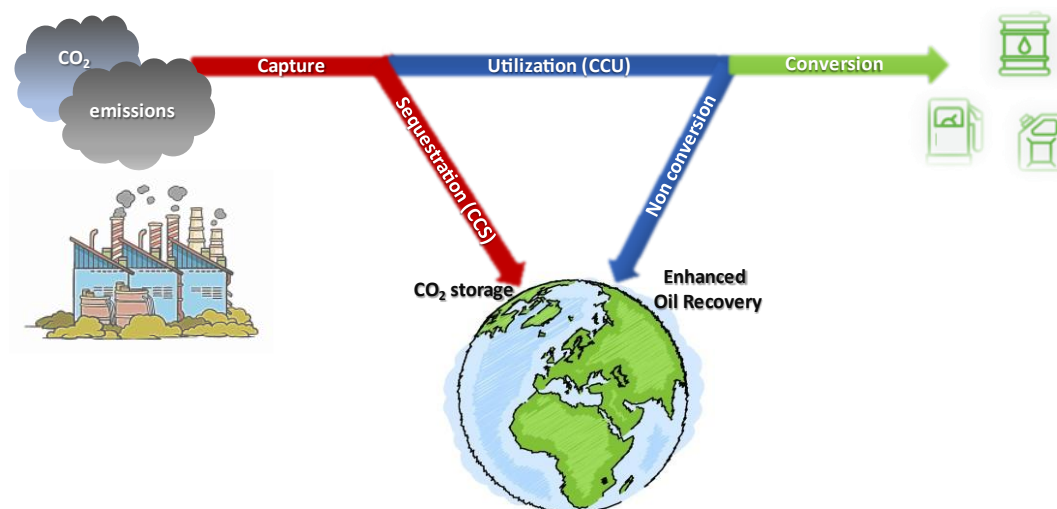


Figure 1. 4: CCUS schematic illustration

### 1.2.C. CO<sub>2</sub> conversion and utilization

As seen in Figure 1.4. CO<sub>2</sub> utilization can be divided into two main categories: a) the use of CO<sub>2</sub> as feedstock and b) as injection fluid for Enhanced Oil Recovery (EOR). For the former case, CO<sub>2</sub> can be converted into commercially valued products, like CO, CH<sub>4</sub>, CH<sub>3</sub>OH, hydrocarbons through several methods. One of them is the heterogeneous catalytic conversion which has been widely studied and can be achieved via two different routes<sup>68</sup>. The first involves a transformation in a multi-step process, using a classical Fischer-Tropsch synthesis through a Reverse Water-gas Shift (RWGS) reaction. The second way involves the CO<sub>2</sub> conversion into methanol (MeOH), followed by MeOH conversion into hydrocarbons. Several catalysts have been synthesized in order to meet the requirements of these processes for enhanced efficiency and high yield<sup>68</sup>. However, the main drawback of this approach is the high energy input that is required to achieve the desired operating conditions (i.e., high temperature and pressure).

Electrocatalysis is also a possible method for CO<sub>2</sub> reduction either using molecular catalysts<sup>69</sup> or metallic electrodes<sup>70</sup>. The electrochemical CO<sub>2</sub> reduction reaction (CO<sub>2</sub>RR) can be performed in an electrocatalytic cell, within aqueous solutions and the main products of the reactions are CO, formate and higher order products. As described by Jones et al. in their review paper, the appropriate choice of electrode can enhance the selectivity of the reaction products<sup>71</sup>. But the increased energy consumption during operation makes the process less environmentally friendly.

On the other hand, photocatalytic conversion of CO<sub>2</sub> into high-added value chemicals and fuels (CH<sub>4</sub>, CH<sub>3</sub>OH) is a more viable and economic approach. In photocatalysis ideally, the required energy is given by solar irradiation, eliminating further costs and

making it a promising approach. Thus, the development of photocatalysts with robust properties and the design of the process with the favorable conditions for enhanced efficiency and yield, are topics that have gained scientists' interest. In this manuscript, we will focus on this method. We chose to focus on this methodology because of this environmentally friendly character.

## II. Photocatalysis

### II.1. Natural Photosynthesis

The sun exists in our solar system since 4.6 billion years approximately and irradiates continuously solar light the Earth's surface across the visible and near-infrared ranges with a small part in the ultraviolet. This irradiation not only helps warm the Earth, but also the sun holds an essential role in the carbon cycle. Namely, through the process of photosynthesis, plants convert  $\text{CO}_2$  into chemically stored energy by using solar light, which produces food, wood, and the biomass from which thereafter fossil fuels are derived. Light harvesting is occurring in the green part of the plants by chlorophyll, a pigment which has  $\text{Mg}^{2+}$  ions in its center, with four pyrrole rings. One of it is bonded to a phytol tail, as seen in Figure 1.5a <sup>72</sup>. Furthermore, photosynthesis also needs a water source, provided to the plants from the soil via their roots. The overall process is comprised of two steps as seen in Figure 1.5b. In photosystem II (PSII) the photoinduced holes oxidize water to produce oxygen and protons. The photoexcited electrons are transferred via the electron transport chain, whereas the released protons are accumulated in one side of the membrane to convert ADP (adenosine diphosphate) into ATP (adenosine triphosphate). In photosystem I (PS I), electrons are excited by photons ( $\lambda \leq 700 \text{ nm}$ ) and the induced holes are quenched by the electrons produced by PSII. This allows the electron lifetime to be prolonged, therefore more reduction reactions can occur. The electrons from PSI are finally used to reduce NADP (nicotinamide adenine dinucleotide phosphate) to NADPH, which, together with ATP, provides the reduction power and energy for the conversion of  $\text{CO}_2$  to sugars <sup>73</sup>. Within this frame, photocatalysis has been introduced in order to mimic natural photosynthesis to produce energy vectors ( $\text{H}_2$ , carbonaceous products) by harnessing solar light as an energy source. Also considering the fact that this source is not going to be ceased, photocatalysis is considered as a viable and environmentally friendly approach.

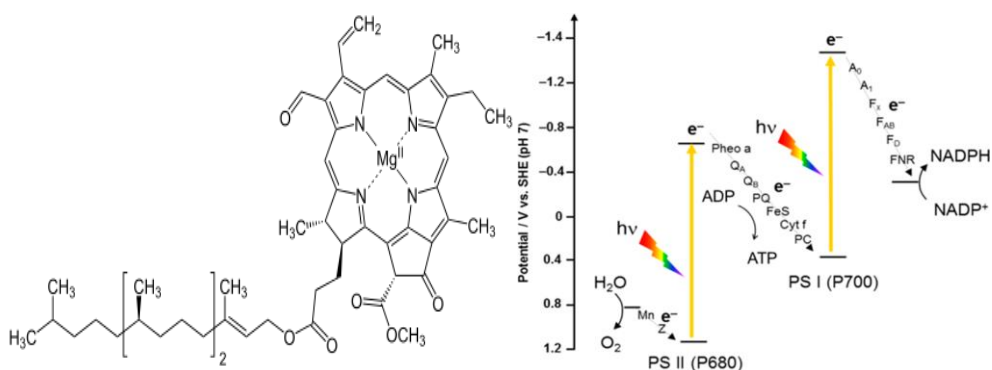


Figure 1. 5: (a) The molecule of Chlorophyll, where natural photosynthesis is taking place, (b) the Schematic Diagram of a Double Excitation Process in Natural Photosynthesis

## II.2. Principles of photocatalysis

The term photocatalysis is a combination of the two words photo- and -catalysis, and it indicates that the rate of a chemical reaction, or its initiation, can change under light exposure and in the presence of a material-the photocatalyst <sup>74</sup>. Under irradiation, photocatalysts are able to generate charge carriers, which are involved in the chemical transformation of the reaction substrates. We can divide these reactions into two categories: the homogeneous and heterogeneous photocatalysis. The former refers to reactions where the reactants and the catalyst are in the same phase, and the latter where the photocatalyst is in a different state. It is of particular importance that the heterogeneous photocatalytic process offers the advantages of an easy separation, recovery and reuse of the catalyst compared to homogeneous photocatalysts. Herein, the case of heterogeneous photocatalysis will be discussed.

The heterogeneous photocatalysis domain has always attracted the scientific community's attention, but this interest grew stronger after 1972. In that time, Fujishima and Honda discovered for the first time the photocatalytic splitting of water by using  $\text{TiO}_2$  electrodes, under light irradiation and by applying an external electrical bias <sup>75</sup>. Photocatalysis is then considered as a promising technology for sustainable solar fuels generation (hydrogen, carbon-based compounds) as alternative fuels. It is also regarded as an approach for environmental remediation, in particular for the air treatment <sup>76</sup> and the degradation of pollutants in water <sup>77</sup>.

## II.3. Mechanism of Photocatalysis

In general, heterogeneous catalysis involves 5 different steps <sup>78,79</sup>:

1. Transfer of the reactants on the surface of the photocatalyst
2. Adsorption of at least one of the reactants
3. Activation of the photocatalyst by light irradiation

## CHAPTER 1

- i. Photon absorption of energy higher than the bandgap Energy,  $E_g$
  - ii. Generation of excited charge carriers ( $e^-$ ,  $h^+$ ) in the semiconductor particles
  - iii. Separation of photogenerated charge carriers and their migration to the surface
  - iv. The recombination of charge carriers in the bulk
  - v. The recombination of charge carriers on the surface
  - vi. Reduction and oxidation reactions on the surface by the  $e^-/h^+$
4. Reaction of the adsorbed species
  5. Desorption of the products

### 11.4. Photocatalysts

#### 11.4.A. Properties

For the purpose of photocatalytic applications, the use of photocatalyst is prerequisite. Photocatalysts are semiconductor materials which hold suitable properties, possess an appropriate bandgap energy, and can be activated under illumination. Specifically, upon irradiation with an energy equal or higher than their bandgap, an electron from the valence band of the semiconductor is excited to the conduction band (CB), leading to the formation of a hole in the valence band (VB). Electrons and holes are named photogenerated charge carriers and can freely move within the semiconductor material. However, as it is depicted in Figure 1.6, part of the charge carriers can recombine without interacting with the adsorbed reactants. Charges that reach the surface of the photocatalyst can initiate chemical reactions with the adsorbed species <sup>79</sup>. In order to minimize the charge carriers' recombination, semiconductors (SCs) with high crystallinity are used, because they exhibit fewer trapping states and recombination sites and enhance charge carriers' mobility <sup>80</sup>.

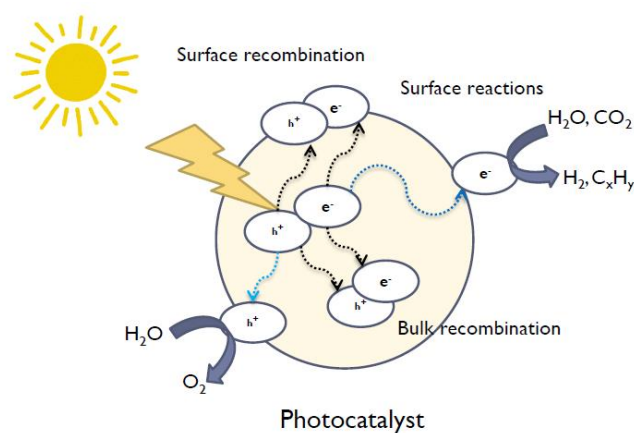


Figure 1. 6: Schematic illustration of the different pathways of photogenerated charge carriers in photocatalyst upon light irradiation

The  $E_g$  is an important property because it determines the wavelengths at which the semiconductor is active. Another crucial parameter that influences the initiation of redox reactions is the relative position of the VB and the CB. From a thermodynamic point of view, the surface reduction and oxidation reactions can be driven by the photogenerated  $e^-$  and  $h^+$ , respectively, only when their reduction and oxidation potentials lie between the CB and VB energy level of the semiconductor. It is worth mentioning that the biggest difference between the CB and the reduction potential of the targeted reaction is, the higher is the thermodynamic driving force. Figure 1.7 shows the band diagrams of the most commonly used SCs, with the redox potential of common reactions.

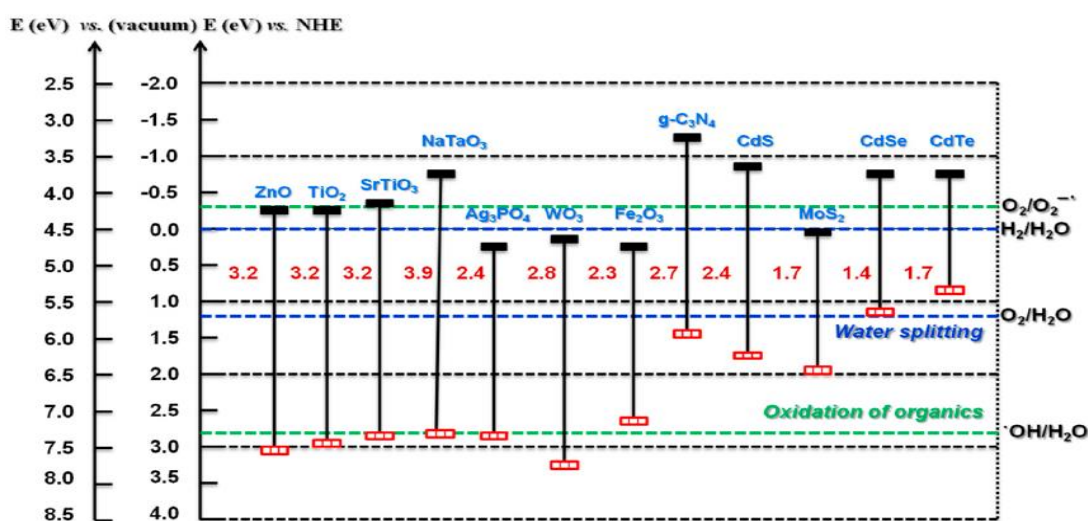


Figure 1. 7: Bands position of different semiconductors, regarding to the redox potential of water splitting reaction

However, it is worth mentioning that the appropriate VB and CB position is not enough when choosing photocatalysts. Chemical stability is also a determining parameter. For example, some of the reported catalysts (e.g., GaAs, CdS) can be easily photo corroded, and are also toxic, when working in aqueous conditions <sup>81</sup>. The properties of the photocatalysts are crucial in order to ensure high efficiency of the overall catalytic process steps (Chapter 1.II.3).

#### II.4.B. Strategies to improve the efficiency of photocatalysts

##### II.4.B.i. Morphology

Regarding catalytic processes, the efficiency is closely related to material properties. Therefore, materials engineering holds a key role towards improving efficiency. As it is mentioned in Chapter 1.II.4.A., adsorption of reactants is a crucial step during photocatalysis. This is not only linked with the available surface area, but also with the affinity of surface species with the reactants. Materials that present a high ratio

of surface-to-volume are considered beneficial for the adsorption and the diffusion of chemical species in their pores. In this direction, materials architecture has become a topic of increasing interest as it offers the potential to create materials with diverse and adaptable properties.

One-dimensional (1-D) nanomaterials possess a large surface-to-volume ratio, enhancing reactants adsorption. Furthermore, the one-dimensional confinement facilitates the transmission of quantum particles, such as photons, phonons and electrons<sup>82</sup>, allegedly resulting to a better charge carriers transport. Specifically, it has been reported that nanowires, nanorods and nanotubes are presenting 200-times fold enhanced charge transfer, comparing to their corresponding nanoparticles<sup>83</sup>. However, the existing methods of 1D nanomaterials fabrication are not favoring their utilization in large scale photocatalytic processes.

Moreover, materials holding sheet-like morphology (two dimensional-2D) are considered advantageous compared to their bulk counterparts and have gained attention over the last few years. Namely, 2D materials possess a small thickness ranging from a single to a few atomic thick layers, whereas the lateral size may extend up to micrometers. Their superior surface area is linked to the available active sites and can ameliorate the interaction with the reactants and enhance the mass transport to the active sites.

Their size constraints and the electron confinement in two dimensions offer them unique physical properties. Specifically, the migration distance is significantly shorter for the charge carriers, reducing the recombination rate<sup>84</sup>. Thus, the photogenerated charge carriers ( $e^-/h^+$ ) are abundant and available to reach the surface's active sites to initiate the redox reactions. Due to the electron confinement effect in thin layered nanomaterials, light absorption is increased even at low flux densities. This can affect the density of charges and consequently the actual electronic band structure<sup>85</sup>. In addition, it is stated that the density of electronic structure at the Fermi level plays a role in the adsorption and the binding of any reactant. More precisely, stronger binding is associated with the height of the center of the electronic structure relative to the energy of the Fermi level<sup>84</sup>.

2D structures can also be used as supports for the development of multicomponent materials, allowing a higher interaction between the different parts<sup>86</sup>. This approach has been investigated in the framework of these studies and will be discussed in [Chapter 2](#).

### II.4.B.ii. Heterojunctions

Coupling of SCs with different bandgap structures can also result in efficient charge separation. This strategy has been also widely studied as an approach to address light adsorption limitations. In this approach, SCs with proper bandgap structures are

required in order to direct the photogenerated  $e^-$  and  $h^+$  in the opposite direction, thus improving the charge separation. Two types of heterojunctions gained interest: the type-II heterojunction and the Z-Scheme heterojunction (Figure 1.8).

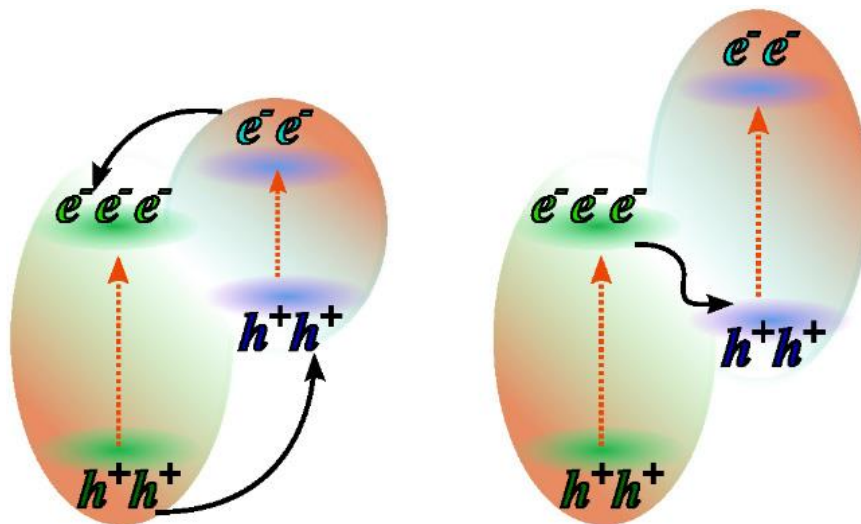


Figure 1. 8: Charge transfer in a type-II (left side) and a Z-scheme (right side) heterojunction:

Regarding type-II heterojunctions, the CB and the VB of SC A are higher than the corresponding bands of SC B. In this configuration, photogenerated holes will migrate to SC A, and the electrons will migrate to SC B, thus inducing a charge separation. A drawback of this approach is that the redox ability will be decreased, since the photogenerated charge carriers are spontaneously transferred from the higher energy band to the one positioned at lower energy levels. Moreover, electron migration to the electron rich conduction band of SC B and hole migration to the hole-rich VB of SC A is unfavorable due to electrostatic repulsions<sup>87</sup>.

In order to overcome these shortcomings, Yu et al. introduced in 2013 the direct Z-Scheme heterojunction where electrons and holes are spatially separated on the SC with the higher reduction and oxidation potential, respectively<sup>88</sup>. This charge-carrier migration pathway resembles the letter “Z” and imitates the natural photosynthetic reaction center<sup>89</sup>. Contrariwise to type-II heterojunctions, the charge transfer is physically more favorable on the direct Z-Scheme heterojunction, because of the electrostatic attraction between  $e^-$  and  $h^+$ <sup>87</sup>.

Up to now, a plethora of heterostructures of different photocatalytic materials has been reported in the literature, with emphasis not only on their electronic properties (i.e., band positions) but also on their morphologies. In particular, several studies have been reported using graphene-like materials in order to create heterojunctions for various photocatalytic applications, like  $H_2$  evolution, pollutant degradation, and  $CO_2$  reduction<sup>90–93</sup>. As a matter of fact, graphene possesses a 2D nanostructure

morphology that eases charge carriers' migration. El-Marouazi et al., managed to synthesize composite materials of  $\text{TiO}_2$  (P25) with different loading of Few-layers-graphene (FLG), aiming for photocatalytic application of  $\text{H}_2$  production from MeOH photoreforming. They found that composite materials with low loadings (0.5-1%) on FLG are 2-3 times more active than bare  $\text{TiO}_2$ . This is attributed to a more efficient charges separation due to electrons delocalization and trapping onto graphene layers well interfaced with  $\text{TiO}_2$  nanoparticles<sup>94</sup>.

Benefiting from the properties of materials bearing sheet-like morphology, the idea of developing heterojunctions between 2D-2D nanomaterials has also been investigated by several research groups. As long as we are targeting enhanced charge migration on heterojunction photocatalysts, the superiority of 2D-2D heterojunction over 0D-2D and 1D-2D heterojunctions is the larger surface contact, as it can be seen in Figure 1.9.

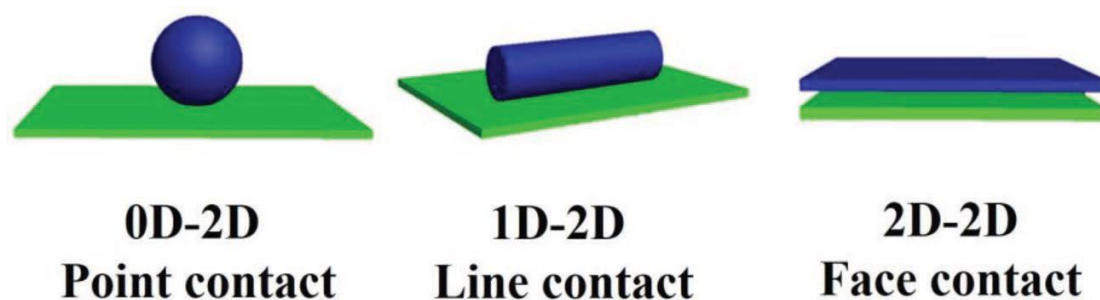


*Figure 1. 9: Schematic illustration of the advantageous contact between both components in 2D-2D composite photocatalysts in comparison to 0D-2D and 0D-1D composites layered composite photocatalysts*

The advantage of 2D-2D heterostructures over 2D-3D heterojunction has been highlighted by Crake and coworkers. In their study,  $\text{TiO}_2$  with bipyramidal or isostructural morphology has been coupled with CN Nanosheets. Both heterojunctions exhibited improved photocatalytic activity compared to bare  $\text{TiO}_2$ . However, the 2D-2D CN/ $\text{TiO}_2$  heterojunction exhibited a more favorable charge separation increasing the availability of photo-induced electrons, as shown by Transient Adsorption Spectroscopy. This is attributed to the enhanced surface contact<sup>95</sup>.

Apart from the cases that have been discussed already, the p-n heterojunction and n-n heterojunctions have been also presented in the literature<sup>96,97</sup>. However, the development of Schottky junctions is the approach that has been investigated the most, and it will be discussed further in the following section.

## II.4.B.iii. Metal deposition

Another effective strategy to ameliorate the charge separation is to develop heterojunctions between metal nanoparticles (MNPs) and SCs. As it is widely known, metals (M) are conductive materials, and the energy that is required to extract one electron from the Fermi level of the metal to the vacuum is described as work function ( $\Phi_M$ ). Semiconducting materials (i.e., oxides) present a higher Fermi level than metals<sup>98</sup> (Fig. 1.10 panel A). Usually n-type SCs are used, because in the p-type SCs the majority of charge carriers are holes that attract the electrons of the metal, resulting in charge neutralization<sup>99</sup>.

When the junction is formed, an interface, called the Schottky barrier, is created. At the interface of SC and MNP,  $e^-$  flow from one material to the other to align the Fermi energy levels to reach the equilibrium, which is called band bending, as it is shown in the panel B at Figure 1.10<sup>80</sup>. The flow of electrons from the semiconductor to the metal results in a depletion of electrons and correspondingly to a hole accumulation to the semiconducting material. Meanwhile the electrons are accumulated to the side of the metal close to the interface. This forms a depletion layer at the junction, which induces a localized potential barrier for the charge carrier, named the Schottky-like barrier (Fig. 1.10c). This barrier effectively assists the electron trapping, inhibiting the flow of  $e^-$  back to the semiconductor. Therefore, the recombination of photogenerated charge carriers is decreased<sup>100</sup>.

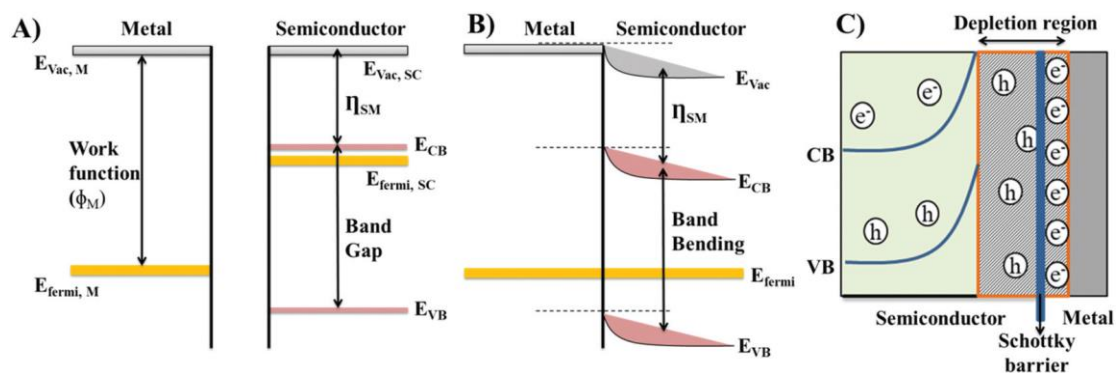


Figure 1. 10: Schottky barrier in the interface of SC/Metal nanoparticle: (a) before contact, (b) after contact

It is important to mention that another prominent feature of the M/SC junctions is the surface plasmonic resonance. In general, surface plasmon designates a collective oscillation of free charges on the surface of a conductive material. Upon light irradiation with frequency equal to the plasmonic resonance of the Metal, electrons are redistributed, thus generating electric field with frequency that varies depending on NPs size, shape and aggregate environment, this phenomenon is called Localized Surface Plasmon Resonance (LSRP)<sup>101</sup>. The mechanism of charge transport and

distribution across the Schottky barrier has been investigated intensively, but the influence of surface plasmon resonance to the photocatalytic mechanism is still under debate.

The mostly studied metals used for metal deposition are Au, Ag and Cu, which present plasmonic resonance into the visible region. Other noble metals able to significantly enhance the catalytic effects upon light irradiation are platinum (Pt) and palladium (Pd). Due to their unfilled d-orbitals, an inter-band excitation is induced and can facilitate reactions at the NPs surface <sup>102</sup>. Also, bimetallic alloy NPs deposition on semiconduction materials, is considered interesting due to the synergistic effects <sup>103</sup>.

As previously discussed, composition and morphology are very important for photocatalytic activity. Thus, the controllable synthesis of metal nanoparticles and deposition on semiconductors is crucial. Up till now, various approaches have been suggested, but the chemical methods present more advantages regarding monodispersity, compared to the physical ones <sup>104</sup>. Therefore, the method of chemical reduction is the most used. Specifically, it involves the synthesis of suspensions, where the metal precursor (metal salt) is dispersed. The addition of a strong reducing agent, like sodium borohydride (NaBH<sub>4</sub>), is mostly used to disperse MNPs of small sizes. In addition, in order to eliminate the NPs aggregation, capping agents are often employed. In general, reduction methods are frequently combined with impregnation methods for the deposition on semiconductors surface. Another method of reduction is photo-deposition where a light irradiation for e<sup>-</sup> generation is used instead of a reducing agent <sup>102</sup>.

## II.5. Artificial Photosynthesis

### *II.5.A. Photocatalytic Water Splitting*

#### *II.5.A.i. Mechanism of photocatalytic Water splitting*

Water splitting is a multi-electron process and endothermic reaction <sup>105</sup>. Specifically, the dissociation of water into H<sub>2</sub> and O<sub>2</sub> is an uphill reaction. The standard Gibbs free energy of the reaction is 237 kJ/mol<sup>106</sup>. In the case of photocatalytic water splitting, the energy required is provided by incident photons and the use of a photocatalyst is necessary. The overall reaction involves two electrochemical half-reactions: the oxidation of water to form O<sub>2</sub> (Eq.1.2) and the reduction of protons to form H<sub>2</sub> (Eq.1.3).

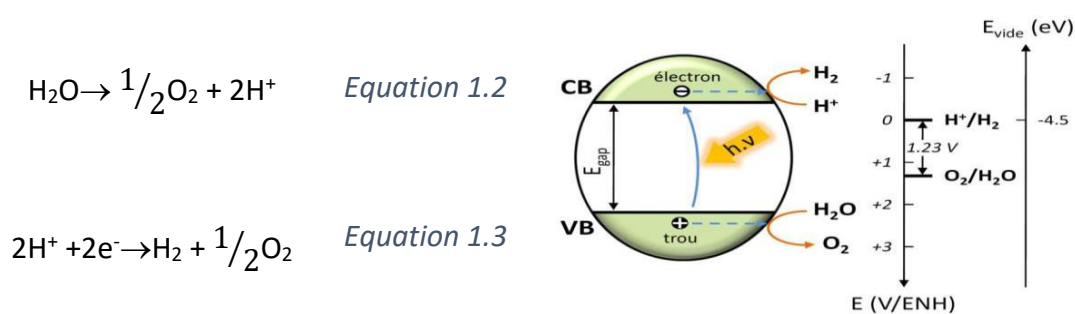


Figure 1. 11: Scheme of the overall photocatalytic water splitting with its redox potentials

It is also important to highlight that the dissociation of water is not spontaneous.  $\text{O}_2$  combines with  $\text{H}_2$  leading to the reverse reaction which is thermodynamically favorable ( $\text{H}_2(\text{g}) + \frac{1}{2} \text{O}_2(\text{g}) \rightarrow \text{H}_2\text{O}(\text{l})$   $\Delta\text{H} = + 57 \text{ Kcal}$ ). For this reason, it is recommended to remove the  $\text{O}_2$  formed during the reaction, by continuous bubbling with inert gases ( $\text{N}_2$ ,  $\text{Ar}$ ).

### III.5.A.ii Parameters that affect the efficiency of Photocatalytic water splitting

Till now, there have been numerous studies of semiconductor photocatalysts for solar energy conversion and environmental purification. However, the relatively low value of overall quantum efficiency limits the use of semiconductor photocatalysts. This is mostly attributed to the high recombination rate of photo-induced  $\text{e}^-/\text{h}^+$  pairs at or near its surface<sup>107</sup>.

In order to suppress the charge recombination, sacrificial reagents in low concentrations are used for their separation. Hole scavengers (electron donors) or electron scavengers (electron acceptors) are recommended in order to promote the  $\text{H}_2$  production reaction and the Oxygen Evolution reaction (OER), respectively. The most commonly used sacrificial reagents are methanol ( $\text{MeOH}$ )<sup>108</sup>, triethanolamine (TEOA)<sup>106</sup> or sodium sulfide/sodium sulfite<sup>109</sup> for oxide, carbon, and sulfide photocatalysts, respectively<sup>110</sup>.  $\text{H}_2$  photoproduction from water splitting in presence of other organic compounds in high concentrations, is called photo-reforming<sup>111</sup>. In this case,  $\text{H}_2$  production is thermodynamically more favorable, because the organic substrates (i.e.,  $\text{MeOH}$ ,  $\text{EtOH}$ ) have a lower oxidation potential than  $\text{H}_2\text{O}$ . Thus, minimizing the formation of  $\text{O}_2$  and consequently inhibiting the reverse reaction<sup>112</sup>.

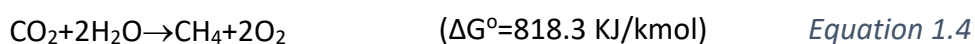
The effect of different sacrificial agents has been investigated in order to elucidate the mechanism of the reaction and how the nature of the sacrificial agent affects efficiency. Wang and coworkers studied the influence of several sacrificial reagents for various types of photocatalysts. Indicatively, their results suggested that TEOA

induced an increased H<sub>2</sub> evolution rate in comparison to the other sacrificial reagents, like methylamine, ethylamine and ethanediamine. TEOA can be oxidized irreversibly, forming a secondary amine and an aldehyde in presence of water <sup>113</sup>. They attributed this observation to the higher permittivity and the lower oxidation potential of TEOA, compared to other organic amine agents. They also mentioned that the length of carbon chain for alcohols or amines SRs, is inversely proportional to the H<sub>2</sub> evolution rate <sup>114</sup>.

### II.5.B. Photocatalytic CO<sub>2</sub> reduction

#### II.5.B.i. Historical review

Catalytic reduction of CO<sub>2</sub> with H<sub>2</sub>O into hydrocarbon fuels such as CH<sub>4</sub> and CH<sub>3</sub>OH is an uphill reaction with a highly positive change in Gibbs free energy, as the following equations show <sup>115</sup>:



By definition, a catalytic reaction has a negative difference in the Gibbs free energy,  $\Delta G^\circ < 0$ , where the catalyst lowers the kinetic barrier of the reaction without it being damaged, used-up, or inactivated <sup>116,117</sup>. In this strict sense, the photocatalytic reduction of CO<sub>2</sub> is not a catalytic process, because it is an uphill reaction, requiring a significant energy input,  $\Delta G^\circ > 0$ , which is provided by the incident photons <sup>118</sup>. However, the term photocatalytic reduction is often adopted in literature.

Halmanns was the pioneer of CO<sub>2</sub> photocatalytic conversion in 1978. He conducted photoelectrochemical CO<sub>2</sub> reduction to HCOOH, HCHO and CH<sub>3</sub>OH, using a p-type GaP electrode <sup>119</sup>. One year later, Inoue and Fujishima examined the CO<sub>2</sub> reduction in presence of water under a Xenon and a Mercury lamp. Since then, studies focused on understanding the reaction mechanism, the parameters influencing the overall efficiency of the process and the product selectivity.

#### II.5.B.ii. Mechanism of photocatalytic reduction of CO<sub>2</sub>

In order to perceive the mechanism of the process, we need initially to take into consideration the nature and the properties of CO<sub>2</sub>. Its linear structure and closed-shell electronic configuration renders CO<sub>2</sub> thermodynamically highly stable <sup>120</sup>, and it is difficult to reduce or oxidize it especially in mild temperatures. Photocatalytic CO<sub>2</sub> reduction by one electron approach is not thermodynamically favorable because it needs a very negative redox potential ( $E^\circ = -1.90 \text{ V}$ , vs NHE), as shown in Figure 1.12 <sup>115,121</sup>. Therefore, CO<sub>2</sub> reduction is more likely to occur via a multi electron transfer and a corresponding proton number. In this approach, the reduction reaction is taking place on the surface. Therefore, the loading of active cocatalysts and the

engineering of surficial defects is crucial in order to enhance the adsorption and promote interactions between active species <sup>122</sup>.

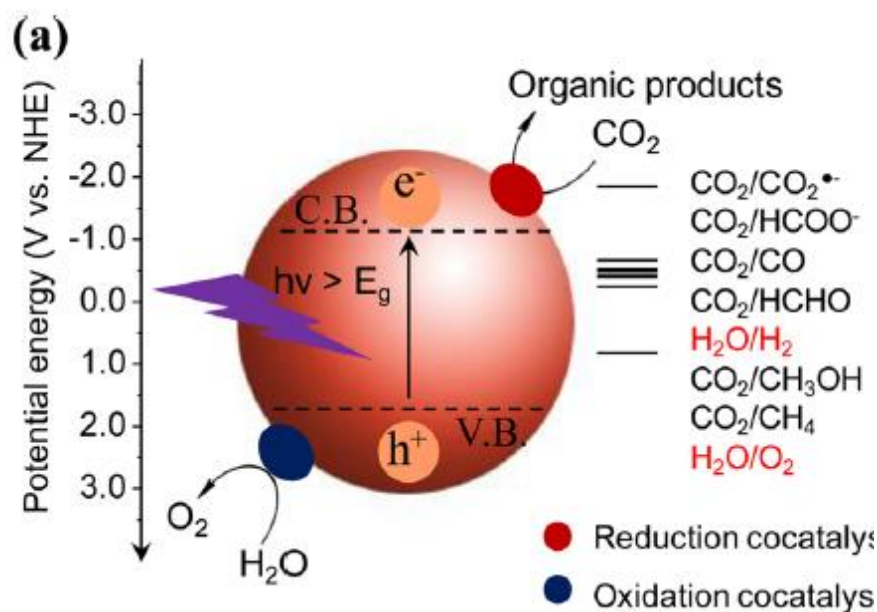


Figure 1. 12: Schema of the photocatalytic CO<sub>2</sub> reduction with its redox potentials

#### II.5.B.ii.a. CO<sub>2</sub> adsorption

The photocatalytic CO<sub>2</sub> reduction is a multistep process involving CO<sub>2</sub> adsorption, activation, and the dissociation of the C-O bond <sup>123</sup>. The initial step is the least studied, even though it is considered very critical for the reaction rate. Specifically, CO<sub>2</sub> is an acidic molecule which can be strongly adsorbed on the photocatalyst surface in presence of basic sites <sup>124</sup>. For instance, basic sites such as -OH and -NH<sub>2</sub> groups apt to donate their protons to CO<sub>2</sub> in order to form a negatively charged HCO<sub>2</sub><sup>δ-</sup> species, which is an important intermediate for carbon-containing chemicals <sup>125</sup>. Dias and coworkers proved that by tuning thermally carbon nitride samples, -NH<sub>2</sub> groups are formed, which are beneficial for CO<sub>2</sub> adsorption. CO<sub>2</sub> sorption isotherms showed that CO<sub>2</sub> uptake at 1 bar and 298 K increases with the thermal treatment, up to about 4 times <sup>126</sup>.

In addition, loading or incorporating alkaline or alkaline-earth metals on the photocatalyst facilitates the CO<sub>2</sub> adsorption, because photocatalysts have a higher affinity toward acidic molecules <sup>125</sup>. For example, Das et al. investigated the case of incorporation of magnesium in the core of organic ligand of the porphyrinic MOF PCN-224, which is considered to improve CO<sub>2</sub> adsorption. CO<sub>2</sub> sorption isotherms were recorded for the pristine MOF PCN-224 and the modified PCN-224(Mg), in order to compare their CO<sub>2</sub> adsorption capacity. The results showed that PCN-

224(Mg) exhibited an exceptionally high CO<sub>2</sub> uptake of 379.86 cc/g at 195 K, almost 1.6 times higher than that of PCN-224<sup>127</sup>.

Also, the presence of oxygen vacancies (V<sub>O</sub>) on the surface of the photocatalyst plays a key role in the CO<sub>2</sub> adsorption. Specifically, the oxygen atom of CO<sub>2</sub> can fill the vacancy site<sup>118</sup>. When the CO<sub>2</sub> is adsorbed, the molecule bends and therefore has a lower barrier for accepting an electron and its LUMO level decreases<sup>128</sup>. It is already shown by Indrakanti and coworkers that oxygen deficient TiO<sub>2</sub> is more beneficial for CO<sub>2</sub> reduction than stoichiometric TiO<sub>2</sub>. In particular, electrons from the conduction band may not be transferred to CO<sub>2</sub>, in irradiated, stoichiometric TiO<sub>2</sub> surfaces<sup>129</sup>.

#### II.5.B.ii.b. CO<sub>2</sub> activation and reduction

It is also important to understand the mode of CO<sub>2</sub> adsorption on the photocatalyst's surface. In order to do so, characterization techniques like in situ DRIFTS<sup>130</sup>, EPR spectroscopy<sup>131</sup> and Scanning Tunnel Microscopy (STM)<sup>132</sup> are employed. Each of the oxygen atoms of CO<sub>2</sub> has a lone pair of electrons and can donate these electrons to surface Lewis acid centers, whereas the carbon atom could also gain electrons from Lewis base centers such as oxide ions, forming a carbonate-like species. In figure 1.13, the three modes of CO<sub>2</sub> adsorption on the photocatalyst's surface are shown.

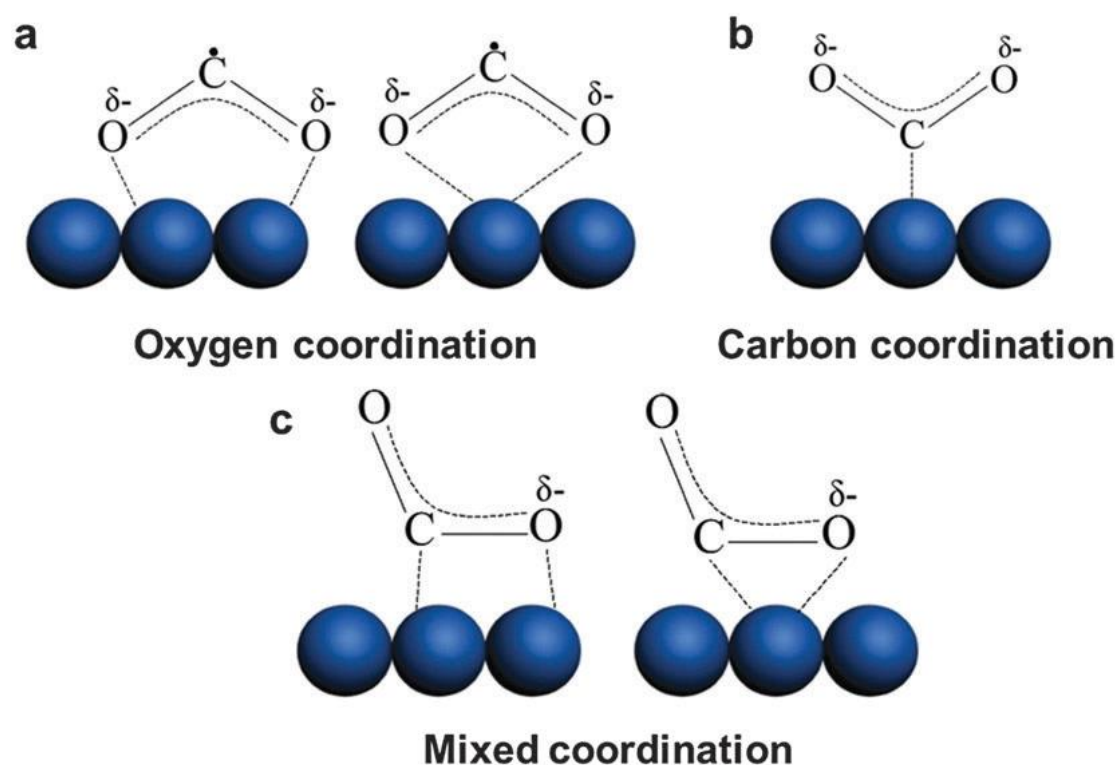


Figure 1. 13: CO<sub>2</sub> adsorption mode on photocatalysts surface by : (a) oxygen coordination, (b) Carbon coordination, (c) mixed coordination.

Specifically, CO<sub>2</sub> can be adsorbed by oxygen coordination mode (Fig. 1.13a), the following reaction step favors the formation of HCOOH, because the carbon atom of CO<sub>2</sub> can bind with hydrogen atom to form HCOO<sup>-</sup>, and consequently with a proton. This pathway is favored in reactions taking place in water because it presents high dielectric constant <sup>133</sup>. In the case of carbon and mixed coordination mode (Fig. 1.13b and 1.13c), the cleavage of C–O bond occurs first, thereinto, carbon monoxide is formed as product. If the catalyst shows moderate adsorption strength, then the CO will remain adsorbed and can act as the intermediate species for other products. However, when CO binds strongly to the metal, it can poison the active site. When CO binds weakly, it desorbs as a final product before any further reduction reaction occurs <sup>134</sup>. In the former case, the adsorbed CO can accept additional electrons and combine with up to four H• to form methyl radical and eventually methane. The methane production needs the least negative reduction potential, but it requires more electrons among C<sub>1</sub> products <sup>122</sup>. Methyl radical can further combine with a hydroxyl radical to result in methanol formation.

In order to reduce CO<sub>2</sub>, the presence of a reducing agent is mandatory. H<sub>2</sub>O is widely studied as an electron donor for this process because it is nontoxic and abundant. However, in this case, H<sub>2</sub>O reduction is a competitive reaction to CO<sub>2</sub> reduction. Therefore, H<sub>2</sub>O adsorption on the catalyst's surface is also of high importance, ensuring that it will be oxidized providing in that way the number of protons necessary for the CO<sub>2</sub> reduction. In 1989, Kurtz et al, used synchrotron radiation photoemission measurements to study the H<sub>2</sub>O adsorption on defective and non-defective TiO<sub>2</sub> catalyst. They showed that the oxygen vacancies found on the surface of TiO<sub>2</sub> annealed under ultra-high vacuum, are beneficial for H<sub>2</sub>O adsorption and dissociation <sup>135</sup>. Years later, after the development of computational method in materials science, Lindin et al. carried out DFT calculations for the adsorption of water on the (110) plane of rutile and confirmed that the defect sites benefited the absorption and dissociation of water. In another study, Bikondoa et al. suggested a mechanism of dissociation on the surface oxygen vacancy after STM visualization, where the H atom is removed and the O atom of the -OH group fills the vacant site <sup>136</sup>. Notably, H<sub>2</sub>O and CO<sub>2</sub> molecules may compete for the same V<sub>O</sub> site and the adsorption of CO<sub>2</sub> can be blocked by H<sub>2</sub>O, since the binding energies of H<sub>2</sub>O molecules are 0.64 eV higher than that of CO<sub>2</sub> on the vacancy site <sup>137</sup>.

Upon activation, the adsorbed CO<sub>2</sub> molecules are subsequently reduced by surface charge carriers. The reduction of CO<sub>2</sub> is a multi-electron process, which is more favorable than the one electron process. The different pathways for the reactions are given in the following equations:

## CHAPTER 1

$\text{CO}_2 + 2\text{e}^- \rightarrow \cdot\text{CO}_2^-$	<i>Equation 1.6</i>	$E^\circ(V \text{ vs. NHE}) = -1.90$
$\text{CO}_2 + 2\text{e}^- + 2\text{H}^+ \rightarrow \text{HCOOH}$	<i>Equation 1.7</i>	$E^\circ(V \text{ vs. NHE}) = -0.61$
$\text{CO}_2 + 2\text{e}^- + 2\text{H}^+ \rightarrow \text{CO} + \text{H}_2\text{O}$	<i>Equation 1.8</i>	$E^\circ(V \text{ vs. NHE}) = -0.53$
$\text{CO}_2 + 4\text{e}^- + 4\text{H}^+ \rightarrow \text{HCHO} + \text{H}_2\text{O}$	<i>Equation 1.9</i>	$E^\circ(V \text{ vs. NHE}) = -0.48$
$\text{CO}_2 + 6\text{e}^- + 6\text{H}^+ \rightarrow \text{CH}_3\text{OH} + \text{H}_2\text{O}$	<i>Equation 1.10</i>	$E^\circ(V \text{ vs. NHE}) = -0.38$
$\text{CO}_2 + 8\text{e}^- + 8\text{H}^+ \rightarrow \text{CH}_4 + 2\text{H}_2\text{O}$	<i>Equation 1.11</i>	$E^\circ(V \text{ vs. NHE}) = -0.24$
$2\text{H}_2\text{O} + 4\text{h}^+ \rightarrow \text{O}_2 + 4\text{H}^+$	<i>Equation 1.12</i>	$E^\circ(V \text{ vs. NHE}) = +0.81$
$2\text{H}^+ + 2\text{e}^- \rightarrow \text{H}_2$	<i>Equation 1.13</i>	$E^\circ(V \text{ vs. NHE}) = +0.42$

As it can be observed by the Eq. 1.12, the water oxidation half-reaction needs 4 holes, rendering the reaction kinetics sluggish<sup>138</sup>. Also, there is a possibility that the oxidation of the reaction intermediates before the carbon products are generated, thus the use of H<sub>2</sub> as electron donor agent minimizes these bottlenecks. Specifically, using H<sub>2</sub> instead of water as the reducing agent could turn CO<sub>2</sub> reduction into exothermic reactions, improving the photocatalytic activity<sup>139</sup>.

### II.5.B.iii Parameters that affect the efficiency of CO<sub>2</sub> reduction

It is also important to highlight that the type of photocatalyst, the thermodynamic reduction and oxidation potentials, the pH of the solution when working in liquid phase, the flow rate and the contact time between the reactant gases and the catalyst, are factors that can influence the final product selectivity<sup>140</sup>. Also, an optimum feed ratio between CO<sub>2</sub> and H<sub>2</sub>O, needs to be used in order to avoid hindering the CO<sub>2</sub> adsorption on the photocatalysts active sites<sup>125</sup>. Furthermore, the type of reactor can affect the efficiency of CO<sub>2</sub> reduction. In their work, Thomson et al. collected data for the kinetics of CO<sub>2</sub> reduction for continuous flow and batch conditions. This study shows that photoreactors are likely to minimize mass-transfer restrictions when working in continuous flow<sup>141</sup>. On the contrary, it has been shown that batch reactors obtain higher photocatalytic performances but lower selectivity because of the accumulation of products inside the reactor<sup>142</sup>.

In addition, the phase of the reaction plays a key role too. Indicatively, carrying out CO<sub>2</sub> reduction experiments in liquid phase, in a slurry reactor enhances the heat and the mass transfer due to the continuous agitation. However, it can reduce the efficiency due to absorption and scattering phenomena by the reaction media<sup>143</sup>. It is also important to highlight the fact that when working with liquid media, the pores of the photocatalyst can be blocked, inhibiting the adsorption and the diffusion of CO<sub>2</sub>. Moreover, when the reaction takes place at gas phase, we can neglect the pH parameter.

Temperature and pressure also play a critical role in the efficiency of photocatalytic CO<sub>2</sub> reduction. For example, both can regulate the CO<sub>2</sub> adsorption on the photocatalysts surface. Specifically, the adsorption potential of CO<sub>2</sub> improves significantly when the temperature decreases and the pressure increases <sup>144</sup>. Also, a temperature augmentation enhances the desorption of the reaction products, and consequently improves the efficiency of the process, as shown by Tahir and Amin <sup>145</sup>.

As can be observed in Eq.1.6-1.11, there is more than one possible product. Thus, the selectivity for the photocatalytic reduction of CO<sub>2</sub> must also be taken into consideration. High selectivity towards specific products formation is highly desirable since it will control the necessity of costly separation processes. Li et al. tried to summarize the influence of different cocatalysts on the selectivity of CO<sub>2</sub> reduction by comparing recent works. Pd, Pt, or Au are mentioned more favorable for CH<sub>4</sub> production; Ag for CO, CH<sub>4</sub>, or CH<sub>3</sub>OH, Cu for hydrocarbons and Cu<sub>2</sub>O, RuO<sub>2</sub>, or NiO<sub>x</sub> for CH<sub>3</sub>OH production <sup>146</sup>.

### III. Carbon nitride

#### III.1. Generalities

Carbon nitride is a metal-free polymeric semiconductor which has gained a lot of interest over the last few years thanks to its intrinsic properties <sup>147</sup>. It possesses various allotropes, such as graphitic-C<sub>3</sub>N<sub>4</sub>, cubic-C<sub>3</sub>N<sub>4</sub>, β- C<sub>3</sub>N<sub>4</sub>, and α- C<sub>3</sub>N<sub>4</sub> <sup>148</sup>. Among them, the most stable allotrope is g-C<sub>3</sub>N<sub>4</sub> <sup>149</sup>. The discovery of g-C<sub>3</sub>N<sub>4</sub> as photocatalyst for H<sub>2</sub> evolution was first reported by Wang et al in 2009 <sup>150</sup>. However, g-C<sub>3</sub>N<sub>4</sub> first appeared longer time ago, when Liebig first synthesized a yellow amorphous insoluble compound, named as melon, via the direct thermal polymerization of ammonium chloride and potassium thiocyanate <sup>151</sup>. Since then, different precursors and various routes of synthesis have been studied and are presented in [Chapter 1.III.3](#).

#### III.2. Properties

C<sub>3</sub>N<sub>4</sub> (CN) possesses high thermal stability up to 600 °C, thanks to the aromatic ring C-N bonds. Furthermore, the stacking with optimized van der Waals interactions between single layers of CN makes it insoluble in most solvents, inducing high chemical resistance <sup>152,153</sup>. As semiconductor material, it possesses a moderate bandgap of 2.7–2.8 eV, implying that it exploits visible range of solar light of around 450–460 nm <sup>154</sup>. This is in consistency with its yellow color. The CB and VB are suitably placed around the water oxidation and reduction potentials, favoring water splitting reaction, as it can be seen in Figure 1.7. CN has a unique two-dimensional layered structure, which is favorable for hybridizing with other components.

### III.3. Methods of Synthesis

CN is easily synthesized through the thermal polycondensation of nitrogen-rich precursors, like melamine<sup>126,155</sup>, urea, thiourea, dicyanamide<sup>156</sup> and cyanamide. Thomas et al. mentioned that the first step of the reaction starts with condensation of the precursors towards melamine, which is observed at around 350 °C. At approximately 390 °C, a condensation reaction occurs, which eliminates ammonia and forms melem monomers, later condensed into melon, a linear polymer of tri-s-triazine units. The presence of melem as an intermediate product was investigated by Jürgens, et al. More precisely, they studied the condensation of melamine rings to Graphitic Carbon Nitride by using characterization techniques like X-ray Powder Diffractometry and Solid-State NMR<sup>157</sup>. Lastly, the formation of the final product is taking place at around 520 °C, after condensation of the units, forming the polymeric CN till it becomes stable up to 600 °C. However, due to incomplete condensation of the amines, the intermediate products cannot be removed and stay as residuals. Therefore, the ratio C/N in the final product is far from the ideal (=0.75). In the final product, carbon and nitrogen atoms present  $sp^2$  hybridization, thus creating a delocalized  $\pi$ -conjugated system in the aromatic ring of the tris-s-triazine ring structure forming 2-D planes. The different planes are connected by the weak van der Waals force with an interlayer space of approximately 0.326 nm<sup>151</sup>.

As it is observed in Figure 1.14, the conditions of the thermal polycondensation process and the properties of the final product differ slightly, depending on which precursor is used. Among them, urea, thiourea and melamine are the most studied precursors. Specifically, Zheng et al. synthesized CN samples from urea or melamine by varying the pyrolysis temperature, and compared their photocatalytic activity towards Rhodamine B degradation<sup>158</sup>. They showed that the samples which are synthesized from urea present better adsorption and photocatalytic properties, at high temperatures. This was attributed to their enhanced surface areas and was coherent with other studies in the literature. In particular, during the pyrolysis of urea, a large sum generated gases, such as  $NH_3$ ,  $H_2O$  and  $CO_2$ , can function as soft templates to produce porous structure<sup>159,160</sup>. Additionally, Martin et al. successfully synthesized Carbon Nitride samples with different precursors (urea, dicyandiamide, thiourea). In their study, they showed that the urea-derived g- $C_3N_4$  evolved hydrogen at approximately  $20000 \text{ mmolh}^{-1} \text{ g}^{-1}$ , 15 times faster than Dicyandiamide-derived and 8 times higher than thiourea-derived g- $C_3N_4$ , as reflected in the turnover number. According to XPS characterization, FTIR spectroscopy,  $\zeta$ -potential measurements and XRD, they showed that both the protonation status and the degree of polymerization can influence the g- $C_3N_4$  hydrogen-evolution rate<sup>161</sup>.

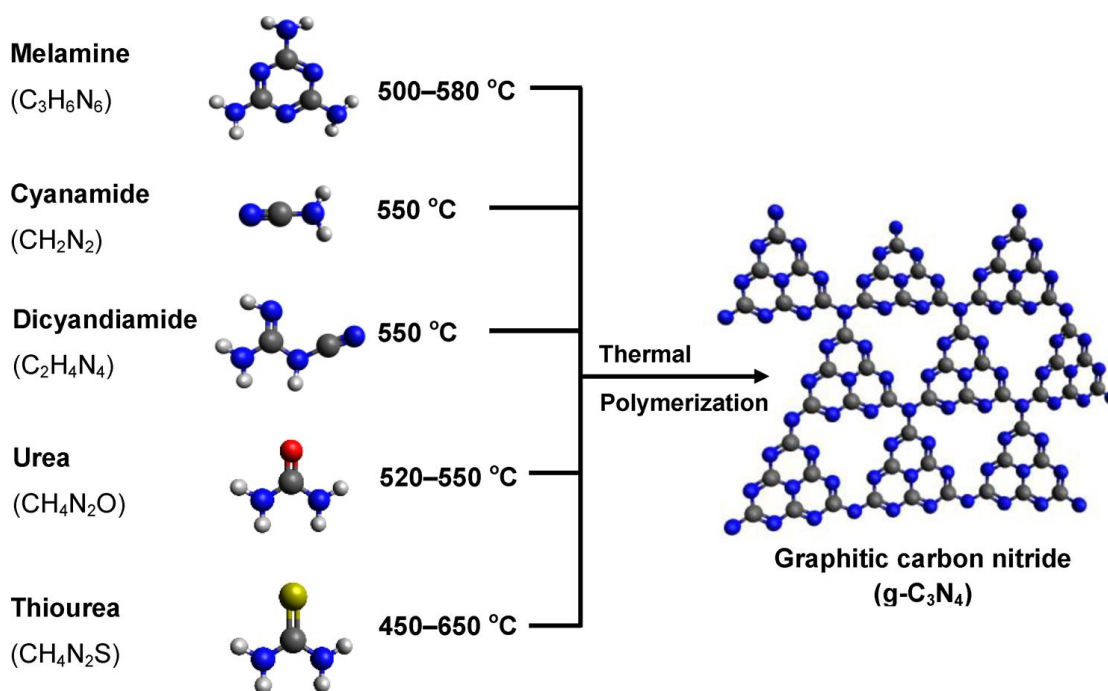


Figure 1. 14: Schematic illustration of the synthesis process of g-C<sub>3</sub>N<sub>4</sub> by thermal polycondensation from different precursors.<sup>162</sup>

Although CN is a promising photocatalyst with an easy synthesis process using low-cost feedstock, it shows some drawbacks which inhibit practical applications. Specifically, when it is prepared by direct polycondensation of C-, N- and H-containing precursors, it possesses poor crystallinity and low surface area (ca. 10 m<sup>2</sup> g<sup>-1</sup>)<sup>150</sup>. To tackle these disadvantages and improve their photocatalytic properties, a lot of strategies can be employed. It is already reported in the literature that the CN presenting 2D morphology have been shown more active in both H<sub>2</sub> production as well as CO<sub>2</sub> reduction<sup>86,95</sup>. As it is mentioned in [Chapter 1.III.2.](#), CN has strong in-plane chemical bonds, but weak out-of-plane interactions. Therefore, it could be relatively easily exfoliated into atomically thin nanosheets by breaking the van der Waals bonds<sup>163</sup>. This breaking can be achieved with an energy input higher than the bond energy, through thermal exfoliation<sup>126</sup>, mechanical exfoliation<sup>164</sup>, liquid exfoliation<sup>165</sup> or ion intercalation<sup>166</sup>. The exfoliation not only results in increased BET surface area but also could facilitate the electron transfer to the surface-active sites<sup>167</sup>.

In their study, de Medeiros et al. performed an exfoliation of melamine derived carbon nitride by thermal and chemical route. They showed that both treatments delaminated the material, but the chemical exfoliation via acidic treatment (i.e., H<sub>2</sub>SO<sub>4</sub>) increased the CN material thickness and induced defects and oxygenated functional groups on the surface, as shown by TEM, XRD and XPS characterization respectively. Whereas the thermal treatment resulted to a blue shift of the light

absorbance, i.e., increase of the  $E_g$  <sup>168</sup>. Compared to the numerous approaches for exfoliation, the thermal treatment is the most appealing thanks to its low-cost, non-toxicity and easy scale-up. Towards this end, Qiu et al. successfully prepared CN nanosheets of ca. 2 nm by calcining bulk CN under  $H_2$ . The synthesized CN nanosheets exhibited improved catalytic activity and stability towards MB degradation, under visible light irradiation, compared to bulk CN. Time-resolved fluorescence spectra showed that the charge carriers generated by CN nanosheets had an average carrier lifetime of 9.799 ns. Which has been improved compared with the one of bulk CN (with 5.156 ns). This implies that the recombination of photogenerated holes and electrons was inhibited in CN nanosheets <sup>169</sup>.

Bottom-up approaches like “hard” and “soft” templating are also widely reported in the literature as versatile techniques to form nanostructured or porous materials. The challenge here lies in the choice of appropriate template structures, which will define the pore shape and size <sup>170</sup>. The first approach uses solution-phase molecules or surfactants in order to direct assembly a material, whereas “hard” templating uses solid materials, like silica, anodized alumina oxide or carbon to cast a second material <sup>107</sup>. Li et al, synthesized mesoporous CN using spherical mesoporous cellular silica foams (MCFs) as a hard template, and ethylenediamine and carbon tetrachloride as precursors. The resulting CN materials possess a relatively high BET surface area of  $\sim 550 \text{ m}^2 \text{ g}^{-1}$ , and a pore volume of  $0.90 \text{ cm}^3 \text{ g}^{-1}$ , with abundant basic sites enhancing the  $\text{CO}_2$  uptake <sup>57</sup>.

In order to enhance light absorption, semiconductor’s bandgap engineering is necessary in order to introduce midgap states. In that regard, defect engineering technique is extensively employed to alter the material’s band structure <sup>171</sup>. In the case of CN, defects can be classified in 4 categories, including Carbon vacancies (CVs), Nitrogen Vacancies (NVs) and derivative functional groups (amino and cyano groups) <sup>172</sup>. Namely, the introduction of vacancies significantly affects the photocatalyst’s band configuration, whereas the amino groups are regarded as charge traps sites reinforcing the charge transport and photocatalytic redox reactions <sup>173,174</sup>.

Another strategy for improving physicochemical properties and photocatalytic activity of CN samples is the modification of its chemical composition. To attain this, doping with metal or with non-metal elements is applied. Namely, non-metal element (such as B, P, O, S) doping has been suggested as effective strategy to tune the electronic structure of CN <sup>162</sup>. It was suggested that the doped P formed new surface states near to the CB bottom of CN. On the other hand, B-related surface states could trap the photogenerated holes so that the charges were separated more efficiently <sup>175</sup>.

Finally, the coupling of SCs is widely studied as an efficient way to overcome fast charge recombination and/or extend light adsorption. These two types of heterojunctions have been discussed in [Chapter 1.III.4.B.ii](#).

Particularly, carbon nitride-based heterojunctions are claimed to facilitate spatial separation and charge mitigation. It can also improve the overall visible-light absorption. Furthermore, the literature mentions that heterojunction composites based on metallic oxide are identified as an efficient pathway to promote the photocatalytic performance of semiconductor materials <sup>176</sup>. An example is the case of TiO<sub>2</sub>/CN heterojunctions between the two most used semiconductors, which has been studied by our lab. Specifically, Marchal et al. synthesized Au-TiO<sub>2</sub>/CN heterojunctions, which showed enhanced visible-light harvesting, efficient charge separation, and enhanced H<sub>2</sub> production, compared to the Au/TiO<sub>2</sub> and Au/CN composite materials <sup>177</sup>.

## IV. Titanium dioxide

### IV.1. Generalities

TiO<sub>2</sub> is a photocatalyst which gained a lot of interest since the 19th century thanks to its high chemical and thermal stability, low cost and non-toxicity. It occurs in nature in three polymorphs: anatase, brookite and rutile. The first two are metastable allotropes which results to thermodynamically stable rutile, when calcined at temperature above T=600 °C <sup>178</sup>. The transformation of phases is achieved with an increase of temperature or pressure and is influenced by several factors, such as the particle size, the concentration of lattice and the presence of surface defects <sup>179</sup>. In particular, Zhang and coworkers studied the transformation of phases in Titania during calcination and found that anatase and brookite structures transformed to the rutile phase after reaching a certain particle size <sup>180</sup>. It is worth mentioning that for particles above 35 nm, rutile is the most stable phase, whereas for nanoparticles below 14 nm anatase is the most stable. In addition, it is already shown that the presence of defect sites, and more precisely the oxygen deficiency, accelerates the transformation <sup>179</sup>.

### IV.2. Properties

All three TiO<sub>2</sub> forms share an octahedral morphology (Fig. 1.15). However, they present different exposed planes. Precisely, anatase is made up of eight facets, in the middle and in the corners of which Ti<sup>4+</sup> and O<sup>2-</sup> atoms are located, resulting in tetragonal structure <sup>181</sup>. The most prevalent facet for anatase nanocrystals is the low energy (101) surface, that coexists with (001) plane. In the case of rutile, the most dominant surfaces are (100) and (110) <sup>182</sup>. The latter is the most thermally stable,

therefore it is the most widely studied in literature. Unlike anatase and rutile which present tetragonal crystal structures, brookite presents an orthorhombic structure, and currently is the less investigated phase of  $\text{TiO}_2$  as photocatalyst.

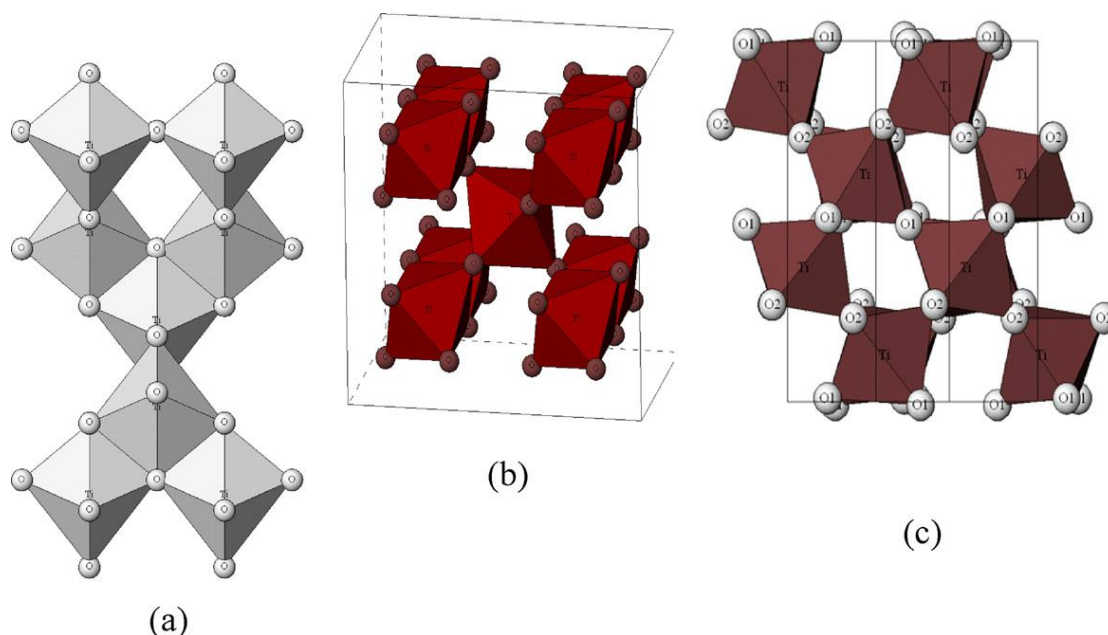


Figure 1. 15: Crystalline structures of: (a) anatase, (b) rutile, (c) brookite

Due to its oxygen deficiency,  $\text{TiO}_2$  is typically an n-type semiconductor. The VB of  $\text{TiO}_2$  is composed of the 2p orbitals of oxygen, while the CB is formed by the 3d orbitals of titanium<sup>183</sup>. Anatase is an indirect semiconductor and presents an  $E_g$  of 3.2 eV, whereas rutile holds a smaller bandgap between the CB and the VB equal to 3.0 eV. In other words, anatase exhibits poorer absorbance towards solar light, however it presents higher photocatalytic activity than rutile. The anatase structure is preferred over other polymorphs for solar cell applications because of its higher electron mobility, low dielectric constant and lower density<sup>81</sup>. It is due to the fact that anatase exhibits longer lifetime of charge carriers. Specifically, Zhang et al. used DFT calculations to examine the excitation of the photogenerated electrons in three polymorphs of  $\text{TiO}_2$ . They showed that there is a direct excitation from the Valence Band to the Conduction band in rutile and brookite, whereas anatase only presents indirect excitations<sup>184</sup>.

Upon light irradiation,  $\text{TiO}_2$  generates charge carriers which can be trapped as  $\text{Ti}^{3+}$  and  $\text{O}^-$  defect site<sup>185</sup>. Spectroscopic techniques are employed to study the lifetime of electrons and holes. Transient absorbance spectroscopy (TAS) can be used to follow the kinetic decay of the photogenerated species. Serpone et al. studied the subnanosecond relaxation dynamics in  $\text{TiO}_2$ , and found that 30 ps upon excitation, electrons are trapped as  $\text{Ti}^{3+}$  species and almost 90% of the photogenerated

electrons are combined in 10 ns<sup>186</sup>. In the case of hole trapping, the reported time is 250 ns<sup>187</sup>. Time-resolved microwave conductivity (TRMC) can also investigate the dynamics of photogenerated charge carriers. This technique measures the relative change of the microwave power reflected from an analyzed sample<sup>188</sup>. Colbeau-Justin et al. employed TRMC method to study the charge carrier's behavior on different polymorphs of TiO<sub>2</sub> (anatase, rutile, mixed anatase/rutile). They found that in anatase, electrons have a longer lifetime<sup>189</sup>.

Another technique which has been used to study the recombination of charge carriers is Photoluminescence. Specifically, charge recombination in TiO<sub>2</sub> can be accompanied by light emission via radiative routes. Both anatase and rutile present an emission peak in the visible and the near-IR wavelength range. The Photoluminescence (PL) for anatase has been related to self-trapped excitons, and, for rutile, to intrinsic sites or to surface bound species<sup>190,191</sup>.

### IV.3. Methods of synthesis

Until now, different synthetic pathways have been reported for the preparation of TiO<sub>2</sub>. The synthesis method allows the control of stoichiometry, morphology, and particle size. Precisely, the solvothermal method gives control over the grain size, the particle morphology, and the crystalline phase. On the other hand, sol-gel method results in TiO<sub>2</sub> with high purity and enhanced homogeneity<sup>179</sup>. In addition, TiO<sub>2</sub> is already commercially available, for example, P25 TiO<sub>2</sub> crystallites are sold by Evonik (Degussa) and contain a mixture of anatase (~80%) and rutile (~20%). Another commercial TiO<sub>2</sub> is Hombikat UV100 consisting only of anatase. This kind of TiO<sub>2</sub> can be directly used as photocatalysts, or after treatment, usually a thermal treatment to remove the surface -OH groups and the amorphous part.

Up till now, TiO<sub>2</sub> has been considered as a promising photocatalyst, but presents a few limitations. The most significant drawback is the limited light adsorption of the solar spectrum. In this context, doping with ions (anionic or cationic) allows a bathochromic shift in the absorbance spectrum. Specifically, it involves the decrease of the bandgap by introducing intra-band gap states<sup>81</sup>. Furthermore, the combination of rutile and anatase improves charge separation. The CB of rutile is more positive than that of anatase. This allows rutile phase to act as an electron sink for photogenerated electrons in anatase/rutile junctions, i.e., electrons flow from anatase CB to rutile CB<sup>192</sup>. Another strategy intending to tackle simultaneously fast charge recombination and enhanced absorbance in visible region, is the deposition of MNPs (Au, Ag). The metal nanoparticles have a bifunctional role, they present high light-adsorption efficacy in the visible domain, and can serve as electron sinks to suppress the electron-hole recombination rate<sup>193</sup>. Lately, development of

heterojunctions between  $\text{TiO}_2$  and Metal Organic Framework structures<sup>194</sup> has also been introduced as a strategy to improve the photocatalytic performance of  $\text{TiO}_2$ .

## V. Metal Organic Frameworks

### V.1. Generalities

Metal Organic Frameworks (MOFs) are a new class of hybrid highly crystalline materials. They are assembled from metal ions or metal clusters linked between them with organic ligands<sup>195</sup>. The choice of metal clusters, organic ligands and their combination is infinite. This renders MOFs as highly versatile materials with tunable properties. The building units of MOFs are carefully chosen according to the needed application. This interesting class of materials have several applications in diverse areas, such as for gas storage<sup>196</sup>, drug delivery<sup>197</sup>, sensors<sup>198</sup>, and catalysis as it can be seen in Figure 1.16<sup>199</sup>.

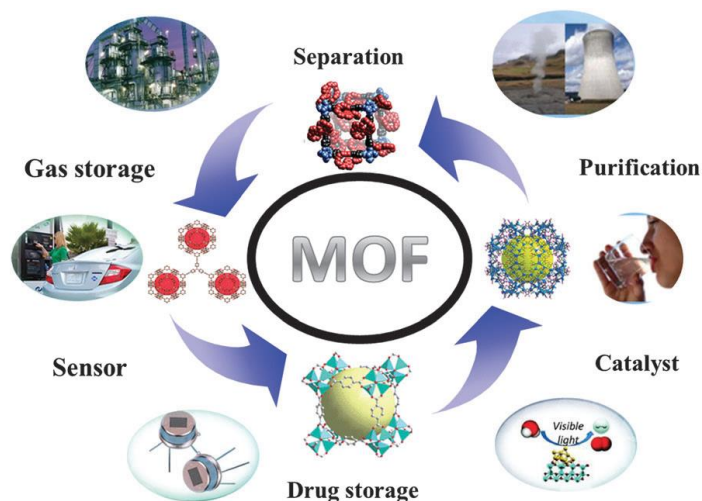


Figure 1. 16: Various applications of MOF materials

Since their first discovery, a lot of different families of MOFs have been developed and reported in the literature. The classification is based on their structure and composition. Some of the biggest families of MOFs include:

1. **Zeolitic Imidazolate Frameworks (ZIFs):** This subcategory of MOFs presents a structure similar to Zeolites. ZIFs contain imidazolate linkers and exhibit exceptional chemical and thermal stability, high surface area, and tunable pore size. A big advantage of this family of materials is that it can be synthesized under mild conditions (i.e., room temperature)<sup>200</sup>.

2. **Porphyrim-Based MOFs:** Porphyrim-based MOFs are a family of MOFs containing porphyrim linkers, which are planar molecules allowing coordination to metal ions or clusters <sup>201</sup>.
3. **UiO-Type MOFs:** UiO-type are named after the University of Oslo, where they were first synthesized. They are composed of Zr oxo-clusters (Zr<sub>6</sub>) and dicarboxylate ligands resulting in highly porous networks <sup>197</sup>. The Zr MOFs are characterized by their large pore sizes and high stability due to their 6-connectivity <sup>202</sup>.
4. **MIL-Type MOFs:** MIL-type MOFs are a family of MOFs, where MIL stands for Materials of Institute Lavoisier, where they were first synthesized. MILs are typically composed of carboxylate and trivalent cations such as iron(Fe), aluminum(Al), gallium(Ga), indium (In), vanadium(V), and chromium (Cr) <sup>203</sup>.

Except for these categories, many other families of MOFs exist, and new families and structures continue to be discovered and synthesized. In the following section, the different methods of MOFs synthesis will be discussed.

## V.2. Methods of synthesis

Different methods of synthetic approaches for MOFs have already been described in the literature. In most cases, MOFs are synthesized under high temperature and pressure via a solvothermal method. Polar solvents are chosen, and the temperature of the reaction is above the boiling point of the solvent. It is shown that high temperature facilitates the bond formation by affecting the crystallization kinetics, and ensures the proper crystallization <sup>204</sup>. Moreover, the solvent can participate in the formation of MOF by weak intermolecular interactions contributing to the crystal stability of the network.

Except for the choice of the proper solvent, the utilization of a modulator is also crucial when synthesizing MOFs, as a mean to control the particle size <sup>205</sup>. Specifically, a large excess of acids is often employed to regulate the nucleation and growth of MOFs during the synthesis, thus avoiding the rapid precipitation of the amorphous product. The most commonly used modulators are hydrochloric (HCl), benzoic (C<sub>6</sub>H<sub>5</sub>COOH) and acetic acid (CH<sub>3</sub>COOH). Another significant role of modulators is the regulation of the crystal phase purity. In detail, Kelty and coworkers showed that MOF-525, MOF-545 and PCN-223 are sharing the same precursors, and the use of a modulator is mandatory in order to favor the synthesis of the desired product <sup>206</sup>.

Another alternative method for MOF synthesis is the sonochemical approach. Precisely, the reaction between the metal centers and the organic ligands takes place under high-energy ultrasonic irradiation. When the solution is irradiated, bubbles are formed and collapse within a short time. This creates local hotspots with

high temperatures and high pressure. The accomplishment of these conditions promotes the initiation of chemical reactions and the immediate formation of crystallization nuclei<sup>207</sup>. Likewise, in the case of solvothermal method, the choice of temperature, the reaction time, and the initial concentration are of high importance for the final morphology and crystal size. In general, sonochemical approaches can generate homogeneous nucleation centers within shorter crystallization time compared to hydrothermal methods<sup>208</sup>.

Like sonochemical method, microwave-assisted method is also employed, resulting in smaller sized materials within short crystallization times<sup>209</sup>. The advantage of this method relies in the ability of polar molecules found on the reaction mixture to orientate with the oscillating electric field upon microwave application. As the molecules are reorientating in respect to the electric field, heating is induced facilitating the nucleation and growth of crystals<sup>210</sup>.

The final step for the synthesis of MOFs is activation, referring to the removal of the guest molecules, i.e., solvents in the pores of the structure acquired during the synthesis process. Specifically, MOFs are synthesized in one, or a combination of high boiling point solvents, such as DMF, DMSO, DEF in the presence of modulators which can be trapped in the porosity of the framework<sup>211</sup>. Numerous strategies for activation have been developed in order to access the highest possible surface area and porosity.

The most common technique is thermal activation, which is also used for other porous materials, like zeolites and is combined with vacuum drying. However, this technique may induce a loss of crystallinity and a collapse of the framework. This can be ascribed to the high surface tension and capillary forces, created while we pass through the liquid-to-gas phase transformation of the guest solvent, during heating<sup>212</sup>. Therefore, a pre-treatment by solvent exchange is carried out. In particular, exchanging the high boiling point solvents with low boiling point is realized by a heat treatment under vacuum. The lower boiling point solvents (acetone, methanol, ethanol) present weaker intermolecular interaction as seen in Figure 1.17, minimizing in this way the aforementioned drawbacks.

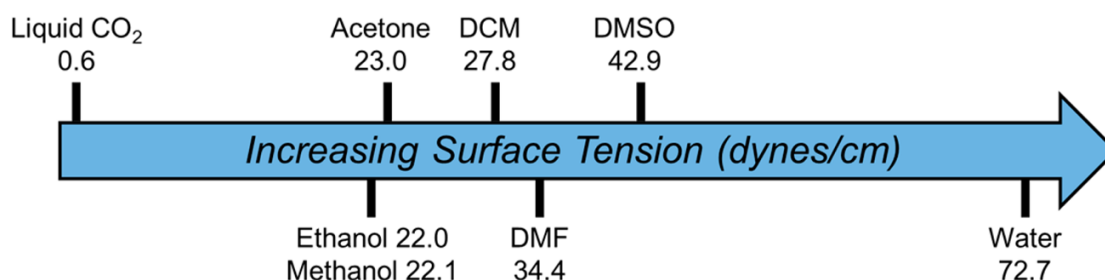


Figure 1. 17: Surface tension of some common organic solvents compared to liquid CO<sub>2</sub>. DCM: dichloromethane; DMF: N,N-dimethylformamide; DMSO: dimethyl sulfoxide<sup>213</sup>

The activation by supercritical CO<sub>2</sub> (sc-CO<sub>2</sub>) is an alternative that has been introduced in 2009 and exhibits various advantages, especially for MOFs with low stability and/or high porosity <sup>214</sup>. The minimization of the drawbacks here lies in the direct gas-to-supercritical phase transformation of CO<sub>2</sub>. The process involves three steps: pre-exchanging the trapped solvent molecules with liquid CO<sub>2</sub> compatible organic solvents, exchanging the organic solvent with liquid CO<sub>2</sub> and evaporating the CO<sub>2</sub> on the supercritical phase <sup>213</sup>. Some other reported activation methods are the freeze-drying method utilizing benzene <sup>215</sup>, and activation by chemical treatment, such as employing highly acidic solutions <sup>216</sup>.

### V.3. MOFs applications

MOFs are considered ideal platforms for gas storage, thanks to their high surface area and the tunable pore metrics. In addition, MOFs possessing organic moieties with polar functional groups have a higher CO<sub>2</sub> adsorption capacity, due to the quadrupole moments of CO<sub>2</sub> molecules <sup>196</sup>. A typical example is the MOF NH<sub>2</sub>-UiO-66, with aminoterephthalic acid (C<sub>8</sub>H<sub>7</sub>NO<sub>4</sub>) as organic ligand, and its parent MOF UiO-66. Sun et al., in their study showed that the amino-functionalized MOF presents higher CO<sub>2</sub> uptake capacity despite the smaller BET surface area comparing to UiO-66 <sup>217</sup>. This observation implies that aromatic molecules functionalized with polar substituents such as OH, NH<sub>2</sub>, and COOH show enhanced interactions with CO<sub>2</sub> <sup>218,219</sup>. Therefore, by designing the MOF structure it is possible to significantly improve CO<sub>2</sub> adsorption capacity and selectivity of these outstanding adsorbents.

Thanks to their crystalline nature, MOFs are also viewed as promising photocatalysts. High crystallinity ensures the charge transfer from the organic ligand to the metal cluster <sup>220</sup>. The tailorable porosity also is facilitating the diffusion of the reactants to the catalytically active sites <sup>221</sup>. In their review article, Ye's group affirm that MOFs or MOF-based composites display promising photocatalytic performance in comparison with traditional semiconductors, specially towards CO<sub>2</sub> reduction <sup>222</sup>. In particular, concerning the process of photocatalytic CO<sub>2</sub> reduction, the benchmark system involves a MOF with apparent quantum efficiency (AQE) of 15.76% at 420 nm with a significantly high selectivity towards formic acid <sup>223</sup>.

It is also shown that metal centers possessing coordinatively unsaturated nodes are isolated and can be considered as single atom active sites. And since we are referring to photocatalysts, the appropriate bandgap and the enhanced optical response is another crucial characteristic that MOFs should have. To this end, the large variety of organic ligands and the rich coordination chemistry of transition metal cations allow huge flexibility for the successful tuning of light absorption <sup>220</sup>. Fu et al. showed that by modifying the organic ligand of the MIL-125(Ti), the optical response extended

## CHAPTER 1

from UV to the visible range. Specifically, when the organic linker of MOF is functionalized with amino groups the absorbance edge is extended to the visible region of the solar spectrum, ca. 550 nm <sup>224</sup>. In another study, Mucho et al. showed that by incorporating -NH<sub>2</sub> groups in the organic ligand, the E<sub>g</sub> of MIL-125(Ti)-NH<sub>2</sub> is decreased. This has been ascribed to the upward shift of VB position due to the lone electron pair of nitrogen atom <sup>225</sup>.

Lately, MOFs are also studied as precursors for metal oxide materials development, in order to profit from their tunable properties and overcome the disadvantages of current methods of synthesis. Moreover, due to the excellent properties that are mentioned above, MOFs are viewed as bifunctional materials for the adsorption and photocatalytic conversion of reactants. In Figure 1.18, the current trends in literature are summarized for the key parameters of MOF-derived or MOF-based materials for solar fuels production. As can be seen, the development of MOF-hybrid materials is realized by coupling with traditional semiconductors, in order to profit from the advantages of both parts. This strategy aims for better charge separation, an enhancement in available surface area and the control over the band structure. In the following section, these approaches will be presented thoroughly.

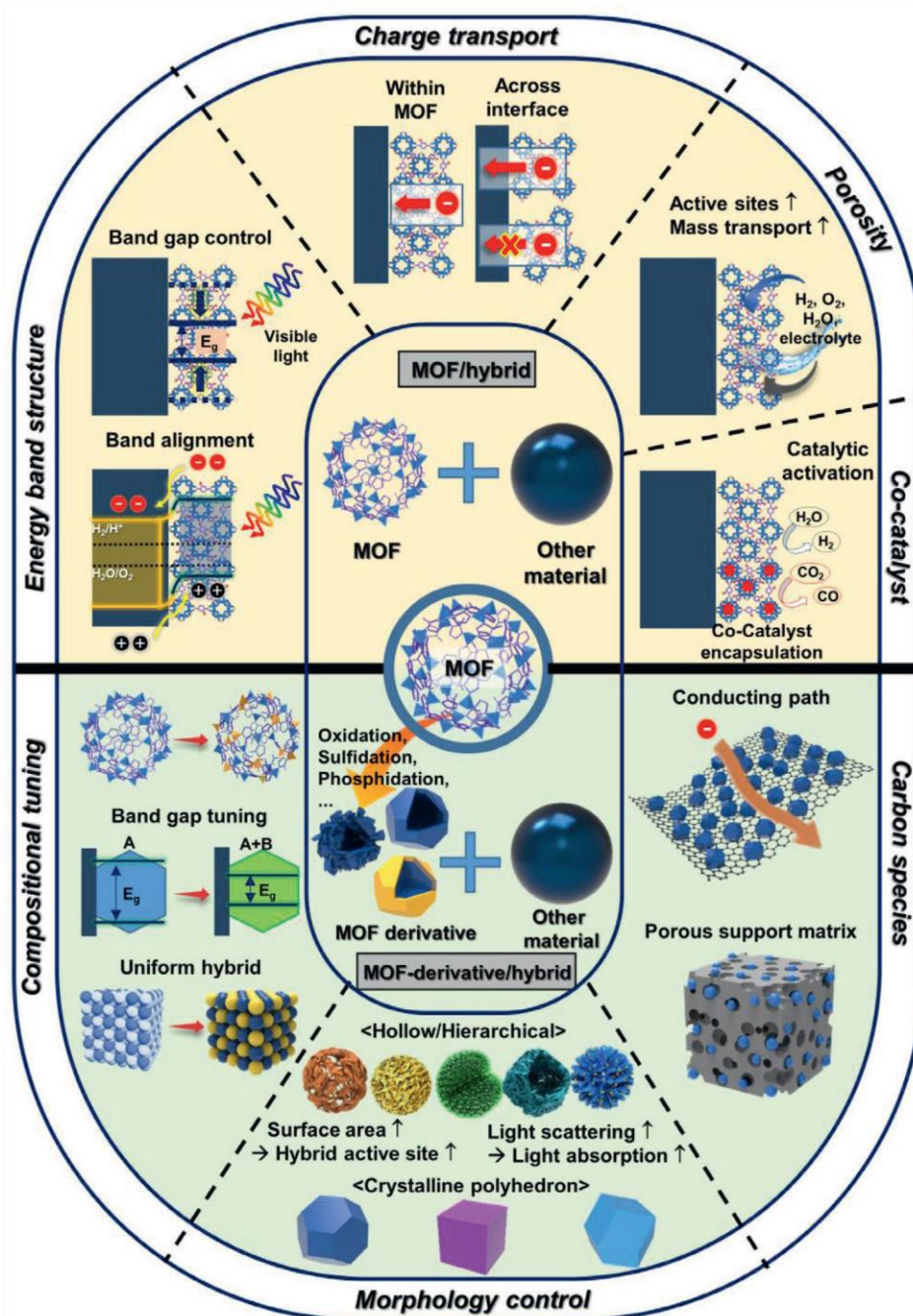


Figure 1. 18: Key parameters of MOF-based or MOF-derived materials <sup>226</sup>

### V.3.A. MOFs as templates for oxides

As previously mentioned, MOFs represent ideal platforms with tunable properties. Recently, the scientific community is working on different strategies and methodologies in order to tune MOFs properties and consequently enhance their photocatalytic efficiency. Except for the composition and structure, morphology at nanoscale holds a key role in the final properties. Transition Metal Oxides (TMOs) are widely used as photocatalysts, but they lack an appropriate porous structure for

mass transfer and, in most cases, efficient light absorption in the bulk. Moreover, they may present particle aggregation, a factor which reduces the exposure of active sites to the substrate. In order to tackle these drawbacks, semiconductor material derived from MOF structures can be obtained by thermal treatment of MOFs at appropriate temperature and atmosphere. This allows us to combine the advantages of the activity of semiconductor and porous structure of MOFs <sup>227</sup>.

It is already shown that nanomaterials derived from MOFs inherit the morphology of their precursors <sup>228,229</sup>. Namely, they can maintain the characteristics of the large specific surface area and well-developed porosity, which are advantageous for photocatalysis <sup>230</sup>. In addition, the metal ions/clusters are homogeneously distributed in MOFs, thus, the size or even the morphology of TMOs can be controlled in order to enhance their photocatalytic performance <sup>231</sup>. Yin et al. synthesized disc-like MIL-125 structures with embedded Pt inside its cavities. Later, the MOF was used as a precursor and resulted in Pt embedded semiconductor supporter (Pt@TiO<sub>2</sub>) for photocatalytic hydrogen production. Specifically, it showed an activity of 4.389 mmol/h/g with the apparent quantum efficiency of 39% at 380 nm, which was 6.4 times higher than for Pt/TiO<sub>2</sub> prepared by traditional synthesis processes.

Except for TiO<sub>2</sub>, Co<sub>3</sub>O<sub>4</sub> is another semiconductor which has been applied in several photocatalytic applications, including photocatalytic CO<sub>2</sub> reduction and H<sub>2</sub> production <sup>232,233</sup>. However, pristine Co<sub>3</sub>O<sub>4</sub> presents a fast charge recombination rate. Tuning the morphology may overcome this disadvantage. As it is mentioned in [Section II.4.B.i.](#), 2-D structures are beneficial not only for the migration of charge carriers to the surface, but also for the substrate transport <sup>86,234</sup>. This consideration is investigated by Chen et al. who synthesized ultrathin Co<sub>3</sub>O<sub>4</sub> nanosheets through a two-step synthesis, using ZIF-67 as a starting MOF. Then, the morphology of ZIF-67 was modified to a 2-D structure via an ion assisted solvothermal method. The MOF obtained was calcined and resulted in Co<sub>3</sub>O<sub>4</sub> nanosheets with porous structure (NS). ZIF-67 was also calcined under the same conditions and resulted in Co<sub>3</sub>O<sub>4</sub> with bulk morphology (Co<sub>3</sub>O<sub>4</sub>-BK), later both were used as photocatalysts towards CO<sub>2</sub> reduction. Particularly, concerning the 2-D material, the CO generation rate was found to be approximately 4.52 μmol h<sup>-1</sup> with selectivity of 70.1%, which was superior to the Co<sub>3</sub>O<sub>4</sub> bulk catalysts (Co<sub>3</sub>O<sub>4</sub>-BK).

### *V.3.B. MOFs as catalytically active centers by controlling their properties in molecular level*

Porphyrins are already studied as molecular catalysts for homogeneous catalysis and electrocatalytic applications, due to their electronic structure, redox properties and robust structure. Except the possibility to change their structure by adding different groups at the periphery of the porphyrin ring and their ability to act as antennas harvesting visible light, they also possess a metalation site core <sup>235</sup>. Metalated

porphyrins are found in several biological applications. For instance, Fe-porphyrin is found in hemoglobin and contributes to the oxygen binding and transport from blood to organs and tissues <sup>236</sup>. Metalated porphyrins also present a site for the axial coordination of electron-donating or electron accepting ligands (i.e., axial ligands). In general, strong axial ligands such as chloride can cause a downfield shift of the metal in metalated porphyrins, possibly due to the effect of deshielding, as shown by Arnold et al <sup>237</sup>. This structural rearrangement may affect the electronic properties of the complex.

However, homogeneous catalysts are posing problems in recovering them from the reaction medium and it is difficult recycling them. In order to tackle these drawbacks, porphyrins were used as photosensitizers for photocatalysts, thanks to their great ability of converting photons to high-energy redox separated states <sup>199</sup>. Lately, they have been incorporated in MOF structures as the organic linker. They are considered an attractive building unit for MOFs because of their rigid structure and tunable peripheral substituents. In addition, the coordinatively unsaturated metal sites which are incorporated into the metalated porphyrin units can act as active sites <sup>238</sup>, and can enhance the gas adsorption ability. There is a plethora of porphyrins which are regarded as MOF organic moieties, but among them TCPP is the most widely studied, thanks its highly symmetric planar aromatic configuration <sup>216,239</sup>. Moreover, it can supply a nitrogen-rich skeleton, making it possible for a greater adsorption of CO<sub>2</sub> during photocatalysis <sup>240</sup>.

Zhang et al worked towards the modular optimization of porphyrin-based MOF PCN-222. This was realized by incorporation of coordinatively unsaturated single Co atoms in a MOF matrix. It resulted in an efficient electron-hole separation in porphyrinic units, as monitored by incident-photon-to-current conversion efficiency (IPCE) characterization and PL measurements. These observations imply directional migration of photogenerated excitons from porphyrin to catalytic Co centers. Furthermore, they observed that Co atoms boosted the CO<sub>2</sub> absorption on the active sites, as proved by in situ FTIR. The incorporation of Co atoms in PCN-222 in a 3.13-fold improvement of CO evolution rate and 5.93-fold enhancement in CH<sub>4</sub> generation rate compared to the parent MOF <sup>241</sup>.

In addition, porphyrinic MOF structures with several metal oxo clusters, have been studied, but among them, the ones with Al and Zr are the most developed lately. They present a high oxidative state and can form numerous bonds rendering the frameworks highly stable. In addition, Zr<sup>IV</sup> presents an important advantage over other first row transition metal ions. Indeed, during the solvothermal synthesis process of the MOF structure, Zr<sup>IV</sup> is not inserted in the porphyrin ring. This offers the possibility of obtaining MOFs with free-base porphyrin linkers <sup>242</sup>. Some common examples of Zr-based MOFs are MOF-525 and MOF-545, which present excellent

adsorption capacity and high stability, thanks to Zr-O clusters. Compared with other Zr-based MOFs, i.e., UiO, they absorb a wider range of visible light, thus it is accredited to their organic ligands. In detail, in the UV-Vis Spectroscopy Spectra, the MOF-525 and MOF-545 present characteristic peaks of an organic linker, a Soret band at 416 nm and four Q bands in the visible region corresponding to  $\pi$ - $\pi^*$  transitions.

Furthermore, Zr<sup>IV</sup>-oxo based frameworks hold Zr carboxylate bonds, which are exerting excellent in hydrolytic and mechanical stability even in acidic conditions <sup>242</sup>. More precisely Feng and coworkers, employed Fe-PCN-222 as biomimetic catalyst, a 3D heme-like MOF synthesized by Fe-TCPP as ligand and highly stable Zr<sub>6</sub> clusters as nodes <sup>216</sup>. The Zr<sub>6</sub> cluster, which was found to be one of the most stable building units for MOF structures, is presumably responsible for the exceptional stability of PCN-222. Prior to catalytic experiments, they proceeded to a treatment of PCN-222(Fe) with concentrated HCl, and it demonstrated exceptionally high chemical stability. This is attributed not only to the strongly polarized Zr-O bond but also to the chelating effect which stabilizes the four bonds between Fe<sup>III</sup> and porphyrin.

### *V.3.C. MOFs as multifunctional materials for enhanced CO<sub>2</sub> adsorption*

In the previous section, we described the approach of modifying the organic ligand by adding a metal. Other methodologies allowing the improvement of MOFs photocatalytic properties are the presence of two different metal clusters <sup>243</sup>, or the presence of mixed organic ligands in the framework <sup>244</sup>, or mixed organic ligands and metal sites simultaneously <sup>245</sup>. In order to control the morphology, the shape and the growth of MOF structures, combining multicomponent MOF particles one on top of another is an interesting strategy. This approach is known as MOF-on-MOF systems and allows the controlled synthesis of core-shell MOF configurations which are considered as a resultful and convenient in order to achieve the synergistic performance of the different components <sup>246</sup>.

Moreover, by building core-shell structures, the electron transport can be enhanced by the transfer through the interface formed between the two layers. In that regard, Zeolitic-imidazole Framework (ZIFs), and more precisely ZIF-8 and ZIF-67, are commonly used for this approach. Their synthesis protocol is relatively easy and they possess matched structures <sup>247,248</sup>. Zhang et al, demonstrated the synthesis of uniform multilayered core-shell MOF crystals including ZIF-67@ZIF-8@ZIF-67 and ZIF-8@ZIF-67@ZIF-8. In addition, they showed that the size of the core and the thickness of the shell could be easily controlled by varying the molar feeding ratio of Zn<sup>2+</sup>/Co<sup>2+</sup>, during the preparation process <sup>249</sup>. Nevertheless, as Tang et al. mentioned in their study, predicting the final ratio of Zn<sup>2+</sup>/Co<sup>2+</sup> is challenging because the actual molar ratio of Zn<sup>2+</sup>/Co<sup>2+</sup> is slightly less than the feeding molar ratio used for the synthesis. This can be attributed to fact that the coordination interaction between Zn

and the organic linker(methyl imidazole (Melm) in this specific case) is stronger than that between Co and Melm <sup>250</sup>.

In an attempt to overcome this challenge and control the morphology of each layer, Avci et al. proceeded to a chemical etching process in different pH values and for different time of the ZIF-67, as it can be observed in Figure 1.19 <sup>251</sup>. Chemical etching was realized by a weak acid (i.e., Xylenol orange) which deprotonates the organic ligand. The generated protons are breaking the coordination bonds between the metal nodes/ions and the organic ligand. Simultaneously, xylenol orange acts as a chelating agent which coordinates the liberated Co(II) ions to form stable and water-soluble Co-XO complexes, minimizing the undesired side reactions <sup>252</sup>. Later, sequential growth of ZIF-8 on top of the etched ZIF-67 was carried out, forming a core-shell configuration. This approach also permits the deposition of inorganic nanoparticles (INPs) between the layers and before the formation of ZIF-8 as a shell layer. It is also important to mention that localized etching in the MOF framework can modify the morphology and can downsize the MOF into smaller particles, decreasing the diffusion pathway of charge carriers <sup>253</sup>.

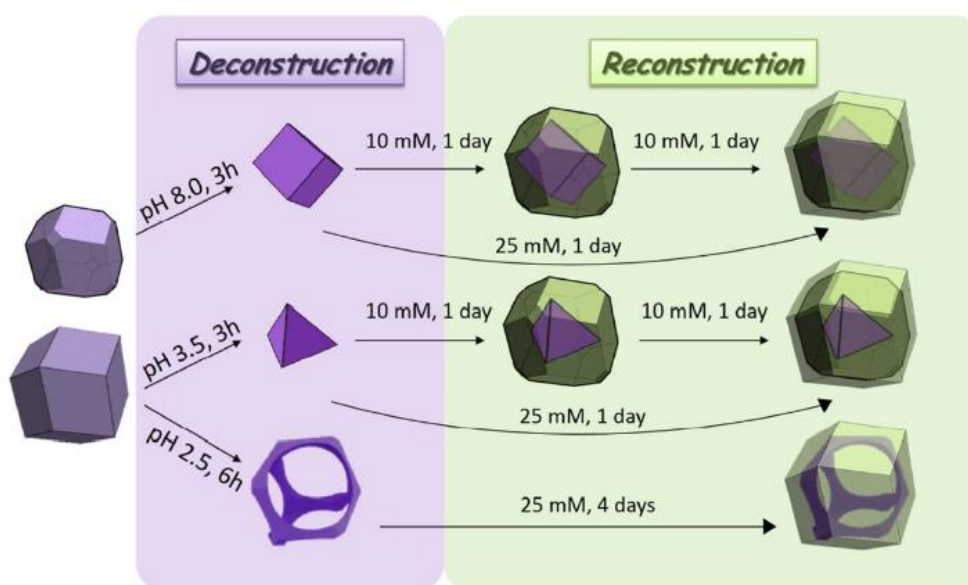


Figure 1. 19: Schematic illustration of the synthetic conditions used to construct the different ZIF-8-on-ZIF-67 particles according to the sequential deconstruction-reconstruction strategy <sup>251</sup>

## VI. Conclusions

The repercussions of excessive emissions of greenhouse gases are obvious. They put in danger not only our planet but also humans and animal populations. Therefore, the approaches towards climate change mitigation need to be put into action urgently. In this chapter we discussed photocatalysis as an environmentally friendly approach. Specifically, it is a pathway allowing the conversion of sunlight energy into chemical energy, by using appropriate materials, called photocatalysts.

Water dissociation and CO<sub>2</sub> conversion are the two main applications of photocatalysis in order to produce solar fuels: hydrogen and C<sub>1</sub>/C<sub>1+</sub> products, respectively. Photocatalytic conversion of CO<sub>2</sub> using H<sub>2</sub>O as electron donor is called artificial photosynthesis. This process may address simultaneously two challenges: the energy shortage and the CO<sub>2</sub> accumulation in the atmosphere, killing two birds with one stone.

The efficiency of photocatalytic reactions is primarily dependent on the properties of the photocatalysts, followed by the reaction conditions. Therefore, it is essential to optimize the materials' properties, which are crucial for their photocatalytic activity, and select favorable operating conditions to achieve higher efficiencies. This study has focused on improving the materials through various strategies.

Carbon nitride and TiO<sub>2</sub> are commonly used semiconductors in photocatalytic applications. Nonetheless, they possess certain limitations, such as the low surface area of carbon nitride, a fast charge recombination and the limited absorption spectrum of TiO<sub>2</sub>. To overcome these shortcomings, various approaches have been proposed, such as exfoliation for carbon nitride and control of morphology and facets for TiO<sub>2</sub>.

Another strategy is the development of heterostructures with materials holding versatile properties. The heterostructure can be between two semiconductor materials or a semiconductor material and a metal organic framework. The latter offers the possibility to enhance the available surface area, allowing a better interaction between the reactants and the photogenerated charges of the photocatalyst, permitting the redox reaction to occur. Coupling a MOF with a SC is the main focus of this experimental research. And the major objective is to improve the:

- Charge carriers' separation
- Overall response to visible light
- CO<sub>2</sub> uptake capacity

As it is mentioned in this chapter, the charge carrier's recombination is one of the main limitations affecting the efficiency of photocatalytic reactions. In that regard,

## CHAPTER 1

the development of heterojunctions allows a better separation of the charges in the two parts of the heterostructure, thus greatly reducing the recombination rate, and extending their lifetimes, as seen in [Section II.4.B.ii.](#)

Furthermore, the photocatalyst's morphology also plays a significant role in better charge separation. Namely, sheet-like materials offer a shorter migration path for electrons, enhancing the utilization of the photoinduced electrons in the catalysts. In case of composite materials where both counterparts hold a 2D morphology, present increased face-to-face contact area which can improve significantly charge carrier's lifetime and concomitantly, enhanced photocatalytic activity.

Another crucial parameter impacting the efficiency of a photocatalytic reaction is the surficial properties of the photocatalysts. Defect engineering and functionalization of the materials surface are widely studied in order to enhance the photocatalytic activity by enforcing the adsorption of the reactants on the catalyst's surface. Specifically, as mentioned in [section II.6.B.](#), CO<sub>2</sub> adsorption is considered the rate determining step of the overall process of photocatalytic conversion. Towards this end, the basic sites and the oxygen vacancies present on the surface of the photocatalytic materials can enhance the overall CO<sub>2</sub> uptake capacity. Also, MOFs with appropriate functional groups and metal nodes can also promote not only the selective adsorption of CO<sub>2</sub>, but also enhance the overall response to visible light of the composite material, as shown in [section V.3.b.](#). In the following chapters, the MOF-based composite materials synthesized in the present PhD studies will be presented, their properties will be discussed, and their photocatalytic activity will be evaluated.

## VII. References

- (1) Houghton, J. Global Warming. *Rep. Prog. Phys.* **2005**, *68* (6), 1343–1403. <https://doi.org/10.1088/0034-4885/68/6/R02>.
- (2) <https://Ourworldindata.Org/Co2-and-Other-Greenhouse-Gas-Emissions#note-1>. [Accessed 14 5 2020].
- (3) H. A. Mooney. The Carbon Balance of Plants. *Annu. Rev. Ecol. Syst.* **3**, 315–346.
- (4) A.S. Raghavendra; K. Padmasree; K. Saradadevi. Interdependence of Photosynthesis and Respiration in Plant Cells: Interactions between Chloroplasts and Mitochondria. *Plant Science* **1994**, *97*, 1–14.
- (5) Quadrelli, R.; Peterson, S. The Energy–Climate Challenge: Recent Trends in CO<sub>2</sub> Emissions from Fuel Combustion. *Energy Policy* **2007**, *35* (11), 5938–5952. <https://doi.org/10.1016/j.enpol.2007.07.001>.
- (6) Masson-Delmotte, V.; Pörtner, H.-O.; Skea, J.; Zhai, P.; Roberts, D.; Shukla, P. R.; Pirani, A.; Pidcock, R.; Chen, Y.; Lonnoy, E.; Moufouma-Okia, W.; Péan, C.; Connors, S.; Matthews, J. B. R.; Zhou, X.; Gomis, M. I.; Maycock, T.; Tignor, M.; Waterfield, T. An IPCC Special Report on the Impacts of Global Warming of 1.5°C above Pre-Industrial Levels and Related Global Greenhouse Gas Emission Pathways, in the Context of Strengthening the Global Response to the Threat of Climate Change, Sustainable Development, and Efforts to Eradicate Poverty. 630.
- (7) European Space Agency, [https://www.esa.int/Applications/Observing\\_the\\_Earth/Copernicus/Sentinel-5P/Coronavirus\\_lockdown\\_leading\\_to\\_drop\\_in\\_pollution\\_across\\_Europe](https://www.esa.int/Applications/Observing_the_Earth/Copernicus/Sentinel-5P/Coronavirus_lockdown_leading_to_drop_in_pollution_across_Europe). [Accessed 15 5 2020]
- (8) IPCC. Special Report on Emissions Scenarios: A Special Report of Working Group III of the Intergovernmental Panel on Climate Change; Cambridge University Press: New York, 2000.
- (9) Clare Breidenich; Daniel Magraw; Anne Rowley; James W. Rubin. The Kyoto Protocol to the United Nations Framework Convention on Climate Change. **1998**, *92* (2).
- (10) United Nations-Treaty series. Montreal Protocol on Substances That Deplete the Ozone Layer; Montreal, 1987; Vol. 1522.
- (11) UNITED NATIONS FRAMEWORK CONVENTION ON CLIMATE CHANGE.
- (12) United Nations. Paris Agreement.
- (13) Conte, M. Hydrogen Economy for a Sustainable Development: State-of-the-Art and Technological Perspectives. *J. Power Sources* **2001**, *100* (1–2), 171–187. [https://doi.org/10.1016/S0378-7753\(01\)00893-X](https://doi.org/10.1016/S0378-7753(01)00893-X).
- (14) Afgan, N. Sustainability Assessment of Hydrogen Energy Systems. *Int. J. Hydrog. Energy* **2004**, *29* (13), 1327–1342. <https://doi.org/10.1016/j.ijhydene.2004.01.005>.
- (15) Gielen, D.; Boshell, F.; Saygin, D.; Bazilian, M. D.; Wagner, N.; Gorini, R. The Role of Renewable Energy in the Global Energy Transformation. *Energy Strategy Rev.* **2019**, *24*, 38–50. <https://doi.org/10.1016/j.esr.2019.01.006>.
- (16) Ming Deng; Markus Leippold; Alexander F. Wagner; Qian Wang. Stock Prices and the Russia-Ukraine War: Sanctions, Energy and ESG; 2022.

## CHAPTER 1

- (17) <https://www.iea.org/fuels-and-technologies/renewables> Renewables - Fuels & Technologies. IEA. <https://www.iea.org/fuels-and-technologies/renewables> (accessed 2022-02-26).
- (18) Shah, A.; Torres, P.; Tscharnner, R.; Wyrsh, N.; Keppner, H. Photovoltaic Technology: The Case for Thin-Film Solar Cells. *Science* **1999**, *285* (5428), 692–698. <https://doi.org/10.1126/science.285.5428.692>.
- (19) Harriman, A. Prospects for Conversion of Solar Energy into Chemical Fuels: The Concept of a Solar Fuels Industry. *Philos. Trans. R. Soc. Math. Phys. Eng. Sci.* **2013**, *371* (1996), 20110415. <https://doi.org/10.1098/rsta.2011.0415>.
- (20) Hirakawa, H.; Hashimoto, M.; Shiraishi, Y.; Hirai, T. Photocatalytic Conversion of Nitrogen to Ammonia with Water on Surface Oxygen Vacancies of Titanium Dioxide. *J. Am. Chem. Soc.* **2017**, *139* (31), 10929–10936. <https://doi.org/10.1021/jacs.7b06634>.
- (21) Yuliati, L.; Yoshida, H. Photocatalytic Conversion of Methane. *Chem. Soc. Rev.* **2008**, *37* (8), 1592. <https://doi.org/10.1039/b710575b>.
- (22) Barber, J.; Tran, P. D. From Natural to Artificial Photosynthesis. *J. R. Soc. Interface* **2013**, *10* (81), 20120984. <https://doi.org/10.1098/rsif.2012.0984>.
- (23) Gust, D.; Moore, T. A.; Moore, A. L. Solar Fuels via Artificial Photosynthesis. *Acc. Chem. Res.* **2009**, *42* (12), 1890–1898. <https://doi.org/10.1021/ar900209b>.
- (24) Tapia, J. F. D.; Lee, J.-Y.; Ooi, R. E. H.; Foo, D. C. Y.; Tan, R. R. A Review of Optimization and Decision-Making Models for the Planning of CO<sub>2</sub> Capture, Utilization and Storage (CCUS) Systems. *Sustain. Prod. Consum.* **2018**, *13*, 1–15. <https://doi.org/10.1016/j.spc.2017.10.001>.
- (25) *World Energy Outlook 2013*; International Energy Agency, Ed.; World Energy Outlook; Paris, 2013.
- (26) C. Ding; L. Yang; J. He. Biological and Fermentative Production of Hydrogen. In *Handbook of Biofuels Production (Second Edition)*; 2016; pp 303–333.
- (27) Araújo, O. de Q. F.; de Medeiros, J. L. Carbon Capture and Storage Technologies: Present Scenario and Drivers of Innovation. *Curr. Opin. Chem. Eng.* **2017**, *17*, 22–34. <https://doi.org/10.1016/j.coche.2017.05.004>.
- (28) Hussin, F.; Aroua, M. K. Recent Trends in the Development of Adsorption Technologies for Carbon Dioxide Capture: A Brief Literature and Patent Reviews (2014–2018). *J. Clean. Prod.* **2020**, *253*, 119707. <https://doi.org/10.1016/j.jclepro.2019.119707>.
- (29) Dawood, F.; Anda, M.; Shafiullah, G. M. Hydrogen Production for Energy: An Overview. *Int. J. Hydrog. Energy* **2020**, *45* (7), 3847–3869. <https://doi.org/10.1016/j.ijhydene.2019.12.059>.
- (30) *Sun and stars | Plasma-Universe.com*. <https://www.plasma-universe.com/sun-and-stars/> (accessed 2022-02-28).
- (31) *Hydrogen as an Energy Carrier*; Winter, C.-J., Nitsch, J., Eds.; Springer Berlin Heidelberg: Berlin, Heidelberg, 1988. <https://doi.org/10.1007/978-3-642-61561-0>.
- (32) *Universal Industrial Gases, Inc...Hydrogen H<sub>2</sub> Properties, Uses, Applications*. <http://www.uigi.com/hydrogen.html> (accessed 2022-02-28).
- (33) *Home - Hydrogen Europe*. <https://hydrogeneurope.eu/> (accessed 2022-02-28).

- (34) Rivkin, C.; Burgess, R.; Buttner, W. *Hydrogen Technologies Safety Guide*; NREL/TP--5400-60948, 1169773; 2015; p NREL/TP--5400-60948, 1169773. <https://doi.org/10.2172/1169773>.
- (35) Kazunari Sasaki; Hai-Wen Li; Akari Hayashi; Junichiro Yamabe; Teppei Ogura; Stephen M. Lyth. *Hydrogen Energy Engineering : A Japanese Perspective*; Springer: Japan, 2016.
- (36) Yip, H. L.; Srna, A.; Yuen, A. C. Y.; Kook, S.; Taylor, R. A.; Yeoh, G. H.; Medwell, P. R.; Chan, Q. N. A Review of Hydrogen Direct Injection for Internal Combustion Engines: Towards Carbon-Free Combustion. *Appl. Sci.* **2019**, *9* (22), 4842. <https://doi.org/10.3390/app9224842>.
- (37) Nazir, H.; Louis, C.; Jose, S.; Prakash, J.; Muthuswamy, N.; Buan, M. E. M.; Flox, C.; Chavan, S.; Shi, X.; Kauranen, P.; Kallio, T.; Maia, G.; Tammeveski, K.; Lympelopoulos, N.; Carcadea, E.; Veziroglu, E.; Iranzo, A.; Kannan, A. M. Is the H<sub>2</sub> Economy Realizable in the Foreseeable Future? Part I: H<sub>2</sub> Production Methods. *Int. J. Hydrog. Energy* **2020**, *45* (27), 13777–13788. <https://doi.org/10.1016/j.ijhydene.2020.03.092>.
- (38) Hydrogen: An Alternative Fuel. In *Solar Energy Conversion and Storage*; Neelu Chouhan, Rajesh Kumar Meena, Eds.; CRC Press, 2015; pp 68–97. <https://doi.org/10.1201/b19148-9>.
- (39) Floristean Alexandru. *EU Regulations and Directives Which Impact the Deployment of FCH Technologies*; HyLAW Project, Deliverable 4.4; 2019.
- (40) Nikolaidis, P.; Poullikkas, A. A Comparative Overview of Hydrogen Production Processes. *Renew. Sustain. Energy Rev.* **2017**, *67*, 597–611. <https://doi.org/10.1016/j.rser.2016.09.044>.
- (41) Nikolaidis, P.; Poullikkas, A. A Comparative Overview of Hydrogen Production Processes. *Renew. Sustain. Energy Rev.* **2017**, *67*, 597–611. <https://doi.org/10.1016/j.rser.2016.09.044>.
- (42) Stenberg, V.; Rydén, M.; Mattisson, T.; Lyngfelt, A. Exploring Novel Hydrogen Production Processes by Integration of Steam Methane Reforming with Chemical-Looping Combustion (CLC-SMR) and Oxygen Carrier Aided Combustion (OCAC-SMR). *Int. J. Greenh. Gas Control* **2018**, *74*, 28–39. <https://doi.org/10.1016/j.ijggc.2018.01.008>.
- (43) Horng, R.-F.; Chou, H.-M.; Lee, C.-H.; Tsai, H.-T. Characteristics of Hydrogen Produced by Partial Oxidation and Auto-Thermal Reforming in a Small Methanol Reformer. *J. Power Sources* **2006**, *161* (2), 1225–1233. <https://doi.org/10.1016/j.jpowsour.2006.06.043>.
- (44) Yan, Y.; Cui, Y.; Zhang, L.; Li, L.; Zhang, J.; Chen, Y.; Tang, Q.; Lin, C. Experimental Investigation of Methane Auto-Thermal Reforming in Hydrogen-Permeable Membrane Reactor for Pure Hydrogen Production. *Int. J. Hydrog. Energy* **2016**, *41* (30), 13069–13076. <https://doi.org/10.1016/j.ijhydene.2016.06.076>.
- (45) Thangalazhy-Gopakumar, S.; Adhikari, S.; Gupta, R. B.; Tu, M.; Taylor, S. Production of Hydrocarbon Fuels from Biomass Using Catalytic Pyrolysis under Helium and Hydrogen Environments. *Bioresour. Technol.* **2011**, *102* (12), 6742–6749. <https://doi.org/10.1016/j.biortech.2011.03.104>.
- (46) The Future of Hydrogen. 203.

- (47) Villafán-Vidales, H. I.; Arancibia-Bulnes, C. A.; Riveros-Rosas, D.; Romero-Paredes, H.; Estrada, C. A. An Overview of the Solar Thermochemical Processes for Hydrogen and Syngas Production: Reactors, and Facilities. *Renew. Sustain. Energy Rev.* **2017**, *75*, 894–908. <https://doi.org/10.1016/j.rser.2016.11.070>.
- (48) Pandey, B.; Prajapati, Y. K.; Sheth, P. N. Recent Progress in Thermochemical Techniques to Produce Hydrogen Gas from Biomass: A State of the Art Review. *Int. J. Hydrog. Energy* **2019**, *44* (47), 25384–25415. <https://doi.org/10.1016/j.ijhydene.2019.08.031>.
- (49) Shahbaz, M.; Al-Ansari, T.; Aslam, M.; Khan, Z.; Inayat, A.; Athar, M.; Naqvi, S. R.; Ahmed, M. A.; McKay, G. A State of the Art Review on Biomass Processing and Conversion Technologies to Produce Hydrogen and Its Recovery via Membrane Separation. *Int. J. Hydrog. Energy* **2020**, *45* (30), 15166–15195. <https://doi.org/10.1016/j.ijhydene.2020.04.009>.
- (50) Chi, J.; Yu, H. Water Electrolysis Based on Renewable Energy for Hydrogen Production. *Chin. J. Catal.* **2018**, *39* (3), 390–394. [https://doi.org/10.1016/S1872-2067\(17\)62949-8](https://doi.org/10.1016/S1872-2067(17)62949-8).
- (51) Chi, J.; Yu, H. Water Electrolysis Based on Renewable Energy for Hydrogen Production. *Chin. J. Catal.* **2018**, *39* (3), 390–394. [https://doi.org/10.1016/S1872-2067\(17\)62949-8](https://doi.org/10.1016/S1872-2067(17)62949-8).
- (52) *Office of energy efficiency and renewable energy.* <https://www.energy.gov/eere/fuelcells/hydrogen-production-thermochemical-water-splitting>.
- (53) Joya, K. S.; Joya, Y. F.; Ocakoglu, K.; van de Krol, R. Water-Splitting Catalysis and Solar Fuel Devices: Artificial Leaves on the Move. *Angew. Chem. Int. Ed.* **2013**, *52* (40), 10426–10437. <https://doi.org/10.1002/anie.201300136>.
- (54) Prasad, U.; Prakash, J.; Gupta, S. K.; Zuniga, J.; Mao, Y.; Azeredo, B.; Kannan, A. N. M. Enhanced Photoelectrochemical Water Splitting with Er- and W-Codoped Bismuth Vanadate with WO<sub>3</sub> Heterojunction-Based Two-Dimensional Photoelectrode. *ACS Appl. Mater. Interfaces* **2019**, *11* (21), 19029–19039. <https://doi.org/10.1021/acsami.9b00150>.
- (55) Hanming Liu; Christopher Consoli; Alex Zapantis. Overview of Carbon Capture and Storage (CCS) Facilities Globally; Melbourne, Australia, 2018.
- (56) M. ARESTA; A. DIBENEDETTO. Industrial Utilization of Carbon Dioxide (CO<sub>2</sub>). In *Developments and innovation in carbon dioxide (CO<sub>2</sub>) capture and storage technology*; Woodhead Publishing Ltd, 2010; Vol. Volume 2: Carbon dioxide (CO<sub>2</sub>) storage and utilisation.
- (57) Li, Q.; Yang, J.; Feng, D.; Wu, Z.; Wu, Q.; Park, S. S.; Ha, C.-S.; Zhao, D. Facile Synthesis of Porous Carbon Nitride Spheres with Hierarchical Three-Dimensional Mesopores for CO<sub>2</sub> Capture. *Nano Res.* **2010**, *3* (9), 632–642. <https://doi.org/10.1007/s12274-010-0023-7>.
- (58) Ghiat, I.; Al-Ansari, T. A Review of Carbon Capture and Utilisation as a CO<sub>2</sub> Abatement Opportunity within the EWF Nexus. *J. CO<sub>2</sub> Util.* **2021**, *45*, 101432. <https://doi.org/10.1016/j.jcou.2020.101432>.
- (59) Hedin, N.; Chen, L.; Laaksonen, A. Sorbents for CO<sub>2</sub> Capture from Flue Gas—Aspects from Materials and Theoretical Chemistry. *Nanoscale* **2010**, *2* (10), 1819. <https://doi.org/10.1039/c0nr00042f>.

- (60) Mumford, K. A.; Wu, Y.; Smith, K. H.; Stevens, G. W. Review of Solvent Based Carbon-Dioxide Capture Technologies. *Front. Chem. Sci. Eng.* **2015**, *9* (2), 125–141. <https://doi.org/10.1007/s11705-015-1514-6>.
- (61) Luis, P.; Van Gerven, T.; Van der Bruggen, B. Recent Developments in Membrane-Based Technologies for CO<sub>2</sub> Capture. *Prog. Energy Combust. Sci.* **2012**, *38* (3), 419–448. <https://doi.org/10.1016/j.pecs.2012.01.004>.
- (62) Mukherjee, A.; Okolie, J. A.; Abdelrasoul, A.; Niu, C.; Dalai, A. K. Review of Post-Combustion Carbon Dioxide Capture Technologies Using Activated Carbon. *J. Environ. Sci.* **2019**, *83*, 46–63. <https://doi.org/10.1016/j.jes.2019.03.014>.
- (63) Leung, D. Y. C.; Caramanna, G.; Maroto-Valer, M. M. An Overview of Current Status of Carbon Dioxide Capture and Storage Technologies. *Renew. Sustain. Energy Rev.* **2014**, *39*, 426–443. <https://doi.org/10.1016/j.rser.2014.07.093>.
- (64) Parshetti, G. K.; Chowdhury, S.; Balasubramanian, R. Biomass Derived Low-Cost Microporous Adsorbents for Efficient CO<sub>2</sub> Capture. *Fuel* **2015**, *148*, 246–254. <https://doi.org/10.1016/j.fuel.2015.01.032>.
- (65) Dubey, A.; Arora, A. Advancements in Carbon Capture Technologies: A Review. *J. Clean. Prod.* **2022**, *373*, 133932. <https://doi.org/10.1016/j.jclepro.2022.133932>.
- (66) Aminu, M. D.; Nabavi, S. A.; Rochelle, C. A.; Manovic, V. A Review of Developments in Carbon Dioxide Storage. *Appl. Energy* **2017**, *208*, 1389–1419. <https://doi.org/10.1016/j.apenergy.2017.09.015>.
- (67) JONATHAN O'CALLAGHAN. *Storing CO<sub>2</sub> underground can curb carbon emissions, but is it safe?*. Horizon the EU research magazine. <https://ec.europa.eu/-and-innovation/eresearchn/horizon-magazine/storing-co2-underground-can-curb-carbon-emissions-it-safe#:~:text=One%20major%20concern%20with%20CCS,underground%2C%20known%20as%20induced%20seismicity>.
- (68) Garba, M. D.; Usman, M.; Khan, S.; Shehzad, F.; Galadima, A.; Ehsan, M. F.; Ghanem, A. S.; Humayun, M. CO<sub>2</sub> towards Fuels: A Review of Catalytic Conversion of Carbon Dioxide to Hydrocarbons. *J. Environ. Chem. Eng.* **2021**, *9* (2), 104756. <https://doi.org/10.1016/j.jece.2020.104756>.
- (69) Boutin, E.; Robert, M. Molecular Electrochemical Reduction of CO<sub>2</sub> beyond Two Electrons. *Trends Chem.* **2021**, *3* (5), 359–372. <https://doi.org/10.1016/j.trechm.2021.02.003>.
- (70) Innocent, B.; Liaigre, D.; Pasquier, D.; Ropital, F.; Léger, J.-M.; Kokoh, K. B. Electro-Reduction of Carbon Dioxide to Formate on Lead Electrode in Aqueous Medium. *J. Appl. Electrochem.* **2009**, *39* (2), 227–232. <https://doi.org/10.1007/s10800-008-9658-4>.
- (71) Jones, J.-P.; Prakash, G. K. S.; Olah, G. A. Electrochemical CO<sub>2</sub> Reduction: Recent Advances and Current Trends. *Isr. J. Chem.* **2014**, *54* (10), 1451–1466. <https://doi.org/10.1002/ijch.201400081>.
- (72) Sunil Kumar; Ramesh Kumar; Ajay Pal; Dharam Singh Chopra. Enzymes. In *Postharvest Physiology and Biochemistry of Fruits and Vegetables, 2019*; 2019; pp 335–358.
- (73) Yiou Wang; Hajime Suzuki; Jijia Xie; Osamu Tomita; David James Martin; Masanobu Higashi; Dan Kong; Ryu Abe; Junwang Tang. Mimicking Natural

- Photosynthesis: Solar to Renewable H<sub>2</sub> Fuel Synthesis by Z-Scheme Water Splitting Systems. *Chem. Rev.* **2018**, *10* (118), 5201–5241.
- (74) Silvia E. Braslavsky; André M. Braun; Alberto E. Cassano; Alexei V. Emeline; Marta I. Litter; Leonardo Palmisano; Valentin N. Parmon; Nick Serpone. Glossary of Terms Used in Photocatalysis and Radiation Catalysis. *Pure Appl Chem* **2011**, *83* (4), 931–1014.
- (75) Fujishima, A.; Honda, K. Electrochemical Photolysis of Water at a Semiconductor Electrode. *Nature* **1972**, *238* (5358), 37–38. <https://doi.org/10.1038/238037a0>.
- (76) Boyjoo, Y.; Sun, H.; Liu, J.; Pareek, V. K.; Wang, S. A Review on Photocatalysis for Air Treatment: From Catalyst Development to Reactor Design. *Chem. Eng. J.* **2017**, *310*, 537–559. <https://doi.org/10.1016/j.cej.2016.06.090>.
- (77) Long, Z.; Li, Q.; Wei, T.; Zhang, G.; Ren, Z. Historical Development and Prospects of Photocatalysts for Pollutant Removal in Water. *J. Hazard. Mater.* **2020**, *395*, 122599. <https://doi.org/10.1016/j.jhazmat.2020.122599>.
- (78) Herrmann, J.-M. Heterogeneous Photocatalysis: Fundamentals and Applications to the Removal of Various Types of Aqueous Pollutants. *Catal. Today* **1999**, *53* (1), 115–129. [https://doi.org/10.1016/S0920-5861\(99\)00107-8](https://doi.org/10.1016/S0920-5861(99)00107-8).
- (79) Jianguo Yu; Mietek Jaroniec; Chuanjia Jiang. Principle and Surface Science of Photocatalysis. In *Surface Science of Photocatalysis*; Interface Science and Technology; Vol. 31.
- (80) Wang, H.; Zhang, L.; Chen, Z.; Hu, J.; Li, S.; Wang, Z.; Liu, J.; Wang, X. Semiconductor Heterojunction Photocatalysts: Design, Construction, and Photocatalytic Performances. *Chem. Soc. Rev.* **2014**, *43* (15), 5234. <https://doi.org/10.1039/C4CS00126E>.
- (81) Gupta, S. M.; Tripathi, M. A Review of TiO<sub>2</sub> Nanoparticles. *Chin. Sci. Bull.* **2011**, *56* (16), 1639–1657. <https://doi.org/10.1007/s11434-011-4476-1>.
- (82) Weng, B.; Liu, S.; Tang, Z.-R.; Xu, Y.-J. One-Dimensional Nanostructure Based Materials for Versatile Photocatalytic Applications. *RSC Adv.* **2014**, *4* (25), 12685. <https://doi.org/10.1039/c3ra47910b>.
- (83) Daulbayev, C.; Sultanov, F.; Bakbolat, B.; Daulbayev, O. 0D, 1D and 2D Nanomaterials for Visible Photoelectrochemical Water Splitting. A Review. *Int. J. Hydrog. Energy* **2020**, *45* (58), 33325–33342. <https://doi.org/10.1016/j.ijhydene.2020.09.101>.
- (84) Ganguly, P.; Harb, M.; Cao, Z.; Cavallo, L.; Breen, A.; Dervin, S.; Dionysiou, D. D.; Pillai, S. C. 2D Nanomaterials for Photocatalytic Hydrogen Production. *ACS Energy Lett.* **2019**, *4* (7), 1687–1709. <https://doi.org/10.1021/acsenergylett.9b00940>.
- (85) Ida, S.; Ishihara, T. Recent Progress in Two-Dimensional Oxide Photocatalysts for Water Splitting. *J. Phys. Chem. Lett.* **2014**, *5* (15), 2533–2542. <https://doi.org/10.1021/jz5010957>.
- (86) Ioannidou, T.; Anagnostopoulou, M.; Christoforidis, K. C. Two-Dimensional Photocatalysts for Energy and Environmental Applications. *Solar* **2022**, *2* (2), 305–320. <https://doi.org/10.3390/solar2020017>.

- (87) Low, J.; Yu, J.; Jaroniec, M.; Wageh, S.; Al-Ghamdi, A. A. Heterojunction Photocatalysts. *Adv. Mater.* **2017**, *29* (20), 1601694. <https://doi.org/10.1002/adma.201601694>.
- (88) Zhang, J.; Hu, Y.; Jiang, X.; Chen, S.; Meng, S.; Fu, X. Design of a Direct Z-Scheme Photocatalyst: Preparation and Characterization of Bi<sub>2</sub>O<sub>3</sub>/g-C<sub>3</sub>N<sub>4</sub> with High Visible Light Activity. *J. Hazard. Mater.* **2014**, *280*, 713–722. <https://doi.org/10.1016/j.jhazmat.2014.08.055>.
- (89) Fornasiero, P.; Christoforidis, K. C. Photocatalysis for Hydrogen Production and CO<sub>2</sub> Reduction: The Case of Copper-catalysts. 16.
- (90) Wan, W.; Yu, S.; Dong, F.; Zhang, Q.; Zhou, Y. Efficient C<sub>3</sub>N<sub>4</sub>/Graphene Oxide Macroscopic Aerogel Visible-Light Photocatalyst. *J. Mater. Chem. A* **2016**, *4* (20), 7823–7829. <https://doi.org/10.1039/C6TA01804A>.
- (91) Xiang, Q.; Yu, J.; Jaroniec, M. Preparation and Enhanced Visible-Light Photocatalytic H<sub>2</sub>-Production Activity of Graphene/C<sub>3</sub>N<sub>4</sub> Composites. *J. Phys. Chem. C* **2011**, *115* (15), 7355–7363. <https://doi.org/10.1021/jp200953k>.
- (92) Li, Y.; Zhang, H.; Liu, P.; Wang, D.; Li, Y.; Zhao, H. Cross-Linked g-C<sub>3</sub>N<sub>4</sub>/RGO Nanocomposites with Tunable Band Structure and Enhanced Visible Light Photocatalytic Activity. *Small* **2013**, *n/a-n/a*. <https://doi.org/10.1002/smll.201203135>.
- (93) Xu, L.; Huang, W.-Q.; Wang, L.-L.; Tian, Z.-A.; Hu, W.; Ma, Y.; Wang, X.; Pan, A.; Huang, G.-F. Insights into Enhanced Visible-Light Photocatalytic Hydrogen Evolution of g-C<sub>3</sub>N<sub>4</sub> and Highly Reduced Graphene Oxide Composite: The Role of Oxygen. *Chem. Mater.* **2015**, *27* (5), 1612–1621. <https://doi.org/10.1021/cm504265w>.
- (94) El Marouazi, H.; Jiménez-Calvo, P.; Breniaux, E.; Colbeau-Justin, C.; Janowska, I.; Keller, V. Few Layer Graphene/TiO<sub>2</sub> Composites for Enhanced Solar-Driven H<sub>2</sub> Production from Methanol. *ACS Sustain. Chem. Eng.* **2021**, *9* (10), 3633–3646. <https://doi.org/10.1021/acssuschemeng.0c06808>.
- (95) Crake, A.; Christoforidis, K. C.; Godin, R.; Moss, B.; Kafizas, A.; Zafeiratos, S.; Durrant, J. R.; Petit, C. Titanium Dioxide/Carbon Nitride Nanosheet Nanocomposites for Gas Phase CO<sub>2</sub> Photoreduction under UV-Visible Irradiation. *Appl. Catal. B Environ.* **2019**, *242*, 369–378. <https://doi.org/10.1016/j.apcatb.2018.10.023>.
- (96) Almojil, S. F.; Almohana, A. I.; Alali, A. F.; Chaturvedi, R.; Mehrez, S.; Mohamed, A.; Rashidi, S.; Cao, Y. A Novel G-C<sub>3</sub>N<sub>4</sub>-Nanosheets/Ni<sub>3</sub>V<sub>2</sub>O<sub>8</sub> n-p Heterojunction Nanocomposite: A Promising Photocatalyst with Enhanced Photocatalytic Degradation of Tetracycline under Visible Light Irradiation. *Mater. Sci. Semicond. Process.* **2022**, *152*, 107034. <https://doi.org/10.1016/j.mssp.2022.107034>.
- (97) Bai, S.; Han, J.; Zhao, Y.; Chu, H.; Wei, S.; Sun, J.; Sun, L.; Luo, R.; Li, D.; Chen, A. RGO Decorated BiVO<sub>4</sub>/Cu<sub>2</sub>O n-n Heterojunction Photoanode for Photoelectrochemical Water Splitting. *Renew. Energy* **2020**, *148*, 380–387. <https://doi.org/10.1016/j.renene.2019.10.044>.
- (98) Khan, M. R.; Chuan, T. W.; Yousuf, A.; Chowdhury, M. N. K.; Cheng, C. K. Schottky Barrier and Surface Plasmonic Resonance Phenomena towards the Photocatalytic Reaction: Study of Their Mechanisms to Enhance Photocatalytic

- Activity. *Catal. Sci. Technol.* **2015**, *5* (5), 2522–2531. <https://doi.org/10.1039/C4CY01545B>.
- (99) Kumari, P.; Bahadur, N.; Kong, L.; O'Dell, L. A.; Merenda, A.; Dumée, L. F. Engineering Schottky-like and Heterojunction Materials for Enhanced Photocatalysis Performance – a Review. *Mater. Adv.* **2022**, *3* (5), 2309–2323. <https://doi.org/10.1039/D1MA01062J>.
- (100) Young, C.; Lim, T. M.; Chiang, K.; Scott, J.; Amal, R. Photocatalytic Oxidation of Toluene and Trichloroethylene in the Gas-Phase by Metallised (Pt, Ag) Titanium Dioxide. *Appl. Catal. B Environ.* **2008**, *78* (1–2), 1–10. <https://doi.org/10.1016/j.apcatb.2007.08.011>.
- (101) Hou, W.; Cronin, S. B. A Review of Surface Plasmon Resonance-Enhanced Photocatalysis. *Adv. Funct. Mater.* **2013**, *23* (13), 1612–1619. <https://doi.org/10.1002/adfm.201202148>.
- (102) Han, P.; Martens, W.; Waclawik, E. R.; Sarina, S.; Zhu, H. Metal Nanoparticle Photocatalysts: Synthesis, Characterization, and Application. *Part. Part. Syst. Charact.* **2018**, *35* (6), 1700489. <https://doi.org/10.1002/ppsc.201700489>.
- (103) Hammoud, L.; Strebler, C.; Toufaily, J.; Hamieh, T.; Keller, V.; Caps, V. The Role of the Gold–Platinum Interface in AuPt/TiO<sub>2</sub>-Catalyzed Plasmon-Induced Reduction of CO<sub>2</sub> with Water. *Faraday Discuss.* **2022**, 10.1039/D2FD00094F. <https://doi.org/10.1039/D2FD00094F>.
- (104) Liu, S.; Chen, G.; Prasad, P. N.; Swihart, M. T. Synthesis of Monodisperse Au, Ag, and Au–Ag Alloy Nanoparticles with Tunable Size and Surface Plasmon Resonance Frequency. *Chem. Mater.* **2011**, *23* (18), 4098–4101. <https://doi.org/10.1021/cm201343k>.
- (105) Colón, G. Towards the Hydrogen Production by Photocatalysis. *Appl. Catal. Gen.* **2016**, *518*, 48–59. <https://doi.org/10.1016/j.apcata.2015.11.042>.
- (106) Fajrina, N.; Tahir, M. A Critical Review in Strategies to Improve Photocatalytic Water Splitting towards Hydrogen Production. *Int. J. Hydrog. Energy* **2019**, *44* (2), 540–577. <https://doi.org/10.1016/j.ijhydene.2018.10.200>.
- (107) Yang, Z.; Zhang, Y.; Schnepf, Z. Soft and Hard Templating of Graphitic Carbon Nitride. *J. Mater. Chem. A* **2015**, *3* (27), 14081–14092. <https://doi.org/10.1039/C5TA02156A>.
- (108) Haider, Z.; Kang, Y. S. Facile Preparation of Hierarchical TiO<sub>2</sub> Nano Structures: Growth Mechanism and Enhanced Photocatalytic H<sub>2</sub> Production from Water Splitting Using Methanol as a Sacrificial Reagent. *ACS Appl. Mater. Interfaces* **2014**, *6* (13), 10342–10352. <https://doi.org/10.1021/am501796m>.
- (109) Linkous, C. A.; Huang, C.; Fowler, J. R. UV Photochemical Oxidation of Aqueous Sodium Sulfide to Produce Hydrogen and Sulfur. *J. Photochem. Photobiol. Chem.* **2004**, *168* (3), 153–160. <https://doi.org/10.1016/j.jphotochem.2004.03.028>.
- (110) Kumaravel, V.; Imam, M.; Badreldin, A.; Chava, R.; Do, J.; Kang, M.; Abdel-Wahab, A. Photocatalytic Hydrogen Production: Role of Sacrificial Reagents on the Activity of Oxide, Carbon, and Sulfide Catalysts. *Catalysts* **2019**, *9* (3), 276. <https://doi.org/10.3390/catal9030276>.
- (111) Christoforidis, K. C.; Fornasiero, P. Photocatalytic Hydrogen Production: A Rift into the Future Energy Supply. *ChemCatChem* **2017**, *9* (9), 1523–1544. <https://doi.org/10.1002/cctc.201601659>.

- (112) Patsoura, A.; Kondarides, D. I.; Verykios, X. E. Photocatalytic Degradation of Organic Pollutants with Simultaneous Production of Hydrogen. *Catal. Today* **2007**, *124* (3–4), 94–102. <https://doi.org/10.1016/j.cattod.2007.03.028>.
- (113) Pellegrin, Y.; Odobel, F. Sacrificial Electron Donor Reagents for Solar Fuel Production. *Comptes Rendus Chim.* **2017**, *20* (3), 283–295. <https://doi.org/10.1016/j.crci.2015.11.026>.
- (114) Wang, M.; Shen, S.; Li, L.; Tang, Z.; Yang, J. Effects of Sacrificial Reagents on Photocatalytic Hydrogen Evolution over Different Photocatalysts. *J. Mater. Sci.* **2017**, *52* (9), 5155–5164. <https://doi.org/10.1007/s10853-017-0752-z>.
- (115) Tu, W.; Zhou, Y.; Zou, Z. Photocatalytic Conversion of CO<sub>2</sub> into Renewable Hydrocarbon Fuels: State-of-the-Art Accomplishment, Challenges, and Prospects. *Adv. Mater.* **2014**, *26* (27), 4607–4626. <https://doi.org/10.1002/adma.201400087>.
- (116) Herrmann, J.-M. Photocatalysis Fundamentals Revisited to Avoid Several Misconceptions. *Appl. Catal. B Environ.* **2010**, *99* (3–4), 461–468. <https://doi.org/10.1016/j.apcatb.2010.05.012>.
- (117) Fujishima, A.; Zhang, X.; Tryk, D. TiO<sub>2</sub> Photocatalysis and Related Surface Phenomena. *Surf. Sci. Rep.* **2008**, *63* (12), 515–582. <https://doi.org/10.1016/j.surfrep.2008.10.001>.
- (118) Habisreutinger, S. N.; Schmidt-Mende, L.; Stolarczyk, J. K. Photocatalytic Reduction of CO<sub>2</sub> on TiO<sub>2</sub> and Other Semiconductors. *Angew. Chem. Int. Ed.* **2013**, *52* (29), 7372–7408. <https://doi.org/10.1002/anie.201207199>.
- (119) Halmann, M. Photoelectrochemical Reduction of Aqueous Carbon Dioxide on P-Type Gallium Phosphide in Liquid Junction Solar Cells. *Nature* **1978**, *275* (5676), 115–116. <https://doi.org/10.1038/275115a0>.
- (120) Nordgren, J.; Selander, L.; Pettersson, L.; Nordling, C.; Siegbahn, K.; Ågren, H. Core State Vibrational Excitations and Symmetry Breaking in the CK and OK Emission Spectra of CO<sub>2</sub>. *J. Chem. Phys.* **1982**, *76* (8), 3928–3932. <https://doi.org/10.1063/1.443509>.
- (121) Lingampalli, S. R.; Ayyub, M. M.; Rao, C. N. R. Recent Progress in the Photocatalytic Reduction of Carbon Dioxide. *ACS Omega* **2017**, *2* (6), 2740–2748. <https://doi.org/10.1021/acsomega.7b00721>.
- (122) Wang, Y.; Chen, E.; Tang, J. Insight on Reaction Pathways of Photocatalytic CO<sub>2</sub> Conversion. *ACS Catal.* **2022**, *12* (12), 7300–7316. <https://doi.org/10.1021/acscatal.2c01012>.
- (123) Ezugwu, C. I.; Liu, S.; Li, C.; Zhuiykov, S.; Roy, S.; Verpoort, F. Engineering Metal-Organic Frameworks for Efficient Photocatalytic Conversion of CO<sub>2</sub> into Solar Fuels. *Coord. Chem. Rev.* **2022**, *450*, 214245. <https://doi.org/10.1016/j.ccr.2021.214245>.
- (124) Liu, L.; Li, Y. Understanding the Reaction Mechanism of Photocatalytic Reduction of CO<sub>2</sub> with H<sub>2</sub>O on TiO<sub>2</sub>-Based Photocatalysts: A Review. *Aerosol Air Qual. Res.* **2014**, *14* (2), 453–469. <https://doi.org/10.4209/aaqr.2013.06.0186>.
- (125) Liu, P.; Peng, X.; Men, Y.-L.; Pan, Y.-X. Recent Progresses on Improving CO<sub>2</sub> Adsorption and Proton Production for Enhancing Efficiency of Photocatalytic CO<sub>2</sub> Reduction by H<sub>2</sub>O. *Green Chem. Eng.* **2020**, *1* (1), 33–39. <https://doi.org/10.1016/j.gce.2020.09.003>.

- (126) Dias, E. M.; Christoforidis, K. C.; Francàs, L.; Petit, C. Tuning Thermally Treated Graphitic Carbon Nitride for H<sub>2</sub> Evolution and CO<sub>2</sub> Photoreduction: The Effects of Material Properties and Mid-Gap States. *ACS Appl. Energy Mater.* **2018**, *1* (11), 6524–6534. <https://doi.org/10.1021/acsaem.8b01441>.
- (127) Das, R.; Manna, S. S.; Pathak, B.; Nagaraja, C. M. Strategic Design of Mg-Centered Porphyrin Metal–Organic Framework for Efficient Visible Light-Promoted Fixation of CO<sub>2</sub> under Ambient Conditions: Combined Experimental and Theoretical Investigation. *ACS Appl. Mater. Interfaces* **2022**, *14* (29), 33285–33296. <https://doi.org/10.1021/acsaem.8b01441>.
- (128) Chang, X.; Wang, T.; Gong, J. CO<sub>2</sub> Photo-Reduction: Insights into CO<sub>2</sub> Activation and Reaction on Surfaces of Photocatalysts. *Energy Environ. Sci.* **2016**, *9* (7), 2177–2196. <https://doi.org/10.1039/C6EE00383D>.
- (129) Indrakanti, V. P.; Schobert, H. H.; Kubicki, J. D. Quantum Mechanical Modeling of CO<sub>2</sub> Interactions with Irradiated Stoichiometric and Oxygen-Deficient Anatase TiO<sub>2</sub> Surfaces: Implications for the Photocatalytic Reduction of CO<sub>2</sub>. *Energy Fuels* **2009**, *23* (10), 5247–5256. <https://doi.org/10.1021/ef9003957>.
- (130) Wu, J. C. S.; Huang, C.-W. In Situ DRIFTS Study of Photocatalytic CO<sub>2</sub> Reduction under UV Irradiation. *Front. Chem. Eng. China* **2010**, *4* (2), 120–126. <https://doi.org/10.1007/s11705-009-0232-3>.
- (131) Shuying Zhu; Shijing Liang; Yuecong Tong; Xiaohan An; Jinlin Long; Xianzhi Fu; Xuxu Wang. Photocatalytic Reduction of CO<sub>2</sub> with H<sub>2</sub>O to CH<sub>4</sub> on Cu(i) Supported TiO<sub>2</sub> Nanosheets with Defective {001}facets. *Phys. Chem. Chem. Phys.* **17**, 9761–9770.
- (132) Acharya, D. P.; Camillone, N.; Sutter, P. CO<sub>2</sub> Adsorption, Diffusion, and Electron-Induced Chemistry on Rutile TiO<sub>2</sub> (110): A Low-Temperature Scanning Tunneling Microscopy Study. *J. Phys. Chem. C* **2011**, *115* (24), 12095–12105. <https://doi.org/10.1021/jp202476v>.
- (133) Sasirekha, N.; Basha, S.; Shanthi, K. Photocatalytic Performance of Ru Doped Anatase Mounted on Silica for Reduction of Carbon Dioxide. *Appl. Catal. B Environ.* **2006**, *62* (1–2), 169–180. <https://doi.org/10.1016/j.apcatb.2005.07.009>.
- (134) Peterson, A. A.; Abild-Pedersen, F.; Studt, F.; Rossmeisl, J.; Nørskov, J. K. How Copper Catalyzes the Electroreduction of Carbon Dioxide into Hydrocarbon Fuels. *Energy Environ. Sci.* **2010**, *3* (9), 1311. <https://doi.org/10.1039/c0ee00071j>.
- (135) Kurtz, R. L.; Stockbauer, R.; Madey, T. E.; Roman, E.; Segovia, J. L. D. SYNCHROTRON RADIATION STUDIES OF H<sub>2</sub>O ADSORPTION ON TiO<sub>2</sub>(110).
- (136) Bikondoa, O.; Pang, C. L.; Ithnin, R.; Muryn, C. A.; Onishi, H.; Thornton, G. Direct Visualization of Defect-Mediated Dissociation of Water on TiO<sub>2</sub>(110). *Nat. Mater.* **2006**, *5* (3), 189–192. <https://doi.org/10.1038/nmat1592>.
- (137) He, H.; Zapol, P.; Curtiss, L. A. A Theoretical Study of CO<sub>2</sub> Anions on Anatase (101) Surface. *J. Phys. Chem. C* **2010**, *114* (49), 21474–21481. <https://doi.org/10.1021/jp106579b>.
- (138) Tang, J.; Durrant, J. R.; Klug, D. R. Mechanism of Photocatalytic Water Splitting in TiO<sub>2</sub>. Reaction of Water with Photoholes, Importance of Charge Carrier Dynamics, and Evidence for Four-Hole Chemistry. *J. Am. Chem. Soc.* **2008**, *130* (42), 13885–13891. <https://doi.org/10.1021/ja8034637>.

- (139) Wang, Y.; Chen, E.; Tang, J. Insight on Reaction Pathways of Photocatalytic CO<sub>2</sub> Conversion. *ACS Catal.* **2022**, *12* (12), 7300–7316. <https://doi.org/10.1021/acscatal.2c01012>.
- (140) Tahir, M.; Amin, N. S. Advances in Visible Light Responsive Titanium Oxide-Based Photocatalysts for CO<sub>2</sub> Conversion to Hydrocarbon Fuels. *Energy Convers. Manag.* **2013**, *76*, 194–214. <https://doi.org/10.1016/j.enconman.2013.07.046>.
- (141) Warren Athol Thompson; Eva Sanchez Fernandez; M.Mercedes Maroto-Valer. Review and Analysis of CO<sub>2</sub> Photoreduction Kinetics. *ACS Sustainable Chem. Eng.* **2020**, *8*, 4677–4692.
- (142) Variar, A. G.; M.S., R.; Ail, V. U.; S., S. P.; K., S.; Tahir, M. Influence of Various Operational Parameters in Enhancing Photocatalytic Reduction Efficiency of Carbon Dioxide in a Photoreactor: A Review. *J. Ind. Eng. Chem.* **2021**, *99*, 19–47. <https://doi.org/10.1016/j.jiec.2021.04.017>.
- (143) Ola, O.; Maroto-Valer, M. M. Review of Material Design and Reactor Engineering on TiO<sub>2</sub> Photocatalysis for CO<sub>2</sub> Reduction. *J. Photochem. Photobiol. C Photochem. Rev.* **2015**, *24*, 16–42. <https://doi.org/10.1016/j.jphotochemrev.2015.06.001>.
- (144) Rabita Mohd Firdaus; Alexandre Desforges; Abdul Rahman Mohamed; Brigitte Vigolo. Progress in Adsorption Capacity of Nanomaterials for Carbon Dioxide Capture: A Comparative Study. *Journal of Cleaner Production* **2021**, *328*, 129553.
- (145) Tahir, M.; Amin, N. S. Photocatalytic CO<sub>2</sub> Reduction and Kinetic Study over In/TiO<sub>2</sub> Nanoparticles Supported Microchannel Monolith Photoreactor. *Appl. Catal. Gen.* **2013**, *467*, 483–496. <https://doi.org/10.1016/j.apcata.2013.07.056>.
- (146) Li, X.; Yu, J.; Jaroniec, M.; Chen, X. Cocatalysts for Selective Photoreduction of CO<sub>2</sub> into Solar Fuels. *Chem. Rev.* **2019**, *119* (6), 3962–4179. <https://doi.org/10.1021/acs.chemrev.8b00400>.
- (147) Kumar, S.; Surendar, T.; Kumar, B.; Baruah, A.; Shanker, V. Synthesis of Highly Efficient and Recyclable Visible-Light Responsive Mesoporous g-C<sub>3</sub>N<sub>4</sub> Photocatalyst via Facile Template-Free Sonochemical Route. *RSC Adv.* **2014**, *4* (16), 8132. <https://doi.org/10.1039/c3ra43942a>.
- (148) Zahra Shariatinia. Graphitic Carbon Nitride : Synthesis and Characterisation. In *Handbook of Carbon-Based Nanomaterials*; 2021.
- (149) Teter, D. M.; Hemley, R. J. Low-Compressibility Carbon Nitrides. *Science* **1996**, *271* (5245), 53–55. <https://doi.org/10.1126/science.271.5245.53>.
- (150) Wang, X.; Maeda, K.; Thomas, A.; Takanabe, K.; Xin, G.; Carlsson, J. M.; Domen, K.; Antonietti, M. A Metal-Free Polymeric Photocatalyst for Hydrogen Production from Water under Visible Light. *Nat. Mater.* **2009**, *8* (1), 76–80. <https://doi.org/10.1038/nmat2317>.
- (151) Lin, H.; Wu, J.; Zhou, F.; Zhao, X.; Lu, P.; Sun, G.; Song, Y.; Li, Y.; Liu, X.; Dai, H. Graphitic Carbon Nitride-Based Photocatalysts in the Applications of Environmental Catalysis. *J. Environ. Sci.* **2023**, *124*, 570–590. <https://doi.org/10.1016/j.jes.2021.11.017>.

- (152) Zhou, Z.; Wang, J.; Yu, J.; Shen, Y.; Li, Y.; Liu, A.; Liu, S.; Zhang, Y. Dissolution and Liquid Crystals Phase of 2D Polymeric Carbon Nitride. *J. Am. Chem. Soc.* **2015**, *137* (6), 2179–2182. <https://doi.org/10.1021/ja512179x>.
- (153) Wang, X.; Blechert, S.; Antonietti, M. Polymeric Graphitic Carbon Nitride for Heterogeneous Photocatalysis. *ACS Catal.* **2012**, *2* (8), 1596–1606. <https://doi.org/10.1021/cs300240x>.
- (154) Zhu, J.; Xiao, P.; Li, H.; Carabineiro, S. A. C. Graphitic Carbon Nitride: Synthesis, Properties, and Applications in Catalysis. *ACS Appl. Mater. Interfaces* **2014**, *6* (19), 16449–16465. <https://doi.org/10.1021/am502925j>.
- (155) Zhai, H.-S.; Cao, L.; Xia, X.-H. Synthesis of Graphitic Carbon Nitride through Pyrolysis of Melamine and Its Electrocatalysis for Oxygen Reduction Reaction. *Chin. Chem. Lett.* **2013**, *24* (2), 103–106. <https://doi.org/10.1016/j.ccl.2013.01.030>.
- (156) Bojdys, M. J.; Müller, J.-O.; Antonietti, M.; Thomas, A. Ionothermal Synthesis of Crystalline, Condensed, Graphitic Carbon Nitride. *Chem. - Eur. J.* **2008**, *14* (27), 8177–8182. <https://doi.org/10.1002/chem.200800190>.
- (157) Jürgens, B.; Irran, E.; Senker, J.; Kroll, P.; Müller, H.; Schnick, W. Melem (2,5,8-Triamino-Tri- s -Triazine), an Important Intermediate during Condensation of Melamine Rings to Graphitic Carbon Nitride: Synthesis, Structure Determination by X-Ray Powder Diffraction, Solid-State NMR, and Theoretical Studies. *J. Am. Chem. Soc.* **2003**, *125* (34), 10288–10300. <https://doi.org/10.1021/ja0357689>.
- (158) Zheng, Y.; Zhang, Z.; Li, C. A Comparison of Graphitic Carbon Nitrides Synthesized from Different Precursors through Pyrolysis. *J. Photochem. Photobiol. Chem.* **2017**, *332*, 32–44. <https://doi.org/10.1016/j.jphotochem.2016.08.005>.
- (159) L. Stradella; M. Argentero. A Study of the Thermal Decomposition of Urea, of Related Compounds and Thiourea Using DSC and TG-EGA. *Thermochimica Acta* **1993**, No. 219, 315–323.
- (160) Li, X.; Zhang, J.; Shen, L.; Ma, Y.; Lei, W.; Cui, Q.; Zou, G. Preparation and Characterization of Graphitic Carbon Nitride through Pyrolysis of Melamine. *Appl. Phys. A* **2009**, *94* (2), 387–392. <https://doi.org/10.1007/s00339-008-4816-4>.
- (161) Martin, D. J.; Qiu, K.; Shevlin, S. A.; Handoko, A. D.; Chen, X.; Guo, Z.; Tang, J. Highly Efficient Photocatalytic H<sub>2</sub> Evolution from Water Using Visible Light and Structure-Controlled Graphitic Carbon Nitride. *Angew. Chem. Int. Ed.* **2014**, *53* (35), 9240–9245. <https://doi.org/10.1002/anie.201403375>.
- (162) Ong, W.-J.; Tan, L.-L.; Ng, Y. H.; Yong, S.-T.; Chai, S.-P. Graphitic Carbon Nitride (g-C<sub>3</sub>N<sub>4</sub>)-Based Photocatalysts for Artificial Photosynthesis and Environmental Remediation: Are We a Step Closer To Achieving Sustainability? *Chem. Rev.* **2016**, *116* (12), 7159–7329. <https://doi.org/10.1021/acs.chemrev.6b00075>.
- (163) Dou, Y.; Liao, T.; Ma, Z.; Tian, D.; Liu, Q.; Xiao, F.; Sun, Z.; Ho Kim, J.; Xue Dou, S. Graphene-like Holey Co<sub>3</sub>O<sub>4</sub> Nanosheets as a Highly Efficient Catalyst for Oxygen Evolution Reaction. *Nano Energy* **2016**, *30*, 267–275. <https://doi.org/10.1016/j.nanoen.2016.10.020>.

- (164) Chebanenko, M. I.; Zakharova, N. V.; Lobinsky, A. A.; Popkov, V. I. Ultrasonic-Assisted Exfoliation of Graphitic Carbon Nitride and Its Electrocatalytic Performance in Process of Ethanol Reforming. *Semiconductors* **2019**, *53* (16), 2072–2077. <https://doi.org/10.1134/S106378261912008X>.
- (165) Yang, S.; Gong, Y.; Zhang, J.; Zhan, L.; Ma, L.; Fang, Z.; Vajtai, R.; Wang, X.; Ajayan, P. M. Exfoliated Graphitic Carbon Nitride Nanosheets as Efficient Catalysts for Hydrogen Evolution Under Visible Light. *Adv. Mater.* **2013**, *25* (17), 2452–2456. <https://doi.org/10.1002/adma.201204453>.
- (166) Xu, J.; Zhang, L.; Shi, R.; Zhu, Y. Chemical Exfoliation of Graphitic Carbon Nitride for Efficient Heterogeneous Photocatalysis. *J. Mater. Chem. A* **2013**, *1* (46), 14766. <https://doi.org/10.1039/c3ta13188b>.
- (167) Sun, Z.; Wang, H.; Wu, Z.; Wang, L. G-C<sub>3</sub>N<sub>4</sub> Based Composite Photocatalysts for Photocatalytic CO<sub>2</sub> Reduction. *Catal. Today* **2018**, *300*, 160–172. <https://doi.org/10.1016/j.cattod.2017.05.033>.
- (168) de Medeiros, T. V.; Porto, A. O.; Bicalho, H. A.; González, J. C.; Naccache, R.; Teixeira, A. P. C. The Effects of Chemical and Thermal Exfoliation on the Physico-Chemical and Optical Properties of Carbon Nitrides. *J. Mater. Chem. C* **2021**, *9* (24), 7622–7631. <https://doi.org/10.1039/D1TC01734A>.
- (169) Qiu, P.; Chen, H.; Xu, C.; Zhou, N.; Jiang, F.; Wang, X.; Fu, Y. Fabrication of an Exfoliated Graphitic Carbon Nitride as a Highly Active Visible Light Photocatalyst. *J. Mater. Chem. A* **2015**, *3* (48), 24237–24244. <https://doi.org/10.1039/C5TA08406G>.
- (170) Thomas, A.; Goettmann, F.; Antonietti, M. Hard Templates for Soft Materials: Creating Nanostructured Organic Materials. *Chem. Mater.* **2008**, *20* (3), 738–755. <https://doi.org/10.1021/cm702126j>.
- (171) Lordi, V.; Erhart, P.; Åberg, D. Charge Carrier Scattering by Defects in Semiconductors. *Phys. Rev. B* **2010**, *81* (23), 235204. <https://doi.org/10.1103/PhysRevB.81.235204>.
- (172) Jiang, L.; Yang, J.; Yuan, X.; Guo, J.; Liang, J.; Tang, W.; Chen, Y.; Li, X.; Wang, H.; Chu, W. Defect Engineering in Polymeric Carbon Nitride Photocatalyst: Synthesis, Properties and Characterizations. *Adv. Colloid Interface Sci.* **2021**, *296*, 102523. <https://doi.org/10.1016/j.cis.2021.102523>.
- (173) Ou, H.; Lin, L.; Zheng, Y.; Yang, P.; Fang, Y.; Wang, X. Tri-*s*-Triazine-Based Crystalline Carbon Nitride Nanosheets for an Improved Hydrogen Evolution. *Adv. Mater.* **2017**, *29* (22), 1700008. <https://doi.org/10.1002/adma.201700008>.
- (174) Kim, J. S.; Oh, J. W.; Woo, S. I. Improvement of the Photocatalytic Hydrogen Production Rate of G-C<sub>3</sub>N<sub>4</sub> Following the Elimination of Defects on the Surface. *Catal. Today* **2017**, *293–294*, 8–14. <https://doi.org/10.1016/j.cattod.2016.11.018>.
- (175) Raziq, F.; Qu, Y.; Humayun, M.; Zada, A.; Yu, H.; Jing, L. Synthesis of SnO<sub>2</sub>/B-P Codoped g-C<sub>3</sub>N<sub>4</sub> Nanocomposites as Efficient Cocatalyst-Free Visible-Light Photocatalysts for CO<sub>2</sub> Conversion and Pollutant Degradation. *Appl. Catal. B Environ.* **2017**, *201*, 486–494. <https://doi.org/10.1016/j.apcatb.2016.08.057>.
- (176) Tang, S.; Zhu, Y.; Li, H.; Xu, H.; Yuan, S. Two-Dimensional Carbon Nitride-Based Composites for Photocatalytic Hydrogen Evolution. *Int. J. Hydrog. Energy* **2019**, *44* (59), 30935–30948. <https://doi.org/10.1016/j.ijhydene.2019.10.020>.

- (177) Marchal, C.; Cottineau, T.; Méndez-Medrano, M. G.; Colbeau-Justin, C.; Caps, V.; Keller, V. Au/TiO<sub>2</sub>-GC<sub>3</sub>N<sub>4</sub> Nanocomposites for Enhanced Photocatalytic H<sub>2</sub> Production from Water under Visible Light Irradiation with Very Low Quantities of Sacrificial Agents. *Adv Energy Mater* **2018**, *12*.
- (178) Yi Hu; H.-L. Tsai; C.-L. Huang. Effect of Brookite Phase on the Anatase-Rutile Transition in Titania Nanoparticles. *Journal of the European Ceramic Society* **2003**, *23*, 691–696.
- (179) Carp Oana; Carolien L. Huisman; Armin Reller. Photoinduced Reactivity of Titanium Dioxide. *Progress in Solid State Chemistry* **2004**, *32*, 33–177.
- (180) Zhang, Q. Effects of Calcination on the Photocatalytic Properties of Nanosized TiO<sub>2</sub> Powders Prepared by TiCl<sub>4</sub> Hydrolysis. *Appl. Catal. B Environ.* **2000**, *26* (3), 207–215. [https://doi.org/10.1016/S0926-3373\(00\)00122-3](https://doi.org/10.1016/S0926-3373(00)00122-3).
- (181) Pelaez, M.; Nolan, N. T.; Pillai, S. C.; Seery, M. K.; Falaras, P.; Kontos, A. G.; Dunlop, P. S. M.; Hamilton, J. W. J.; Byrne, J. A.; O’Shea, K.; Entezari, M. H.; Dionysiou, D. D. A Review on the Visible Light Active Titanium Dioxide Photocatalysts for Environmental Applications. *Appl. Catal. B Environ.* **2012**, *125*, 331–349. <https://doi.org/10.1016/j.apcatb.2012.05.036>.
- (182) Fujishima, A.; Zhang, X.; Tryk, D. TiO<sub>2</sub> Photocatalysis and Related Surface Phenomena. *Surf. Sci. Rep.* **2008**, *63* (12), 515–582. <https://doi.org/10.1016/j.surfrep.2008.10.001>.
- (183) A. Tony Paxton; Le Thiên-Nga. Electronic Structure of Reduced Titanium Dioxide. *Phys. Rev. B* **1998**, 1579.
- (184) Zhang, J.; Zhou, P.; Liu, J.; Yu, J. New Understanding of the Difference of Photocatalytic Activity among Anatase, Rutile and Brookite TiO<sub>2</sub>. *Phys. Chem. Chem. Phys.* **2014**, *16* (38), 20382–20386. <https://doi.org/10.1039/C4CP02201G>.
- (185) Tachikawa, T.; Fujitsuka, M.; Majima, T. Mechanistic Insight into the TiO<sub>2</sub> Photocatalytic Reactions: Design of New Photocatalysts. *J. Phys. Chem. C* **2007**, *111* (14), 5259–5275. <https://doi.org/10.1021/jp069005u>.
- (186) Nick Serpone; Darren Lawless; Rafail F. Khairutdinov; Ezio Pelizzetti. Subnanosecond Relaxation Dynamics in TiO<sub>2</sub> Colloidal Sols (Particle Sizes R<sub>p</sub>=1.0-13.4 Nm). Relevance to Heterogeneous Photocatalysis. *J. Phys. Chem.* **1995**, *99* (45), 16655–16661.
- (187) Schneider, J.; Matsuoka, M.; Takeuchi, M.; Zhang, J.; Horiuchi, Y.; Anpo, M.; Bahnemann, D. W. Understanding TiO<sub>2</sub> Photocatalysis: Mechanisms and Materials. *Chem. Rev.* **2014**, *114* (19), 9919–9986. <https://doi.org/10.1021/cr5001892>.
- (188) Colbeau-Justin, C.; Valenzuela, M. A. Time-Resolved Microwave Conductivity (TRMC) a Useful Characterization Tool for Charge Carrier Transfer in Photocatalysis: A Short Review. *Rev Mex Fis* **2013**, *11*.
- (189) Colbeau-Justin, C.; Kunst, M.; Huguenin, D. Structural Influence on Charge-Carrier Lifetimes in TiO<sub>2</sub> Powders Studied by Microwave Absorption. 9.
- (190) Tang, H.; Prasad, K.; Sanjinès, R.; Schmid, P. E.; Lévy, F. Electrical and Optical Properties of TiO<sub>2</sub> Anatase Thin Films. *J. Appl. Phys.* **1994**, *75* (4), 2042–2047. <https://doi.org/10.1063/1.356306>.

- (191) Asahi, R.; Taga, Y.; Mannstadt, W.; Freeman, A. J. Electronic and Optical Properties of Anatase TiO<sub>2</sub>. *Phys. Rev. B* **2000**, *61* (11), 7459–7465. <https://doi.org/10.1103/PhysRevB.61.7459>.
- (192) Jiaguo Yu; Huogen Yu; Bei Cheng; Minghua Zhou; Xiujian Zhao. Enhanced Photocatalytic Activity of TiO<sub>2</sub> Powder (P25) by Hydrothermal Treatment. *Journal of Molecular Catalysis A: Chemical* **2006**, *253*, 112–118.
- (193) Bathla, A.; Lee, J.; Younis, S. A.; Kim, K.-H. Recent Advances in Photocatalytic Reduction of CO<sub>2</sub> by TiO<sub>2</sub>- and MOF-Based Nanocomposites Impregnated with Metal Nanoparticles. *Mater. Today Chem.* **2022**, *24*, 100870. <https://doi.org/10.1016/j.mtchem.2022.100870>.
- (194) Crake, A.; Christoforidis, K. C.; Gregg, A.; Moss, B.; Kafizas, A.; Petit, C. The Effect of Materials Architecture in TiO<sub>2</sub>/MOF Composites on CO<sub>2</sub> Photoreduction and Charge Transfer. *Small* **2019**, *15* (11), 1805473. <https://doi.org/10.1002/sml.201805473>.
- (195) Cook, T. R.; Zheng, Y.-R.; Stang, P. J. Metal–Organic Frameworks and Self-Assembled Supramolecular Coordination Complexes: Comparing and Contrasting the Design, Synthesis, and Functionality of Metal–Organic Materials. *Chem. Rev.* **2013**, *113* (1), 734–777. <https://doi.org/10.1021/cr3002824>.
- (196) Ghanbari, T.; Abnisa, F.; Wan Daud, W. M. A. A Review on Production of Metal Organic Frameworks (MOF) for CO<sub>2</sub> Adsorption. *Sci. Total Environ.* **2020**, *707*, 135090. <https://doi.org/10.1016/j.scitotenv.2019.135090>.
- (197) Abánades Lázaro, I.; Forgan, R. S. Application of Zirconium MOFs in Drug Delivery and Biomedicine. *Coord. Chem. Rev.* **2019**, *380*, 230–259. <https://doi.org/10.1016/j.ccr.2018.09.009>.
- (198) Chocarro-Ruiz, B.; Pérez-Carvajal, J.; Avci, C.; Calvo-Lozano, O.; Alonso, M. I.; MasPOCH, D.; Lechuga, L. M. A CO<sub>2</sub> Optical Sensor Based on Self-Assembled Metal–Organic Framework Nanoparticles. *J. Mater. Chem. A* **2018**, *6* (27), 13171–13177. <https://doi.org/10.1039/C8TA02767F>.
- (199) Wang, J.-L.; Wang, C.; Lin, W. Metal–Organic Frameworks for Light Harvesting and Photocatalysis. *ACS Catal.* **2012**, *2* (12), 2630–2640. <https://doi.org/10.1021/cs3005874>.
- (200) Sun, Y.; Zhang, N.; Yue, Y.; Xiao, J.; Huang, X.; Ishag, A. Recent Advances in the Application of Zeolitic Imidazolate Frameworks (ZIFs) in Environmental Remediation: A Review. *Environ. Sci. Nano* **2022**, *9* (11), 4069–4092. <https://doi.org/10.1039/D2EN00601D>.
- (201) Zhang, X.; Wasson, M. C.; Shayan, M.; Berdichevsky, E. K.; Ricardo-Noordberg, J.; Singh, Z.; Papazyan, E. K.; Castro, A. J.; Marino, P.; Ajoyan, Z.; Chen, Z.; Islamoglu, T.; Howarth, A. J.; Liu, Y.; Majewski, M. B.; Katz, M. J.; Mondloch, J. E.; Farha, O. K. A Historical Perspective on Porphyrin-Based Metal–Organic Frameworks and Their Applications. *Coord. Chem. Rev.* **2021**, *429*, 213615. <https://doi.org/10.1016/j.ccr.2020.213615>.
- (202) Bai, Y.; Dou, Y.; Xie, L.-H.; Rutledge, W.; Li, J.-R.; Zhou, H.-C. Zr-Based Metal–Organic Frameworks: Design, Synthesis, Structure, and Applications. *Chem. Soc. Rev.* **2016**, *45* (8), 2327–2367. <https://doi.org/10.1039/C5CS00837A>.

- (203) Janiak, C.; Vieth, J. K. MOFs, MILs and More: Concepts, Properties and Applications for Porous Coordination Networks (PCNs). *New J. Chem.* **2010**, *34* (11), 2366. <https://doi.org/10.1039/c0nj00275e>.
- (204) Raptopoulou, C. P. Metal-Organic Frameworks: Synthetic Methods and Potential Applications. **2021**, 32.
- (205) Forgan, R. S. Modulated Self-Assembly of Metal–Organic Frameworks. *Chem. Sci.* **2020**, *11* (18), 4546–4562. <https://doi.org/10.1039/D0SC01356K>.
- (206) Kelty, M. L.; Morris, W.; Gallagher, A. T.; Anderson, J. S.; Brown, K. A.; Mirkin, C. A.; Harris, T. D. High-Throughput Synthesis and Characterization of Nanocrystalline Porphyrinic Zirconium Metal–Organic Frameworks. *Chem. Commun.* **2016**, *52* (50), 7854–7857. <https://doi.org/10.1039/C6CC03264H>.
- (207) Al Amery, N.; Abid, H. R.; Al-Saadi, S.; Wang, S.; Liu, S. Facile Directions for Synthesis, Modification and Activation of MOFs. *Mater. Today Chem.* **2020**, *17*, 100343. <https://doi.org/10.1016/j.mtchem.2020.100343>.
- (208) Lee, Y.-R.; Kim, J.; Ahn, W.-S. Synthesis of Metal-Organic Frameworks: A Mini Review. *Korean J. Chem. Eng.* **2013**, *30* (9), 1667–1680. <https://doi.org/10.1007/s11814-013-0140-6>.
- (209) SungHwa Jhung; Jin-Ho Lee; Paul M. Forster; Gerard Ferey; Anthony K. Cheetham; Jong-San Chang. Microwave Synthesis of Hybrid Inorganic–Organic Porous Materials: Phase-Selective and Rapid Crystallization. *Chem. Eur. J.* **2006**, No. 12, 7899–7905.
- (210) *Metal-Organic Framework Materials*; MacGillivray, L. R., Lukehart, C. M., Eds.; Wiley: Chichester, West Sussex, 2014.
- (211) Zhang, X.; Chen, Z.; Liu, X.; Hanna, S. L.; Wang, X.; Taheri-Ledari, R.; Maleki, A.; Li, P.; Farha, O. K. A Historical Overview of the Activation and Porosity of Metal–Organic Frameworks. *Chem. Soc. Rev.* **2020**, *49* (20), 7406–7427. <https://doi.org/10.1039/D0CS00997K>.
- (212) Mondloch, J. E.; Karagiari, O.; Farha, O. K.; Hupp, J. T. Activation of Metal–Organic Framework Materials. *CrystEngComm* **2013**, *15* (45), 9258. <https://doi.org/10.1039/c3ce41232f>.
- (213) Howarth, A. J.; Peters, A. W.; Vermeulen, N. A.; Wang, T. C.; Hupp, J. T.; Farha, O. K. Best Practices for the Synthesis, Activation, and Characterization of Metal–Organic Frameworks. *Chem. Mater.* **2017**, *29* (1), 26–39. <https://doi.org/10.1021/acs.chemmater.6b02626>.
- (214) Nelson, A. P.; Farha, O. K.; Mulfort, K. L.; Hupp, J. T. Supercritical Processing as a Route to High Internal Surface Areas and Permanent Microporosity in Metal–Organic Framework Materials. *J. Am. Chem. Soc.* **2009**, *131* (2), 458–460. <https://doi.org/10.1021/ja808853q>.
- (215) Ma, L.; Jin, A.; Xie, Z.; Lin, W. Freeze Drying Significantly Increases Permanent Porosity and Hydrogen Uptake in 4,4-Connected Metal–Organic Frameworks. *Angew. Chem. Int. Ed.* **2009**, *48* (52), 9905–9908. <https://doi.org/10.1002/anie.200904983>.
- (216) Feng, D.; Gu, Z.-Y.; Li, J.-R.; Jiang, H.-L.; Wei, Z.; Zhou, H.-C. Zirconium-Metalloporphyrin PCN-222: Mesoporous Metal-Organic Frameworks with Ultrahigh Stability as Biomimetic Catalysts. *Angew. Chem. Int. Ed.* **2012**, *51* (41), 10307–10310. <https://doi.org/10.1002/anie.201204475>.

- (217) Sun, D.; Fu, Y.; Liu, W.; Ye, L.; Wang, D.; Yang, L.; Fu, X.; Li, Z. Studies on Photocatalytic CO<sub>2</sub> Reduction over NH<sub>2</sub>-Uio-66(Zr) and Its Derivatives: Towards a Better Understanding of Photocatalysis on Metal-Organic Frameworks. *Chem. - Eur. J.* **2013**, *19* (42), 14279–14285. <https://doi.org/10.1002/chem.201301728>.
- (218) Torrisi, A.; Bell, R. G.; Mellot-Draznieks, C. Functionalized MOFs for Enhanced CO<sub>2</sub> Capture. *Cryst. Growth Des.* **2010**, *10* (7), 2839–2841. <https://doi.org/10.1021/cg100646e>.
- (219) Torrisi, A.; Mellot-Draznieks, C.; Bell, R. G. Impact of Ligands on CO<sub>2</sub> Adsorption in Metal-Organic Frameworks: First Principles Study of the Interaction of CO<sub>2</sub> with Functionalized Benzenes. I. Inductive Effects on the Aromatic Ring. *J Chem Phys* **14**.
- (220) Chen, Y.; Wang, D.; Deng, X.; Li, Z. Metal–Organic Frameworks (MOFs) for Photocatalytic CO<sub>2</sub> Reduction. *Catal Sci Technol* **2017**, *7* (21), 4893–4904. <https://doi.org/10.1039/C7CY01653K>.
- (221) Diercks, C. S.; Liu, Y.; Cordova, K. E.; Yaghi, O. M. The Role of Reticular Chemistry in the Design of CO<sub>2</sub> Reduction Catalysts. *Nat. Mater.* **2018**, *17* (4), 301–307. <https://doi.org/10.1038/s41563-018-0033-5>.
- (222) Li, Y.; Xu, H.; Ouyang, S.; Ye, J. Metal–Organic Frameworks for Photocatalysis. *Phys. Chem. Chem. Phys.* **2016**, *18* (11), 7563–7572. <https://doi.org/10.1039/C5CP05885F>.
- (223) Hao, Y.-C.; Chen, L.-W.; Li, J.; Guo, Y.; Su, X.; Shu, M.; Zhang, Q.; Gao, W.-Y.; Li, S.; Yu, Z.-L.; Gu, L.; Feng, X.; Yin, A.-X.; Si, R.; Zhang, Y.-W.; Wang, B.; Yan, C.-H. Metal-Organic Framework Membranes with Single-Atomic Centers for Photocatalytic CO<sub>2</sub> and O<sub>2</sub> Reduction. *Nat. Commun.* **2021**, *12* (1), 2682. <https://doi.org/10.1038/s41467-021-22991-7>.
- (224) Yanghe Fu; Dengrong Sun; Yongjuan Chen; Renkun Huang; Zhengxin Ding; Xianzhi Fu; Zhaohui Li. An Aminofunctionalized Titanium Metal–Organic Framework Photocatalyst with Visible-Light-Induced Activity for CO<sub>2</sub> Reduction. *Angew. Chem. Int. Ed.* **2012**, No. 51, 3364–3367.
- (225) Musho, T.; Li, J.; Wu, N. Band Gap Modulation of Functionalized Metal–Organic Frameworks. *Phys Chem Chem Phys* **2014**, *16* (43), 23646–23653. <https://doi.org/10.1039/C4CP03110E>.
- (226) Ji-Won Yoon; Jae-Hyeok Kim; Changyeon Kim; Ho Won Jang; Jong-Heun Lee. MOF-Based Hybrids for Solar Fuel Production. *Adv. Energy Mater.* **2021**, *11*, 2003052.
- (227) Yin, Z.; Song, T.; Zhou, W.; Wang, Z.; Ma, Y. Highly Isolated Pt NPs Embedded in Porous TiO<sub>2</sub> Derived from MIL-125 with Enhanced Photocatalytic Hydrogen Production Activity. *J. Catal.* **2021**, *402*, 289–299. <https://doi.org/10.1016/j.jcat.2021.08.039>.
- (228) Wang, S.; Guan, B. Y.; Lu, Y.; Lou, X. W. “David.” Formation of Hierarchical In<sub>2</sub>S<sub>3</sub>–CdIn<sub>2</sub>S<sub>4</sub> Heterostructured Nanotubes for Efficient and Stable Visible Light CO<sub>2</sub> Reduction. *J. Am. Chem. Soc.* **2017**, *139* (48), 17305–17308. <https://doi.org/10.1021/jacs.7b10733>.
- (229) Ren, J.-T.; Zheng, Y.-L.; Yuan, K.; Zhou, L.; Wu, K.; Zhang, Y.-W. Self-Templated Synthesis of Co<sub>3</sub>O<sub>4</sub> Hierarchical Nanosheets from a Metal–Organic

- Framework for Efficient Visible-Light Photocatalytic CO<sub>2</sub> Reduction. *Nanoscale* **2020**, *12* (2), 755–762. <https://doi.org/10.1039/C9NR08669B>.
- (230) Su, Y.; Ao, D.; Liu, H.; Wang, Y. MOF-Derived Yolk–Shell CdS Microcubes with Enhanced Visible-Light Photocatalytic Activity and Stability for Hydrogen Evolution. *J. Mater. Chem. A* **2017**, *5* (18), 8680–8689. <https://doi.org/10.1039/C7TA00855D>.
- (231) Zhiqiang Xie; Wangwang Xu; Xiaodan Cui; Ying Wang. Recent Progresses on Metal-Organic Frameworks and Their Derived Nanostructures for Energy and Environmental Applications. *ChemSusChem* **2017**, *10*, 1645–1663.
- (232) Choi, J. Y.; Lim, C. K.; Park, B.; Kim, M.; Jamal, A.; Song, H. Surface Activation of Cobalt Oxide Nanoparticles for Photocatalytic Carbon Dioxide Reduction to Methane. *J. Mater. Chem. A* **2019**, *7* (25), 15068–15072. <https://doi.org/10.1039/C9TA04323C>.
- (233) Zhu, S.; Li, X.; Jiao, X.; Shao, W.; Li, L.; Zu, X.; Hu, J.; Zhu, J.; Yan, W.; Wang, C.; Sun, Y.; Xie, Y. Selective CO<sub>2</sub> Photoreduction into C<sub>2</sub> Product Enabled by Charge-Polarized Metal Pair Sites. *Nano Lett.* **2021**, *21* (5), 2324–2331. <https://doi.org/10.1021/acs.nanolett.1c00383>.
- (234) Gao, C.; Meng, Q.; Zhao, K.; Yin, H.; Wang, D.; Guo, J.; Zhao, S.; Chang, L.; He, M.; Li, Q.; Zhao, H.; Huang, X.; Gao, Y.; Tang, Z. Co<sub>3</sub>O<sub>4</sub> Hexagonal Platelets with Controllable Facets Enabling Highly Efficient Visible-Light Photocatalytic Reduction of CO<sub>2</sub>. *Adv. Mater.* **2016**, *28* (30), 6485–6490. <https://doi.org/10.1002/adma.201601387>.
- (235) Huh, S. Porphyrinic Metal–Organic Frameworks from Custom-Designed Porphyrins. **2016**, 25.
- (236) Gary R.Krieger; Scott D.Philips. Blood. In *Encyclopedia of Toxicology (Second Edition)*; 2005; pp 323–329.
- (237) Dennis P. Arnold; John P. Bartley. Tin Porphyrins. 6. Tin-119 Chemical Shifts and Line Widths of Tin(IV) Complexes of Tetraphenyl-, Tetra-p-Tolyl-, and Octaethylporphyrin. *Inorg. Chem.* **1994**, *33* (7), 1486–1490.
- (238) Huabin Zhang; Jing Wei; Juncai Dong; Guigao Liu; Li Shi; Pengfei An; Guixia Zhao; Jintao Kong; Xiaojun Wang; Xianguang Meng; Jing Zhang; Jinhua Ye. Efficient Visible-Light-Driven Carbon Dioxide Reduction by a Single-Atom Implanted Metal–Organic Framework. *Angew. Chem. Int. Ed.* **2016**, *55*, 1–6.
- (239) Fateeva, A.; Chater, P. A.; Ireland, C. P.; Tahir, A. A.; Khimyak, Y. Z.; Wiper, P. V.; Darwent, J. R.; Rosseinsky, M. J. A Water-Stable Porphyrin-Based Metal–Organic Framework Active for Visible-Light Photocatalysis. *Angew. Chem. Int. Ed.* **2012**, *51* (30), 7440–7444. <https://doi.org/10.1002/anie.201202471>.
- (240) Lohse, M. S.; Bein, T. Covalent Organic Frameworks: Structures, Synthesis, and Applications. *Adv. Funct. Mater.* **2018**, *28* (33), 1705553. <https://doi.org/10.1002/adfm.201705553>.
- (241) Zhang, H.; Wei, J.; Dong, J.; Liu, G.; Shi, L.; An, P.; Zhao, G.; Kong, J.; Wang, X.; Meng, X.; Zhang, J.; Ye, J. Efficient Visible-Light-Driven Carbon Dioxide Reduction by a Single-Atom Implanted Metal–Organic Framework. *Angew. Chem. Int. Ed.* **2016**, *55* (46), 14310–14314. <https://doi.org/10.1002/anie.201608597>.

- (242) Sreehari Surendran Rajasree; Xinlin Li; Pravas Deria. Physical Properties of Porphyrin-Based Crystalline Metal–organic Frameworks. *COMMUNICATIONS CHEMISTRY* **2021**, No. 4, 47.
- (243) Sun, D.; Liu, W.; Qiu, M.; Zhang, Y.; Li, Z. Introduction of a Mediator for Enhancing Photocatalytic Performance via Post-Synthetic Metal Exchange in Metal–Organic Frameworks (MOFs). *Chem. Commun.* **2015**, 51 (11), 2056–2059. <https://doi.org/10.1039/C4CC09407G>.
- (244) Chavan, S. M.; Shearer, G. C.; Svelle, S.; Olsbye, U.; Bonino, F.; Ethiraj, J.; Lillerud, K. P.; Bordiga, S. Synthesis and Characterization of Amine-Functionalized Mixed-Ligand Metal–Organic Frameworks of UiO-66 Topology. *Inorg. Chem.* **2014**, 53 (18), 9509–9515. <https://doi.org/10.1021/ic500607a>.
- (245) Yeob Lee; Sangjun Kim; Jeung Ku Kang; Seth M. Cohen. Photocatalytic CO<sub>2</sub> Reduction by a Mixed Metal (Zr/Ti), Mixed Ligand Metal–Organic Framework under Visible Light Irradiation. *Chem. Commun.* **2015**, 51, 5735.
- (246) Liu, M.; Xing, Z.; Li, Z.; Zhou, W. Recent Advances in Core–Shell Metal Organic Frame-Based Photocatalysts for Solar Energy Conversion. *Coord. Chem. Rev.* **2021**, 446, 214123. <https://doi.org/10.1016/j.ccr.2021.214123>.
- (247) Guo, C.; Guo, J.; Zhang, Y.; Wang, D.; Zhang, L.; Guo, Y.; Ma, W.; Wang, J. Synthesis of Core–Shell ZIF-67@Co-MOF-74 Catalyst with Controllable Shell Thickness and Enhanced Photocatalytic Activity for Visible Light-Driven Water Oxidation. *CrystEngComm* **2018**, 20 (47), 7659–7665. <https://doi.org/10.1039/C8CE01266K>.
- (248) Zheao Huang; Jianqing Zhou; Yingying Zhao; Hengbin Cheng; Gongxuan Lu; Antoni W. Morawski; Ying Yu. Stable Core–Shell ZIF-8@ZIF-67 MOFs Photocatalyst for Highly Efficient Degradation of Organic Pollutant and Hydrogen Evolution. *Journal of Materials Research* **36**, 602–614.
- (249) Zhang, J.; Zhang, T.; Xiao, K.; Cheng, S.; Qian, G.; Wang, Y.; Feng, Y. Novel and Facile Strategy for Controllable Synthesis of Multilayered Core–Shell Zeolitic Imidazolate Frameworks. *Cryst. Growth Des.* **2016**, 16 (11), 6494–6498. <https://doi.org/10.1021/acs.cgd.6b01161>.
- (250) Tang, J.; Salunkhe, R. R.; Zhang, H.; Malgras, V.; Ahamad, T.; Alshehri, S. M.; Kobayashi, N.; Tominaka, S.; Ide, Y.; Kim, J. H.; Yamauchi, Y. Bimetallic Metal–Organic Frameworks for Controlled Catalytic Graphitization of Nanoporous Carbons. *Sci. Rep.* **2016**, 6 (1), 30295. <https://doi.org/10.1038/srep30295>.
- (251) Avci, C.; Yazdi, A.; Tarrés, M.; Bernoud, E.; Bastús, N. G.; Puntès, V.; Imaz, I.; Ribas, X.; MasPOCH, D. Sequential Deconstruction–Reconstruction of Metal–Organic Frameworks: An Alternative Strategy for Synthesizing (Multi)-Layered ZIF Composites. *ACS Appl. Mater. Interfaces* **2018**, 10 (28), 23952–23960. <https://doi.org/10.1021/acsami.8b05098>.
- (252) Avci, C.; Ariñez-Soriano, J.; Carné-Sánchez, A.; Guillerm, V.; Carbonell, C.; Imaz, I.; MasPOCH, D. Post-Synthetic Anisotropic Wet-Chemical Etching of Colloidal Sodalite ZIF Crystals. *Angew. Chem. Int. Ed.* **2015**, 54 (48), 14417–14421. <https://doi.org/10.1002/anie.201507588>.
- (253) Cai, Z.; Wang, Z.; Xia, Y.; Lim, H.; Zhou, W.; Taniguchi, A.; Ohtani, M.; Kobiro, K.; Fujita, T.; Yamauchi, Y. Tailored Catalytic Nanoframes from Metal–Organic Frameworks by Anisotropic Surface Modification and Etching for the Hydrogen

## CHAPTER 1

Evolution Reaction. *Angew. Chem. Int. Ed.* **2021**, *60* (9), 4747–4755.  
<https://doi.org/10.1002/anie.202010618>.

## CHAPTER 1



## Chapter 2: Materials and Methods

## Table of figures

FIGURE 2.1: SCHEMATIC ILLUSTRATION OF CN SYNTHESIS .....	73
FIGURE 2.2: SCHEMATIC ILLUSTRATION OF ZIF-67 .....	74
FIGURE 2. 3: SCHEMATIC ILLUSTRATION OF THE SYNTHESIS $CO_3O_4$ -BK AND $CO_3O_4$ -NS .....	75
FIGURE 2. 4: SCHEMATIC ILLUSTRATION OF THE SYNTHESIS $CO_3O_4$ -BK AND $CO_3O_4$ -NS AND THE COMPOSITE DEVELOPMENT.....	76
FIGURE 2. 5: SYNTHESIS ROUTES OF (A) PCN-224 AND (B) CU-PCN-224.....	77
FIGURE 2. 6: SCHEMATIC ILLUSTRATION OF THE SYNTHESIS OF MULTILAYERED ZIF-TiO <sub>2</sub> COMPOSITES	79
FIGURE 2. 7: SCHEME OF THE PT NPS DEPOSITION BY CHEMICAL REDUCTION .....	80
FIGURE 2. 8: XPS CHARACTERIZATION PRINCIPLE.....	83
FIGURE 2. 9: SCHEMATIC ILLUSTRATION OF THE SET-UP USED TO PERFORM THE PHOTOCURRENT MEASUREMENTS (LEFT), WORKING ELECTRODE: CATALYST DEPOSITED ON ITO (RIGHT) .....	86
FIGURE 2. 10: SCHEMATIC ILLUSTRATION OF THE BASIC PRINCIPLE OF (A): UV/VIS IN STATIONERY- STATE AND (B) TRANSIENT ABSORPTION SPECTROSCOPY .....	87
FIGURE 2. 11: STRUCTURES OF COMMONLY USED COMPOUNDS AS SPIN TRAPS.....	90
FIGURE 2. 12: ENERGY DIAGRAM SHOWING ABSORPTION OF LIGHT, AND EMISSION THROUGH FLUORESCENCE AND PHOSPHORESCENCE .....	90
FIGURE 2. 13: PICTURE OF THE PHOTOCATALYTIC SET-UP USED FOR THE PHOTOCATALYTIC WATER SPLITTING .....	92
FIGURE 2. 14: SCHEMATIC ILLUSTRATION OF THE CO <sub>2</sub> REDUCTION SET-UP .....	94
FIGURE 2. 15: PICTURE OF THE PHOTOCATALYTIC SET-UP USED FOR THE CO <sub>2</sub> REDUCTION TESTS IN CONTINUOUS FLOW CONDITIONS .....	95
FIGURE 2. 16: (A) IRRADIATION SPECTRA OF HG LAMP (150W, CERAMIC-METAL-HALIDE, C- TOPSPOT, STRASSELEC SARL) AND (B) PICTURE OF THE GAS/SOLID PHOTOREACTOR.....	95

### Introduction

In this chapter, three main parts of the present PhD studies are discussed. The protocols of synthesis for the materials development are presented. This includes the development of three different series of materials used for photocatalytic applications. The applied conditions during the material's synthesis and the influence of the parameters used are also explained. Furthermore, the characterization techniques employed for the structural, electronic, compositional, and morphological characterization are also discussed. Finally, the set-ups used for the photocatalytic evaluation of the prepared photocatalysts are presented. Specifically:

1. The first part is dedicated to carbon nitride synthesis and its modification using a facile thermal treatment. The influence of the thermal treatment temperature on the properties of the final material is given. In addition, the synthesis protocols of the different categories of MOFs (i.e., ZIFs, PCN) used are shown. Following the methods applied for the development of the individual materials, the approaches for the development of multi-component structures are discussed, and the parameter for developing different MOF content is scrutinized. Finally, the method of metal nanoparticles deposition via chemical reduction, is presented.
2. This second part focuses on the experimental techniques employed for the characterization of the synthesized photocatalysts. Their fundamental principles are presented, and the equipment used is shown.
3. In the last part, the experimental configurations used for the photocatalytic evaluation of the synthesized materials towards CO<sub>2</sub> reduction and H<sub>2</sub>O splitting, are explained, and described in detail.

The results of the materials characterization and their photocatalytic performance will be discussed in [Chapters 3-5](#).

## I. Synthesis protocols

### I.1. Carbon nitride

For the synthesis of CN, melamine is used as nitrogen-rich precursor. The choice of this precursor is based on the relatively high yield of synthesis compared to other precursors (i.e., urea). Furthermore, the method of thermal polycondensation is one of the simplest that is reported. Specifically, in a typical synthesis of carbon nitride, 30.1 g of melamine ( $C_3H_6N_6$ , 99%, Sigma-Aldrich) are added inside an alumina crucible with a cover and then placed in a muffled furnace under static air. Then, a ramping rate of  $5^\circ C \text{ min}^{-1}$  is used to reach the operating temperature. This is followed by an isotherm at  $550^\circ C$  for 4 hours<sup>1</sup>. Finally, the materials are let to cool down naturally. During the thermal polycondensation reaction, a cover must be used in order to maintain the melamine vapors that, thereafter, will be condensed to form the heptazine units. The ramping rate and the condensation temperature are chosen carefully based on studies already reported, in order to ensure the decomposition of the precursors and the condensation of the building units is to the highest possible extent, respectively. After the end of the thermal treatment (yield=50%), the material resulted are collected and grounded to fine powder using an agate mortar. The yellow powder collected was denoted as  $CN_{as}$  (15.0 g). The collected material is followingly subjected to a second thermal treatment, where the influence of the temperature is examined. Specifically, 2 g of  $CN_{as}$  are placed in an open alumina crucible in a muffle oven under static air. It is then treated thermally with a heating rate of  $5^\circ C \text{ min}^{-1}$  for 2 hours at different temperatures. Specifically, 530, 550 and  $570^\circ C$ . The thermally modified materials are denoted as  $CN_{530}$ ,  $CN_{550}$ ,  $CN_{570}$ , indicating the temperature of the thermally treated process applied. The mass of samples collected after the second thermal treatment is given in Table 2.1. It is highlighted that treating the as synthesized CN at temperatures equal to or higher than  $600^\circ C$  leads to the total removal of CN since no material is recovered. The schematic illustration of Carbon Nitride synthesis is depicted in Figure 2.1.

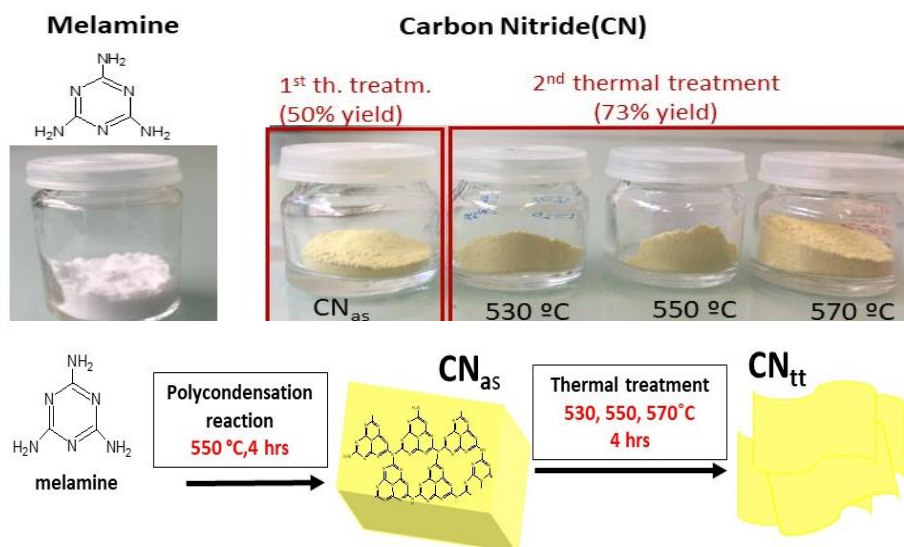


Figure 2.1: Schematic illustration of CN synthesis

Table 2.1: Mass loss (%) of CN materials after second thermal treatment

samples	Initial mass (g)	Final mass (g)	Mass loss (%) *
CN <sub>530</sub>	2.0000	1.627	18.35
CN <sub>550</sub>	2.0000	1.444	27.4
CN <sub>570</sub>	2.0000	1.445	27.5

\*Mass loss (%) = (initial mass-final mass)/initial mass

## 1.2. Titanium dioxide

In the present dissertation, different TiO<sub>2</sub> structures are considered for the needs of the experiments. Commercially available TiO<sub>2</sub> (Hombikat UV100) is used. It is 100% anatase with crystallite size 8 nm and of total surface area equal to 300 m<sup>2</sup> g<sup>-1</sup>. The above characteristics, in combination with the benefits of anatase phase over rutile (mentioned in [Chapter 1](#)) rendered TiO<sub>2</sub> UV100 a desirable semiconductor for the development of composite materials.

## 1.3.MOFs

## 1.3.a. ZIF-67 and Co-MOF synthesis

The synthesis of MOF structures is more complex than the synthesis of carbon nitride and in most cases requires more than one step. Among MOFs, synthesis protocols for the development of ZIF structures are easier and faster. In the framework of the present dissertation one of the MOF structures that is investigated is ZIF-67. This specific crystallized structure is comprised of  $\text{Co}^{2+}$  metal nodes and imidazolate chemical moieties as the organic linker. Its structure is shown in Figure 2.2. ZIF-67 is chosen because the synthesis protocol is relatively easy and straightforward. It can be synthesized quickly in ambient conditions via a sonochemical method, without using toxic solvents (i.e., N,N-dimethylformamide). The protocol for the development of ZIF-67 is adopted by the literature <sup>2</sup>. It involves the preparation of two different solutions. The first contains the metal node precursor and the second the organic linker. Specifically, Solution A is prepared by dissolving 1.113 g of cobalt (II) nitrate hexahydrate ( $\text{Co}(\text{NO}_3)_2$ , 98%, Sigma-Aldrich) in 30 ml of methanol (>99.99%, Carbo Erba) and solution B by dissolving 1.236 g of methylimidazole ( $\text{CH}_3\text{C}_3\text{H}_3\text{N}_2$ , 98%, Sigma-Aldrich) in 30 ml of methanol. The two solutions are mixed. Specifically, solution A is added drop by drop to solution B under continuous sonication at room temperature. The color of the solution changes rapidly upon mixing the two solutions. The resulting mixture is further sonicated for 20 min at room temperature. The purple ZIF-67 material is collected via filtration and washed thoroughly with methanol via filtration to remove any unreacted reagents. Finally, it is vacuum dried at 65 °C overnight.



Figure 2.2: Schematic illustration of ZIF-67

The parent ZIF-67 structure is post modified in order to alter the morphology. The modification process involves a facile solvothermal treatment in the presence of  $\text{Co}^{2+}$  <sup>3</sup>. In detail, 1.85 g of ZIF-67 are dispersed in methanol and then mixed with a solution of methanol containing 1.63 g of  $\text{Co}(\text{NO}_3)_2 \cdot 6\text{H}_2\text{O}$  with the aid of sonication. The

resulting mixture is then transferred into a Teflon-lined stainless-steel autoclave and heated at 120 °C for 1 h. The material (labeled m-ZIF-67) is collected, washed with methanol several times and vacuum dried at 65 °C overnight.

### 1.3.a.i. Synthesis of Oxides derived from MOFs

The prepared ZIF-67 and m-ZIF-67 structures are used as precursors to develop cobalt oxides ( $\text{Co}_3\text{O}_4$ ) of different morphology. For the development of bulk  $\text{Co}_3\text{O}_4$  (labeled  $\text{Co}_3\text{O}_4\text{-Bk}$ ) and  $\text{Co}_3\text{O}_4$  nanosheets (labeled  $\text{Co}_3\text{O}_4\text{-NS}$ ), the prepared ZIF-67 and m-ZIF-67 are calcined in an open alumina crucible at 350 °C for 2 h using a 5 °C  $\text{min}^{-1}$  heating ramp in a muffled furnace <sup>2</sup>. A schematic representation of the synthesis protocol is given in Figure 2.3

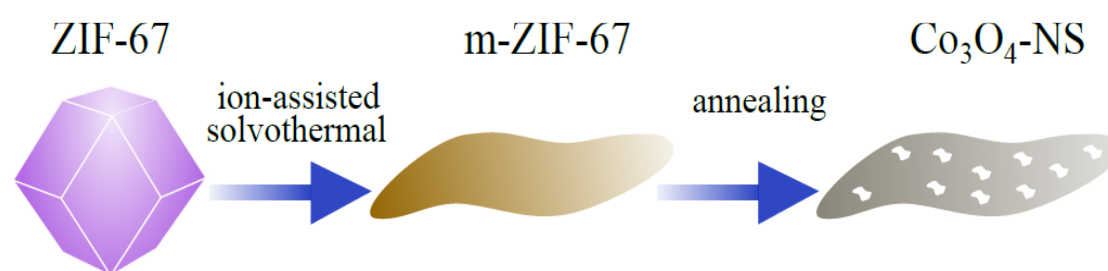


Figure 2. 3: Schematic illustration of the synthesis  $\text{Co}_3\text{O}_4\text{-bk}$  and  $\text{Co}_3\text{O}_4\text{-NS}$

A simple process is applied for the development of  $\text{Co}_3\text{O}_4/\text{CN}$  nanocomposites (Figure 2.4). 200 mg of pre-synthesized  $\text{CN}_{570}$  material are placed in 40 ml of methanol and are sonicated for 1 hour. A specific amount of ZIF-67 or m-ZIF-67 is dispersed in methanol, sonicated for 5 mins and then added in the CN dispersion. The resulting mixture is further sonicated for 10 min at room temperature, stirred for 2 h under ambient conditions and finally dried using a rotor evaporator. The material is collected and calcined at 350 °C for 2 h using a 5 °C  $\text{min}^{-1}$  ramping rate at static air. The same conditions as applied for the development of the pure  $\text{Co}_3\text{O}_4$ . The amount of  $\text{Co}_3\text{O}_4$  in the final nanocomposite is controlled by varying the amount of ZIF-67 and m-ZIF-67 in the synthesis process. In the end, Nanocomposites with 3, 5, 7 and 10 % m-ZIF-67 nominal weight are developed. Materials developed using different amounts of m-ZIF-67 as the  $\text{Co}_3\text{O}_4$  precursor are labeled  $\text{Co}_x\text{-NS-CN}_{570}$ , where x stands for the m-ZIF-67 nominal weight (i.e., for the material  $\text{Co}_3\text{-NS-CN}_{570}$ , 3wt.% m-ZIF-67 is deposited on the  $\text{CN}_{570}$  material).

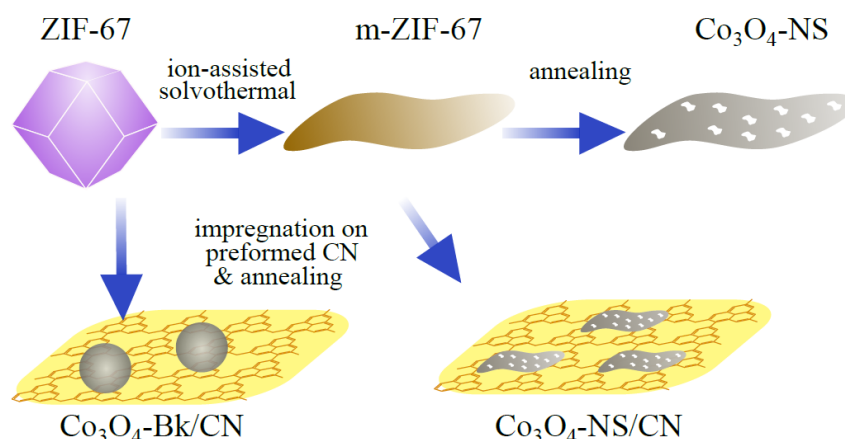


Figure 2. 4: Schematic illustration of the synthesis  $\text{Co}_3\text{O}_4\text{-bk}$  and  $\text{Co}_3\text{O}_4\text{-NS}$  and the composite development

The same process is applied for the development of a nanocomposite where the ZIF-67 instead of m-ZIF-67 is used as the Co-precursor. This is labeled  $\text{Co}_3\text{-Bk-CN}_{570}$ . Also, a physical mixture is used to couple  $\text{Co}_3\text{O}_4\text{-Ns}$  and CN, in order to compare it with the composites that are formed via in situ growth. This process involved the sonication of a specific quantity of  $\text{Co}_3\text{O}_4\text{-Ns}$  and CN in different methanolic solutions. The prepared dispersions are mixed under sonication and incubated under stirring for 2 h. The solvent is removed using a rotor evaporator and the final sample is calcined at  $350\text{ }^\circ\text{C}$  for 2 h using a  $5\text{ }^\circ\text{C min}^{-1}$  ramping rate.

### 1.3.b. PCN-224 and Me-PCN-224

Porous coordination network (PCN) is another subclass of MOFs with well-defined topology. We are particularly interested in Zr-based MOFs due to stability related issues arising from the strong interaction between Zr(IV) and carboxylate<sup>4</sup>. Zr-based porphyrinic MOFs in different topologies can be synthesized using the same Zr metal precursor and TCPP as the organic linker, varying only the temperature and the modulator under a similar set of solvothermal synthesis conditions. In this work we focus on PCN-224, that is composed of porphyrin ligands and Zr<sub>6</sub> cluster nodes<sup>5</sup>.

The synthesis of PCN-224 was carried out via a solvothermal route in an autoclave reactor based on a protocol already published in the literature<sup>6</sup>. For this synthesis, the purity of the organic ligand is very important. Therefore, commercially available porphyrin is used. Specifically, a mixture of 0.173 g  $\text{H}_2\text{TCPP}$  ( $\text{C}_{48}\text{H}_{30}\text{N}_4\text{O}_8$ , Dye content 75 %, Sigma-Aldrich), 0.288 g of Zirconium (IV) Chloride ( $\text{ZrCl}_4$ ,  $\geq 99.5\%$ , Sigma-Aldrich) and 9.73 g benzoic acid ( $\text{C}_6\text{H}_5\text{COOH}$ , Sigma-Aldrich) are added in 29 ml N,N-dimethylformamide ( $(\text{CH}_3)_2\text{NOCH}$ ,  $\geq 99.9\%$ , CARLO ERBA). The mixture is sonicated until all the precursors are dissolved. Then, the greenish solution is transferred to a 90 ml capacity Teflon-lined autoclave reactor and heated at  $120\text{ }^\circ\text{C}$  for 48 hours (Figure 2.5a). After cooling down the resultant powder is collected after filtration

and washed several times with DMF to remove the unreacted starting ligands, the inorganic species and the trapped benzoic acid. The powder received is denoted PCN-224. A solvent-exchange method was used to activate the MOF. Specifically, the MOF is washed with acetone in order to remove the non-volatile solvent followed by vacuum treatment at 120 °C overnight.

Besides the as synthesized parent PCN-224, the role of metalation of the organic ligand is also investigated. For the case of the MOF with the metalated organic ligand (M-PCN-224), the same protocol is followed, but prior to the synthesis, the metalation of the organic ligand takes place. Namely, copper was chosen for the integration of the metal in the core of the porphyrin. A protocol that has already been reported in the literature is adapted with some slight modifications <sup>7</sup> (Figure 2.5.b). The metalation involves a direct substitution under reflux conditions. More precisely, 0.3047 g  $\text{Cu}(\text{NO}_3)_2 \cdot 3\text{H}_2\text{O}$  ( $\geq 99.9\%$ , Sigma-Aldrich) and 0.1970 g  $\text{H}_2\text{TCPP}$  (i.e., 5/1 molar ratio) are dissolved in 15 ml of DMF, and kept in a round bottom flask. The solution is heated at 150 °C using an oil bath for 5 hours. In this synthesis, DMF has a dual role in this reaction: It acts as a solvent, but also at the temperatures used, DMF decomposes to form dimethylamine, which is basic enough to deprotonate both the pyrroles and the carboxylic acid moieties, enabling the metalation and polymerization reactions, respectively <sup>8</sup>. Then, the solution is let to cool down naturally. The precipitate is collected by filtration and is rinsed with DMF and EtOH to remove the unreacted precursors. A change of color is evidenced. The resultant brown powder is denoted Cu-TCPP and vacuum dried at 120 °C overnight.

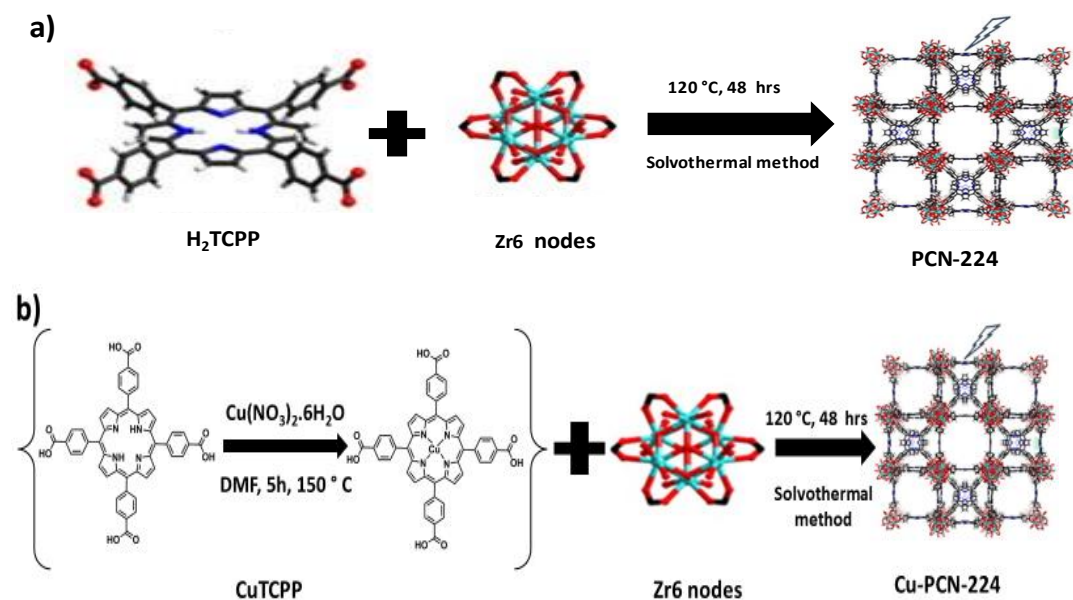


Figure 2. 5: Synthesis routes of (a) PCN-224 and (b) Cu-PCN-224

The development of the composites is realized by in situ formation of MOF on TiO<sub>2</sub> (Hombikat, UV100), by adding 1.663 g TiO<sub>2</sub> powder directly in the autoclave reactor during the synthesis of the MOF structure. Different composites are developed using MOFs that hold Cu-TCPP as the organic linker. The composites are denoted as PCN/TiO<sub>2</sub> and Cu-PCN/TiO<sub>2</sub> using H<sub>2</sub>TCPP and CuTCPP as precursors, respectively.

### *1.3.c. Multi-layered ZIFs (ZIF-8-on-ZIF-67)*

Multiphase MOF structures through the coupling of ZIF-8 and ZIF-67 are also developed. The synthesis route is depicted in Figure 2.6. The sonochemical synthesis that has been described in Section 2.1.3.a. has been followed in order to synthesize ZIF-67 nanoparticles. The prepared ZIF-67 is treated with a chemical etching process protocol<sup>9</sup>. In this process, 0.051 g of pre-synthesized ZIF-67 is dispersed in 5 ml deionized water and sonicated for 15 minutes. Then, 80 mg of Xylenol orange tetrasodium salt (C<sub>31</sub>H<sub>28</sub>N<sub>2</sub>Na<sub>4</sub>O<sub>13</sub>S, Sigma-Aldrich) are dissolved in 5 ml of deionized (DI) water. The pH of the solution is adjusted at 2.5 using HCl aqueous solutions. The two solutions are mixed and kept under stirring at ambient conditions. After 6 hours of agitation the purple powder (80 mg) is collected by filtration, rinsed with DI water several times to remove the residuals of XO and finally vacuum dried at 60 °C overnight. It is important to highlight that the pH value affects the structure of the etched MOFs<sup>10</sup>. In addition, during the etching process, the XO has a dual role. It protonates the organic ligand and is chelated to the liberated metal ions preventing the undesired collapse of the structure<sup>11</sup>.

The growth of ZIF-8 is realized in-situ on etched ZIF-67 nanoparticles, according to a facile protocol<sup>12</sup>. In detail, two different solutions of the precursors of ZIF-8 are prepared by dissolving 0.249 g Zn(NO<sub>3</sub>)•6H<sub>2</sub>O (98%, Sigma-Aldrich) in 40 ml MeOH (solution A) and 0.072 g 2-methylimidazole are dissolved in 40 ml MeOH, accordingly. In the meantime, 79 mg of etched ZIF-67 are dispersed in 80 ml MeOH and sonicated for 15 minutes. Then, the three solutions were mixed and kept under agitation (500 rpm) in ambient conditions for 4 days. The powder is collected by filtration, rinsed, and dried under vacuum overnight to remove the residuals of the volatile solvents. The prepared multi-layered ZIF material is denoted as ZIF-8-on-ZIF-67.

For the development of nanocomposite materials, a simple wet-impregnation method under stirring is carried out. Specifically, a certain mass of multi-layered ZIF was added in 20 ml DI water with a proper quantity of commercial TiO<sub>2</sub> powder (Hombikat, UV100). The solvent is removed naturally under stirring and the collected powder is dried at 65 °C overnight under vacuum. Different nanocomposite materials are developed by varying the amount of the added TiO<sub>2</sub> powder resulting in nanocomposite materials bearing 1%, 5% and 10 wt.% nominal content of ZIF

structures. Following the same procedure, composite materials of ZIF-67/TiO<sub>2</sub> and ZIF-8/TiO<sub>2</sub> holding 5% MOF content were synthesized acting as reference materials.

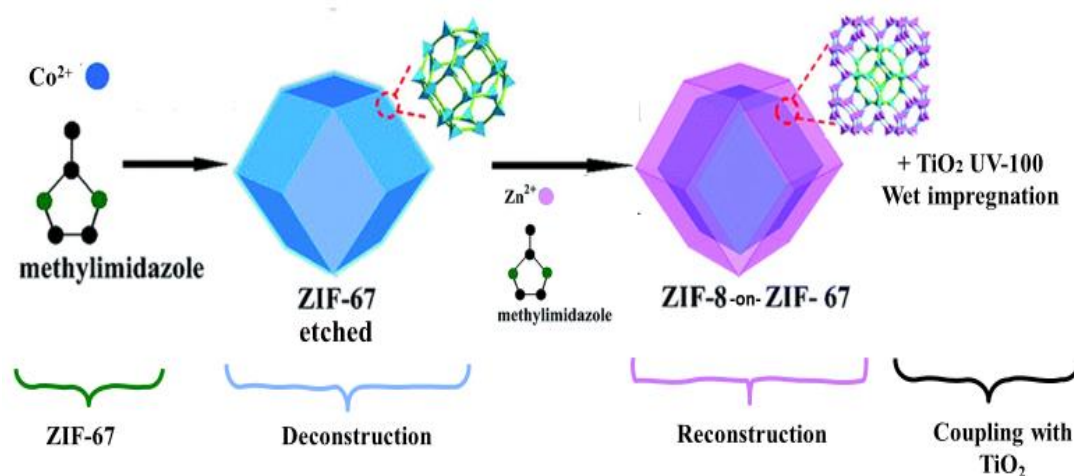


Figure 2. 6: Schematic illustration of the synthesis of multilayered ZIF-TiO<sub>2</sub> composites

#### 1.4. Platinum Deposition

As mentioned in the first chapter, platinum NPs are commonly used as co-catalysts for photocatalytic reactions, especially in the water splitting process. This is based on several reasons such as the stability of the Pt nanoparticles under working conditions and the tendency not to form agglomerates, contrary to Au NPs. The deposition of platinum NPs is based on a method that is already reported in the literature and the steps followed are shown in Figure 2.7. It provides Pt NPs with homogeneous physico-chemical characteristics in terms of structure, morphology and size. In detail, the deposition of Pt is realized by a chemical reduction method, using H<sub>2</sub>PtCl<sub>6</sub> (8 wt. % in H<sub>2</sub>O, Sigma-Aldrich) as the metal precursor and NaBH<sub>4</sub> (≥98.0%, Sigma-Aldrich) as the reducing agent. Firstly, the sample (0.200 g) is dispersed in 40 ml deionized water and kept stirring for 30 min while purging with N<sub>2</sub> to remove dissolved oxygen. Afterwards, a proper quantity of H<sub>2</sub>PtCl<sub>6</sub> (ca. 50 μl), equivalent to 1 wt.% of Pt with respect to the catalyst, is added followed by 15 min stirring. Then, a 0.1 M NaBH<sub>4</sub> aqueous solution is added quickly followed by 1 hour stirring. The whole process was performed under N<sub>2</sub> flow. After that, the final solid product was collected by filtration and was dried at 100 °C overnight.

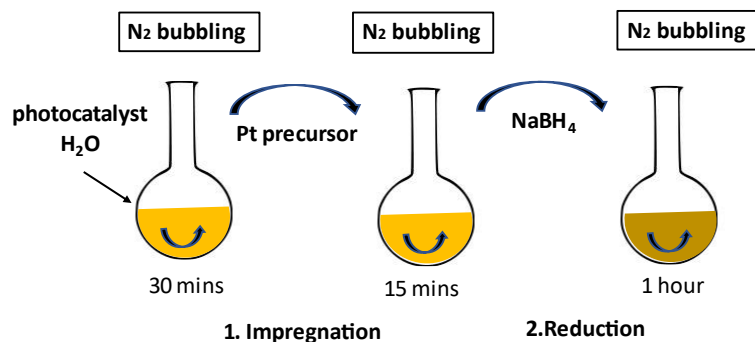


Figure 2. 7: Scheme of the Pt NPs deposition by chemical reduction

## II. Characterization techniques

### II.1. Thermogravimetric Analysis (TGA)

Thermogravimetric (TGA) or Thermogravimetal analysis is a method that monitors the weight of a sample while the temperature is increasing in a controlled gas atmosphere in the chamber. This analytical technique determines the thermal stability, the composition and the estimation of the volatile components or water content.

The apparatus that is used for this study is a Q 5000IR from TA Instruments equipped with an auto sampler and a balance with sensitivity equal to 0.1 $\mu$ g. The atmosphere can be controlled using either an inert gas like nitrogen or an oxidant like air. The temperature can range up to 900°C and the heating rate can be between 0.1 to 500°C min<sup>-1</sup>. For all analysis performed herein a high-resolution dynamic (Hi-Res Dynamic) analysis method is used. The heating rate (from 4 to 50°C min<sup>-1</sup>) is automatically adjusted according to the loss of mass (optimization of curves and time of test).

### II.2. X-Ray Diffraction (XRD)

The method of X-ray diffraction is a non-destructive method to characterize the structure of crystalline materials. It gives information for the crystal orientation and other structural parameters, such as the interplanar distance and the size of crystallite. The interplanar spacing of the crystal ( $d$ ) is found by Bragg's Law (Equation 2.1):

$$n \lambda = 2d \sin\theta$$

Equation 2.1

## CHAPTER 2

Another parameter that can be calculated by XRD patterns is the mean crystallite size (D) by using the Debye-Scherrer equation that is shown below:

$$D = \frac{K \cdot \lambda}{\beta \cdot \cos(\vartheta)} \quad \text{Equation 2.2}$$

Where, n stands for the "order" of reflection,

K is the Scherer's constant equal to 0.94,

$\lambda$  is the X-ray wavelength (1.54178 Å),

$\beta$  is full width of the diffraction peak at half maximum of its height (FWHM),

$\vartheta$  is the angle of the diffraction peak in radians.

X-ray diffraction (XRD) measurements are carried out using a Bruker D8-Advance diffractometer equipped with a Lynx Eye detector operating at 40 kV and 40 mA, using K $\alpha$  radiation of Cu.

### II.3. BET

The analysis of the total specific surface area, the evaluation of the pore volume and the distribution of the pore size are crucial factors that can be determined by the BET method (Brunnauer-Emmett-Teller) <sup>13</sup>. This method involves nitrogen physisorption on the sample's surface because it's a gas that does not chemically react with the material. For the purposes of the present thesis, nitrogen adsorption-desorption isotherms were obtained using a Micromeritics ASAP 2420 porosimeter at 77. The specific surface area ( $S_{\text{BET}}$ ) is calculated in the range of pressure  $P/P^0=0.05-0.3$ . The analysis method applied varied depending on the structure of the material analyzed, i.e., materials with microporosity.

### II.4. X-Ray Photoelectron Spectroscopy (XPS)

X-Ray photoelectron Spectroscopy is a technique for measuring the electrons emitted from the surface of the analyzed samples and derived from the atoms of the materials. During the XPS analysis, the sample is irradiated with a beam of X-rays with penetration depth of 1  $\mu\text{m}$ , electrons can be excited in this entire volume. However, electrons are extracted only from the narrow solid part of the investigated material. XPS spectra are obtained by measuring the kinetic energy of electrons that are emitted from the top 1–10 nm, as shown in Figure 2.8. Kinetic energy of electrons is related to the binding energy as expressed by the Equation 2.3:

$$E_b = h\nu - E_{\text{kin}} - W_f \quad \text{Equation 2.3}$$

Where  $E_b$ : binding energy

$E_{kin}$ : kinetic energy

$W_f$ : Work function

XPS also determines the binding states of the elements. Binding energy depends upon several factors, including the element from which the electron is emitted, the orbital from which the electron is ejected and the chemical environment of the atom from which the electron is emitted. Therefore, XPS is used to estimate the elements on the surface of the photocatalyst. The data processing is realized by using the software CasaXPS. The surface atomic ratios can be calculated by found based on the area of the peak (Gaussian-Lorentzian(30) shaped) using a Shirley-type background, corrected by experimental sensitivity factor of the normalized photo ionization cross-section of the atomic subshells as determined by Scofield<sup>14</sup>. The elemental composition of the surface is calculated by the following equation:

$$X_i (\%) = \frac{\frac{A_i}{ASF_i}}{\sum_i^n \frac{A_i}{ASF_i}} \quad \text{Equation 2.4}$$

Where  $A_i$  : is the area of the peak that corresponds to the core level of the  $i$  element

$ASF_i$  :is the atomic sensitivity factor of the  $i$  element for the specific core level

$n$ : is the number of peaks ( $\equiv$  *elements*)

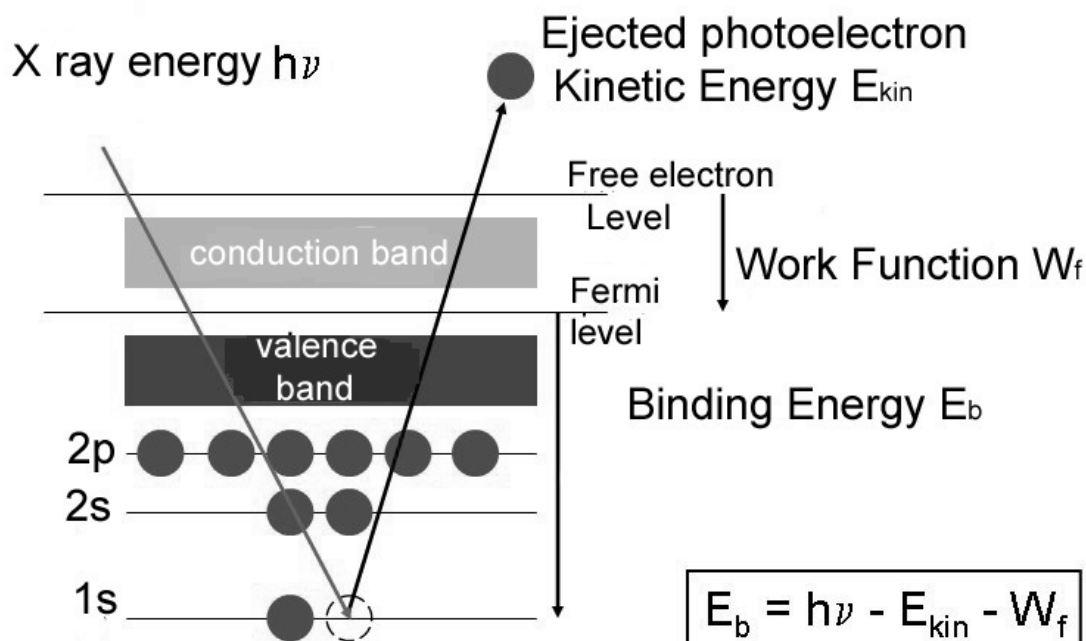


Figure 2. 8: XPS characterization principle

X-ray photoelectron spectroscopy (XPS) measurements were performed on an ultrahigh vacuum (UHV) Thermo-VG scientific Spectrometer equipped with an electron hemispheric analyzer CLAM4 (MCD). The irradiation source is generated by a double anode of Al  $K_{\alpha}$  X-ray (1486.6 eV). The shift due to charging effects of the surface is corrected by calibrating with the adventitious carbon peak at 284.6 eV.

## II.5. Scanning Electron Microscopy (SEM)

Scanning Electron Microscopy (SEM) is a technique widely used to examine the structure and the morphology of samples by using a high-energy electron beam that scans the sample's surface. The electrons interact with the different atoms of the surface and produce various signals giving high-resolution images. When the electrons strike the specimen, inelastic, elastic, and incoherent elastic backscattering can occur. Backscattered electrons (BSE) are beam electrons that are reflected from the sample and can provide information about the distribution of different elements in the sample according to their atomic number. While secondary electrons (SE), resulting from the inelastic scattering that occurs some nanometers deeper than the surface are giving information about the topology.

The characterization by SEM is realized by Zeiss Gemini SEM 500 using a Schottky Field Emission Gun (FEG) and took place in ICPEES facilities. This Scanning Electron Microscope is equipped with five detectors and one detector for X-rays for microanalysis. This permits the elemental analysis of the sample similarly to XPS

principle. However, in this case the photoemitted electrons are stroked out of a bigger volume.

## II.6. Transmission Electron Microscopy (TEM)

Transmission Electron Microscopy is also a characterization technique similar to SEM, however as its name indicates, in this case the images are produced by the electrons that are transmitted through the sample. In order to enhance the transmission, ultra-thin specimens are required. Therefore, prior to analysis they have been grinded and dispersed via sonication in ethanol and then dropped on a copper grid holder. It is also worth mentioning that TEM provides a much higher spatial resolution than SEM and facilitates analysis of the features on an atomic scale (in the range of a few nanometers). Likewise, SEM, X-ray Energy Dispersive Spectroscopy can be carried out too.

The IPCMS institute, where the TEM characterization took place, disposes a Jeol 2100F microscope with working Voltage 200 kV, equipped with Energy Dispersive Spectroscopy (EDS) and Charge Coupled device (CCD) cameras.

## II.7. UV-Visible Spectroscopy (UV/Vis)

Spectroscopy is a characterization technique that is based on the interactions between light and matter. Phenomena like absorption, transmission and reflection are occurring. Specifically, Ultraviolet–visible spectroscopy (UV–Vis or UV/Vis) corresponds to the part of the ultraviolet and visible regions of the electromagnetic spectrum. Absorption spectra of chemical species (atoms, molecules, or ions) are generated when a beam of electromagnetic energy (i.e., light) is passed through a sample, and the chemical species absorb a part of the photons of the electromagnetic energy passing through the sample. The absorption band is characteristic for every compound because it is equal to the energy difference of each ground/excited state pair, as described by Planck's equation. The dependence between transmittance and absorbance is expressed by the following equation:

$$A = -\log T = -\log \left( \frac{I}{I_0} \right) \quad \text{Equation 2.5}$$

Where  $I_0$ : initial beam intensity and

$I$ : intensity of the beam transmitted

Noteworthy, in the field of semiconductors the use of Ultraviolet–visible spectroscopy allows us to estimate their energy bandgap ( $E_g$ ). In the case of solid samples, UV-Vis Diffuse Reflectance Spectroscopy analyses the electromagnetic radiation versus the wavelength that is being reflected from the sample's surface

and is collected with the help of an integrating sphere. The mathematical approach that describes the diffuse reflectance is formulated by Paul Kubelka and Frank Munk (K-M) and is given in the equation 2.6:

$$F(R_{\infty}) = \frac{(1-R_{\infty})^2}{2R_{\infty}} \quad \text{Equation 2.6}$$

where  $R_{\infty}$ : ratio of the reflectance of the analyzed surface to the reflectance of the standard sample

As it was mentioned above, the DR-spectra can be used for the estimation of semiconductors  $E_g$ , by exploiting Tauc's Equation:

$$(F(R_{\infty}) * hv)^{1/n} = B(hv - E_g) \quad \text{Equation 2.7}$$

Where  $F(R_{\infty})$ : Kubelka-Munk term

$hv$ : photon's energy (eV)

$E_g$ : Energy bandgap (eV)

$n$ : equals to  $\frac{1}{2}$  for direct and to 2 for indirect semiconductors

By the plot of the term  $(F(R_{\infty}) * hv)^{1/n}$  versus the  $hv$  and extrapolating the linear part of the spectrum, we can determine the  $E_g$  by finding the intersection with the X-axis for zero reflectance. DR-UV-vis absorption spectra were recorded in the range of 200-800 nm using a PerkinElmer Lambda 950 Scan spectrophotometer equipped with integrating sphere using  $BaSO_4$  as reference.

## II.8. Infrared Spectroscopy (IR)

Infrared Spectroscopy is the measurement of the interaction between the infrared radiation and the matter, the infrared region (400 nm-1 mm wavelength) of the electromagnetic spectrum causes asymmetric *bonds* to stretch, bend, and/or vibrate. This characterization technique is used for the identification of chemical bonds and functional groups and consequently for the determination of the molecular structure. It can be applied especially for organic samples in gas, liquid, and solid phases. In addition, it is a quick and non-destructive method that needs no sample preparation. In the framework of this study, the Attenuated Total Reflectance is recorded by Nicolet iS10 FT-IR spectrometer in the range of 400-4000  $cm^{-1}$ .

## II.9. Photoelectrochemical analysis

Photocurrent measurements are of particular importance to investigate the ability of a photocatalyst to generate charges, a parameter that is critical in photocatalytic applications<sup>15</sup>. It is considered to be a good technique that records the current signal under illumination when a potential is applied at the photoelectrochemical cell. In presence of the voltage bias, the photoinduced  $e^-$  are attracted by the external field and the charge carriers' separation is enhanced<sup>15</sup>. The cyclic voltammetry curves are recorded under light irradiation and under dark conditions. The difference between the collected photocurrent in both cases can reflect the rate of photoinduced carriers in the photoelectro-chemical (PEC) process.

Herein, photoelectrochemical experiments were performed in a 3 electrode PEC cell (Figure 2.9), using a platinum mesh as counter electrode and a mercurous sulfate reference electrode (MSE;  $V^0$  MSE = 0.64 V vs RHE) in an alkaline electrolyte (0.01 M NaOH, 0.1 M Na<sub>2</sub>SO<sub>4</sub>). For the fabrication of the working electrode an Indium Tin Oxide coated (ITO) glass coated with a thin carbon film by PVD, was used to drop cast the catalyst as a thin homogeneous film (catalyst loading ca. 0.1 mg cm<sup>-2</sup>). Prior to cyclic voltammetry, measurements in open circuit voltage have been carried out and the cell was purged with nitrogen for 30 min. Cyclic voltammetry (CV) was performed with a Biologic SP-300 potentiostat, with an applied potential ranging from - 1.0 V to 0.4 V vs MSE (0.35 to 1.75 vs RHE), at a 10 mV s<sup>-1</sup> scan rate. This protocol was applied under dark and illuminated conditions using a Xe arc lamp (Newport; 300W; equipped with AM1.5G filter; incident power density on the cell 100 mW cm<sup>-2</sup>). In order to calculate the photocurrent density, the current at potential 1.23 eV vs. RHE under dark conditions was subtracted by the current recorded at potential 1.23 eV vs. RHE under illumination conditions. The obtained current is attributed to the photoexcited electrons.

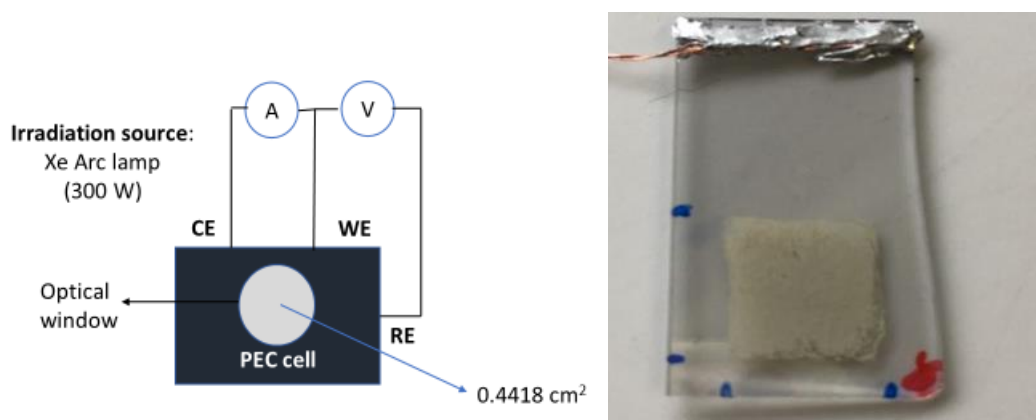


Figure 2. 9: Schematic illustration of the set-up used to perform the photocurrent measurements (left), working electrode: catalyst deposited on ITO (right)

## II.10. Transient absorption spectroscopy (TAS)

Transient absorption spectroscopy is a technique that is employed to study the charge dynamics of an irradiated photocatalyst, including monitoring the lifetime, the time scale of the trapping, the transfer and recombination of photogenerated charge carriers in semiconductors<sup>16</sup>. This technique is based on pump-probe measurements, where the pump initiates the photoexcitation of the sample, and the probe measures the optical absorption of the sample in various times<sup>17</sup>.

As seen in Figure 2.10, in stationary UV/Vis spectroscopy the measurements involve the ground state sample (panel A). On the contrary, in TAS both ground state and excited state are measured (panel B). Specifically, in a typical TAS experiment, a pump pulse excites the sample that is in the ground state and the absorbance ( $A_g$ ) of the pulse is measured. Subsequently, a weak probe pulse is sent through the excited sample and again the absorbance ( $A_e$ ) of the probe pulse is measured<sup>18</sup>. The absorbance difference ( $\Delta A$ ) is then calculated by the following equation (Eq. 2.8):

$$\Delta A(\lambda, \tau) = A^*(\lambda, \tau) - A^0(\lambda)$$

Equation 2.8

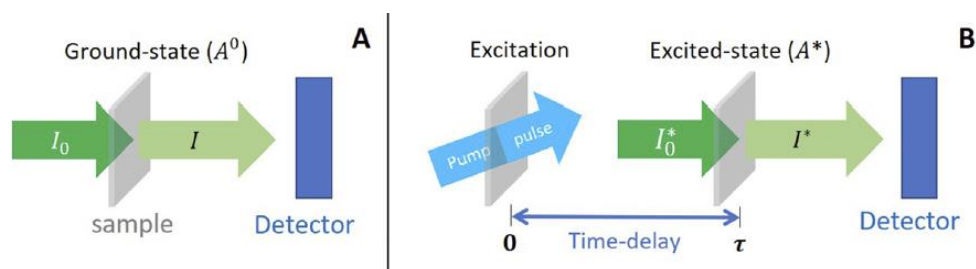


Figure 2. 10: Schematic Illustration of the basic principle of (a): UV/Vis in stationary-state and (b) Transient Absorption Spectroscopy

Where  $A^*(\lambda, \tau)$  and  $A^0(\lambda)$ , represent the absorbance of the excited and ground state samples, respectively.  $\lambda$  stands for the wavelength and  $\tau$  for the time delay. Therefore, spectra at different times are collected. The  $\Delta A$  spectrum contains three electronic contributions: the ground state bleach, the stimulated emission, and the excited state absorption<sup>19</sup>. The kinetic curve of TAS sheds light to the decay of the charge carriers and their recombination. In this context, the photocatalyst with the slower TA decay kinetics (i.e., increase of the charge lifetime) will present higher photocatalytic activity<sup>20</sup>.

Herein, TAS is applied from the microsecond to second timescale in diffuse reflection mode. A Nd:YAG laser (OPOTEK Opolette 355 II, ~6 ns pulse width) is used as the excitation source, generating 355 nm UV light from the third harmonic (~0.63 mJ cm<sup>-2</sup> per pulse, repetition rate of 0.8 Hz). A 100 W Bentham IL1 quartz halogen lamp is used as the probe light source. Long pass filters (Comar Instruments) were placed

between the lamp and sample to minimize short wavelength irradiation of the sample. Transient changes in diffuse reflectance from the sample is collected by a 2" diameter, 2" focal length lens and relayed to a monochromator (Oriel Cornerstone 130) and measured at select wavelengths between 550 and 1000 nm from 10  $\mu$ s to 1 s. Time-resolved changes in diffuse reflectance are collected using a Si photodiode (Hamamatsu S3071). Data at times faster than 3.6 ms was recorded using an oscilloscope (Tektronics DPO3012) after passing through an amplifier box (Costronics), whereas data slower than 3.6 ms is recorded on a National Instrument DAQ card (NI USB-6251). Each kinetic trace is obtained from an average of at least 100 laser pulses. Acquisitions are triggered by a photodiode (Thorlabs DET10A) from laser scatter. Data is acquired and processed using home-built software written in Labview. Measurements are carried out in air at  $19 \pm 2$  °C, with powder samples pressed between 2 microscope slides (VWR).

The TAS experiments are carried out at the Molecular science research hub of Imperial College of London, in the framework of a fruitful collaboration with Dr. Andreas Kafizas.

### II.11. Electron paramagnetic resonance (EPR)

Electron Paramagnetic Resonance (EPR) or Electron Spin Resonance (ESR) is a method to study materials with unpaired electrons. The principle is based on the resonance of electrons of atoms as a result of high frequency electromagnetic radiation absorption in presence of external magnetic field <sup>21</sup>. Species that can be monitored by EPR are paramagnetic species with odd integer spins including organic and inorganic radicals, crystal defects (i.e., vacancies, interstitials), dopant atoms and both free and trapped charge carriers <sup>22</sup>. It is a versatile tool used extensively to study photocatalysts.

Generally, the principal energy level of unpaired electron can be split into two separate energy levels with opposite spin orbital momentum under the application of an external magnetic field <sup>23</sup>. The electron Zeeman interaction occurs between the unpaired electrons and external magnetic field and eliminates the degeneracy of electron spin states. When it is then exposed to the appropriate microwave radiation or magnetic field, the magnetic dipole transitions could occur and produce paramagnetic resonance absorption. The g-factor originates from the spin-orbit coupling interaction, is not affected by the external magnetic field and reflects the intrinsic property of each paramagnetic center. With reference to this value we can identify the specific paramagnetic species <sup>24</sup>.

The EPR measurements presented in this work are realized in the Lab of Physical Chemistry of Materials & Environment at University of Ioannina, by the PhD student Areti Zindrou. A Bruker ER200D spectrometer equipped with an Agilent 5310A

frequency counter, operating at X-Band was used to record the EPR spectra. The spectrometer was running under a home-made software based on LabView <sup>25</sup>. Spectra were recorded at liquid nitrogen temperature (77 K) using the following instrumental conditions: 9.55 GHz microwave frequency, 50.00 kHz modulation frequency, 4 Gauss peak-to-peak modulation amplitude. The samples (10 mg) were irradiated in-situ using an arc Xenon lamp (model: Oriel 6293) operating with 450 W input power equipped with a water-filter. Before irradiation, samples were analyzed under dark conditions. These spectra were subtracted from the data recorded under illumination. After recording the spectra under irradiation, the sample was warmed at room temperature for 15 min in the dark, and frozen instantly at 77 K. This reestablished the EPR intensity at the level of dark conditions.

In situ EPR studies are also a powerful tool to unravel catalytic mechanisms. However, as in all in situ spectroscopic techniques, the analyte lifetime limits the species concentration and may prevent it reaching detectable levels, favoring the spectroscopic observation of the longest-lived species <sup>26</sup>. Therefore, in order to overcome this barrier, short-lived radicals can be trapped for analysis using spin traps to form more stable radicals. More precisely, this method involves the addition of a compound, typically organic nitron or nitroso, called spin-traps. The most typical spin-trap structures are given in Figure 2.11. Spin-traps react with reactive radicals (for example •OH or •OOH), and result to the formation of a radical adduct than can be subsequently identified <sup>27</sup>. In photocatalytic systems, this allows the detection and quantification of reactive oxygen species formed from the photoexcited charge carriers. In this regard, we can unravel the relationship between band structure and photocatalytic activity since formation of specific reactive oxygen species depends solely on the level of the CB and VB of the catalyst.

Herein, the EPR technique was used for in situ spin-trap experiments using a protocol already published in the literature <sup>28</sup>. The 5,5-dimethyl-1-pyrroline *N*-oxide (DMPO) was used as spit trap for the detection of superoxide anion radicals ( $O_2^{\bullet-}$ ) at room temperature. A suspension of 1 mg·mL<sup>-1</sup> of the catalyst in methanol was sonicated for 10 min. Then, 100 μL of the above suspension was mixed with 100 μL of 0.005 M DMPO directly in the EPR flat cell. A quartz EPR flat cell was used, that was irradiated by an arc Xenon lamp operating with 450 W input power equipped with a water-filter. EPR spectra were obtained at room temperature after 15 min irradiation of the methanolic suspension of the photocatalyst.

## CHAPTER 2

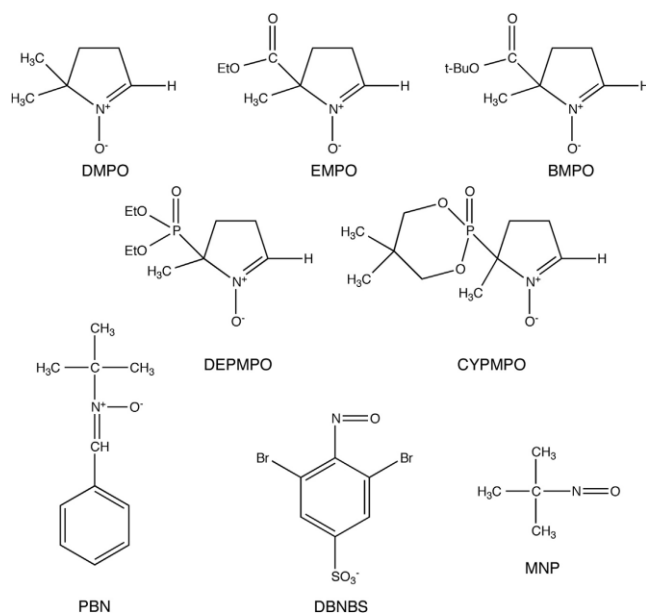


Figure 2. 11: Structures of commonly used compounds as spin traps

### II.12. Photoluminescence Measurements (PL)

Photoluminescence is defined as the radiation emitted from the electronic excited state of a molecule to its ground state after absorption of light energy from an external energy source (Figure 2.12) <sup>29</sup>. In the case of semiconductor materials, photoluminescence spectroscopy (PL) is widely studied to investigate the recombination phenomena of  $e^-/h^+$  pairs and, hence, provide information for the separation of the photogenerated charge carriers <sup>30</sup>. Therefore, the lower the PL intensity the more efficient the separation of charge carriers is.

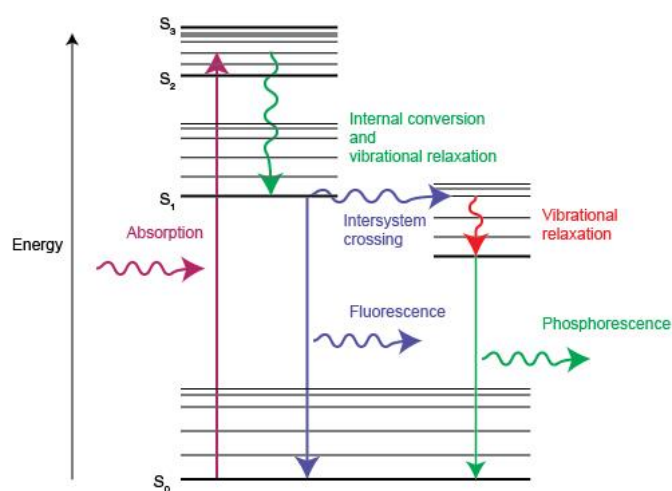


Figure 2. 12: Energy diagram showing absorption of light, and emission through fluorescence and phosphorescence

The PL measurements were recorded by the spectrofluorometer S2 Jobin Yvon at ICPEES in collaboration with Dr. Julien Massue. The excitation wavelength of irradiation is at 370 nm with a slit of 3 nm. Additionally, a filter at 395 nm was used to cut off the double harmonic peak and the samples were used without any further preparation.

### II.13. Temperature-programmed Desorption (TPD)

Chemisorption is a phenomenon that occurs under the influence of chemical bond as forces of attraction between the adsorbed molecules and the adsorbent. The chemisorption energy between the gas molecules and adsorbents can vary significantly depending on the bond strength <sup>31</sup>. The temperature programmed desorption (TPD) technique is used to evaluate the active sites on the surface area of the photocatalyst. This is possible by the use of appropriate probe gases. Basic gases (i.e., NH<sub>3</sub>) are used for the estimation of acidic active sites, and vice versa. The classification of the active sites by strength (i.e., weak or strong), is based on the temperature of desorption. The stronger the active sites are, the higher the energy needed to desorb the probe gas. While using CO<sub>2</sub> as probe gas, TPD is an indirect method to measure the CO<sub>2</sub> uptake capacity of the catalysts that are aimed for artificial photosynthesis and estimating the basic sites on the surface of the catalyst.

The TPD experiments are comprised of 4 steps:

- The first step concerns the sample pretreatment. It involves the heating of the photocatalyst under inert atmosphere (He, Air Liquide, ALPHAGAZ2, 99,9999%), in order to evacuate any residual species (solvents) or impurities from the atmosphere adsorbed (H<sub>2</sub>O, CO<sub>2</sub>) on the surface.
- Later after cooling down to the ambient temperature, the second step involves the adsorption of the probe gas (CO<sub>2</sub>, Air Liquide, 99.9995%). The sample is in contact with the flow of the probe gas flow that is adsorbed on the catalyst surface.
- The following step is the purging of the surface with a carrier gas flow at the same temperature. This step permits the desorption of the loosely adsorbed (physiosorbed) species or any residual probe gas in the flow.
- The last step involves the species' desorption of the catalyst upon heating with a linear rate under a carrier gas flow. The change of the reaction gas that is desorbed from the surface upon heating is monitored with a downstream detector as a function of temperature.

A temperature-programmed desorption (TPD) study is carried out by MICROMERITICS AutoChem II 2920-Chemisorption analyzer, equipped with a thermal conductivity detector (TCD) to estimate the volume of desorbed gases, and a GC-Mass spectrometer (Pfeiffer vacuum) to identify the gases evolved. Initially, 50

mg of sample is pretreated at 190°C for 1 h to remove any trapped solvents and water, and then is cooled down to 40°C. Later, the sample is let in contact with He for 1 hour to remove the physisorbed species. The profile of gases desorbed is recorded at the rate of 15 C min<sup>-1</sup> ranging from 40 to 250°C under He flow, in order to avoid any thermal decomposition of the catalyst. The CO<sub>2</sub> desorption is detected by monitoring the mass spectroscopy signal for m/z=44. The results were analyzed by using the proper software (AutoChem II 2920 V3.05).

### III. Photocatalytic set-ups

#### III.1. Set up for photocatalytic H<sub>2</sub>O splitting

The photocatalytic evaluation of the prepared photocatalysts towards hydrogen production from the water splitting reaction is performed in liquid phase. The set up that is used is shown in Figure 2.13.

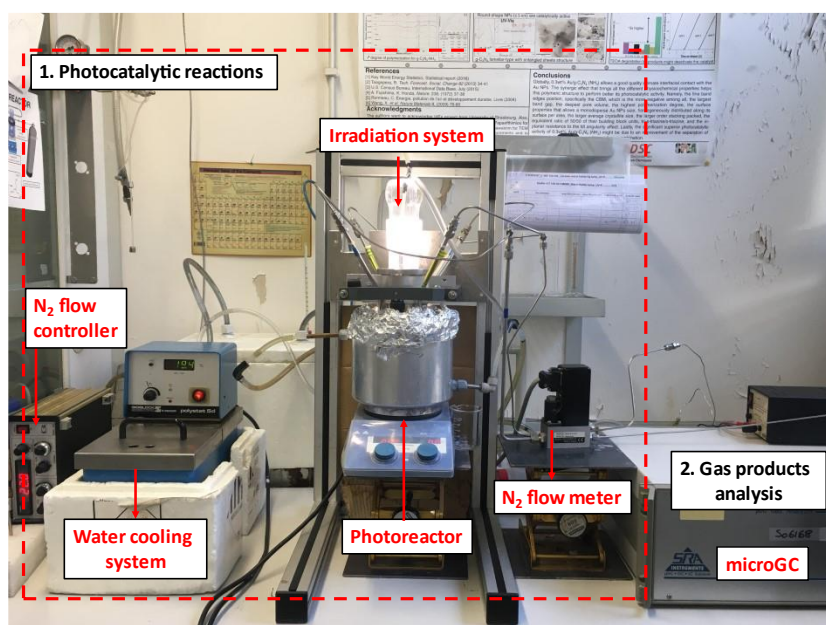


Figure 2. 13: Picture of the photocatalytic set-up used for the photocatalytic water splitting

The photocatalyst (150mg) is added in the medium of the reaction (water and sacrificial agent, 99/1 v/v %) inside a quartz reactor (V=1 L). The suspension is kept under stirring for better homogeneity. For all the tests of photocatalytic water splitting, triethanolamine (TEOA) is used as sacrificial agent. The reactor is illuminated by a lamp that simulates solar light, (ceramic-metal-halide Hg lamp-150 W, C-Topspot, StrassElec SARL). The lamp is placed inside a quartz tube, and the

latter was immersed inside the photoreactor. The temperature during the test was kept at  $20 \pm 1$  °C, by employing a water-cooling system.

Prior to irradiation the photocatalytic mixture is purged with N<sub>2</sub> gas (Alphagas 2, Smartop, 6.0) with a specific flowrate (100 ml min<sup>-1</sup>) in order to remove air. The flowrate was settled and maintained by using a flow controller. Then the lamp is turned-on, and the evolved gases are analyzed by means of a micro-chromatography in gas phase (micro-GC, R-3000, SRA instrument). The micro-GC is equipped with three different modules and one thermal conductivity detector (TCD) at each. The first comprises a Molsieve column with Argon (Ar, Alphagaz 2, SMARTOP) as carrier gas for the identification and quantification of H<sub>2</sub>. The second module also possesses a Molsieve column that uses He as carrier gas to follow the O<sub>2</sub> evolution. The last compartment employs a PlotQ column as well alimented with He as carrier and is used to detect CO<sub>2</sub> and other light carbonaceous products. Photocatalytic reactions were monitored for 3 h.

The samples are tested towards water splitting reaction for 3 hours and the mean rate of hydrogen production ( $r_{H_2}$ ) is determined once the reaction reaches the steady state. It is calculated according to the following equation:

$$r_{H_2} (\mu mol. h^{-1}. g^{-1}) = \frac{C_{H_2} * \dot{V}_{N_2}}{V_m * m_{cat}} \quad \text{Equation 2.9}$$

Where  $C_{H_2}$ : concentration of evolved H<sub>2</sub> in ppm

$\dot{V}_{N_2}$ : Volumetric flow rate of N<sub>2</sub> (100 ml.min<sup>-1</sup>)

$V_m$ : Molar volume equal to 24 L.mol<sup>-1</sup>, that corresponds to the occupied volume of 1 mole of gas at T=20 °C and P=1 atm

$m_{cat}$ : mass of photocatalyst that is used for the test.

### III.2. Set up for Photocatalytic CO<sub>2</sub> reduction

The photocatalytic conversion of CO<sub>2</sub> is realized in gas phase, in two different set ups with different working conditions. The first one uses H<sub>2</sub> as reducing agent and the experiments are performed in batch conditions. The other works under continuous flow of CO<sub>2</sub>, with water as electron donor. Both pilots used are described in detail in the following section.

#### III.2.a. Photocatalytic reduction of CO<sub>2</sub> in batch conditions

For the photocatalytic reduction of CO<sub>2</sub>, a gas/solid photoreactor was used. Irradiation is performed from the top of the reactor through a quartz window using

as light source a Xe arc 300 W lamp (Newport). The lamp is equipped with a water filter. The schematic illustration of the set-up is given in Figure 2.14.

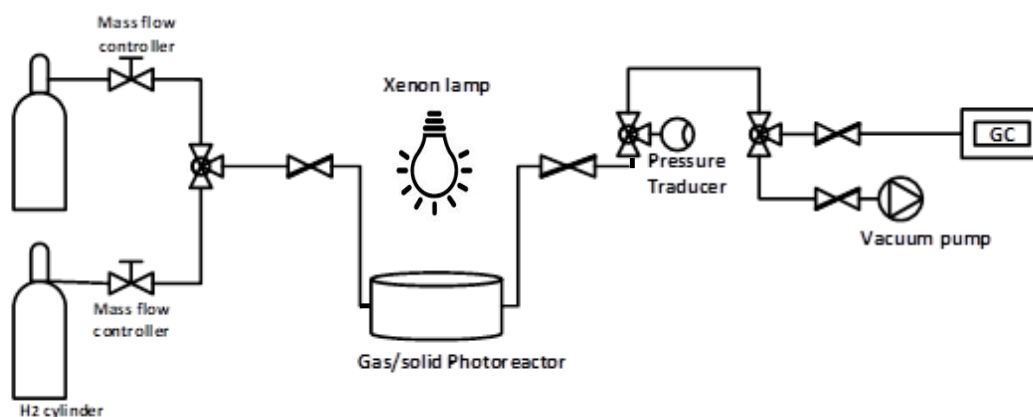


Figure 2. 14: Schematic illustration of the CO<sub>2</sub> reduction set-up

The photocatalyst (20 mg) is deposited as a thin film on a 9.5 cm<sup>2</sup> glass disk followed by vacuum treatment at 90 °C overnight. The photoreactor was vacuumed and refilled five times with the reactant gases (research grade (99.999%) CO<sub>2</sub> and H<sub>2</sub>). Prior to testing, the reactor is purged for 20 min with a CO<sub>2</sub>/H<sub>2</sub> ratio of 1.5 (vol/vol) using 30 ml min<sup>-1</sup> flow rate and sealed at 1.10 bar. Mass flow controllers are used to regulate the CO<sub>2</sub>/H<sub>2</sub> ratio. The reaction has been monitored for 6 h and the evolved gases are analyzed periodically using a GS equipped with TCD and FID detector. During all the reactions, the temperature is maintained at 20 °C by means of a cryostat. In this set-up the influence of electron donor is also examined, using H<sub>2</sub>O as reducing agent.

### *III.2.b. Photocatalytic reduction of CO<sub>2</sub> under continuous flow*

The photocatalytic set up (Figure 2.15) that works under continuous flow conditions, is comprised of three main parts. The first part involves the generation of the reactant gases. Specifically, a defined flow (0.3 ml min<sup>-1</sup>) of research grade CO<sub>2</sub> (Air product, ≥99.5%) is passing through a water saturator which is kept at ambient temperature and feeds the reactor. The flow is regulated by a mass flow controller (Bronkhorst).

## CHAPTER 2

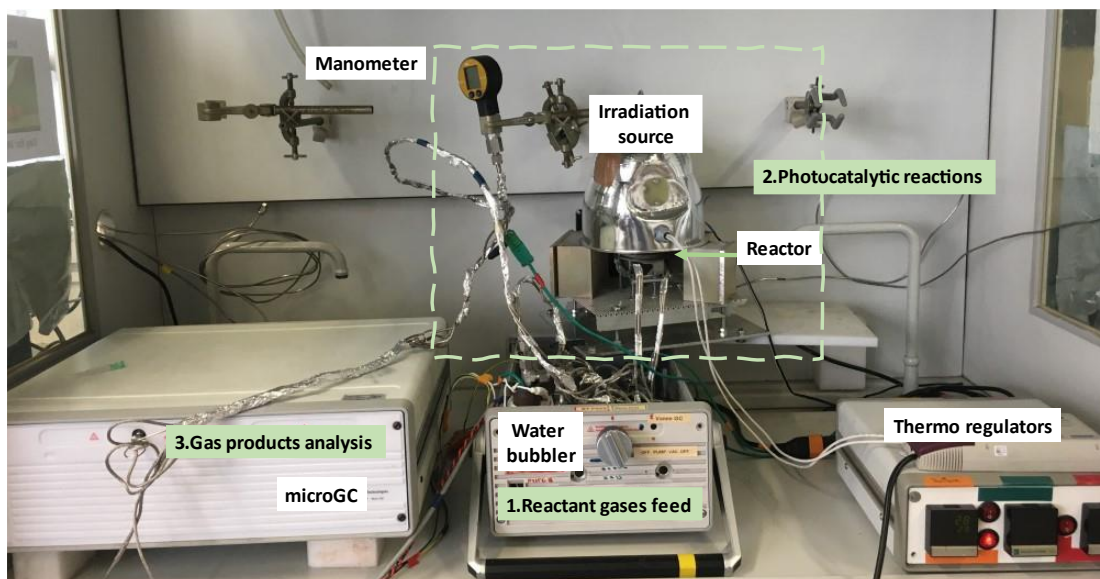


Figure 2. 15: Picture of the photocatalytic set-up used for the  $\text{CO}_2$  reduction tests in continuous flow conditions

The second part involves the photocatalytic reactor. More precisely, the reactor is made from Stainless steel and has a volume capacity of 6 ml. The upper part of the reaction is a quartz glass, from where the reactor is irradiated. The irradiation system consists of a Hg lamp (150W, Ceramic-Metal-Halide, C-Topspot, StrassElec SARL) that is placed 6 cm higher than the quartz window of the reactor. There is also the possibility of using a UV light cut off filter ( $>420$  nm). The irradiation of the lamp is recorded with the use of a radiometer (ILT900-R, International Light Technologies), and the emission spectrum of the lamp is depicted in Figure 2.16a.

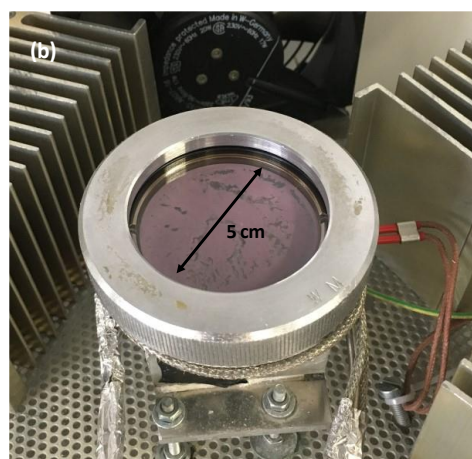
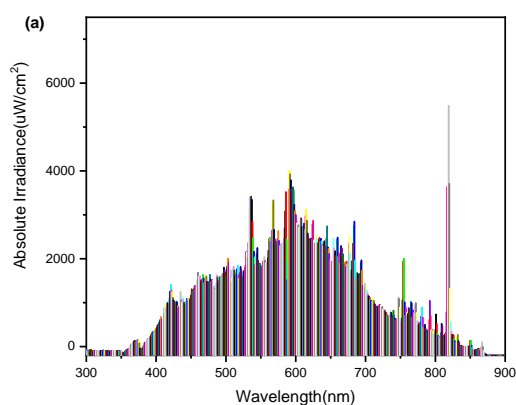


Figure 2. 16: (a) Irradiation spectra of Hg lamp (150W, Ceramic-Metal-Halide, C-Topspot, StrassElec SARL) and (b) picture of the gas/solid photoreactor

## CHAPTER 2

The third part is related to the equipment that is used to analyze the evolved gases, namely, a micro-GC (Agilent 3000A SRA Instrument). For the identification of the several possible evolved gases, the micro-GCM disposes 4 different independent channels. The first module can detect H<sub>2</sub>, CH<sub>4</sub>, O<sub>2</sub>, N<sub>2</sub>, CO, by using a MSSA column and Ar as gas carrier. CO<sub>2</sub> has been analyzed in the second channel by a PlotU column alimented by Helium, as Gas carrier. The third independent channel disposes a STABILWAX column. The fourth module possesses an OV1 column (He: carrier gas) and detects H<sub>2</sub>O. The evolution of the gas products is followed every 15 minutes, in order to have insights to the reaction kinetics. In this regard, the formulas that are used to calculate the rate of production of the evolved gases, are shown in Eq (2.10).

$$r_X(\mu\text{mol g}^{-1} \text{h}^{-1}) = \frac{[X] \cdot \dot{V}}{V_m \cdot m_{cat}} \quad \text{Equation 2.10}$$

Where [X]: the concentration of the evolved gas (CH<sub>4</sub>, CO, H<sub>2</sub>) in ppm

$\dot{V}$  : volumetric flow rate of gas (L min<sup>-1</sup>)

$V_m$ : Molar volume equal to 24 L mol<sup>-1</sup>, that corresponds to the occupied volume of 1 mole of gas in STP conditions.

$m_{cat}$ : mass of photocatalyst that is used for the test

The product selectivity of the reaction is given in the following equations (2.11)- (2.13):

$$S_{CH_4}(\%) = \frac{r_{CH_4}}{r_{CH_4} + r_{H_2} + r_{CO}} \quad \text{Equation 2.11}$$

$$S_{CO}(\%) = \frac{r_{CO}}{r_{CH_4} + r_{H_2} + r_{CO}} \quad \text{Equation 2.12}$$

$$S_{H_2}(\%) = \frac{r_{H_2}}{r_{CH_4} + r_{H_2} + r_{CO}} \quad \text{Equation 2.13}$$

However, as demonstrated in [Chapter 1](#), the CO<sub>2</sub> reduction may result in various carbonaceous products (i.e., CO, CH<sub>4</sub>, CH<sub>3</sub>OH), which require different number of electrons upon their formation. Therefore, the electronic activity and electronic selectivity of the reaction may be calculated by the given equations (2.14)-(2.17):

$$r_{e-}(\mu\text{mol g}^{-1} \text{h}^{-1}) = \frac{\dot{V}}{V_m \cdot m_{cat}} * (8 * [CH_4] + 2 * [CO] + 2 * [H_2]) \quad \text{Equation 2.14}$$

$$S_{CH_4}(\%) = \frac{8 * r_{CH_4}}{8 * r_{CH_4} + 2 * r_{H_2} + 2 * r_{CO}} \quad \text{Equation 2.15}$$

$$S_{CO}(\%) = \frac{2 * r_{CO}}{8 * r_{CH_4} + 2 * r_{H_2} + 2 * r_{CO}} \quad \text{Equation 2.16}$$

## CHAPTER 2

$$S_{H_2}(\%) = \frac{2 * r_{H_2}}{8 * r_{CH_4} + 2 * r_{H_2} + 2 * r_{CO}} \quad \text{Equation 2.17}$$

where  $r_{CH_4}$ ,  $r_{CO}$ ,  $r_{H_2}$  methane, carbon monoxide and hydrogen production mean rate, respectively.

## IV. References

- (1) Christoforidis, K. C.; Syrgiannis, Z.; La Parola, V.; Montini, T.; Petit, C.; Stathatos, E.; Godin, R.; Durrant, J. R.; Prato, M.; Fornasiero, P. Metal-Free Dual-Phase Full Organic Carbon Nanotubes/g-C<sub>3</sub>N<sub>4</sub> Heteroarchitectures for Photocatalytic Hydrogen Production. *Nano Energy* **2018**, *50*, 468–478. <https://doi.org/10.1016/j.nanoen.2018.05.070>.
- (2) Chen, W.; Han, B.; Tian, C.; Liu, X.; Liang, S.; Deng, H.; Lin, Z. MOFs-Derived Ultrathin Holey Co<sub>3</sub>O<sub>4</sub> Nanosheets for Enhanced Visible Light CO<sub>2</sub> Reduction. *Applied Catalysis B: Environmental* **2019**, *244*, 996–1003. <https://doi.org/10.1016/j.apcatb.2018.12.045>.
- (3) Yang, J.; Zhang, F.; Lu, H.; Hong, X.; Jiang, H.; Wu, Y.; Li, Y. Hollow Zn/Co ZIF Particles Derived from Core-Shell ZIF-67@ZIF-8 as Selective Catalyst for the Semi-Hydrogenation of Acetylene. *Angew. Chem. Int. Ed.* **2015**, *54* (37), 10889–10893. <https://doi.org/10.1002/anie.201504242>.
- (4) Schaate, A.; Roy, P.; Godt, A.; Lippke, J.; Waltz, F.; Wiebcke, M.; Behrens, P. Modulated Synthesis of Zr-Based Metal-Organic Frameworks: From Nano to Single Crystals. *Chem. Eur. J.* **2011**, *17* (24), 6643–6651. <https://doi.org/10.1002/chem.201003211>.
- (5) Ma, J.; Wang, W.; Li, Y.; Lu, Z.; Tan, X.; Han, H. Novel Porphyrin Zr Metal–Organic Framework (PCN-224)-Based Ultrastable Electrochemiluminescence System for PEDV Sensing. *Anal. Chem.* **2021**, *93* (4), 2090–2096. <https://doi.org/10.1021/acs.analchem.0c03836>.
- (6) Jin, P.; Wang, L.; Ma, X.; Lian, R.; Huang, J.; She, H.; Zhang, M.; Wang, Q. Construction of Hierarchical ZnIn<sub>2</sub>S<sub>4</sub>@PCN-224 Heterojunction for Boosting Photocatalytic Performance in Hydrogen Production and Degradation of Tetracycline Hydrochloride. *Applied Catalysis B: Environmental* **2021**, *284*, 119762. <https://doi.org/10.1016/j.apcatb.2020.119762>.
- (7) Wang, L.; Duan, S.; Jin, P.; She, H.; Huang, J.; Lei, Z.; Zhang, T.; Wang, Q. Anchored Cu(II) Tetra(4-Carboxyphenyl)Porphyrin to P25 (TiO<sub>2</sub>) for Efficient Photocatalytic Ability in CO<sub>2</sub> Reduction. *Applied Catalysis B: Environmental* **2018**, *239*, 599–608. <https://doi.org/10.1016/j.apcatb.2018.08.007>.
- (8) Zhang, J.; White, G. B.; Ryan, M. D.; Hunt, A. J.; Katz, M. J. Dihydrolevoglucosenone (Cyrene) As a Green Alternative to *N,N*-Dimethylformamide (DMF) in MOF Synthesis. *ACS Sustainable Chem. Eng.* **2016**, *4* (12), 7186–7192. <https://doi.org/10.1021/acssuschemeng.6b02115>.
- (9) Avci, C.; Yazdi, A.; Tarrés, M.; Bernoud, E.; Bastús, N. G.; Puentes, V.; Imaz, I.; Ribas, X.; MasPOCH, D. Sequential Deconstruction–Reconstruction of Metal–Organic Frameworks: An Alternative Strategy for Synthesizing (Multi)-Layered ZIF Composites. *ACS Appl. Mater. Interfaces* **2018**, *10* (28), 23952–23960. <https://doi.org/10.1021/acsami.8b05098>.
- (10) Sun, Y.; Shi, J.; Zhang, S.; Wu, Y.; Mei, S.; Qian, W.; Jiang, Z. Hierarchically Porous and Water-Tolerant Metal–Organic Frameworks for Enzyme Encapsulation. *Ind. Eng. Chem. Res.* **2019**, *58* (28), 12835–12844. <https://doi.org/10.1021/acs.iecr.9b02164>.
- (11) Feng, Y.; Yao, J. Tailoring the Structure and Function of Metal Organic Framework by Chemical Etching for Diverse Applications. *Coordination*

- Chemistry Reviews* **2022**, *470*, 214699.  
<https://doi.org/10.1016/j.ccr.2022.214699>.
- (12) García-Palacín, M.; Martínez, J. I.; Paseta, L.; Deacon, A.; Johnson, T.; Malankowska, M.; Téllez, C.; Coronas, J. Sized-Controlled ZIF-8 Nanoparticle Synthesis from Recycled Mother Liquors: Environmental Impact Assessment. *ACS Sustainable Chem. Eng.* **2020**, *8* (7), 2973–2980.  
<https://doi.org/10.1021/acssuschemeng.9b07593>.
- (13) Bardestani, R.; Patience, G. S.; Kaliaguine, S. Experimental Methods in Chemical Engineering: Specific Surface Area and Pore Size Distribution Measurements—BET, BJH, and DFT. *Can. J. Chem. Eng.* **2019**, *97* (11), 2781–2791.  
<https://doi.org/10.1002/cjce.23632>.
- (14) Scofield, J. H. Hartree-Slater Subshell Photoionization Cross-Sections at 1254 and 1487 EV. *Journal of Electron Spectroscopy and Related Phenomena* **1976**, *8* (2), 129–137. [https://doi.org/10.1016/0368-2048\(76\)80015-1](https://doi.org/10.1016/0368-2048(76)80015-1).
- (15) Luo, C.; Ren, X.; Dai, Z.; Zhang, Y.; Qi, X.; Pan, C. Present Perspectives of Advanced Characterization Techniques in TiO<sub>2</sub>-Based Photocatalysts. *ACS Appl. Mater. Interfaces* **2017**, *9* (28), 23265–23286.  
<https://doi.org/10.1021/acsami.7b00496>.
- (16) Dai, Y.; Yu, J.; Cheng, C.; Tan, P.; Ni, M. Engineering the Interfaces in Water-Splitting Photoelectrodes – an Overview of the Technique Development. *J. Mater. Chem. A* **2020**, *8* (15), 6984–7002.  
<https://doi.org/10.1039/D0TA01670E>.
- (17) Miao, T. J.; Tang, J. Characterization of Charge Carrier Behavior in Photocatalysis Using Transient Absorption Spectroscopy. *J. Chem. Phys.* **2020**, *152* (19), 194201. <https://doi.org/10.1063/5.0008537>.
- (18) Zhang, L.; Ran, J.; Qiao, S.-Z.; Jaroniec, M. Characterization of Semiconductor Photocatalysts. *Chem. Soc. Rev.* **2019**, *48* (20), 5184–5206.  
<https://doi.org/10.1039/C9CS00172G>.
- (19) Berera, R.; van Grondelle, R.; Kennis, J. T. M. Ultrafast Transient Absorption Spectroscopy: Principles and Application to Photosynthetic Systems. *Photosynth Res* **2009**, *101* (2–3), 105–118. <https://doi.org/10.1007/s11120-009-9454-y>.
- (20) Cowan, A. J.; Durrant, J. R. Long-Lived Charge Separated States in Nanostructured Semiconductor Photoelectrodes for the Production of Solar Fuels. *Chem. Soc. Rev.* **2013**, *42* (6), 2281–2293.  
<https://doi.org/10.1039/C2CS35305A>.
- (21) M. Maghraby, A. Introductory Chapter: Electron Paramagnetic Resonance. In *Topics From EPR Research*; M. Maghraby, A., Ed.; IntechOpen, 2019.  
<https://doi.org/10.5772/intechopen.83028>.
- (22) Al-Madanat, O.; Nunes, B. N.; AlSalka, Y.; Hakki, A.; Curti, M.; Patrocinio, A. O. T.; Bahnemann, D. W. Application of EPR Spectroscopy in TiO<sub>2</sub> and Nb<sub>2</sub>O<sub>5</sub> Photocatalysis. *Catalysts* **2021**, *11* (12), 1514.  
<https://doi.org/10.3390/catal11121514>.
- (23) Xia, P.; Cheng, B.; Jiang, J.; Tang, H. Localized  $\pi$ -Conjugated Structure and EPR Investigation of g-C<sub>3</sub>N<sub>4</sub> Photocatalyst. *Applied Surface Science* **2019**, *487*, 335–342. <https://doi.org/10.1016/j.apsusc.2019.05.064>.

## CHAPTER 2

- (24) Kaleem-ur-Rahman Naveed; Li Wang; Haojie Yu; Raja Summe Ullah; Muhammad Haroon; Shah Fahad; Jiyang Li; Tarig Elshaarani; Rizwan Ullah Khan; Ahsan Nazir. Recent Progress in the Electron Paramagnetic Resonance Study of Polymers. *Polym. Chem.* **2018**, No. 9, 3306–3335.
- (25) Grigoropoulou, G.; Christoforidis, K. C.; Louloudi, M.; Deligiannakis, Y. Structure-Catalytic Function Relationship of SiO<sub>2</sub>-Immobilized Mononuclear Cu Complexes: An EPR Study. *Langmuir* **2007**, 23 (20), 10407–10418. <https://doi.org/10.1021/la700815d>.
- (26) Bonke, S. A.; Risse, T.; Schnegg, A.; Brückner, A. In Situ Electron Paramagnetic Resonance Spectroscopy for Catalysis. *Nat Rev Methods Primers* **2021**, 1 (1), 33. <https://doi.org/10.1038/s43586-021-00031-4>.
- (27) Davies, M. J. Detection and Characterisation of Radicals Using Electron Paramagnetic Resonance (EPR) Spin Trapping and Related Methods. *Methods* **2016**, 109, 21–30. <https://doi.org/10.1016/j.ymeth.2016.05.013>.
- (28) Ioannidou, T.; Anagnostopoulou, M.; Papoulis, D.; Christoforidis, K. C.; Vasiliadou, I. A. UiO-66/Palygorskite/TiO<sub>2</sub> Ternary Composites as Adsorbents and Photocatalysts for Methyl Orange Removal. *Applied Sciences* **2022**, 12 (16), 8223. <https://doi.org/10.3390/app12168223>.
- (29) Liqiang, J.; Yichun, Q.; Baiqi, W.; Shudan, L.; Baojiang, J.; Libin, Y.; Wei, F.; Honggang, F.; Jiazhong, S. Review of Photoluminescence Performance of Nano-Sized Semiconductor Materials and Its Relationships with Photocatalytic Activity. *Solar Energy Materials and Solar Cells* **2006**, 90 (12), 1773–1787. <https://doi.org/10.1016/j.solmat.2005.11.007>.
- (30) Zhao, G.; Wu, H.; Feng, R.; Wang, D.; Xu, P.; Wang, H.; Guo, Z.; Chen, Q. Bimetallic Zeolitic Imidazolate Framework as an Intrinsic Two-Photon Fluorescence and PH-Responsive MR Imaging Agent. *ACS Omega* **2018**, 3 (8), 9790–9797. <https://doi.org/10.1021/acsomega.8b00923>.
- (31) Kwon, S.; Fan, M.; DaCosta, H. F. M.; Russell, A. G.; Berchtold, K. A.; Dubey, M. K. CO<sub>2</sub> Sorption. In *Coal Gasification and Its Applications*; Elsevier, 2011; pp 293–339. <https://doi.org/10.1016/B978-0-8155-2049-8.10010-5>.

Chapter 3:

MOF-derived  
composites

$\text{Co}_3\text{O}_4\text{-CN}$

## Table of figures

FIGURE 3.1 : TGA PROFILES OF THE PURE CN <sub>570</sub> , PURE OXIDES AND COMPOSITE MATERIALS.....	107
FIGURE 3. 2 : (A) XRD PATTERNS OF THE PURE CN MATERIALS TREATED AT DIFFERENT TEMPERATURES, (B) SCHEMATIC ILLUSTRATION OF INTER- AND INTRA-LAYER DISTANCE IN CN STRUCTURE .....	109
FIGURE 3. 3: XRD PATTERNS OF THE A) ZIF-67, M-ZIF-67 AND CO <sub>3</sub> O <sub>4</sub> AND B) COMPOSITES. ....	111
FIGURE 3. 4 : ATR SPECTRA OF A) THE PURE CN SAMPLES AS SYNTHESIZED AND THERMALLY TREATED AND B) CO <sub>3</sub> O <sub>4</sub> (BULK AND NANOSHEETS) AND COMPOSITE MATERIALS.....	112
FIGURE 3. 5 : NITROGEN PHYSISORPTION ISOTHERMS OF THE PURE CN (LEFT PANEL) AND THE COMPOSITES MATERIALS (RIGHT PANEL) .....	113
FIGURE 3. 6: XPS SURVEY SPECTRA .....	114
FIGURE 3. 7: (A) C 1s, (B) N 1s, (C) Co 2P <sub>3/2</sub> AND (D) O 1s HIGH-RESOLUTION XPS SPECTRA OF THE PURE CN AND CO <sub>3</sub> O <sub>4</sub> AND COMPOSITE MATERIALS .....	116
FIGURE 3. 8: CO <sub>2</sub> -TPD PROFILES OF THE BARE CN, CN <sub>570</sub> , CO <sub>3</sub> O <sub>4</sub> -NS AND THE CO <sub>3</sub> -NS-CN <sub>570</sub> COMPOSITE. ....	117
FIGURE 3. 9: DR UV-VIS SPECTRA OF (A) THE CN SAMPLES AND (B) THE NANOCOMPOSITES .....	118
FIGURE 3. 10 : PLOTS USED TO ESTIMATE BAND GAP ENERGIES OF THE (A) PURE CN MATERIALS AND (B) THE PURE CO <sub>3</sub> O <sub>4</sub> -BK AND CO <sub>3</sub> O <sub>4</sub> -NS MATERIALS.....	119
FIGURE 3. 11: SEM IMAGES OF (A) CN <sub>AS</sub> , (B) CN <sub>570</sub> , (C) ZIF-67, (D) M- ZIF-67, (E) CO <sub>3</sub> O <sub>4</sub> -BK AND (F) CO <sub>3</sub> O <sub>4</sub> -NS.....	120
FIGURE 3. 12: TEM IMAGES OF (A) CO <sub>3</sub> O <sub>4</sub> -BK, (B) CO <sub>3</sub> O <sub>4</sub> -NS, (C) CO <sub>7</sub> -BK-CN <sub>570</sub> , (D) CO <sub>7</sub> -NS- CN <sub>570</sub> AND HRTEM IMAGES OF (E) CO <sub>3</sub> O <sub>4</sub> -BK AND (F) CO <sub>3</sub> O <sub>4</sub> -NS .....	122
FIGURE 3. 13: EDX SPECTRA OF THE PURE CO <sub>3</sub> O <sub>4</sub> -NS MATERIAL (BLACK LINE) AND THE CO <sub>7</sub> -NS- CN <sub>570</sub> COMPOSITE (PURPLE LINE). THE PEAKS IN THE 8-9 KEV REGION CORRESPOND TO CU-GRID USED.....	123
FIGURE 3. 14 : TRANSIENT ABSORPTION DECAY KINETICS OF (A) CN <sub>570</sub> , (B) CO <sub>3</sub> -NS-CN <sub>570</sub> , (C) CO <sub>3</sub> - BK-CN <sub>570</sub> , (D) CO <sub>3</sub> O <sub>4</sub> -NS AND (E) CO <sub>3</sub> O <sub>4</sub> -BK. SAMPLES WERE MEASURED IN AIR, EXCITED WITH A 355 NM LASER PULSE (~6 NS PULSE WIDTH, ~0.0.63 MJ CM <sup>-2</sup> , 0.8 Hz) AND TRANSIENT CHANGES IN ABSORPTION WERE PROBED AT 550 TO 1000 NM FROM 10 MS TO 1 S. ....	125
FIGURE 3. 15: TRANSIENT ABSORPTION SPECTRA AT THE SELECT TIMES OF 10 MS, 100 MS, 1 MS, 10 MS, 100 MS AND 0.9 S AFTER EXCITATION OF (A) CN <sub>570</sub> , (B) CO <sub>3</sub> -NS-CN <sub>570</sub> , (C) CO <sub>3</sub> -BK- CN <sub>570</sub> , D) CO <sub>3</sub> O <sub>4</sub> -NS AND (E) CO <sub>3</sub> O <sub>4</sub> -BK. SAMPLES WERE MEASURED IN AIR, EXCITED WITH A 355 NM LASER PULSE (~6 NS PULSE WIDTH, ~0.0.63 MJ CM <sup>-2</sup> , 0.8 Hz) AND TRANSIENT CHANGES IN ABSORPTION WERE PROBED AT 550 TO 1000 NM FROM 10 MS TO 1 S. ....	126
FIGURE 3. 16: (A) NORMALIZED TRANSIENT ABSORPTION DECAY KINETICS AT THE PROBE WAVELENGTH OF 800 NM FOR CN <sub>570</sub> , CO <sub>3</sub> -NS-CN <sub>570</sub> , CO <sub>3</sub> -BK-CN <sub>570</sub> , CO <sub>3</sub> O <sub>4</sub> -NS AND CO <sub>3</sub> O <sub>4</sub> -BK. TRANSIENT ABSORPTION SPECTRA AT THE SELECT TIMES OF (B) 10 MS, (C) 1 MS AND (D) 100 MS AFTER EXCITATION FOR CN <sub>570</sub> , CO <sub>3</sub> -NS-CN <sub>570</sub> , CO <sub>3</sub> -BK-CN <sub>570</sub> , CO <sub>3</sub> O <sub>4</sub> -NS AND CO <sub>3</sub> O <sub>4</sub> -BK. .....	127
FIGURE 3. 17: EPR SPECTRA OF THE PURE CN <sub>570</sub> AND THE CO <sub>7</sub> -NS-CN <sub>570</sub> COMPOSITE UNDER IRRADIATION. 10 MG OF THE MATERIAL WERE IRRADIATED IN-SITU IN THE EPR QUARTZ TUBE	

## CHAPTER 3

<i>USING AN ARC XENON LAMP OPERATING WITH 450 W INPUT POWER EQUIPPED WITH A WATER-FILTER. ....</i>	129
<i>FIGURE 3. 18: RELATIVE EPR SIGNAL INTENSITY (A) AND PHOTOCURRENTS AT 1.23 V VS RHE (B) OF THE BARE CN<sub>570</sub> AND COMPOSITES CATALYST. ....</i>	129
<i>FIGURE 3. 19: CYCLIC VOLTAMMETRY CURVES PERFORMED IN ALKALINE ELECTROLYTE (0.01 M NaOH, 0.1 M Na<sub>2</sub>SO<sub>4</sub>) AT A 10 MV S<sup>-1</sup> OF THE CN<sub>570</sub>, CO<sub>3</sub>O<sub>4</sub>-NS AND THE CO7-NS-CN<sub>570</sub> NANOCOMPOSITE UNDER DARK AND ILLUMINATION CONDITIONS. (Xe ARC LAMP NEWPORT; 300W; EQUIPPED WITH AM1.5G FILTER; INCIDENT POWER DENSITY ON THE CELL 100 MW.CM<sup>-2</sup>). ....</i>	130
<i>FIGURE 3. 20: PHOTOCATALYTIC CO PRODUCTION RATES BY PURE CN CATALYSTS .....</i>	131
<i>FIGURE 3. 21: PHOTOCATALYTIC CO PRODUCTION RATES BY THE PURE COBALT OXIDE CATALYSTS AND NANOCOMPOSITES BEARING CO<sub>3</sub>O<sub>4</sub>-BK AND CO<sub>3</sub>O<sub>4</sub>-NS.....</i>	133
<i>FIGURE 3. 22: PHOTOCATALYTIC RESULTS OF CO<sub>2</sub> REDUCTION WITH WATER AS ELECTRON DONOR FOR CO7-NS-CN<sub>570</sub> .....</i>	134
<i>FIGURE 3. 23: PHOTOCATALYTIC CO PRODUCTION RATES BY THE REFERENCE REACTIONS. ....</i>	135
<i>FIGURE 3. 24: H<sub>2</sub> PRODUCTION RATES BY THE CN<sub>As</sub>, CN<sub>570</sub> AND CO7-NS-CN<sub>570</sub> CATALYSTS USING PT AS CO-CATALYST AND TEOA AS SACRIFICIAL AGENT. ....</i>	136
<i>FIGURE 3. 25: DMPO SPIN-TRAPPING EPR SPECTRA OF THE CN<sub>570</sub> AND THE CO7-NS-CN<sub>570</sub> MATERIALS IN METHANOL DISPERSION FOR THE DETECTION OF THE DMPO-O<sub>2</sub> • — SPIN-ADDUCT.....</i>	137
<i>FIGURE 3. 26 : PHOTOCATALYTIC CO PRODUCTION RATES BY : A) RECYCLING REACTIONS PERFORMED USING THE MOST ACTIVE CO7-NS-CN<sub>570</sub> CATALYST AND B) CO EVOLUTION OVER A 6 H REACTION TIME UNDER UV–VIS ILLUMINATION FOR THE FRESH AND THE USED FOR 5 TIMES CO7-NS-CN<sub>570</sub> CATALYST. ....</i>	138
<i>FIGURE 3. 27: CHARACTERIZATION OF THE CO7-NS-CN<sub>570</sub> CATALYST USED AFTER FIVE CONSECUTIVE TIMES: A) XPS ; B) TGA ; C) ATR.....</i>	139

## CHAPTER 3

## Introduction

This chapter focuses on the  $\text{Co}_3\text{O}_4\text{-CN}$  composite materials, their characterization, and their application as photocatalysts for  $\text{CO}_2$  reduction. The synthesis process used has been described in detail in [Chapter 2.1](#). The aims of this work are to identify the properties of the prepared materials that are linked with catalytic activity. This study focuses on different aspects including the effect of morphology at the nanoscale on the structure and the activity. It is divided in two main parts:

- (1) The first part interpretes the results acquired from the characterization techniques that are employed for the characterization of the nanocomposite materials and their individual counterparts. More precisely, a multi-characterization methodology is applied to investigate in detail:
  - a. The structural properties,
  - b. the electronic properties linked with the optical and charge formation properties,
  - c. the morphological properties and
  - d. to study thoroughly the behavior of charge carriers generated upon irradiation.
- (2) The second part presents the results of the photocatalytic activity of the prepared materials. Namely, the photocatalysts were evaluated towards:
  - a.  $\text{CO}_2$  reduction reaction and
  - b.  $\text{H}_2\text{O}$  splitting.

The photocatalytic results in combination with the catalysts' properties are used to shed light to the mechanism of the reaction. The above results are also published in *ACS Applied Materials and Interfaces* with title: *MOF-derived defective  $\text{Co}_3\text{O}_4$  in Carbon nitride composites for  $\text{CO}_2$  photoreduction and  $\text{H}_2$  production*.

## I. Characterization of Co<sub>3</sub>O<sub>4</sub>-CN nanocomposites

### I.1. Structural and compositional characterization

#### *TGA*

As mentioned in [section 2.1.1.](#), CN<sub>as</sub> samples are submitted to a second thermal treatment aiming on the chemical and morphological modification, as expected by the literature. Also, the Co<sub>3</sub>O<sub>4</sub>/CN nanocomposite materials are developed by in situ mixing the MOF templates and CN and then calcining them to form the oxides on the CN surface. In order to estimate the final content of Co<sub>3</sub>O<sub>4</sub> on the CN materials, we are based on the fact that the two counterparts present different thermal stabilities. In this direction, the quantification of the deposited oxide is performed by means of TGA and the results of pure CN samples (CN<sub>as</sub>, CN<sub>570</sub>) and the prepared composite materials are shown in Figure 3.1.

The thermally treated CN<sub>570</sub> presents thermal stability up to approximately 570 °C. Complete oxidation is performed between 580 and 615 °C. It is already reported that hydrogen terminated C–N sheet is energetically more stable, and thus has a high thermal stability <sup>1</sup>. On the contrary, pure oxides (both Co<sub>3</sub>O<sub>4</sub>-NS and Co<sub>3</sub>O<sub>4</sub>-Bk) present low weight loss (5-8% up to 650 °C). These results provide critical information. The stability of CN<sub>570</sub> up to 580 °C indicates that the thermal treatment applied for the development of the Co<sub>3</sub>O<sub>4</sub>/CN nanocomposite materials does not affect the CN content.

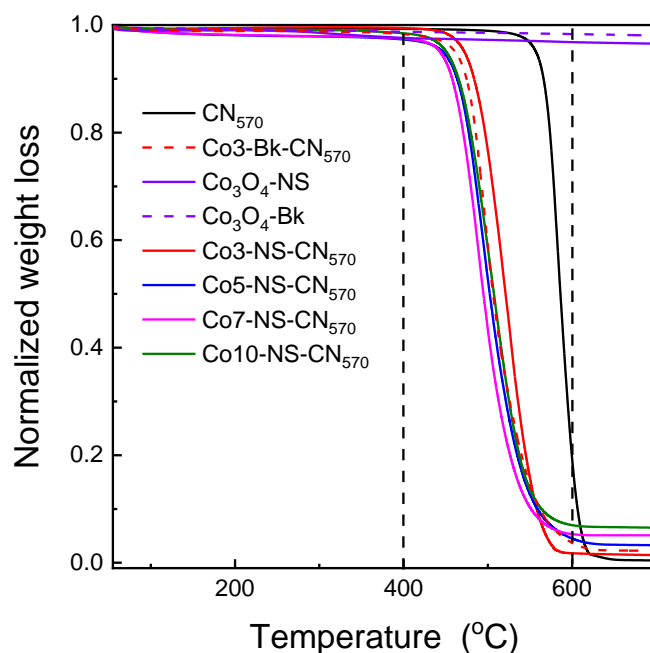


Figure 3.1 : TGA profiles of the pure  $CN_{570}$ , pure oxides and composite materials.

The TGA profiles can be divided into 3 steps. In the first part, at temperatures up to 400 °C, the desorption of water and adsorbates is observed. In the range of 400-600 °C we observe the decomposition of carbon nitride structures. Specifically, the decomposition of the pure  $CN_{570}$  sample begins at temperatures above 585 °C and the decomposition of all composites begins at lower temperatures (ca. 450 °C). This is most likely due to the presence of the oxide that promotes oxidation at lower temperatures<sup>2</sup>. This observation further verifies that the temperature chosen for the calcination step (i.e., 350 °C) for the formation of the oxides does not affect the CN part. The third and last part of the TGA profiles, is observed for temperatures above 600 °C where only  $Co_3O_4$  remains in the nanocomposites. The mass at 650 °C is used to calculate the content of  $Co_3O_4$  on the composite materials. In all composites, the  $Co_3O_4$  amount is less than the nominal m-ZIF-67 amount used in the synthesis process. This might originate from the decomposition of the organic part of the MOF structure. The content of  $Co_3O_4$  is given in Table 3.1. It is clearly seen that increasing the ZIF-67 and m-ZIF-67 amount in the synthesis process progressively increases the content of the  $Co_3O_4$  in the final composite.

## CHAPTER 3

Table 3.1:  $\text{Co}_3\text{O}_4$  loading on the nanocomposites materials as estimated by TGA

<b>Sample</b>	<b><math>\text{Co}_3\text{O}_4</math> content (%)</b>
<b>CN<sub>570</sub></b>	-
<b><math>\text{Co}_3\text{O}_4</math>-Bk</b>	100
<b><math>\text{Co}_3\text{O}_4</math>-NS</b>	100
<b>Co3-Bk-CN<sub>570</sub></b>	2.4
<b>Co3-NS-CN<sub>570</sub></b>	1.6
<b>Co5-NS-CN<sub>570</sub></b>	3.6
<b>Co7-NS -CN<sub>570</sub></b>	5.2
<b>Co10-NS -CN<sub>570</sub></b>	6.8

### XRD

XRD analysis is performed in order to get information on the structure of the prepared materials. Information related to the effect of the post-thermal treatment on the as-synthesized CN and the presence of both phases in the composite are obtained. Figure 3.2 shows the XRD patterns of the CN<sub>as</sub> and the thermally treated CN materials. They all present two diffraction peaks centered at ca. 13° and 27.7°. This is in line with the results in the literature for CN materials and clearly indicates the formation of the carbon nitride structure. The two diffraction peaks are attributed to the (100) and (002) crystal planes of CN, respectively, e.g., the interplanar spacing in the tri-s-triazine units and the stacking of conjugated layers within the CN structure<sup>3</sup>. By observing closer the (002) diffraction peak which is displayed in the inset graph, we can witness a shift to higher angles by increasing the temperature of the thermal treatment. This is assigned to the improved stacking of the CN sheets. The decrease of the layers distance is probably linked with the planarization of the single layers allowing better packing<sup>4,5</sup>.

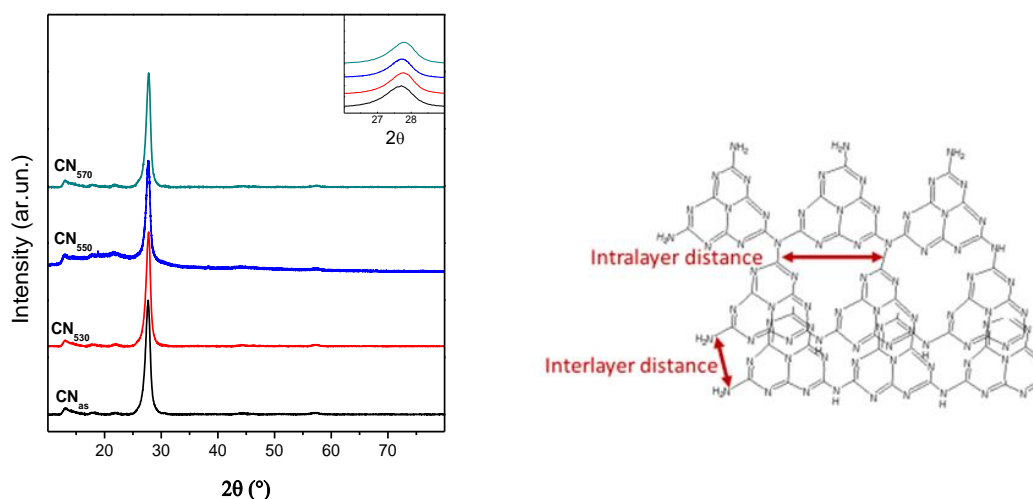


Figure 3. 2 : (a) XRD Patterns of the pure CN materials treated at different temperatures, (b) Schematic illustration of inter- and intra-layer distance in CN structure

The interplanar distance ( $d$ ) was calculated by using the Bragg's law (Chapter 2.II.2) for all CN materials. A small decrease is evidenced in the CN<sub>570</sub> sample compared with the CN<sub>as</sub> as shown in Table 3.2. Regarding the crystallite size ( $D$ ) that is calculated by Scherrer's equation, it is noticed that the second thermal treatment induced an increase (8.01 nm) compared to the crystallite size of CN<sub>as</sub> (7.37 nm). Based on the aforementioned calculations, we can also estimate the number of layers for the prepared CN materials, by using Equation 3.1. We can consider that the thickness of the layer is negligible compared to the interplanar distance between two layers. Thus, we can see that the increasing temperature leads to progressive planarization and higher order of nanosheets.

$$\text{Number of layers} = \frac{D}{d} \quad \text{Equation 3.1}$$

## CHAPTER 3

*Table 3.2: Interplanar distance, crystallite size and number of layers for the prepared CN materials calculated by XRD*

sample	D <sup>1</sup> (nm)	d <sup>2</sup> (nm)	Number of layers
CN <sub>as</sub>	7.37	0.333	22
CN <sub>530</sub>	7.99	0.322	24
CN <sub>550</sub>	8.01	0.320	25
CN <sub>570</sub>	9.02	0.322	28

<sup>1</sup>CALCULATED BY SCHERRER'S EQUATION    <sup>2</sup> CALCULATED BY BRAGG'S LAW

Figure 3.3a presents the XRD patterns of the ZIF-67, the solvothermally post-treated m-ZIF-67 and the obtained oxides after calcination of the two MOF structures. The ZIF-67 showed the typical diffraction pattern of that particular MOF (Figure 3.3a) <sup>6</sup>. The sharp diffraction peaks indicate the high crystallinity of ZIF-67. Solvothermal treatment of ZIF-67 in the presence of Co<sup>2+</sup> results in a different XRD pattern suggesting a phase transformation <sup>6-8</sup>. These two structures were then calcined to obtain pure Co<sub>3</sub>O<sub>4</sub>. The Co<sub>3</sub>O<sub>4</sub>-NS sample obtained after calcining the solvothermally treated m-ZIF-67 displays diffraction peaks centered at 19°, 31.4°, 36.7°, 38.5°, 45°, 56°, 59.5°, 65.3° and 77.1°. These are attributed to (111), (220), (311), (222), (400), (422), (511), (440) and (622), planes of Face-centered cubic phase of spinel Co<sub>3</sub>O<sub>4</sub>, respectively (JCPDS card, No 74-2120) <sup>6</sup>. A similar XRD pattern is detected for the Co<sub>3</sub>O<sub>4</sub>-Bk sample obtained after calcining the as-synthesized ZIF-67. As evidenced in Figure 3.3b, the XRD patterns of the nanocomposites contain diffraction peaks of their individual counter parts. The XRD pattern of the composites is dominated by the diffraction peaks of CN. This is expected given the high content of CN in the composites as evidenced by TGA. The intensity of the Co<sub>3</sub>O<sub>4</sub> diffraction peaks is proportional to the amount used in the synthesis. No obvious differences are detected when comparing the XRD patterns of the pure materials with that of the composites. These data confirm the presence of both CN and Co<sub>3</sub>O<sub>4</sub> in the nanocomposites suggesting the formation of a heterojunction without changing the phase of the individual parts in the composites.

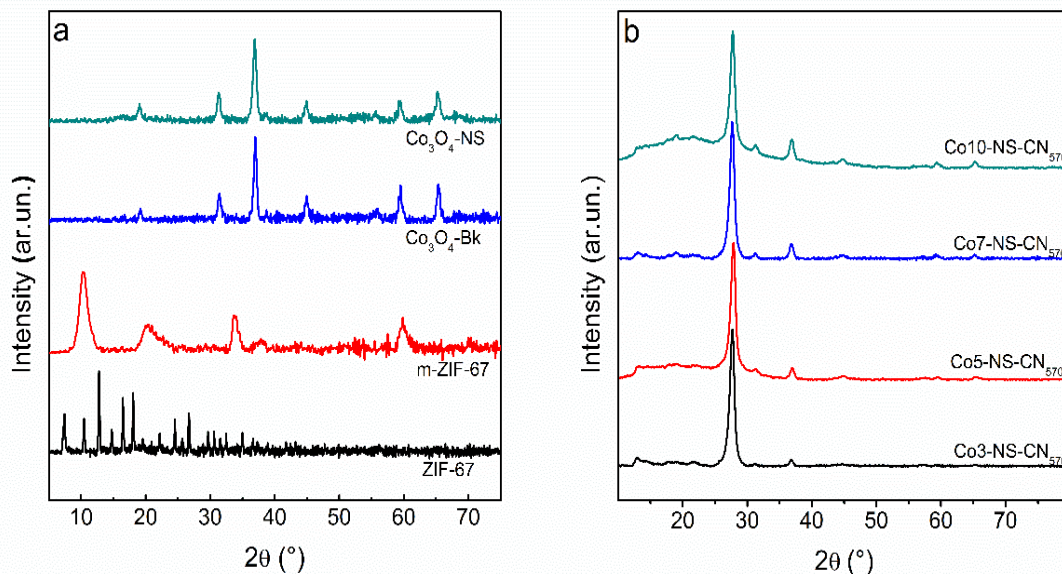


Figure 3. 3: XRD Patterns of the a) ZIF-67, m-ZIF-67 and  $\text{Co}_3\text{O}_4$  and b) composites

#### ATR

Additional structural information is obtained with ATR spectroscopy. In Figure 3.4a we can observe that all the CN-based materials presented the characteristic spectral features of carbon nitride building units. In detail, the sharp band centered at  $810\text{ cm}^{-1}$  is attributed to the tri-s-triazine vibrations within the CN structure<sup>4,9</sup>. In addition, bands of the C—N stretching and bending vibrations of N heterocycles are detected in the  $1200\text{--}1800\text{ cm}^{-1}$  region. The bands observed at high wavenumbers (ca.  $3200\text{ cm}^{-1}$ ) are ascribed to the N—H groups<sup>4,10</sup>. This is normal because carbon nitride samples synthesized by thermal polymerization contain a certain number of NH/NH<sub>2</sub> groups due to incomplete condensation of the amine groups in the precursor. These groups form hydrogen bonds that help maintaining the intralayer order<sup>11</sup>. Careful inspection of this region reveals that the band intensity increases with increasing the temperature of the post-thermal treatment. This can be ascribed to the formation of structural defects resulting in the formation of more amino groups at the edges of the tri-s-triazine units when a second thermal treatment is applied<sup>4</sup>.

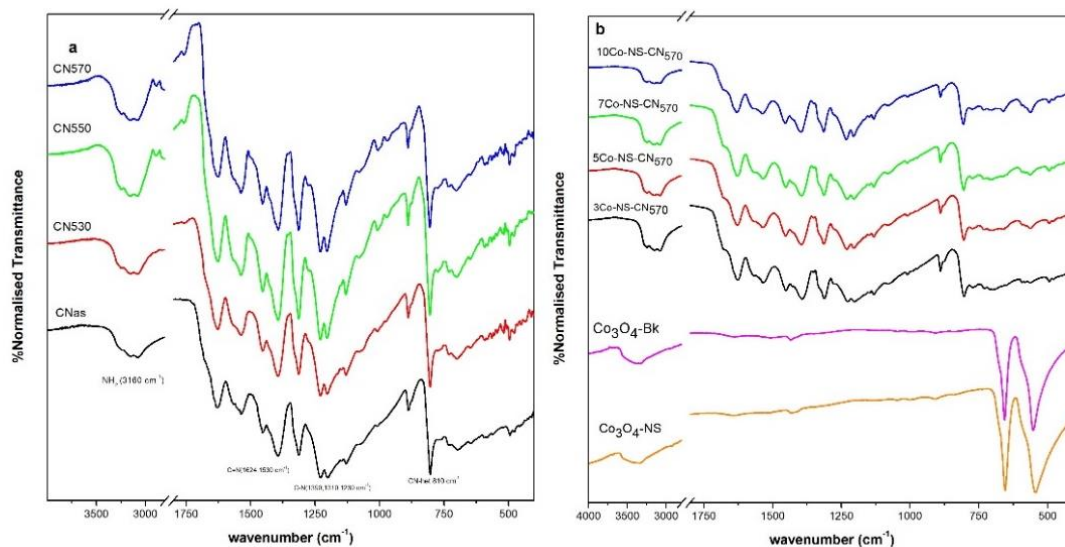


Figure 3.4 : ATR spectra of (a) the pure CN samples as synthesized and thermally treated and (b)  $\text{Co}_3\text{O}_4$  (bulk and Nanosheets) and composite materials.

ATR spectroscopy is also applied to study the structure of the prepared composite materials (Figure 3.4b). As evidenced, no obvious differences are detected in the characteristic CN vibrational modes of the composites compared with the bare CN materials. This further indicates that the CN structure remained unaltered during the coupling with  $\text{Co}_3\text{O}_4$ , in agreement with the XRD results. In addition, new bands ascribed to  $\text{Co}_3\text{O}_4$  are detected. Specifically, the bands centered at 660 and 555  $\text{cm}^{-1}$  are attributed to the Co-O vibration modes, verifying the presence of  $\text{Co}_3\text{O}_4$  on the nanocomposites<sup>12</sup>. These bands are also detected in both pure oxides. It is also worth mentioning that the intensity of these bands is proportional to the loading of the  $\text{Co}_3\text{O}_4$  precursors. Finally, the observed increase of the band at high wavelengths (ca. 3600-3200  $\text{cm}^{-1}$ ) is attributed to O—H bonds, from the water adsorbed.

### BET

Specific surface area also holds a significant role in the reactant's adsorption and thus in photocatalytic applications. The textural properties of the catalysts were investigated by  $\text{N}_2$  adsorption/desorption isotherms acquired at 77 K. The physisorption isotherms are given in Figure 3.5 and the BET specific surface area (SSA) of the prepared materials is given in Table 3.3. As can be observed they present a Type IV isotherms with hysteresis loop. This may indicate mesoporosity. The post thermal treatment induces an increase in the BET SSA approximately 3 times compared with the  $\text{CN}_{\text{as}}$ . This has been previously assigned to the thermal exfoliation of the CN structure and to the formation of structural defects on the polymeric structure, that are also suggested by ATR<sup>4</sup>, as well as to the partial amorphization of the structure<sup>13</sup>.  $\text{Co}_3\text{O}_4$ -NS presented an enhanced surface area (ca.

## CHAPTER 3

57 m<sup>2</sup> g<sup>-1</sup>) compared to Co<sub>3</sub>O<sub>4</sub>-Bk, while an increase in SSA is observed in all nanocomposites, which can be attributed to the presence of the oxide.

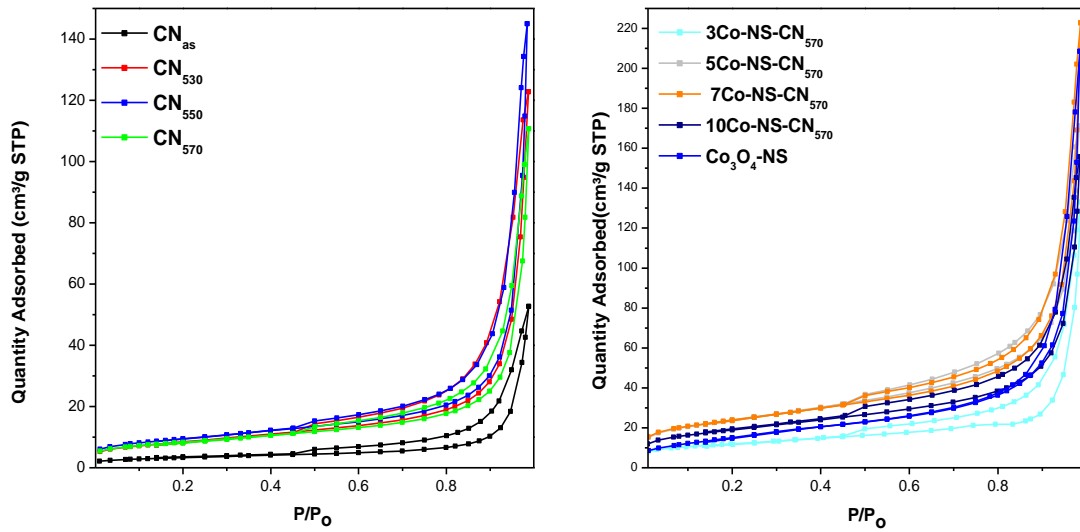


Figure 3. 5 : Nitrogen physisorption isotherms of the pure CN (left panel) and the composites materials (right panel)

Table 3.3: Specific surface area, micropore volume, energy bandgap and Co<sub>3</sub>O<sub>4</sub> loading for the nanocomposites and their counterparts.

Sample	SSA (m <sup>2</sup> g <sup>-1</sup> )	E <sub>g</sub> (eV)
CN <sub>as</sub>	11.62	2.86
CN <sub>530</sub>	30.42	2.86
CN <sub>550</sub>	33.65	2.75
CN <sub>570</sub>	29.41	2.72
Co <sub>3</sub> O <sub>4</sub> -Bk	38.18	2.35
Co <sub>3</sub> O <sub>4</sub> -NS	57.49	2.35
Co3-Bk-CN <sub>570</sub>	43.87	-
Co3-NS-CN <sub>570</sub>	41.60	-
Co5-NS-CN <sub>570</sub>	84.85	-
Co7-NS -CN <sub>570</sub>	84.27	-
Co10-NS -CN <sub>570</sub>	67.36	-

## XPS

The chemical composition of the catalysts was further investigated using XPS analysis. Survey spectra of the pure materials and composites are given in Figure 3.6. C and N are detected for bare CN materials and while Co and O for the composites and pure oxides. On the contrary, peaks attributed to C, N, Co and O are detected in the composite materials. All pure CN samples present the typical chemical states of C and N, specifically as it shown in Figure 3.7a., The high-resolution C 1s spectra have two contributions centered at 284.6 and 287.7 eV, corresponding to C—C and N—C=N<sub>2</sub> of the tri-s-triazine, respectively<sup>14</sup>. Regarding the N 1s XPS spectra of the pure CN samples, they can be deconvoluted into three peaks centered at 398.4 eV, 400.2 eV and 401.0 eV as it is shown in Figure 3.7b. These are attributed to the C=N—C, N—C<sub>3</sub> and —NH<sub>2</sub> chemical species, respectively<sup>4,15,16</sup>. Comparing the individual N 1s spectra of the pure CN<sub>as</sub> and CN<sub>570</sub> samples, the intensity of the terminal amino groups is higher in the case of the thermally treated CN<sub>570</sub> sample, as shown in Table 2. This suggests the formation of structural defect sites that give rise to increased —NH<sub>2</sub> groups during the second thermal treatment. This finding is in accordance with the ATR results, supporting the observed increased BET SSA. This is also confirmed by the change in the C/N ratio (Equation 2.4), namely 0.82 for CN<sub>570</sub> sample and 0.85 for pristine CN. It can be also seen that for both samples, the ratio is far from the stoichiometric (C/N=0.75)

In addition, a small shift of the main nitrogen peak by 0.2 eV to lower binding energies is observed in the composite materials compared with the pure CN<sub>570</sub>. This probably originates from an interaction with the Co<sub>3</sub>O<sub>4</sub> phase in the composite.

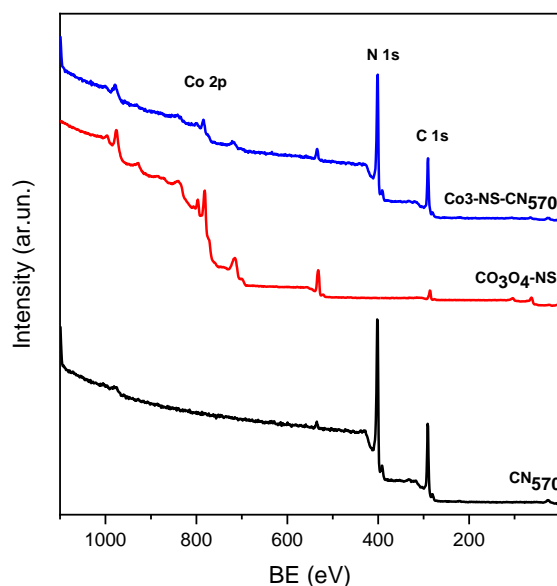


Figure 3. 6: XPS Survey spectra

The survey spectra of the  $\text{Co}_3\text{O}_4\text{-Bk}$  and  $\text{Co}_3\text{O}_4\text{-NS}$  materials display peaks related with C, Co and O. The presence of C is assigned to adventitious carbon species. In both samples, the two peaks expanding in the region 800-776 eV are ascribed to the Co  $2p_{3/2}$  and Co  $2p_{1/2}$ <sup>17</sup>. Focusing on the Co  $2p_{3/2}$  peak (Figure 3.7c), a clear difference on the relative peak area of the individual components was observed for the  $\text{Co}_3\text{O}_4\text{-Bk}$  and  $\text{Co}_3\text{O}_4\text{-NS}$  sample. This indicates a difference in the  $\text{Co}^{2+}/\text{Co}^{3+}$  ratio. In the case of  $\text{Co}_3\text{O}_4\text{-Bk}$ , the  $\text{Co}^{2+}/\text{Co}^{3+}$  ratio is close to the theoretical value (ca. 0.46) while in the  $\text{Co}_3\text{O}_4\text{-NS}$  sample is increased to 0.73.

It is reported that O 1s peak can be fitted by three curves, in low, medium, and high energies. In Figure 3.7d, we show that the O 1s peak can be deconvoluted into three peaks, centered at 529.2, 531.1 and 531.7 eV. The first peak can be associated with the O atoms from the lattice bonded to metal cations, which are the stoichiometric oxidation state. The peak at 531.1 eV is attributed to oxygen vacant sites that are O ions bonded to non-stoichiometric oxidized cations<sup>18,19</sup>. The peak centered at 531.7 is attributed to the presence of loosely bound oxygen on the surface of the catalyst, i.e., -OH groups from  $\text{H}_2\text{O}$  absorbed. The relative intensity of the defective O-species has been increased in the  $\text{Co}_3\text{O}_4\text{-NS}$  compared with the  $\text{Co}_3\text{O}_4\text{-Bk}$  sample (Figure 3.7d). This observation supports the difference in the  $\text{Co}^{2+}/\text{Co}^{3+}$  ratio. These results suggest the presence of more  $\text{Co}^{2+}$  in the  $\text{Co}_3\text{O}_4\text{-NS}$  sample and the formation of oxygen vacancies as charge neutrality species<sup>18,19</sup>.

Concerning the composite samples, the C 1s and N 1s spectra are in consistency with the pure  $\text{CN}_{570}$  sample (Figure 3.7a and 3.7b). As in the case of pure oxides, the relative abundance of  $\text{Co}^{2+}$  and  $\text{Co}^{3+}$  differs in the composites bearing  $\text{Co}_3\text{O}_4\text{-Bk}$  and  $\text{Co}_3\text{O}_4\text{-NS}$  (Figure 3.7c). In the  $\text{Co}_3\text{-Bk-CN}_{570}$  sample the  $\text{Co}^{2+}/\text{Co}^{3+}$  ratio is 0.5 while in the  $\text{Co}_3\text{-NS-CN}_{570}$  is increased to 0.68. More importantly, the defect sites of the pure  $\text{Co}_3\text{O}_4\text{-NS}$  are maintained in the final composite materials. Therefore, the XPS analysis verifies that the coupling process adopted for the development of the composites maintains the chemical states of both phases, especially the defect sites of the pure  $\text{Co}_3\text{O}_4\text{-NS}$  which are important for the catalytic mechanism.

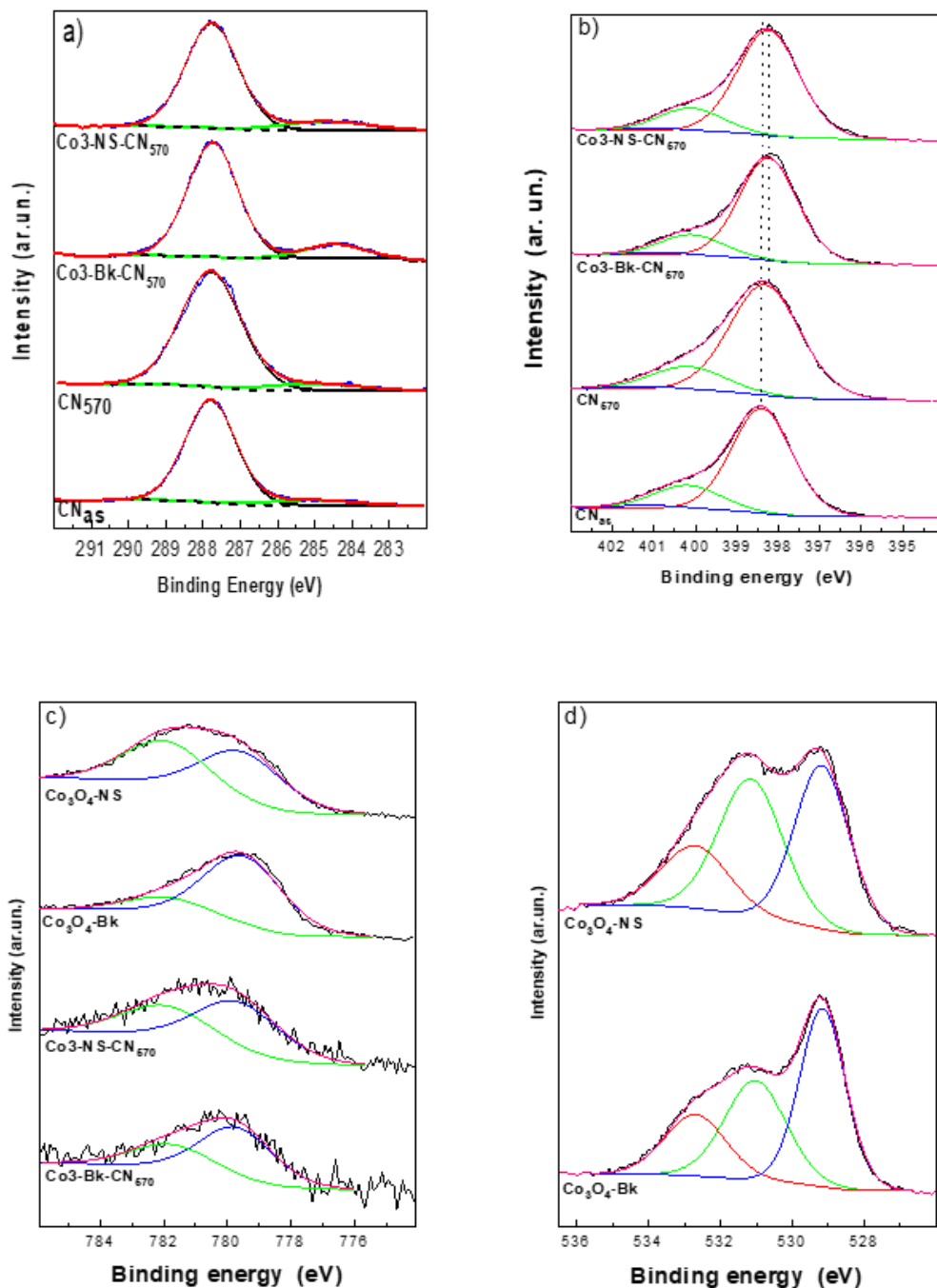


Figure 3. 7: (a) C 1s, (b) N 1s, (c) Co 2p<sub>3/2</sub> and (d) O 1s high-resolution XPS spectra of the pure CN and Co<sub>3</sub>O<sub>4</sub> and composite materials

### CO<sub>2</sub> Uptake capacity

It has been recently documented that the affinity of the substrate with the surface of CN plays vital role in activity<sup>13</sup>. The prepared photocatalysts are destined for CO<sub>2</sub> reduction, and as is mentioned in section 1.II.5.B.ii.a. CO<sub>2</sub> adsorption is the rate determining step of the process. Herein, the CO<sub>2</sub> uptake ability of the prepared

materials and the quantification of the basic sites on the catalyst surface are estimated by means of temperature programmed desorption of CO<sub>2</sub> (CO<sub>2</sub>-TPD). In Figure 3.8 the CO<sub>2</sub>-TPD profiles of the pure CN<sub>as</sub>, CN<sub>570</sub> and Co<sub>3</sub>O<sub>4</sub>-NS materials as well as the Co3-NS-CN<sub>570</sub> composite are presented. The two peaks detected at 120 and 370 °C correspond to medium and strong surface basic sites. Specifically, in the former case CO<sub>2</sub> is more loosely attached. The latter, in the composite material is attributed solely to the presence of the oxide as evidenced by the CO<sub>2</sub>-TPD profile of the Co<sub>3</sub>O<sub>4</sub>-NS material. Concerning the bare Carbon Nitride materials it is already demonstrated in the literature, that as the C/N ratio is decreasing in the six-membered C-N-C rings, more basic sites are generated in the surface of CN<sup>20</sup>. By integrating the areas beneath the curves shown in Figure 3.8, we can witness that CN<sub>570</sub> presents almost 2 times higher CO<sub>2</sub> uptake ability than the CN<sub>as</sub> material. This is likely linked with the increase of the amino groups formed during the second thermal treatment. It is worth mentioning that the Co<sub>3</sub>O<sub>4</sub>-NS and Co3-NS-CN<sub>570</sub> materials show larger amount of adsorbed CO<sub>2</sub> compared with the pure CN materials. Specifically, the Co3-NS-CN<sub>570</sub> presented a ca. 3-fold increase in the relative CO<sub>2</sub> adsorption amount compared with the pure CN<sub>570</sub>. This can be explained by the presence of oxygen vacant sites in the oxide, as it is already mentioned in Chapter 1 and explained in the following, that contribute significantly in the adsorption of CO<sub>2</sub> due to the higher binding energy in such sites than regular sites<sup>21-24</sup>.

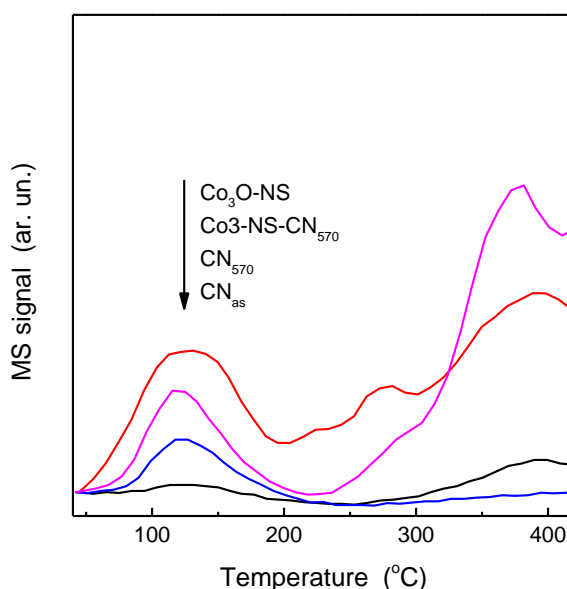


Figure 3. 8: CO<sub>2</sub>-TPD profiles of the bare CN, CN<sub>570</sub>, Co<sub>3</sub>O<sub>4</sub>-NS and the Co3-NS-CN<sub>570</sub> composite.

## 1.2. Characterization of optical properties

*UV/Vis Spectroscopy*

The light absorption properties of the prepared photocatalysts were studied by DR-UV-Vis Spectroscopy. The converted UV-Vis absorption spectra of the pure CN materials and the  $\text{Co}_x\text{-NS-CN}_{570}$  are given in Figure 3.9a and 3.9b, respectively. According to the UV-Vis DRS characterization results, the light absorption edge of the pure CN materials is observed at approximately 490 nm. This corresponds to the intrinsic electronic  $\pi \rightarrow \pi^*$  transition<sup>10</sup>. The second thermal treatment induced a small shift of the absorption edge to higher wavelengths and an increase of the light absorption in the region 450-550 nm (inset in Figure 3.7a). This is observed more clearly in the  $\text{CN}_{570}$  sample. In figure 3.10a the Tauc plots of the CN samples are presented in order to estimate the  $E_g$  values. The detected shift of the absorbance edge is also expressed in the band gap energy that is shifted from 2.86 to 2.81 eV as the temperature of the thermal treatment increases. On the other hand, the pure  $\text{Co}_3\text{O}_4\text{-NS}$  and  $\text{Co}_3\text{O}_4\text{-Bk}$  samples hold an estimated  $E_g$  value of 2.33 eV (Figure 3.10b). Concerning the optical properties of the composites, their light absorption is extended to the whole visible region. This is solely ascribed to  $\text{Co}_3\text{O}_4$  (Figure 3.9b). As is also evidenced in Figure 3.9b, the sample with the higher  $\text{Co}_3\text{O}_4$  content presented the highest light absorption.

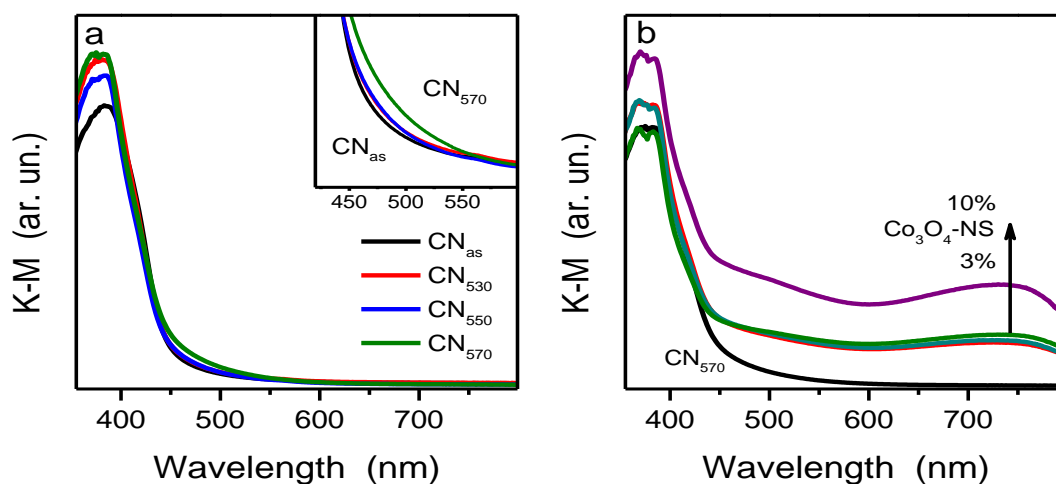


Figure 3. 9: DR UV-vis spectra of (a) the CN samples and (b) the nanocomposites

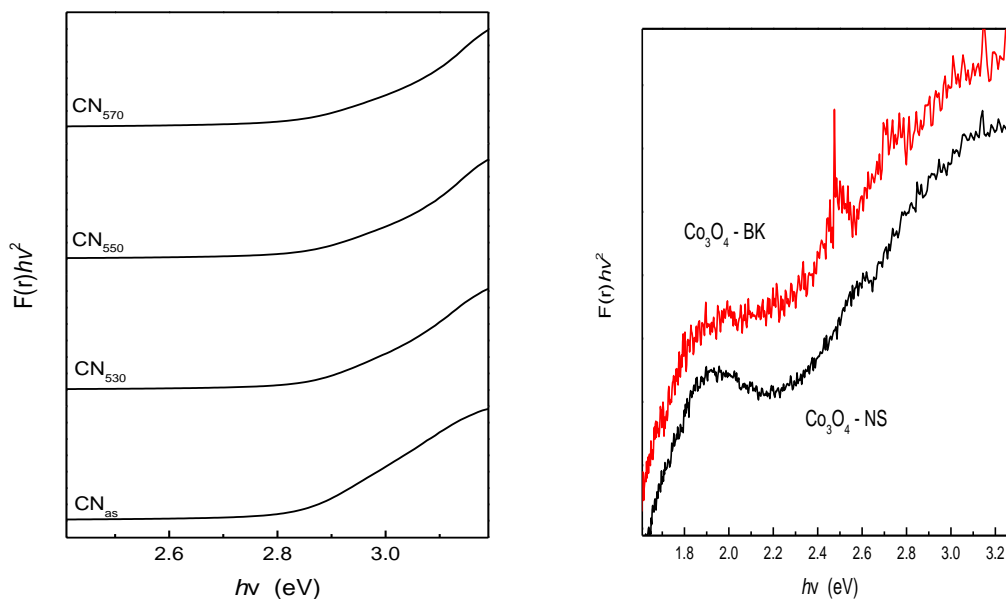


Figure 3. 10 : Plots used to estimate band gap energies of the (a) pure CN materials and (b) the pure  $\text{Co}_3\text{O}_4\text{-BK}$  and  $\text{Co}_3\text{O}_4\text{-NS}$  materials

### I.3. Morphological Characterization

#### SEM

In section 3.1.1., it is shown by XRD characterization that the second thermal treatment of CN materials and the solvothermal treatment of ZIF-67 in the presence of  $\text{Co}^{2+}$  resulted in phase transformation. In order to study the effect on morphology and to further characterize the different phases on the composites, the samples were examined by Scanning Electron Microscopy (SEM) and Transmission Electron Microscopy (TEM). As we can detect in Figure 3.11a the  $\text{CN}_{\text{as}}$  sample possess a bulky morphology and consists of sintered grains. Whereas the thermally treated  $\text{CN}_{570}$  presents smoother and flatter surface. This is in accordance with the suggested from XRD increase in planarization of the structure. Closer inspection reveals cracks, structural defects and micropores with smaller aggregates in the thermally treated materials (Figure 3.11b). Concerning MOF samples, in Figure 3.11c it can be seen that ZIF-67 presents a uniform rhombic dodecahedron structure of approximately 300 nm. These are in accordance with the literature<sup>6</sup>. Modification of the parental ZIF-67 via a solvothermal treatment resulted in a leaf-like 2D structure (Figure 3.11d). The oxides derived from the calcination of the two MOF structures maintain the morphology of their precursors (Figure 3.11e and 3.11f). Calcination of the m-ZIF-67 2D structure results in the formation of the oxide with ultrathin morphology (Figure 3.11f). On the other hand, the  $\text{Co}_3\text{O}_4\text{-BK}$  material inherited the ZIF-67 morphology. These results clearly show the shape control of the oxide induced through the modification of the parent MOF structure used as template. This might

have an effect on the interaction of the oxide with the planar surface of the CN structure<sup>25-27</sup>.

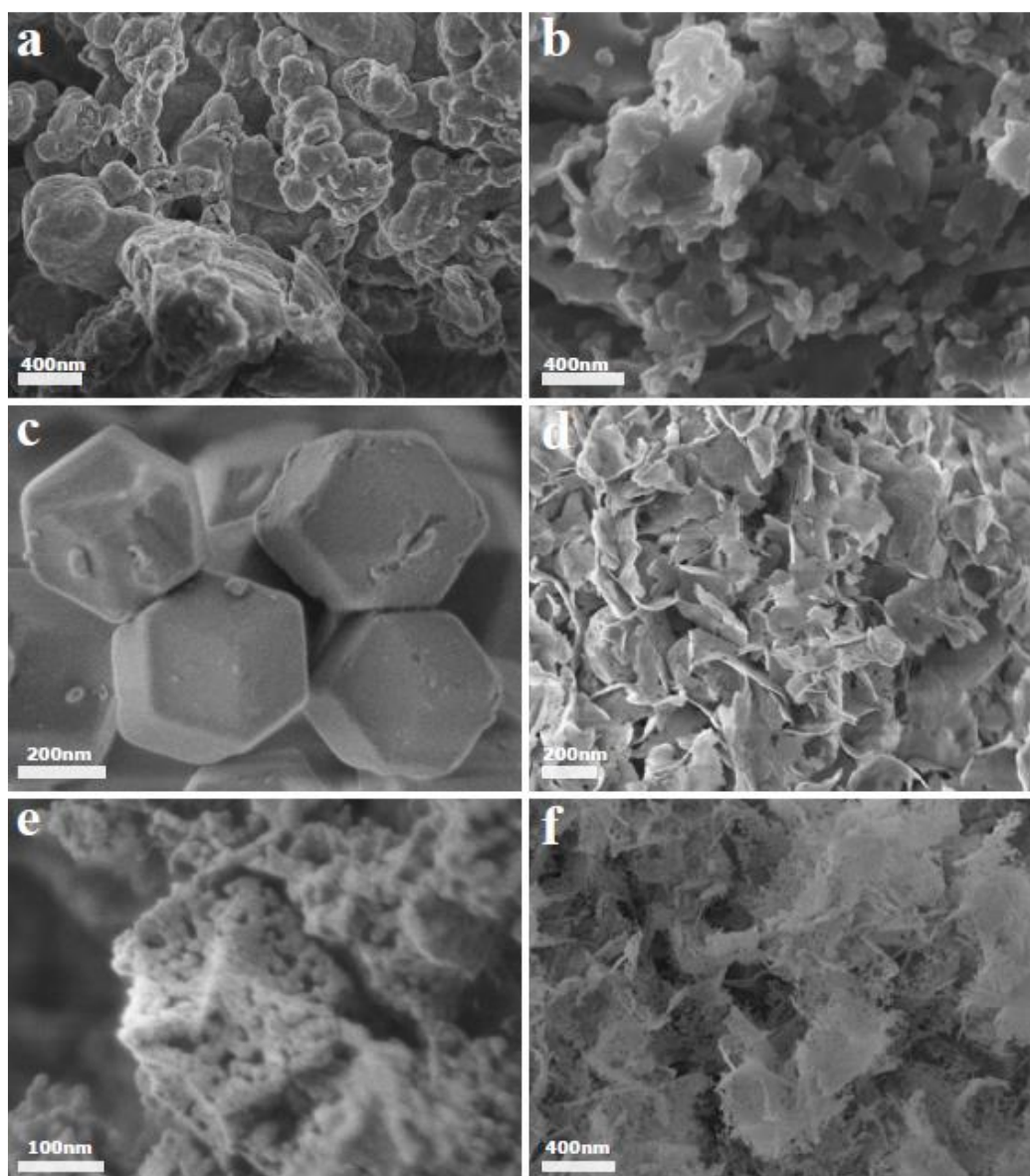


Figure 3. 11: SEM images of (a)  $CN_{os}$ , (b)  $CN_{570}$ , (c) ZIF-67, (d) *m*-ZIF-67, (e)  $Co_3O_4$ -bk and (f)  $Co_3O_4$ -NS

### TEM

TEM images of the prepared pure oxides and the composites are given in Figure 3.12. The 2D ultrathin structure of the  $Co_3O_4$ -NS sample is clearly observed together with many mesopores (Figure 3.12b). These defects in the structure are not seen in the  $Co_3O_4$ -Bk sample (Figure 3.12a). Concerning the nanocomposite materials, the morphology of both oxides is maintained in the composite as indicated in Figure 3.12c and 3.12d. Another observation that can be made is that  $Co_3O_4$ -NS are well dispersed on CN with their lateral side interacting with the planar surface of  $CN_{570}$  (Figure 3.12d). This suggests the formation of an interphase between the 2D

structure of  $\text{Co}_3\text{O}_4$ -NS and the surface of CN. On the contrary, larger aggregates are observed when using the  $\text{Co}_3\text{O}_4$ -Bk, as in the case of the  $\text{Co}_3\text{-Bk-CN}_{570}$  composite (Figure 3.12c). The high-resolution TEM images indicate the well crystallized structures of the oxide. In the  $\text{Co}_3\text{O}_4$ -Bk sample (Figure 3.12e), primary nanoparticles of different crystallographic orientation are observed and lattice fringes with an interspacing of 0.46 and 0.24 nm are detected. These are indexed to the (111) and (311) planes, respectively<sup>28,29</sup>. The lattice spacing of 0.280 and 0.235 nm resolved in the  $\text{Co}_3\text{O}_4$ -NS sample correspond to the (220) and (222) crystal planes, respectively (Figure 3.12f)<sup>7,18,28,30</sup>. This suggests that the dominant exposed planes are {112} in the  $\text{Co}_3\text{O}_4$ -NS sample, since they are the only planes normal to both (220) and (222) planes. {112} are the usual main exposed planes in 2D  $\text{Co}_3\text{O}_4$  structures<sup>28,31,32</sup>. The presence of  $\text{Co}_3\text{O}_4$  on CN was also evidenced by TEM-EDX analysis (Figure 3.13). The pure  $\text{Co}_3\text{O}_4$ -NS EDX spectrum is dominated by Co and O atoms while in the  $\text{Co}_7\text{-NS-CN}_{570}$  material C and N are also detected. Overall, the TEM analysis verified the formation of  $\text{Co}_3\text{O}_4$  crystals of nanosheet morphology when the solvothermally treated m-ZIF-67 is used as precursor and suggested the formation of a tight interphase between the 2D structure of the  $\text{Co}_3\text{O}_4$ -NS and the planar surface of CN.

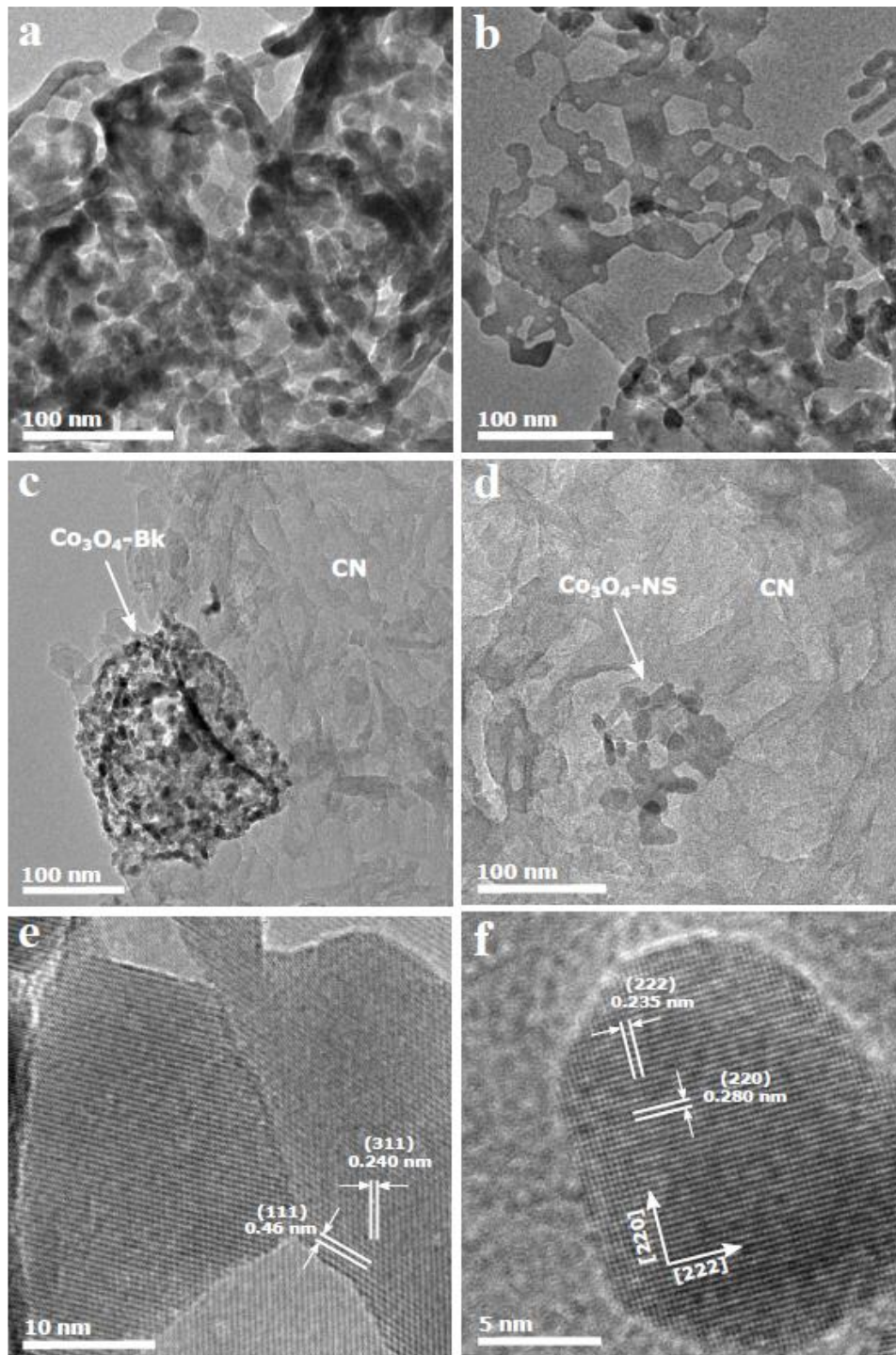


Figure 3. 12: TEM images of (a)  $\text{Co}_3\text{O}_4\text{-Bk}$ , (b)  $\text{Co}_3\text{O}_4\text{-NS}$ , (c)  $\text{Co}_7\text{-bk-CN}_{570}$ , (d)  $\text{Co}_7\text{-NS-CN}_{570}$  and HRTEM images of (e)  $\text{Co}_3\text{O}_4\text{-Bk}$  and (f)  $\text{Co}_3\text{O}_4\text{-NS}$ .

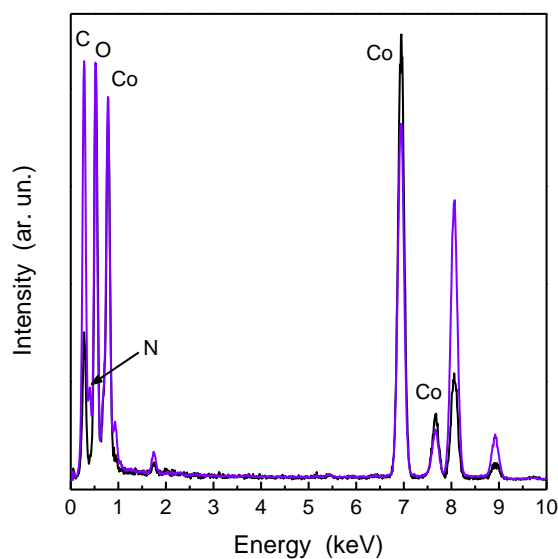


Figure 3. 13: EDX spectra of the pure  $\text{Co}_3\text{O}_4\text{-NS}$  material (black line) and the  $\text{Co}_7\text{-NS-CN}_{570}$  composite (purple line). The peaks in the 8-9 keV region correspond to Cu-grid used.

#### 1.4. Characterization of electronic properties-Studies of Charge carriers' behavior

##### *Transient absorption Spectroscopy (TAS)*

TAS has previously been used to monitor charge carrier behavior in a range photocatalytic materials, including carbon nitrides<sup>3,4,25,33</sup>. Herein, we employ TAS to investigate the charge carrier behavior in carbon nitride ( $\text{CN}_{570}$ ), cobalt oxide ( $\text{Co}_3\text{O}_4\text{-NS}$  and  $\text{Co}_3\text{O}_4\text{-BK}$ ) and their composites ( $\text{Co}_3\text{-NS-CN}_{570}$ ,  $\text{Co}_3\text{-BK-CN}_{570}$ ). Samples are investigated in air, excited using a 355 nm laser. The transient absorption decay kinetics at different wavelengths and spectra at select times of each individual sample are provided in Figure 3.14 and Figure 3.15, respectively. In order to compare the transient absorption behavior of all samples, the normalized transient absorption decay kinetics at a probe wavelength of 800 nm are gathered in Figure 3.16a, and transient absorption spectra at 10  $\mu\text{s}$  (Figure 3.16b), 1 ms (Figure 3.16c) and 100 ms (Figure 3.16d) after excitation.

At most probe wavelengths, the modified carbon nitride -  $\text{CN}_{570}$  - showed exponential decay dynamics on a log timescale, similar to previous works<sup>4</sup>. This type of decay follows dispersive power law dynamics, which have been assigned to trap/detrap limited bimolecular recombination<sup>34,35</sup>. From 10  $\mu\text{s}$ , the time taken for half of the charge carriers to recombine ( $t_{50\%}$ ) was  $\sim 1$  ms (Figure 3.14a). Transient absorption spectra show a broadband absorption across the visible, with stronger

absorption in the blue than in the red (Figure 3.15a). Both forms of cobalt oxide -  $\text{Co}_3\text{O}_4\text{-NS}$  and  $\text{Co}_3\text{O}_4\text{-BK}$  - show similar transient absorption behavior. In this case, electron-hole recombination was significantly faster, with transient decays showing a  $t_{50\%}$  of  $\sim 50 \mu\text{s}$  (approximately 20 times faster than  $\text{CN}_{570}$ ), which decay to zero by  $\sim 1 \text{ ms}$  (Figures 3.14d and e). Transient absorption spectra exhibit a distinct peak absorption at  $\sim 800 \text{ nm}$ , and near zero absorption in the blue and NIR (Figures 3.15d and e). For the cases of the carbon nitride and cobalt oxide composites -  $\text{Co}_3\text{-NS-CN}_{570}$ ,  $\text{Co}_3\text{-BK-CN}_{570}$  - similar behavior is observed in both materials. The transient absorption decays in these composites are similar to that of the pure carbon nitride, showing a  $t_{50\%}$  of  $\sim 0.5 \text{ ms}$  (Figures 3.14b and c). However, the transient absorption spectra hold features of both the CN (broadband absorption) and  $\text{Co}_3\text{O}_4$  (peak at  $800 \text{ nm}$ ) (Figures 3.14b and c). Importantly, the  $\text{Co}_3\text{O}_4$  spectral feature is significantly longer lived in these composites than in the parent materials. We can see this by comparing transient absorption spectra at  $10 \mu\text{s}$  (Figure 3.16b),  $1 \text{ ms}$  (Figure 3.16c) and  $100 \text{ ms}$  (Figure 3.16d) after excitation. In the cobalt oxides and the composites, a peak at  $\sim 800 \text{ nm}$ , which is attributed to charge carriers on  $\text{Co}_3\text{O}_4$ , is clearly observed at  $10 \mu\text{s}$  after excitation. However, at  $1$  and  $100 \text{ ms}$  after excitation, this peak is lost in the cobalt oxides but remains in the composites. This shows that charge carriers on cobalt oxide sites in the composites have an extended lifetime of more than a factor of 100 as compared with cobalt oxide alone. Across all timescales, the  $\text{Co}_3\text{-NS-CN}_{570}$  composite show higher absorption in the red than the  $\text{Co}_3\text{-BK-CN}_{570}$  composite, which is indicative of a higher degree of charge carriers present on cobalt oxide sites in  $\text{Co}_3\text{-NS-CN}_{570}$  as compared with the  $\text{Co}_3\text{-BK-CN}_{570}$ . On the other hand, charge carrier lifetime on carbon nitride sites in the composites do not differ significantly from the parent material.

### CHAPTER 3

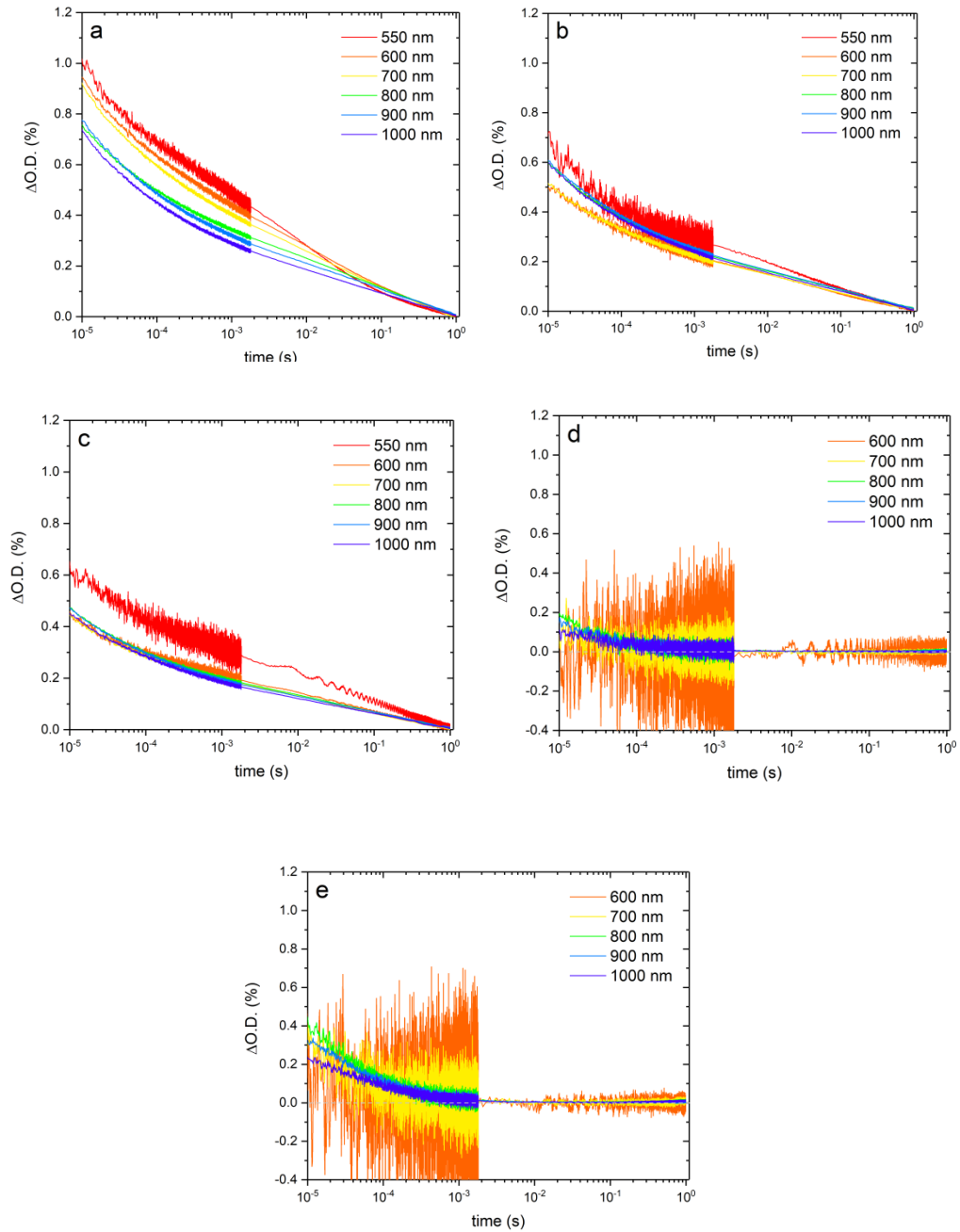


Figure 3. 14 : Transient absorption decay kinetics of (a)  $CN_{570}$ , (b)  $Co_3-NS-CN_{570}$ , (c)  $Co_3-BK-CN_{570}$ , (d)  $Co_3O_4-NS$  and (e)  $Co_3O_4-BK$ . Samples were measured in air, excited with a 355 nm laser pulse ( $\sim 6$  ns pulse width,  $\sim 0.0.63$  mJ cm $^{-2}$ , 0.8 Hz) and transient changes in absorption were probed at 550 to 1000 nm from 10  $\mu$ s to 1 s.

## CHAPTER 3

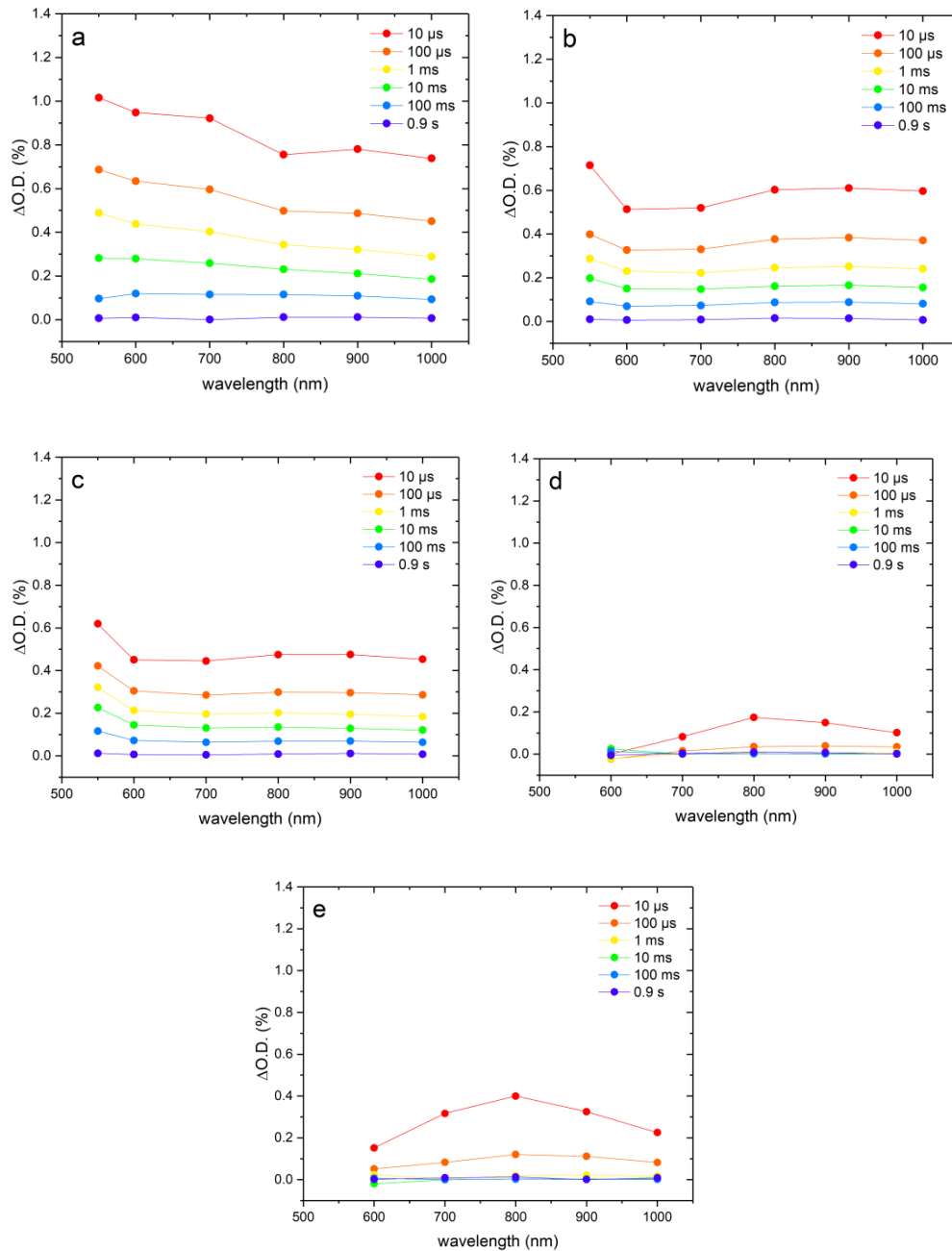


Figure 3.15: Transient absorption spectra at the select times of 10  $\mu$ s, 100  $\mu$ s, 1 ms, 10 ms, 100 ms and 0.9 s after excitation of (a)  $CN_{570}$ , (b)  $Co_3NS-CN_{570}$ , (c)  $Co_3BK-CN_{570}$ , (d)  $Co_3O_4-NS$  and (e)  $Co_3O_4-BK$ . Samples were measured in air, excited with a 355 nm laser pulse ( $\sim 6$  ns pulse width,  $\sim 0.0.63$  mJ  $cm^{-2}$ , 0.8 Hz) and transient changes in absorption were probed at 550 to 1000 nm from 10  $\mu$ s to 1 s.

Qualitatively speaking, the spectra observed in the composites are not the sum of the spectra of the two parent materials from which they are composed. This is because the composite contains only a small amount of cobalt oxide (3 wt.%), yet the spectra obtained contain similar contributions from cobalt oxide as compared with the parent materials (100 wt.%). For this to occur, there must be charge transfer between the two phases in the composite.

Overall, transient absorption spectroscopy results suggest the presence of a charge transfer between CN and  $\text{Co}_3\text{O}_4$  in the composites resulting in significantly longer-lived charges on cobalt oxide sites compared with the cobalt oxide parent material (extended lifetime from  $\sim 1$  ms to  $> 100$  ms). Comparing the two composites, there is a higher degree of absorption in the red region of the electromagnetic spectrum in  $\text{Co3-NS-CN}_{570}$  than  $\text{Co3-BK-CN}_{570}$ , which is indicative of a higher degree of charge transfer where cobalt oxide nanosheets are used as compared with the bulk material. In other words, the TAS data suggest that the morphology of the cobalt oxide affects the charge transfer process.

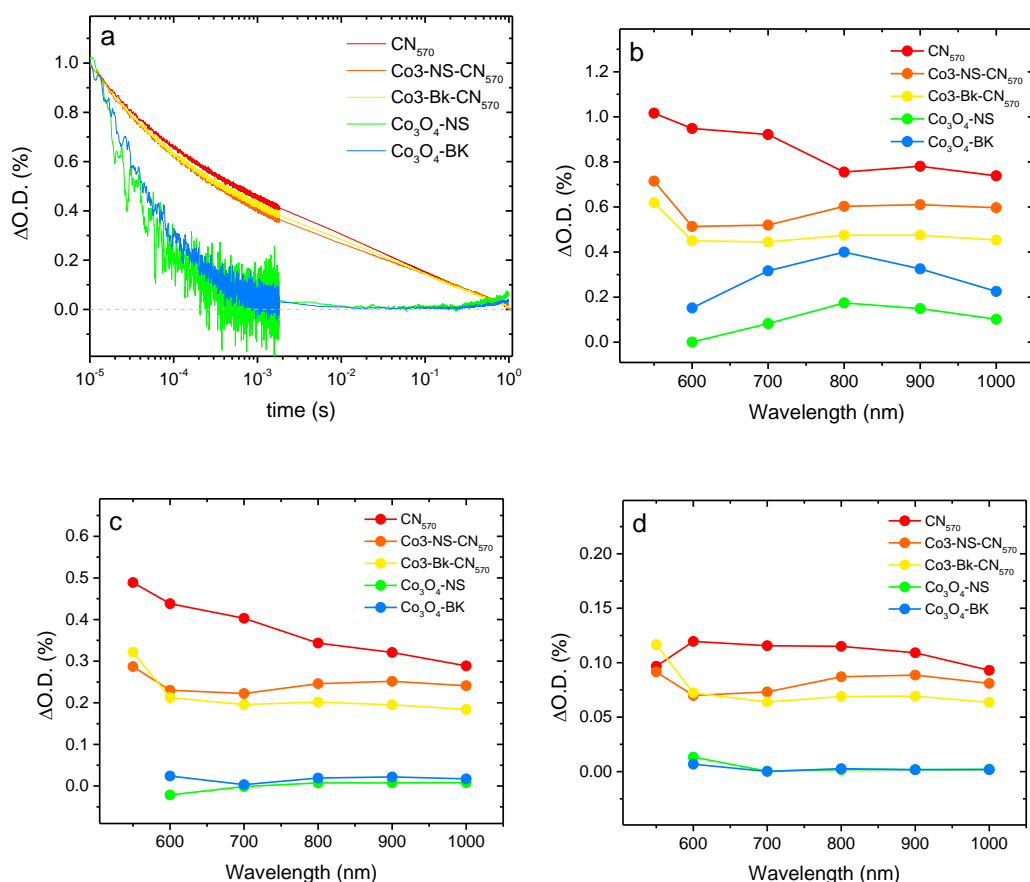


Figure 3. 16: (a) Normalized transient absorption decay kinetics at the probe wavelength of 800 nm for  $\text{CN}_{570}$ ,  $\text{Co3-NS-CN}_{570}$ ,  $\text{Co3-BK-CN}_{570}$ ,  $\text{Co}_3\text{O}_4\text{-NS}$  and  $\text{Co}_3\text{O}_4\text{-BK}$ . Transient absorption spectra at the select times of (b) 10  $\mu\text{s}$ , (c) 1 ms and (d) 100 ms after excitation for  $\text{CN}_{570}$ ,  $\text{Co3-NS-CN}_{570}$ ,  $\text{Co3-BK-CN}_{570}$ ,  $\text{Co}_3\text{O}_4\text{-NS}$  and  $\text{Co}_3\text{O}_4\text{-BK}$ .

### Electron paramagnetic resonance (EPR) spectroscopy

Since photogenerated charges play crucial role in photocatalysis, in-situ EPR spectroscopy is used to study their formation. EPR it is a versatile tool to detect  $e^-/h^+$  pairs in semiconductors<sup>36,37</sup>. All samples present a single Lorentzian peak centered

at  $g=2.0034$  under light irradiation, typical for unpaired electrons on the aromatic carbons of the main building unit of CN<sup>3,37</sup>. Representative spectra are given in Figure 3.17. The same signal is observed under dark conditions. This signal has been subtracted from all data obtained under light irradiation. Therefore, the reported EPR signal intensity originates from light excitation and indicates the formation of photogenerated species. It must be highlighted that warming the sample at room temperature for 15 min after irradiation reestablishes the EPR intensity at the level of the dark conditions as a result of  $e^-/h^+$  recombination. This further verifies that the observed EPR signal under light irradiation is associated with photogenerated charges.

EPR spectroscopy is also applied to provide quantitative estimates on the charges formed upon irradiation. Figure 3.18a displays the relative EPR signal intensity of the photogenerated electrons for the pure CN<sub>570</sub> and the composites Co3-Bk-CN<sub>570</sub>, Co3-NS-CN<sub>570</sub> and Co7-NS-CN<sub>570</sub>. The introduction of the oxide in both phases (bulk or nanosheets) increased the abundance of the photogenerated electrons. A significant difference in the signal intensity is observed comparing the composites bearing Co<sub>3</sub>O<sub>4</sub>-Bk and Co<sub>3</sub>O<sub>4</sub>-NS. Deposition of Co<sub>3</sub>O<sub>4</sub>-Bk on CN<sub>570</sub> results in a ca. 27% increase of the EPR signal intensity compared with the pure CN<sub>570</sub> catalyst. However, an impressive 2.5-fold increase is evidenced in the Co7-NS-CN<sub>570</sub>. In addition, the content of the Co<sub>3</sub>O<sub>4</sub>-NS also affects the charges formed under irradiation. The Co7-NS-CN<sub>570</sub> composite increases the EPR signal intensity by ca. 16 % compared with the Co3-NS-CN<sub>570</sub>. These results clearly highlight the effect of the Co<sub>3</sub>O<sub>4</sub>-NS content but most importantly, the effect of Co<sub>3</sub>O<sub>4</sub> morphology (bulk vs. nanosheets) on the photogenerated charges.

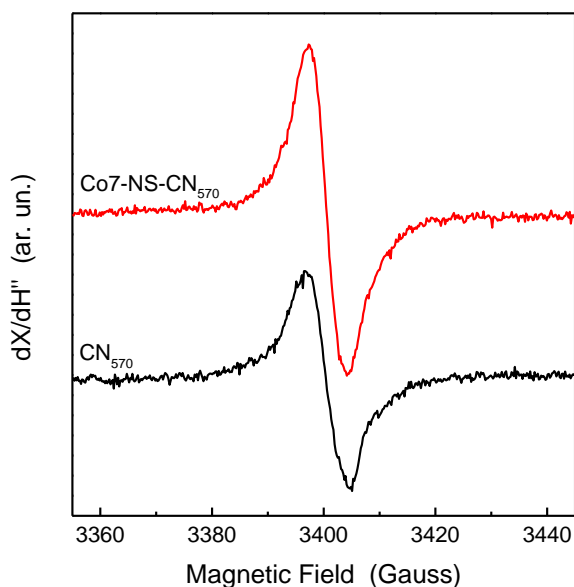


Figure 3. 17: EPR spectra of the pure  $CN_{570}$  and the  $Co7-NS-CN_{570}$  composite under irradiation. 10 mg of the material were irradiated in-situ in the EPR quartz tube using an arc Xenon lamp operating with 450 W input power equipped with a water-filter.

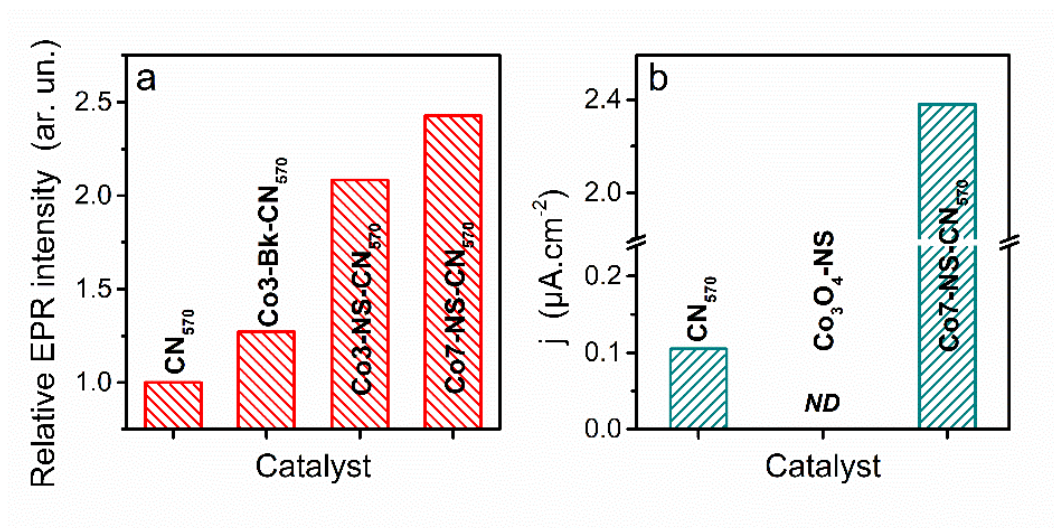


Figure 3. 18: Relative EPR signal intensity (a) and photocurrents at 1.23 V vs RHE (b) of the bare  $CN_{570}$  and composites catalyst.

#### Photoelectrochemical measurements

To further study the photogenerated charges, photoelectrochemical analysis is performed in order to reveal differences in the behavior of charges formed among the different samples upon light irradiation for water splitting. Cyclic voltammetry

curves are given in Figure 3.19 and are performed in alkaline electrolyte as indicated in Chapter 2.II.9., to avoid cobalt oxide dissolution. Figure 3.18b compares the photocurrent of the most active Co7-NS-CN<sub>570</sub> composite with the reference CN<sub>570</sub> and Co<sub>3</sub>O<sub>4</sub>-NS materials at a potential of 1.23V vs RHE. The individual components show no noticeable or low photocurrent while the Co7-NS-CN<sub>570</sub> composite exhibit a significant anodic photocurrent of 2.3  $\mu\text{A}\cdot\text{cm}^{-2}$  associated to water oxidation with an onset potential at 0.9 V vs RHE. The low photocurrent for CN<sub>570</sub> can be explained by the high position of the valence band (relatively to the OER) and their low catalytic activity for OER. In the case of Co<sub>3</sub>O<sub>4</sub> nanosheets no photocurrent is measured. The 20 times enhanced photocurrent for the composite suggests an improved charge separation at the interface between CN and cobalt-based material. These data infer that oxidative reaction rates are improved in the Co7-NS-CN<sub>570</sub> catalyst most likely due to the formation of a heterojunction that results in efficient charge separation <sup>4</sup>.

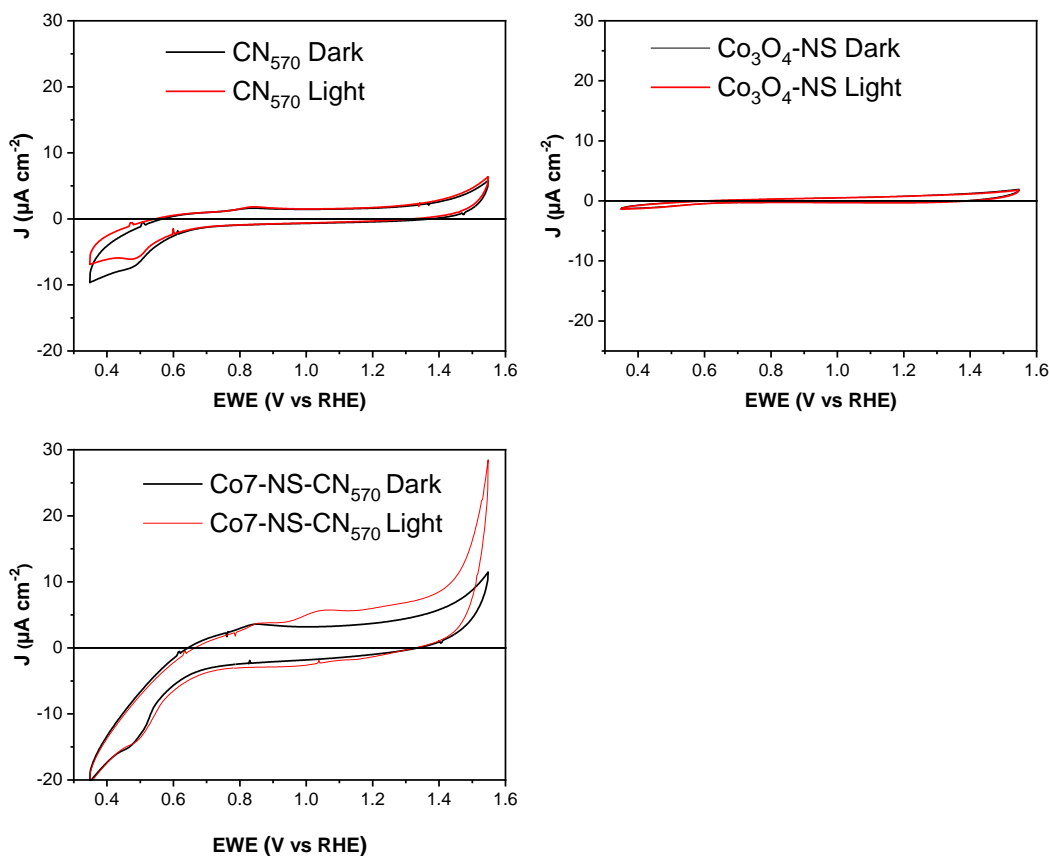


Figure 3. 19: Cyclic Voltammetry curves performed in alkaline electrolyte (0.01 M NaOH, 0.1 M Na<sub>2</sub>SO<sub>4</sub>) at a 10  $\text{mV s}^{-1}$  of the CN<sub>570</sub>, Co<sub>3</sub>O<sub>4</sub>-NS and the Co7-NS-CN<sub>570</sub> nanocomposite under dark and illumination conditions. (Xe arc lamp Newport; 300W; equipped with AM1.5G filter; incident power density on the cell 100  $\text{mW cm}^{-2}$ ).

## II. Photocatalytic activity of $\text{Co}_3\text{O}_4\text{-CN}$ nanocomposites

### II.1. $\text{CO}_2$ photoreduction results

All prepared materials were applied as catalysts for the photocatalytic reduction of  $\text{CO}_2$  in the gas phase at ambient temperature, using  $\text{H}_2$  as the electron donor. Under these conditions, only  $\text{CO}$  is detected in the gas phase. The results are shown in Figure 3.20-3.21. The activity of the pure CN materials was first evaluated. As seen in Figure 3.20, among the different pure CN materials prepared, the one treated at the highest temperature ( $\text{CN}_{570}$ ) presents the highest  $\text{CO}$  production rate. Specifically, an approximately 55 % increase of the  $\text{CO}$  production rate is observed compared with the as-synthesized CN. This has been previously seen in similar materials and has been attributed to structural and electronic modifications induced through the second thermal treatment<sup>4</sup>. Based on these findings, the  $\text{CN}_{570}$  material was chosen for the development of composites through the coupling with cobalt oxides.

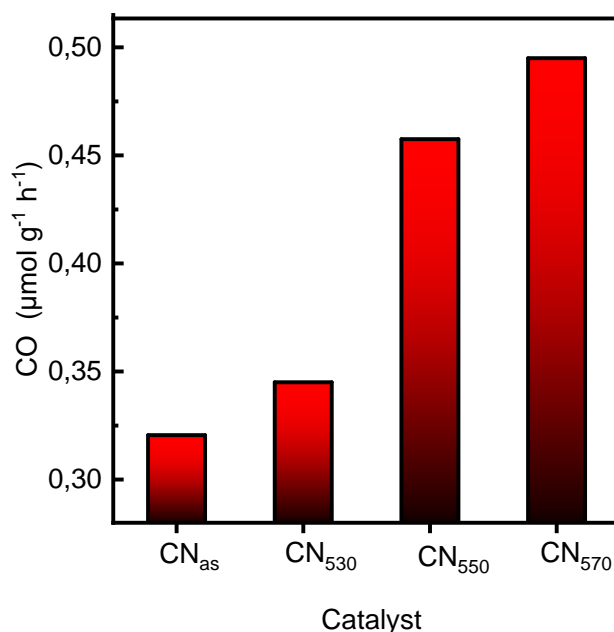


Figure 3. 20: Photocatalytic  $\text{CO}$  production rates by pure CN catalysts

Then, the pure oxides and the composite materials were tested. No  $\text{CO}$  evolution is observed when using the  $\text{Co}_3\text{O}_4\text{-Bk}$  material. On the contrary, the  $\text{Co}_3\text{O}_4\text{-NS}$  presents some activity, however, low (Figure 3.21). Nevertheless, this observation highlights the importance of morphology in the catalytic activity that induces further electronic modifications expressed on the  $\text{Co}^{2+}/\text{Co}^{3+}$  relative surface abundance. Recently, the increased  $\text{Co}^{2+}/\text{Co}^{3+}$  ratio in  $\text{Co}_3\text{O}_4$  nanosheets has been shown beneficial in  $\text{CO}_2$

photocatalytic reduction through electron donation to adsorbed CO<sub>2</sub> molecules<sup>19</sup>. The Co3-Bk-CN<sub>570</sub> composite presents a moderate activity matching the activity of the bare CN<sub>570</sub> catalyst. For comparison, the activity of the pure CN<sub>570</sub> is also given in Figure 3.22. More importantly, CO evolution is increased by ca. 35% when using the Co3-NS-CN<sub>570</sub> composite compared with the CN<sub>570</sub> catalyst. Focusing on materials properties, this observation offers two important information. First, the detected catalytic activity increase in the Co3-NS-CN<sub>570</sub> catalyst is solely attributed to the Co<sub>3</sub>O<sub>4</sub> morphology and not to any changes induced to CN originating from other parts of the MOF structure. Second, it highlights the critical role of Co<sub>3</sub>O<sub>4</sub> morphology on the activity of the composite. Based on these results, the effect of the Co<sub>3</sub>O<sub>4</sub>-NS content in the composites was studied in detail.

The rate of CO production is progressively increased using the Co5-NS-CN<sub>570</sub> and Co7-NS-CN<sub>570</sub> composites, with the latest presenting an impressive 2-fold increased CO evolution rate compared with the pure CN<sub>570</sub>. Further increase of the Co<sub>3</sub>O<sub>4</sub>-NS content results in a decrease of the photoactivity, however, still 70% higher than the bare CN<sub>570</sub> catalyst (Figure 3.21). The observed decrease may originate from the overloading with Co<sub>3</sub>O<sub>4</sub> as it has been seen in many other composite materials<sup>2</sup>. The results of the photocatalytic CO<sub>2</sub> reduction using the prepared composites are in line with recent contributions in the literature where Co<sub>3</sub>O<sub>4</sub> composites including oxygen deficient Co<sub>3</sub>O<sub>4</sub> were coupled with light sensitizers<sup>6,38,39</sup>. Light sensitizers such as metal complexes are not stable under working conditions with obvious disadvantages for practical application. It must be highlighted that, herein, no light sensitizers are used and oxygen vacancies in Co<sub>3</sub>O<sub>4</sub> are formed as a result of the morphology control.

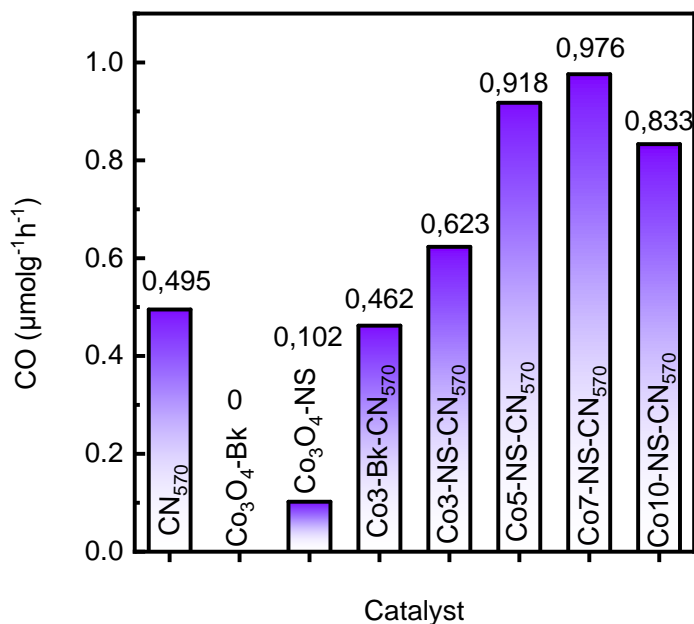


Figure 3. 21: Photocatalytic CO production rates by the pure cobalt oxide catalysts and nanocomposites bearing Co<sub>3</sub>O<sub>4</sub>-Bk and Co<sub>3</sub>O<sub>4</sub>-NS

So far, the catalytic data clearly suggest that the morphology at the nanoscale of the Co<sub>3</sub>O<sub>4</sub> affects the CO<sub>2</sub> reduction ability of the pure oxide but, most importantly, has a large impact on the activity of the prepared composites. It is well known that photocatalytic activity is governed by many parameters. Among these parameters, the charge handling ability and the interaction with the substrate are considered essential<sup>40–42</sup>. The photocatalytic results are in accordance with the observations of TAS, EPR spectroscopy and photoelectrochemical analysis. Specifically, the enhanced lifetime of charge carriers by efficient charge separation in the composite materials played a key role in the improvement of their photocatalytic activity. Also, the superior CO<sub>2</sub> adsorption properties of the composite materials, as shown by TPD technique, enhanced the overall CO<sub>2</sub> reduction process.

Furthermore, the influence of the electron donor for the CO<sub>2</sub> conversion reaction is also studied. Herein, a reaction with H<sub>2</sub>O vapor as reducing agent is performed for the most active photocatalyst (Co7-NS-CN<sub>570</sub>). As can be observed in Figure 3.22, CO and H<sub>2</sub> are detected at rates 0.58 μmol g<sup>-1</sup> h<sup>-1</sup> and 0.35 μmol g<sup>-1</sup> h<sup>-1</sup>. The detected CO rate observed under these conditions corresponds to the ca. 60% of the CO produced when using H<sub>2</sub> as the electron donor. In this case, the photogenerated electrons are consumed by two competitive reactions, the CO<sub>2</sub> reduction and the H<sub>2</sub>O splitting reaction. As it is already mentioned in [Chapter 1.II.5.B.ii.b](#), the latter one is more favorable due to the lower number of electrons that are required.

However, it is important to highlight that under these conditions the catalyst remains selective to CO (ca. 62%).

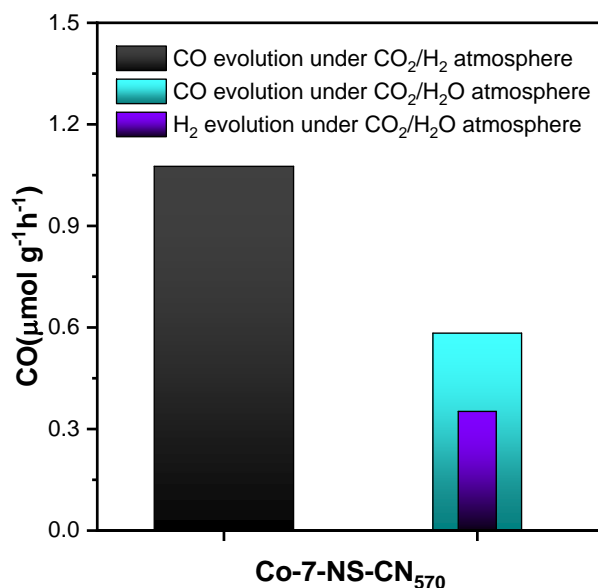


Figure 3. 22: Photocatalytic results of  $\text{CO}_2$  reduction with water as electron donor for  $\text{Co}_7\text{-NS-CN}_{570}$

In order to elucidate the factors that control  $\text{CO}_2$  reduction, a series of reference reactions were performed (Figure 3.23). No improvement in photoactivity is observed using composite materials prepared through the coupling of  $\text{CN}_{570}$  with ZIF-67 or m-ZIF-67 (i.e., the precursors of  $\text{Co}_3\text{O}_4\text{-Bk}$  and  $\text{Co}_3\text{O}_4\text{-NS}$ ) compared with the bare  $\text{CN}_{570}$ . This verifies that formation of the  $\text{Co}_3\text{O}_4$  phase in the composites plays a critical role in activity. In all reference reactions, e.g., in the absence of catalyst, light or  $\text{CO}_2$ , no CO is detected. Special attention must be given to the reference reaction performed using the most active catalyst ( $\text{Co}_7\text{-NS-CN}_{570}$ ) under identical conditions but in the absence of  $\text{CO}_2$  (i.e.,  $\text{Ar}/\text{H}_2$  atmosphere) that resulted in no CO evolution. This clearly shows that the observed CO in the catalytic reactions originates from the reduction of  $\text{CO}_2$  and not from any side reactions on the surface of the catalyst.

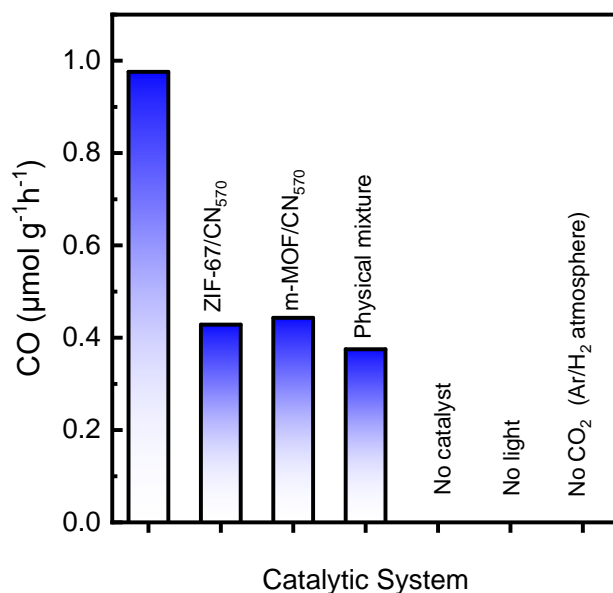


Figure 3. 23: Photocatalytic CO production rates by the reference reactions.

## II.2. Photocatalytic H<sub>2</sub>O splitting results

The developed materials were also tested in the photocatalytic hydrogen evolution reaction using Pt as co-catalyst (protocol described in [Chapter 2](#)) and TEOA as the electron donor. These reactions were performed in the liquid phase (i.e., in water/TEOA 100/1 v/v) in the setup previously presented. The results are given in Figure 3.24. In agreement with the literature<sup>4,43,44</sup>, thermal modification of the as-synthesized CN results in a ca. 18 % enhanced H<sub>2</sub> production rate while the Co7-NS-CN<sub>570</sub> catalyst further increased activity by ca. 35 % with respect to the pure CN<sub>570</sub>.

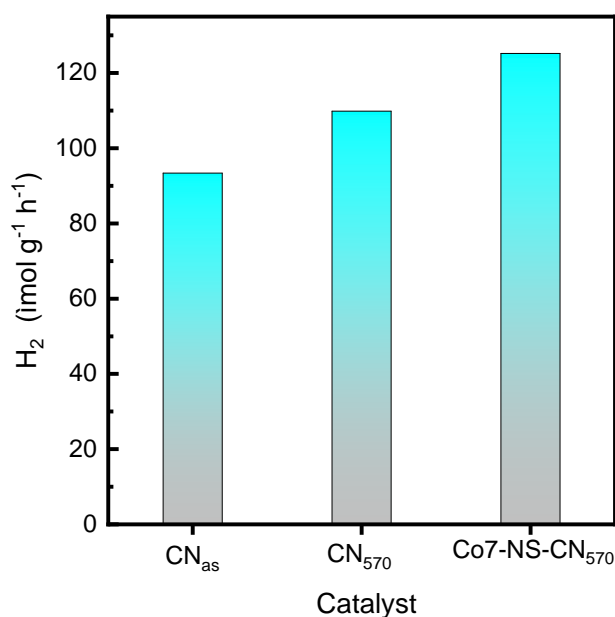


Figure 3. 24: H<sub>2</sub> production rates by the CN<sub>as</sub>, CN<sub>570</sub> and Co7-NS-CN<sub>570</sub> catalysts using Pt as co-catalyst and TEOA as sacrificial agent.

### II.3. Proposed mechanism

According to the above results, charge availability is increased and a charge transfer between the two phases is suggested upon formation of the composite. To further study the charge transfer mechanism, in-situ spin trap EPR spectroscopy experiments were realized using DMPO as spin trap. The EPR signals are depicted in Figure 3.25, and the conditions of the experiment were mentioned in Section 2.II.11. Both CN<sub>570</sub> and Co7-NS-CN<sub>570</sub> methanolic suspensions presented a six-line spectrum characteristic of the DMPO-O<sub>2</sub><sup>•-</sup> spin-adduct under light irradiation<sup>45</sup>. These data clearly indicate that both materials were able to produce O<sub>2</sub><sup>•-</sup> under irradiation. Specifically, the intensity of the DMPO-O<sub>2</sub><sup>•-</sup> spin-adduct EPR signal of the Co7-NS-CN<sub>570</sub> composite was enhanced by ca. 1.4 times compared with the reference CN<sub>570</sub>. This suggests an improvement in the photogenerated e<sup>-</sup> in the composite. The standard redox potential O<sub>2</sub>/O<sub>2</sub><sup>•-</sup> couple is -0.33eV<sup>46</sup>. Therefore, the detection of O<sub>2</sub><sup>•-</sup> verifies the ability of both pure CN<sub>570</sub> and composite materials to reduce H<sup>+</sup> and CO<sub>2</sub><sup>47</sup>.

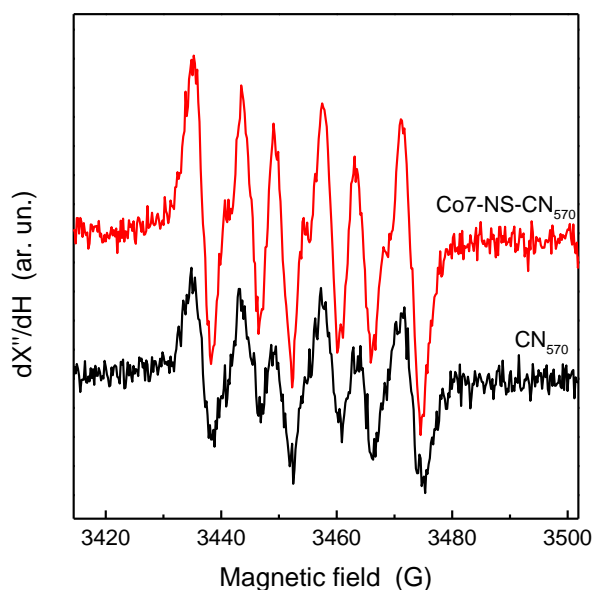


Figure 3. 25: DMPO spin-trapping EPR spectra of the  $\text{CN}_{570}$  and the  $\text{Co7-NS-CN}_{570}$  materials in methanol dispersion for the detection of the  $\text{DMPO-O}_2^{\cdot -}$  spin-adduct.

As explained in Section 1.II.4.B.ii., when heterojunction formation is achieved the two types of heterojunctions can occur. In order to determine if it is a type-II heterojunction or a Z-Scheme heterojunction, it is prerequisite to know the bandgap structure of the counterparts. Due to the presence of  $\text{NH/NH}_2$  groups as electron donors, CN is a typical n-type semiconductor and similar MOF-derived  $\text{Co}_3\text{O}_4$  NS have been developed and ascribed as n-type semiconductive nanomaterials in recent studies<sup>48–50</sup>. Based on previous reports in the literature, for the pristine CN the CB and the VB are estimated  $\sim -1.1$  and  $1.6$  V (vs.NHE) at  $\text{pH} = 0$ , respectively. For the case of 2D  $\text{Co}_3\text{O}_4$  nanomaterials, the band structure is  $-0.7$  V for CB minimum and  $1.65$  V (vs. NHE) for VB maximum<sup>31,51</sup>, implying that a Type-II heterojunction may be formed. In such heterojunctions, photogenerated charges are spontaneously transferred at different parts of the composite via the interface formed. Recent studies in similar  $\text{Co}_3\text{O}_4/\text{CN}$  composites have also demonstrated a Z-scheme charge transfer mechanism<sup>46,52,53</sup>. Both charge transfer mechanisms could lead to improved charge separation efficiency, reducing charge recombination phenomena. This charge transfer mechanism improves charge separation, as demonstrated by TAS, EPR and electrochemical analysis and, therefore, enhances the lifetime of charges that drive photocatalytic reactions. The increased lifetime and the decreased charge recombination rate in the composites has crucial effect in both  $\text{CO}_2$  reduction and  $\text{H}_2$  production. In the specific case of  $\text{CO}_2$  reduction, the improved activity is also linked with the enhanced  $\text{CO}_2$  adsorption at the  $\text{Co}_3\text{O}_4\text{-NS}$  site where also accumulation of

photogenerated charges takes place due to the charge transfer mechanism in the heterojunction <sup>21,41</sup>. Based on the above analysis, the enhanced CO<sub>2</sub> reduction in composites bearing Co<sub>3</sub>O<sub>4</sub>-NS is attributed to the combined material features related to the increased lifetime of charges and CO<sub>2</sub> adsorption. These properties are controlled by the thermal modification of CN, the content of the oxide and the morphology of the Co<sub>3</sub>O<sub>4</sub> at the nanoscale.

#### II.4. Photocatalyst stability test

It is of high importance that the catalyst can be recycled and retain its activity after several cycles of reactions. Therefore, the most active photocatalyst was used 5 times, and the result of the activity are shown in figure 3.26a. It can be seen that the prepared catalyst (Co7-NS-CN<sub>570</sub>) presents no significant deactivation in the photocatalytic performance after 5 consecutive photocatalytic runs. Namely, an activity loss of approximately 10% is observed. The stability is also evidenced by the kinetic data in Figure 3.26b that shows a linear progression for both the fresh catalyst and the fifth run.

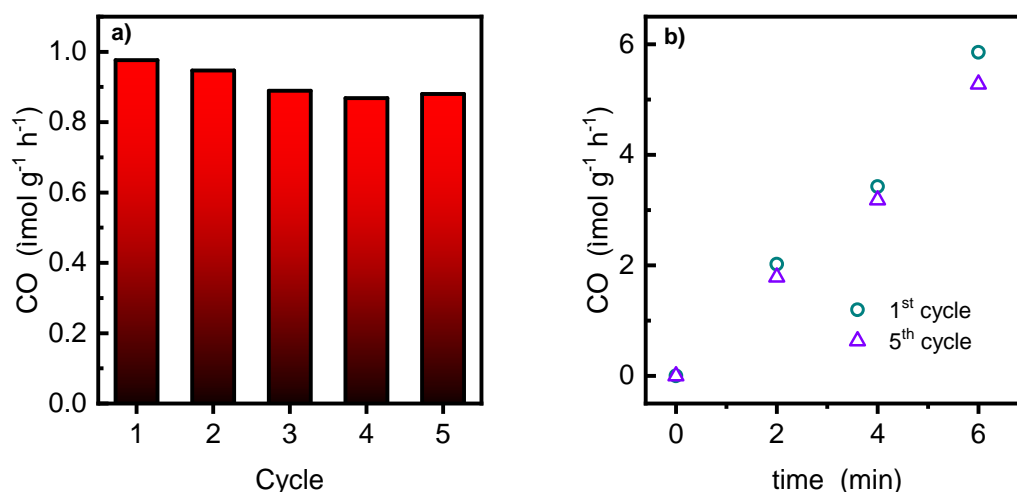


Figure 3. 26 : Photocatalytic CO production rates by: a) recycling reactions performed using the most active Co7-NS-CN<sub>570</sub> catalyst and b) CO evolution over a 6 h reaction time under UV-vis illumination for the fresh and the used for 5 times Co7-NS-CN<sub>570</sub> catalyst.

Furthermore, by definition catalyst is a substance or a material that increases the rate of a chemical reaction without itself undergoing any permanent chemical change. Therefore, it is crucial to ensure that after the catalytic reaction the photocatalyst is not degraded and not altered chemically. To confirm its photocatalytic stability, in addition to the recycling photocatalytic tests one needs to perform post-reaction characterization. Specifically, in order to investigate this, post

## CHAPTER 3

structural and chemical characterization after the 5<sup>th</sup> consequent test was realized by means of TGA, XPS and ATR. Namely, as it is depicted in Figure 3.27a, the  $\text{Co}^{2+}/\text{Co}^{3+}$  ratio as well as the  $\text{Co}_3\text{O}_4$  content on the material was eventually unaltered (Figure 3.27b). In addition, as seen in the ATR spectra displayed in Figure 3.27c, all characteristic peaks of the composites were maintained, indicating that the catalytic test didn't induce any modification on the photocatalyst properties.

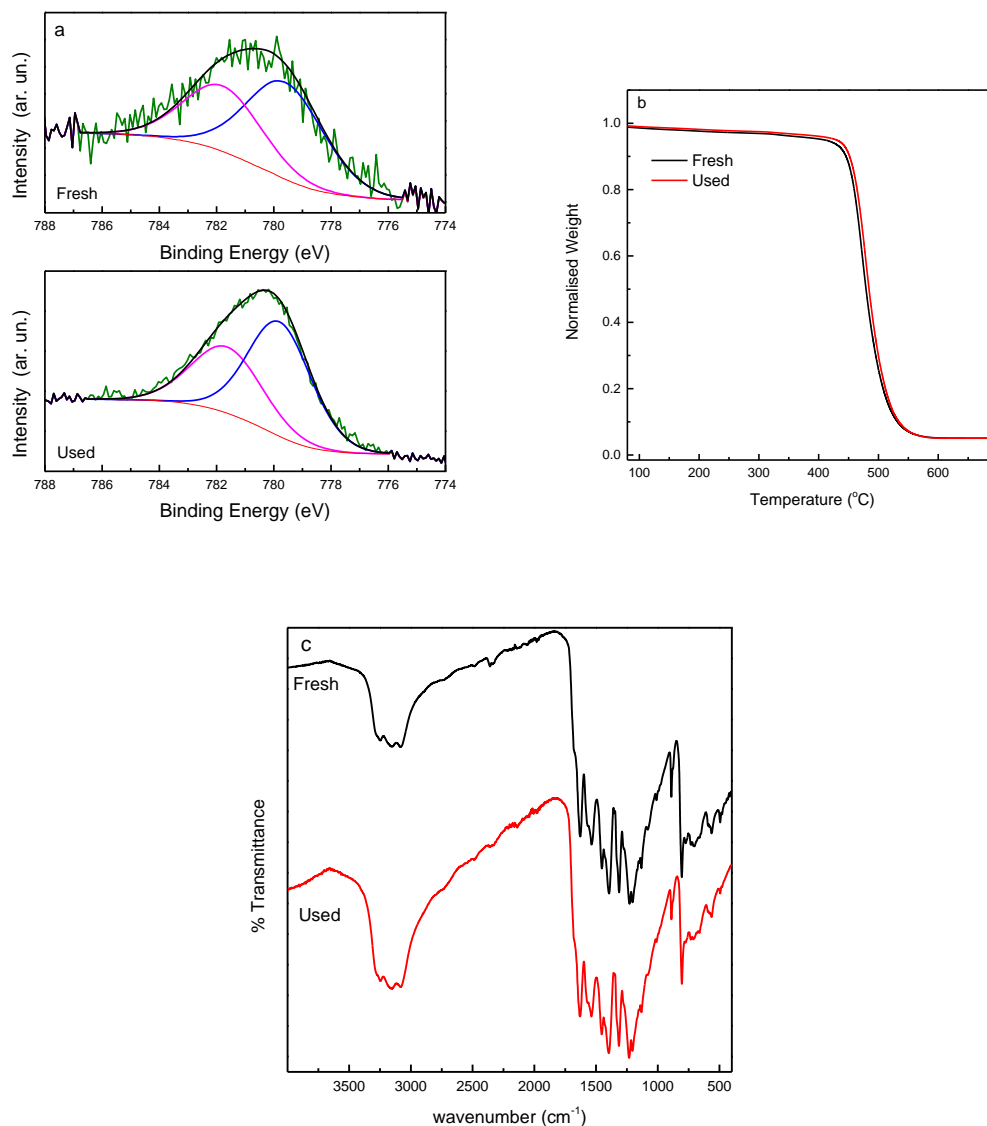


Figure 3. 27: Characterization of the Co7-NS-CN<sub>570</sub> catalyst used after five consecutive times: (a) XPS, (b) TGA, (c) ATR.

### III. Conclusions

Novel  $\text{Co}_3\text{O}_4/\text{CN}$  composite materials have been successfully synthesized and optimized towards improved photoactivity for both  $\text{CO}_2$  reduction and  $\text{H}_2$  production, i.e., artificial photosynthesis. The optimization of the composite included modification of both parts. Initially, CN materials were successfully synthesized by thermal polycondensation of melamine. Following a second thermal treatment, a better planarization of the layers was achieved. This has been shown by information provided by XRD patterns and SEM images. Especially, it is more pronounced for the sample that has been thermally treated at  $570^\circ\text{C}$ . Besides morphology, a modification of the carbon nitride related with the abundance of terminal  $-\text{NH}_2$  groups was evidenced based on ATR and XPS N 1s spectra. Specifically, the intensity of the bands corresponding to N–H bonds is increased gradually as the temperature of the treatment is increased. Theoretical deconvolution revealed that the peak attributed to N- $\text{H}_2$  species presents a double area for the XPS spectra of  $\text{CN}_{570}$ , compared to pristine CN. The adapted modification process induced also a 3-fold increase of the total available specific surface area, which, in combination with the more abundant basic sites, also resulted to the enhancement of the  $\text{CO}_2$  uptake capacity by 2 times, as shown by Temperature programmed desorption. The superior properties of  $\text{CN}_{570}$  sample over the  $\text{CN}_{\text{as}}$  allowed the increase of CO production rate by ca. 55%.

Second,  $\text{CN}_{570}$  was further optimized by coupling with  $\text{Co}_3\text{O}_4$  derived using MOF structures as template. The functionalization is realized in a facile single step synthesis, through the application of a MOF-based synthesis process for the development of ultrathin  $\text{Co}_3\text{O}_4$  nanosheets. As shown by electron microscopy images, this pathway not only allows the morphology control but also the concomitant control of  $\text{Co}^{2+}/\text{Co}^{3+}$  ratio, and the formation of oxygen vacancy sites. The latter is proved by XPS analysis. The matched morphology (i.e., 2D morphology of  $\text{Co}_3\text{O}_4$ -NS and planar surface of  $\text{CN}_{570}$ ) allows an increase in the contact between the two parts in the composite enhancing their interaction.

The enhanced interaction between the two counterparts is also beneficial for the charge carrier's lifetime. As evidenced by TAS, there is a decrease on the charge recombination rates for the composite materials. The formation of the heterostructure also enhanced the availability of photogenerated electrons as verified by EPR and electrochemical analyses. Second, the presence of oxide ( $\text{Co}_3\text{O}_4$ ) in the composite material, and namely the oxygen vacancies that it presents also significantly improved  $\text{CO}_2$  adsorption (3-fold increase). It worths to mention that better charge separation and consequently longer lifetimes, also increases the possibility for the redox reaction to occur by the photogenerated charge carriers. Moreover, the enhanced  $\text{CO}_2$  uptake capacity can ensure the higher interaction

## CHAPTER 3

between the reactant gases, that are adsorbed on the surface with the electrons, rendering the CO<sub>2</sub> conversion more favorable. The superior properties of the composite material compared to the individual counterparts, contributed to a higher activity towards CO formation. The influence of the content of the oxide was studied in detail, indicating that the activity can be increased by 3-times with higher loadings (e.g., Co7-NS-CN<sub>570</sub>). The most active sample was also tested for the reaction of artificial photosynthesis and showed selectivity towards C<sub>1+</sub> products rather than the competitive H<sub>2</sub> formation reaction.

Herein, we already showed that the adapted strategy that includes the combined modification of both parts in the final composite, can result on the improvements of the electronic properties and CO<sub>2</sub> adsorption, allowing the enhancement of their properties and thereafter the photocatalytic activity. This was further highlighted by comparing the photocatalytic performance of composite that bares Co<sub>3</sub>O<sub>4</sub> in bulk morphology, which is less active than the 2-D counterpart composite.

## IV. References

- (1) Zhao, Y.; Liu, Z.; Chu, W.; Song, L.; Zhang, Z.; Yu, D.; Tian, Y.; Xie, S.; Sun, L. Large-Scale Synthesis of Nitrogen-Rich Carbon Nitride Microfibers by Using Graphitic Carbon Nitride as Precursor. *Adv. Mater.* **2008**, *20* (9), 1777–1781. <https://doi.org/10.1002/adma.200702230>.
- (2) Christoforidis, K. C.; Montini, T.; Bontempi, E.; Zafeiratos, S.; Jaén, J. J. D.; Fornasiero, P. Synthesis and Photocatalytic Application of Visible-Light Active  $\beta$ -Fe<sub>2</sub>O<sub>3</sub>/g-C<sub>3</sub>N<sub>4</sub> Hybrid Nanocomposites. *Applied Catalysis B: Environmental* **2016**, *187*, 171–180. <https://doi.org/10.1016/j.apcatb.2016.01.013>.
- (3) Christoforidis, K. C.; Syrgiannis, Z.; La Parola, V.; Montini, T.; Petit, C.; Stathatos, E.; Godin, R.; Durrant, J. R.; Prato, M.; Fornasiero, P. Metal-Free Dual-Phase Full Organic Carbon Nanotubes/g-C<sub>3</sub>N<sub>4</sub> Heteroarchitectures for Photocatalytic Hydrogen Production. *Nano Energy* **2018**, *50*, 468–478. <https://doi.org/10.1016/j.nanoen.2018.05.070>.
- (4) Dias, E. M.; Christoforidis, K. C.; Francàs, L.; Petit, C. Tuning Thermally Treated Graphitic Carbon Nitride for H<sub>2</sub> Evolution and CO<sub>2</sub> Photoreduction: The Effects of Material Properties and Mid-Gap States. *ACS Appl. Energy Mater.* **2018**, *1* (11), 6524–6534. <https://doi.org/10.1021/acsaem.8b01441>.
- (5) Niu, P.; Zhang, L.; Liu, G.; Cheng, H.-M. Graphene-Like Carbon Nitride Nanosheets for Improved Photocatalytic Activities. *Adv. Funct. Mater.* **2012**, *22* (22), 4763–4770. <https://doi.org/10.1002/adfm.201200922>.
- (6) Chen, W.; Han, B.; Tian, C.; Liu, X.; Liang, S.; Deng, H.; Lin, Z. MOFs-Derived Ultrathin Holey Co<sub>3</sub>O<sub>4</sub> Nanosheets for Enhanced Visible Light CO<sub>2</sub> Reduction. *Applied Catalysis B: Environmental* **2019**, *244*, 996–1003. <https://doi.org/10.1016/j.apcatb.2018.12.045>.
- (7) Xiaofen Xiao; Chun-Ting He; Shenglong Zhao; Jing Li; Wensheng Lin; Zhongke Yuan; Qiang Zhang; Shuangyin Wang; Liming Dai; Dingshan Yu. A General Approach to Cobalt-Based Homobimetallic Phosphide Ultrathin Nanosheets for Highly Efficient Oxygen Evolution in Alkaline Media. *Journal of American Chemical Society* **2008**, *13048*, 16136–16137.
- (8) Yang, J.; Zhang, F.; Lu, H.; Hong, X.; Jiang, H.; Wu, Y.; Li, Y. Hollow Zn/Co ZIF Particles Derived from Core-Shell ZIF-67@ZIF-8 as Selective Catalyst for the Semi-Hydrogenation of Acetylene. *Angew. Chem. Int. Ed.* **2015**, *54* (37), 10889–10893. <https://doi.org/10.1002/anie.201504242>.
- (9) Li, X.; Zhang, J.; Shen, L.; Ma, Y.; Lei, W.; Cui, Q.; Zou, G. Preparation and Characterization of Graphitic Carbon Nitride through Pyrolysis of Melamine. *Appl. Phys. A* **2009**, *94* (2), 387–392. <https://doi.org/10.1007/s00339-008-4816-4>.
- (10) Valery N. Khabashesku; John L. Zimmerman; John L. Margrave. Power Synthesis and Characterisation of Amorphous Carbon Nitride. *Chemistry of Materials* **2000**.
- (11) Xiao, J.; Han, Q.; Cao, H.; Rabeah, J.; Yang, J.; Guo, Z.; Zhou, L.; Xie, Y.; Brückner, A. Number of Reactive Charge Carriers—A Hidden Linker between Band Structure and Catalytic Performance in Photocatalysts. *ACS Catal.* **2019**, *9* (10), 8852–8861. <https://doi.org/10.1021/acscatal.9b02426>.

- (12) Kaviyarasu, K.; Raja, A.; Devarajan, P. A. Structural Elucidation and Spectral Characterizations of Co<sub>3</sub>O<sub>4</sub> Nanoflakes. *Spectrochimica Acta Part A: Molecular and Biomolecular Spectroscopy* **2013**, *114*, 586–591. <https://doi.org/10.1016/j.saa.2013.04.126>.
- (13) Filippini, G.; Longobardo, F.; Forster, L.; Criado, A.; Di Carmine, G.; Nasi, L.; D'Agostino, C.; Melchionna, M.; Fornasiero, P.; Prato, M. Light-Driven, Heterogeneous Organocatalysts for C–C Bond Formation toward Valuable Perfluoroalkylated Intermediates. *Sci. Adv.* **2020**, *6* (46), eabc9923. <https://doi.org/10.1126/sciadv.abc9923>.
- (14) Pablo Jimenez-Calvo; Clement Marchal; Thomas Cottineau; Valerie Caps; Valerie Keller. Influence of Gas Atmosphere during Synthesis of G-C<sub>3</sub>N<sub>4</sub> for Enhanced Photocatalytic H<sub>2</sub> Production from Water on Au/g-C<sub>3</sub>N<sub>4</sub> Composites. *J. Mater. Chem. A* **2019**, *7* (1).
- (15) Chen, L.; Man, Y.; Chen, Z.; Zhang, Y. Ag/g-C<sub>3</sub>N<sub>4</sub> Layered Composites with Enhanced Visible Light Photocatalytic Performance. *Mater. Res. Express* **2016**, *3* (11), 115003. <https://doi.org/10.1088/2053-1591/3/11/115003>.
- (16) Wang, S.; Li, C.; Wang, T.; Zhang, P.; Li, A.; Gong, J. Controllable Synthesis of Nanotube-Type Graphitic C<sub>3</sub>N<sub>4</sub> and Their Visible-Light Photocatalytic and Fluorescent Properties. *J. Mater. Chem. A* **2014**, *2* (9), 2885. <https://doi.org/10.1039/c3ta14576j>.
- (17) Liping Zhong; Thomas Kropp; Walid Baaziz; Ovidiu Ersen; Detre Teschner; Robert Schlögl; Manos Mavrikakis; Spyridon Zafeiratos. Correlation Between Reactivity and Oxidation State of Cobalt Oxide Catalysts for CO Preferential Oxidation. *ACS Catalysis* **2019**, *9*.
- (18) Li, K.; Chen, C.; Bian, X.; Sun, T.; Jia, J. Electrolytic Nitrate Reduction Using Co<sub>3</sub>O<sub>4</sub> Rod-like and Sheet-like Cathodes with the Control of (220) Facet Exposure and Co<sup>2+</sup>/Co<sup>3+</sup> Ratio. *Electrochimica Acta* **2020**, *362*, 137121. <https://doi.org/10.1016/j.electacta.2020.137121>.
- (19) Zhu, S.; Li, X.; Jiao, X.; Shao, W.; Li, L.; Zu, X.; Hu, J.; Zhu, J.; Yan, W.; Wang, C.; Sun, Y.; Xie, Y. Selective CO<sub>2</sub> Photoreduction into C<sub>2</sub> Product Enabled by Charge-Polarized Metal Pair Sites. *Nano Lett.* **2021**, *21* (5), 2324–2331. <https://doi.org/10.1021/acs.nanolett.1c00383>.
- (20) Zhu, J.; Xiao, P.; Li, H.; Carabineiro, S. A. C. Graphitic Carbon Nitride: Synthesis, Properties, and Applications in Catalysis. *ACS Appl. Mater. Interfaces* **2014**, *6* (19), 16449–16465. <https://doi.org/10.1021/am502925j>.
- (21) Rawool, S. A.; Yadav, K. K.; Polshettiwar, V. Defective TiO<sub>2</sub> for Photocatalytic CO<sub>2</sub> Conversion to Fuels and Chemicals. *Chem. Sci.* **2021**, *12* (12), 4267–4299. <https://doi.org/10.1039/D0SC06451C>.
- (22) Thompson, T. L.; Diwald, O.; Yates, J. T. CO<sub>2</sub> as a Probe for Monitoring the Surface Defects on TiO<sub>2</sub> (110) Temperature-Programmed Desorption. *J. Phys. Chem. B* **2003**, *107* (42), 11700–11704. <https://doi.org/10.1021/jp030430m>.
- (23) Lee, J.; Sorescu, D. C.; Deng, X. Electron-Induced Dissociation of CO<sub>2</sub> on TiO<sub>2</sub> (110). *J. Am. Chem. Soc.* **2011**, *133* (26), 10066–10069. <https://doi.org/10.1021/ja204077e>.
- (24) Zhang, Y.; Xia, B.; Ran, J.; Davey, K.; Qiao, S. Z. Atomic-Level Reactive Sites for Semiconductor-Based Photocatalytic CO<sub>2</sub> Reduction. *Adv. Energy Mater.* **2020**, *10* (9), 1903879. <https://doi.org/10.1002/aenm.201903879>.

- (25) Crake, A.; Christoforidis, K. C.; Godin, R.; Moss, B.; Kafizas, A.; Zafeiratos, S.; Durrant, J. R.; Petit, C. Titanium Dioxide/Carbon Nitride Nanosheet Nanocomposites for Gas Phase CO<sub>2</sub> Photoreduction under UV-Visible Irradiation. *Applied Catalysis B: Environmental* **2019**, *242*, 369–378. <https://doi.org/10.1016/j.apcatb.2018.10.023>.
- (26) Ganguly, P.; Harb, M.; Cao, Z.; Cavallo, L.; Breen, A.; Dervin, S.; Dionysiou, D. D.; Pillai, S. C. 2D Nanomaterials for Photocatalytic Hydrogen Production. *ACS Energy Lett.* **2019**, *4* (7), 1687–1709. <https://doi.org/10.1021/acseenergylett.9b00940>.
- (27) Lu, Q.; Yu, Y.; Ma, Q.; Chen, B.; Zhang, H. 2D Transition-Metal-Dichalcogenide-Nanosheet-Based Composites for Photocatalytic and Electrocatalytic Hydrogen Evolution Reactions. *Adv. Mater.* **2016**, *28* (10), 1917–1933. <https://doi.org/10.1002/adma.201503270>.
- (28) Hu, L.; Peng, Q.; Li, Y. Selective Synthesis of Co<sub>3</sub>O<sub>4</sub> Nanocrystal with Different Shape and Crystal Plane Effect on Catalytic Property for Methane Combustion. *J. Am. Chem. Soc.* **2008**, *130* (48), 16136–16137. <https://doi.org/10.1021/ja806400e>.
- (29) Liu, Y.; Zhu, G.; Ge, B.; Zhou, H.; Yuan, A.; Shen, X. Concave Co<sub>3</sub>O<sub>4</sub> Octahedral Mesocrystal: Polymer-Mediated Synthesis and Sensing Properties. *CrystEngComm* **2012**, *14* (19), 6264. <https://doi.org/10.1039/c2ce25788b>.
- (30) Jeon, H. S.; Jee, M. S.; Kim, H.; Ahn, S. J.; Hwang, Y. J.; Min, B. K. Simple Chemical Solution Deposition of Co<sub>3</sub>O<sub>4</sub> Thin Film Electrocatalyst for Oxygen Evolution Reaction. *ACS Appl. Mater. Interfaces* **2015**, *7* (44), 24550–24555. <https://doi.org/10.1021/acsami.5b06189>.
- (31) Gao, C.; Meng, Q.; Zhao, K.; Yin, H.; Wang, D.; Guo, J.; Zhao, S.; Chang, L.; He, M.; Li, Q.; Zhao, H.; Huang, X.; Gao, Y.; Tang, Z. Co<sub>3</sub>O<sub>4</sub> Hexagonal Platelets with Controllable Facets Enabling Highly Efficient Visible-Light Photocatalytic Reduction of CO<sub>2</sub>. *Adv. Mater.* **2016**, *28* (30), 6485–6490. <https://doi.org/10.1002/adma.201601387>.
- (32) Li, W.; Wang, Y.; Cui, X. Y.; Yu, S.; Li, Y.; Hu, Y.; Zhu, M.; Zheng, R.; Ringer, S. P. Crystal Facet Effects on Nanomagnetism of Co<sub>3</sub>O<sub>4</sub>. *ACS Appl. Mater. Interfaces* **2018**, *10* (22), 19235–19247. <https://doi.org/10.1021/acsami.8b03934>.
- (33) Miao, T. J.; Tang, J. Characterization of Charge Carrier Behavior in Photocatalysis Using Transient Absorption Spectroscopy. *J. Chem. Phys.* **2020**, *152* (19), 194201. <https://doi.org/10.1063/5.0008537>.
- (34) Jenny Nelson; Rosemary E. Chandler. Random Walk Models of Charge Transfer and Transport in Dye Sensitized Systems. *Coordination Chemistry Reviews* **2004**, *248*, 1181–1194.
- (35) Moss, B.; Lim, K. K.; Beltram, A.; Moniz, S.; Tang, J.; Fornasiero, P.; Barnes, P.; Durrant, J.; Kafizas, A. Comparing Photoelectrochemical Water Oxidation, Recombination Kinetics and Charge Trapping in the Three Polymorphs of TiO<sub>2</sub>. *Sci Rep* **2017**, *7* (1), 2938. <https://doi.org/10.1038/s41598-017-03065-5>.
- (36) Christoforidis, K. C.; Fernández-García, M. Photoactivity and Charge Trapping Sites in Copper and Vanadium Doped Anatase TiO<sub>2</sub> Nano-Materials. *Catal. Sci. Technol.* **2016**, *6* (4), 1094–1105. <https://doi.org/10.1039/C5CY00929D>.
- (37) Actis, A.; Melchionna, M.; Filippini, G.; Fornasiero, P.; Prato, M.; Salvadori, E.; Chiesa, M. Morphology and Light-Dependent Spatial Distribution of Spin

- Defects in Carbon Nitride. *Angew Chem Int Ed* **2022**, *61* (43). <https://doi.org/10.1002/anie.202210640>.
- (38) Long, D.; Li, X.; Yin, Z.; Fan, S.; Wang, P.; Xu, F.; Wei, L.; Tadé, M. O.; Liu, S. Novel Co<sub>3</sub>O<sub>4</sub> @ CoFe<sub>2</sub>O<sub>4</sub> Double-Shelled Nanoboxes Derived from Metal–Organic Framework for CO<sub>2</sub> Reduction. *Journal of Alloys and Compounds* **2021**, *854*, 156942. <https://doi.org/10.1016/j.jallcom.2020.156942>.
- (39) Zhang, Q.; Yang, P.; Zhang, H.; Zhao, J.; Shi, H.; Huang, Y.; Yang, H. Oxygen Vacancies in Co<sub>3</sub>O<sub>4</sub> Promote CO<sub>2</sub> Photoreduction. *Applied Catalysis B: Environmental* **2022**, *300*, 120729. <https://doi.org/10.1016/j.apcatb.2021.120729>.
- (40) Christoforidis, K. C.; Montini, T.; Fittipaldi, M.; Jaén, J. J. D.; Fornasiero, P. Photocatalytic Hydrogen Production by Boron Modified TiO<sub>2</sub>/Carbon Nitride Heterojunctions. *ChemCatChem* **2019**, *11* (24), 6408–6416. <https://doi.org/10.1002/cctc.201901703>.
- (41) Crake, A.; Christoforidis, K. C.; Kafizas, A.; Zafeiratos, S.; Petit, C. CO<sub>2</sub> Capture and Photocatalytic Reduction Using Bifunctional TiO<sub>2</sub>/MOF Nanocomposites under UV–Vis Irradiation. *Applied Catalysis B: Environmental* **2017**, *210*, 131–140. <https://doi.org/10.1016/j.apcatb.2017.03.039>.
- (42) Christoforidis, K. C. G-C<sub>3</sub>N<sub>4</sub>/Ag<sub>3</sub>PO<sub>4</sub> Based Binary and Ternary Heterojunction for Improved Photocatalytic Removal of Organic Pollutants. *International Journal of Environmental Analytical Chemistry* **2021**, 1–16. <https://doi.org/10.1080/03067319.2021.1901282>.
- (43) Tu, W.; Xu, Y.; Wang, J.; Zhang, B.; Zhou, T.; Yin, S.; Wu, S.; Li, C.; Huang, Y.; Zhou, Y.; Zou, Z.; Robertson, J.; Kraft, M.; Xu, R. Investigating the Role of Tunable Nitrogen Vacancies in Graphitic Carbon Nitride Nanosheets for Efficient Visible-Light-Driven H<sub>2</sub> Evolution and CO<sub>2</sub> Reduction. *ACS Sustainable Chem. Eng.* **2017**, *5* (8), 7260–7268. <https://doi.org/10.1021/acssuschemeng.7b01477>.
- (44) Niu, P.; Qiao, M.; Li, Y.; Huang, L.; Zhai, T. Distinctive Defects Engineering in Graphitic Carbon Nitride for Greatly Extended Visible Light Photocatalytic Hydrogen Evolution. *Nano Energy* **2018**, *44*, 73–81. <https://doi.org/10.1016/j.nanoen.2017.11.059>.
- (45) Miao, X.; Yue, X.; Ji, Z.; Shen, X.; Zhou, H.; Liu, M.; Xu, K.; Zhu, J.; Zhu, G.; Kong, L.; Shah, S. A. Nitrogen-Doped Carbon Dots Decorated on g-C<sub>3</sub>N<sub>4</sub>/Ag<sub>3</sub>PO<sub>4</sub> Photocatalyst with Improved Visible Light Photocatalytic Activity and Mechanism Insight. *Applied Catalysis B: Environmental* **2018**, *227*, 459–469. <https://doi.org/10.1016/j.apcatb.2018.01.057>.
- (46) Jin, C.; Wang, M.; Li, Z.; Kang, J.; Zhao, Y.; Han, J.; Wu, Z. Two Dimensional Co<sub>3</sub>O<sub>4</sub>/g-C<sub>3</sub>N<sub>4</sub> Z-Scheme Heterojunction: Mechanism Insight into Enhanced Peroxymonosulfate-Mediated Visible Light Photocatalytic Performance. *Chemical Engineering Journal* **2020**, *398*, 125569. <https://doi.org/10.1016/j.cej.2020.125569>.
- (47) Christoforidis, K. C.; Montini, T.; Fittipaldi, M.; Jaén, J. J. D.; Fornasiero, P. Photocatalytic Hydrogen Production by Boron Modified TiO<sub>2</sub>/Carbon Nitride Heterojunctions. *ChemCatChem* **2019**, *11* (24), 6408–6416. <https://doi.org/10.1002/cctc.201901703>.
- (48) Chen, W.; Han, B.; Tian, C.; Liu, X.; Liang, S.; Deng, H.; Lin, Z. MOFs-Derived Ultrathin Holey Co<sub>3</sub>O<sub>4</sub> Nanosheets for Enhanced Visible Light CO<sub>2</sub> Reduction.

- Applied Catalysis B: Environmental* **2019**, *244*, 996–1003. <https://doi.org/10.1016/j.apcatb.2018.12.045>.
- (49) Vidyasagar, D.; Ghugal, S. G.; Umare, S. S.; Banavoth, M. Extended  $\pi$ -Conjugative n-p Type Homostructural Graphitic Carbon Nitride for Photodegradation and Charge-Storage Applications. *Sci Rep* **2019**, *9* (1), 7186. <https://doi.org/10.1038/s41598-019-43312-5>.
- (50) Yeh, T.-F.; Teng, C.-Y.; Chen, S.-J.; Teng, H. Nitrogen-Doped Graphene Oxide Quantum Dots as Photocatalysts for Overall Water-Splitting under Visible Light Illumination. *Adv. Mater.* **2014**, *26* (20), 3297–3303. <https://doi.org/10.1002/adma.201305299>.
- (51) Wang, X.; Maeda, K.; Thomas, A.; Takanabe, K.; Xin, G.; Carlsson, J. M.; Domen, K.; Antonietti, M. A Metal-Free Polymeric Photocatalyst for Hydrogen Production from Water under Visible Light. *Nature Mater* **2009**, *8* (1), 76–80. <https://doi.org/10.1038/nmat2317>.
- (52) Zhao, X.; Lu, Z.; Ji, R.; Zhang, M.; Yi, C.; Yan, Y. Biomass Carbon Modified Z-Scheme g-C<sub>3</sub>N<sub>4</sub>/Co<sub>3</sub>O<sub>4</sub> Heterojunction with Enhanced Visible-Light Photocatalytic Activity. *Catalysis Communications* **2018**, *112*, 49–52. <https://doi.org/10.1016/j.catcom.2018.04.003>.
- (53) Zheng, J.; Zhang, L. Designing 3D Magnetic Peony Flower-like Cobalt Oxides/g-C<sub>3</sub>N<sub>4</sub> Dual Z-Scheme Photocatalyst for Remarkably Enhanced Sunlight Driven Photocatalytic Redox Activity. *Chemical Engineering Journal* **2019**, *369*, 947–956. <https://doi.org/10.1016/j.cej.2019.03.131>.

Chapter 4:  
Composites of (Me)-PCN-  
224/ TiO<sub>2</sub>

## Table of Figures

FIGURE 4. 1 : TGA PROFILES OF COMPOSITE MATERIALS AND INDIVIDUAL COUNTERPARTS .....	151
FIGURE 4. 2 : XRD PATTERNS OF MOFs, TiO <sub>2</sub> AND THE COMPOSITE MATERIALS .....	153
FIGURE 4. 3 : IR SPECTRA OF METALATED AND NON-METALATED PORPHYRIN .....	154
FIGURE 4. 4 : IR SPECTRA FOR METALATED AND NON-METALATED MOFs AND THEIR COMPOSITES. THE GREEN LINES ARE A GUIDE TO THE EYE. ....	155
FIGURE 4. 5: BET ANALYSIS RESULTS OF TiO <sub>2</sub> , MOFs, AND COMPOSITES.....	156
FIGURE 4. 6: CO <sub>2</sub> PROFILE DURING TEMPERATURE -PROGRAMMED DESORPTION FOR COMPOSITE AND INDIVIDUAL MATERIALS.....	158
FIGURE 4. 7: UV/VISIBLE SPECTRA OF FREE-BASE PORPHYRIN AND METALATED PORPHYRIN.....	159
FIGURE 4. 8: DR-UV-VIS SPECTRA OF MOFs, TiO <sub>2</sub> AND COMPOSITES MATERIALS .....	160
FIGURE 4. 9 : TAUC PLOTS OF TiO <sub>2</sub> AND COMPOSITE MATERIALS .....	161
FIGURE 4. 10: XPS SURVEY SPECTRA .....	162
FIGURE 4. 11 : XPS OF CORE LEVELS OF (A) CARBON, (B) NITROGEN, (C) OXYGEN, (D) ZIRCONIUM AND (E) TITANIUM.....	164
FIGURE 4. 12: SEM IMAGES OF (A) PCN-224, (B) PCN-224/TiO <sub>2</sub> , (C) CU-PCN-224 AND (D) CU-PCN-224/TiO <sub>2</sub> .....	165
FIGURE 4. 13: SEM-EDX RESULTS FOR CU-PCN-224.....	166
FIGURE 4. 14: PHOTOCATALYTIC RESULTS OF PRISTINE PCN-224, CU INCORPORATED PCN-224, TiO <sub>2</sub> AND THEIR COMPOSITE MATERIALS.....	168
FIGURE 4. 15: ELECTRONIC PRODUCTIVITY FOR TiO <sub>2</sub> AND PORPHYRINIC MOF COMPOSITE MATERIALS .....	168
FIGURE 4.16 : H <sub>2</sub> O SPLITTING RESULTS FOR 1%PT-TiO <sub>2</sub> , 1%PT-PCN-224/TiO <sub>2</sub> AND PCN-224/TiO <sub>2</sub> .....	169

## Introduction

This chapter focuses on MOFs PCN-224 and Cu-PCN-224 with free and metalated core in their organic ligand, respectively, and their coupling with TiO<sub>2</sub> UV100. Initially, the effect of the presence of MOF on TiO<sub>2</sub> for the development of composites is examined and evaluated in the photocatalytic reduction of CO<sub>2</sub> and H<sub>2</sub> production. Later, MOFs comprised of organic ligands with metalated core are used for the formation of the composites and the influence of the metal is investigated. The protocol of synthesis of MOFs and the development of the heterostructures have been described in detail in [Section 2.1.](#) This chapter is divided in two parts:

1. In the first part, the information that is obtained based on the characterization techniques is used to shed light to the properties of the prepared materials. The methods used to study the photocatalyst focus on structural, optical, chemical, and morphological characterization.
2. The second part presents the results of the photocatalytic activity of the prepared materials. Namely, the photocatalysts are evaluated towards:
  - a. CO<sub>2</sub> reduction reaction and
  - b. H<sub>2</sub>O splitting.

Finally, the photocatalytic activity of the prepared materials is discussed taking on the basis the information gained from their physicochemical characterization.

## I. Characterization of (Me-PCN-224)/TiO<sub>2</sub> composites

### I.1. Characterization of structural properties

#### TGA

As seen in [Chapter 2](#), the development of heterostructures is carried out by direct growth of PCN-224 on TiO<sub>2</sub>. Thus, the percentage of MOF on the composite may differ from the nominal content. Therefore, quantitative analysis of the MOF content is performed by means of thermogravimetric analysis (TGA). The TGA profiles of the composite materials and their individual counterparts are given in Figure 4.1. It can be clearly observed that the two counterparts present different thermal stability. The profiles can be divided into 3 parts (indicated by different colors in Figure 4.1). Firstly, the mass loss at temperatures up to 120 °C is ascribed to the removal of the residual solvents (i.e., ethanol) used for the synthesis and the activation of MOFs. The second weight loss is observed in the temperature range from 120 °C to 400 °C. This is ascribed to the dehydration of the Zr<sub>6</sub>O<sub>4</sub>(OH)<sub>4</sub> nodes to Zr<sub>6</sub>O<sub>6</sub> in PCN-224 and Cu-PCN-224 <sup>1</sup>. In the third part, a significant weight loss from 400°C to 520°C is displayed and corresponds to the decomposition of the organic ligand in the framework. The MOF with copper functionalized ligands (Cu-PCN-224) presents higher thermal stability than the pristine MOF (PCN-224). The temperature onset of the Cu-PCN-224 is approximately at 510 °C while that of the pristine PCN-224 at ca. 425 °C. It may imply that copper contributes to the higher thermal stability of the structure. As expected, TiO<sub>2</sub> is thermally more stable than the MOF containing structures. The TiO<sub>2</sub> TGA profile contains two distinct regions In the first region (25-300°C) there is a constant mass loss attributed to the removal of adsorbates <sup>2,3</sup>. In the region 350-600 °C the loss of –OH groups is observed <sup>4</sup>. Concerning the composite materials, it is observed that the temperature onset is lower compared with the pure MOF-structures. More precisely, the temperature onset of Cu-PCN-224/TiO<sub>2</sub> is at 410 °C. This observation infers that the presence of TiO<sub>2</sub> accelerates the decomposition of MOFs in high temperatures. This effect is more intense in the case of copper functionalized composites.

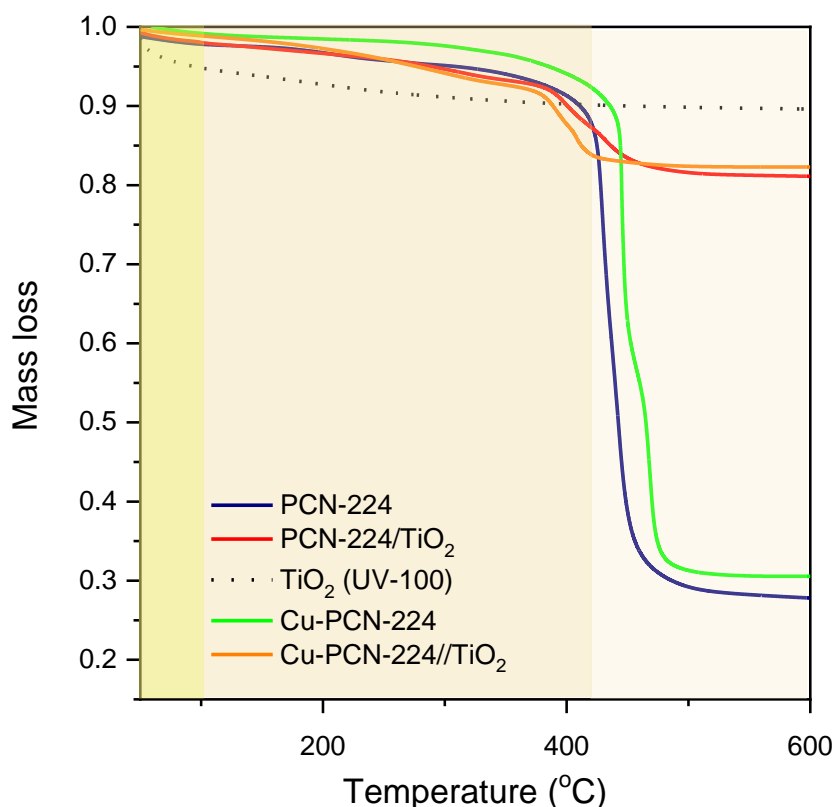


Figure 4. 1 : TGA profiles of composite materials and individual counterparts

The TGA profiles were used to obtain information regarding the content of the different parts in the composites. The mass remaining at 600 °C is used to estimate the MOF content in the composite materials. To this end, the following equations (Eq. 4.1-4.3) are used and the content of MOFs on the final nanocomposite is shown in Table 4.1. As can be seen, the composites containing Cu in the organic moieties of the MOF present higher content. This is probably linked with the presence of Cu. This is already reported in previous studies, where MOFs were synthesized in presence of other metal oxides. In particular, it is shown that the basic surface of a metal oxide can promote the nucleation of Cu containing MOFs containing acidic ligands<sup>5</sup>.

$$(\Delta mass\ loss)_i = (Final\ mass)_i - (Final\ mass)_{MOF} \quad \text{Equation 4.1}$$

$$X_{TiO_2} = \frac{(\Delta mass\ loss)}{TiO_2\ Final\ mass - PCN-224\ Final\ mass} \quad \text{Equation 4.2}$$

$$X_{PCN-224} = 1 - X_{TiO_2}$$

Equation 4.3

Where  $x_{TiO_2}^{theo}$  is the expected  $TiO_2$  content base on the unmodified PCN-224 synthesis yield

Table 4. 1 : Thermal gravimetric analysis of  $TiO_2$ , Cu-PCN-224 and Cu-PCN-224/ $TiO_2$  composites (Cu-PCN-Ti).

	Final mass (% mass)	$\Delta$ mass loss (% mass)	$x_{TiO_2}$ (% mass)	$X_{PCN-224}$ (% mass)
<b>TiO<sub>2</sub></b>	89	-	100.0	0.0
<b>PCN-Ti</b>	81.1	52.8	87	13.0
<b>Cu-PCN-Ti</b>	82.3	51.8	85	15
<b>PCN-224</b>	28.3	-	0.0	100.0
<b>Cu-PCN-224</b>	30.5	-	0.0	100.0

#### XRD

XRD analysis is performed in order to get information regarding the crystal structure of MOFs and detect the difference phases in the nanocomposites. The XRD patterns of the prepared materials (MOFs and composites) are shown in Figure 4.2. All XRD patterns are in accordance with the literature <sup>6</sup>. The patterns of both pristine PCN-224 and Cu functionalized PCN-224 exhibit diffraction peaks at 6.5°, 8.0°, 9.2°, 11.2° and 13.8°. These correspond to the (002), (022), (222), (004), (224) and (006) crystal facets, respectively <sup>7</sup>. In the case of Cu-PCN-224 we can see that the peak centered at 6.5°, presents lower relative intensity compared to PCN-224 pattern. This indicates that the facet (002) is more pronounced. As we can observe by comparing the diffractograms of pristine and Cu coordinated-PCN-224, the coordination of the porphyrin doesn't alter the crystal structure of the MOF. Concerning  $TiO_2$ , UV-100 is of pure anatase phase as it can be seen by its XRD pattern <sup>8</sup>. Its crystallite size can be found by using Scherrer equation and it equals to 89.7 Å. The XRD patterns of the composite materials present diffraction peaks that correspond to both counterparts. This finding clearly suggests that the MOF structure is successfully formed in the presence of  $TiO_2$ . Additionally, another important information that can be concluded is that the  $TiO_2$  phase is not modified during the solvothermal reaction applied for the synthesis of the MOF.

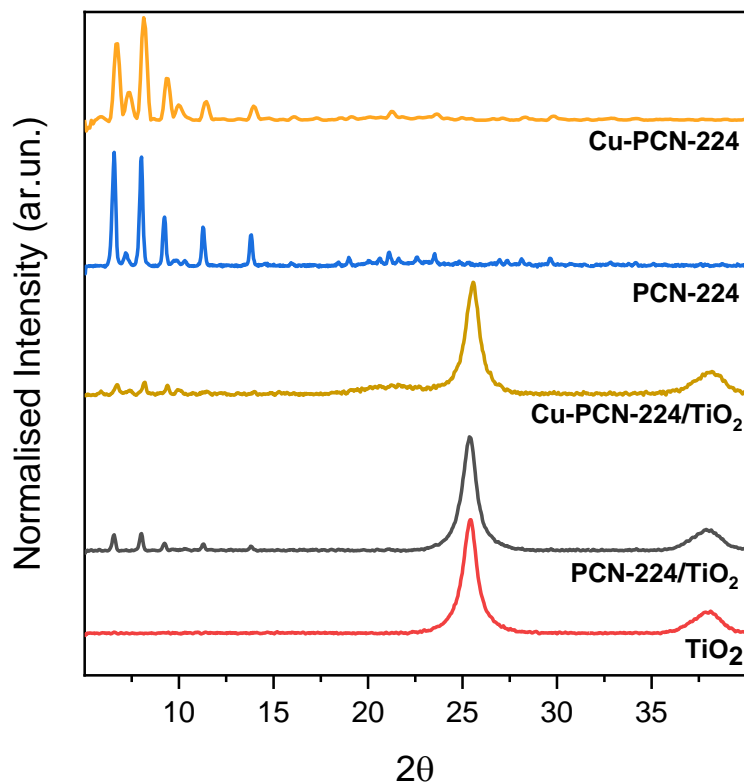


Figure 4. 2 : XRD patterns of MOFs,  $\text{TiO}_2$  and the composite materials

#### ATR

Structural information on the prepared materials was also obtained using ATR spectroscopy. Firstly, the ATR spectra of the  $\text{H}_2\text{TCPP}$  and  $\text{Me-TCPP}$  are presented in Figure 4.3). It can be seen that they both hold the characteristic bands of benzene and C–O bond at  $1400$  and  $1638\text{ cm}^{-1}$ , respectively. The peaks observed at the spectra of the free-base porphyrin at  $965$  and  $3300\text{ cm}^{-1}$  are attributed to the vibration and stretching modes of the N–H bond at the core of the porphyrin ring<sup>9</sup>. These bands are not observed in the ATR spectra of metalated porphyrin. Furthermore, the Cu functionalized porphyrin presents a new peak at  $1000\text{ cm}^{-1}$  that is attributed to the Cu–N bond<sup>10,11</sup>. These are the first important observations and indicate the successful coordination of the metal in the core of the porphyrin ring. It is important to mention that the excess of the metal M with respect to the porphyrin in the reaction mixture (molar ratio  $\text{TCPP}/\text{MCl}_2 = 1:5$ ) during the porphyrin metalation step did not interfere with the structural ion/ion clusters.

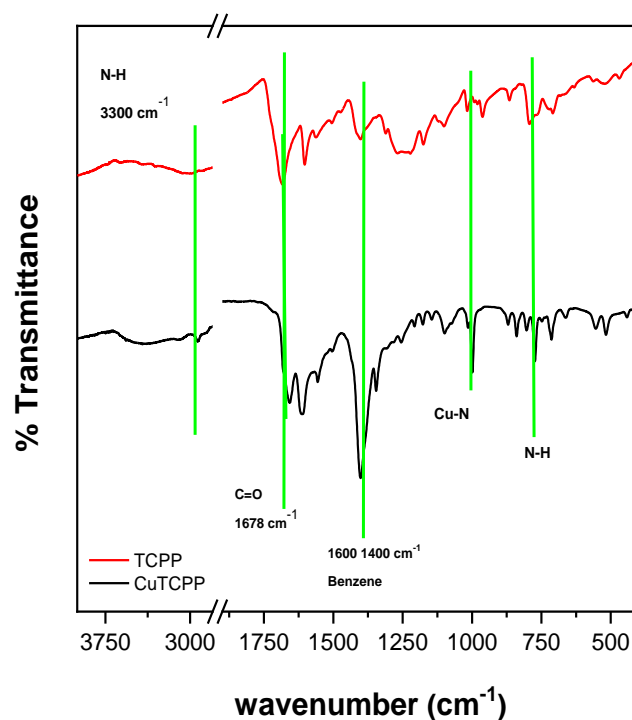


Figure 4. 3 :IR spectra of metalated and non-metalated porphyrin

In Figure 4.4, the ATR spectra of PCN-224 and Cu-PCN-224 as well as of the pure  $\text{TiO}_2$  and the composite materials are shown. The two peaks centered at 1650 and 1264  $\text{cm}^{-1}$  can be ascribed to C–O and C–OH asymmetric vibrations. Close inspection of the spectra reveal that the intensity of these peaks is decreased in the case of PCN-224 and Cu-PCN-224<sup>12</sup>. This may suggest that the –COOH groups of the  $\text{H}_2\text{TCPP}$  ligand participate in the coordination with  $\text{Zr}^{4+}$ , i.e. the metal of the MOF<sup>13</sup>. Furthermore, the peak located at 650  $\text{cm}^{-1}$  is attributed to Zr-OH bond formation, confirming the presence of the MOF structure<sup>14</sup>. Simultaneously, we observe an increase of the peaks at 1413 and 1585  $\text{cm}^{-1}$ , which are attributed to the vibration of the (-O-C-O-) groups, confirming the presence of dicarboxylate<sup>15</sup>. Similarly, to the ATR spectra of the CuTCPP, the spectra of the Cu functionalized MOF (i.e., Cu-PCN-224), don't present any peak corresponding to the N-H bond of the porphyrin core (3300  $\text{cm}^{-1}$ ).

On the other hand,  $\text{TiO}_2$  is relatively inactive in the IR region. It shows two broad peaks at 3280  $\text{cm}^{-1}$  and at 500-800  $\text{cm}^{-1}$  that correspond to the stretching of the O-H groups and to the Ti-O-Ti vibrations, respectively<sup>7</sup>. Also, the peak observed at 1622  $\text{cm}^{-1}$  that is ascribed to the bending vibration of O-H bond from hydroxyl groups or water adsorbed on the surface<sup>16</sup>. The characteristics peaks of the PCN-224 and  $\text{TiO}_2$  are also detected in the ATR spectrum of all composite materials,

confirming the successful growth of the MOF on  $\text{TiO}_2$ . The peak at  $2350\text{ cm}^{-1}$  corresponds to the  $\text{CO}_2$  of the atmosphere and it is attributed to the calibration of the spectrometer. Overall, ATR spectroscopy provides direct evidence for the metalation of the porphyrin ring and the presence of both  $\text{TiO}_2$  and MOF phases in the composite materials.

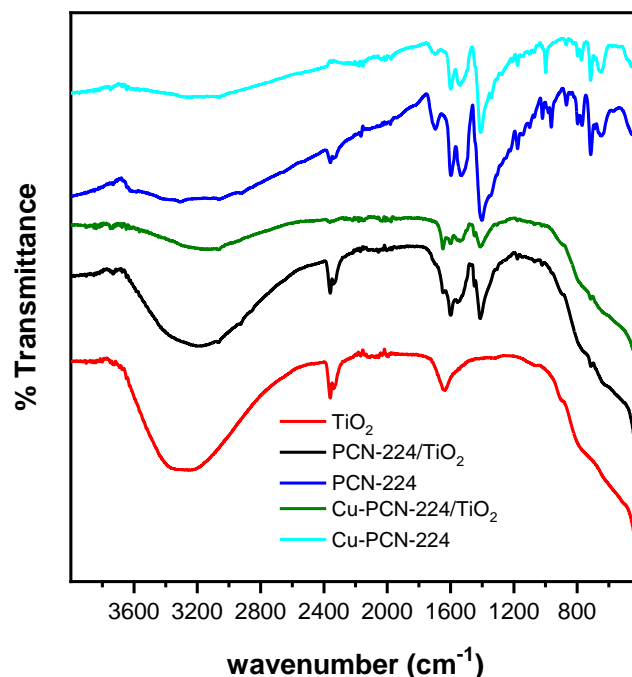


Figure 4. 4 : IR spectra for metalated and non-metalated MOFs and their composites. The green lines are a guide to the eye.

#### BET

Surface area is a key parameter in photocatalytic reduction of  $\text{CO}_2$ , and MOFs are considered to contribute significantly to the porosity of the catalyst, enhancing the interaction of the substrate and the active sites of the catalyst. Therefore,  $\text{N}_2$  sorption/desorption isotherms at 77 K were analyzed to get further insights into the properties of the prepared materials, as seen in Figure 4.5. The BET specific surface area (SSA) of the individual counterparts and composite materials are presented in Table 4.2. The MOF structures exhibit a type I isotherm, in consistency with their crystal structure indicating microporosity<sup>1,17</sup>. As expected, the surface area of MOF materials is significantly high (ca.  $1700\text{ m}^2\text{ g}^{-1}$ ). This can be attributed to the 3-D large open channels in the framework, which makes most of the pore surface accessible<sup>17</sup>. It can also be observed that the presence of Cu in the core of the organic ligand doesn't affect the specific surface area of the MOF structure. The slight increase

observed can be considered negligible and attributed to the lack of precision at low pressures.  $\text{TiO}_2$  shows a typical type-IV isotherm with hysteresis loops of type H3 at relative pressure range of 0.45–1.0, indicating the presence of mesoporous structure

18.

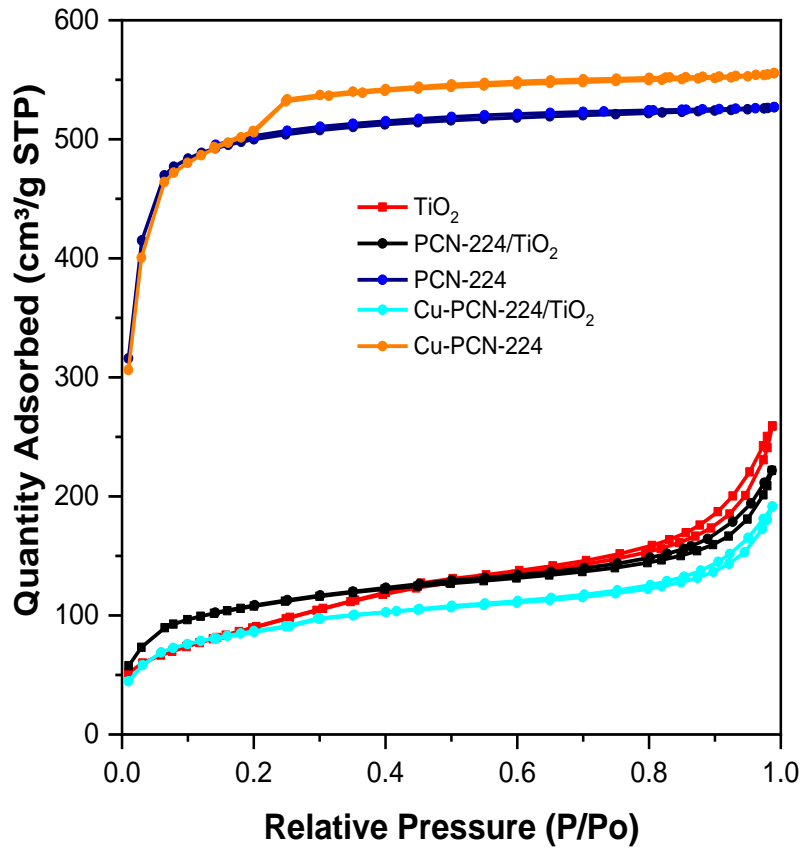


Figure 4. 5: BET analysis results of  $\text{TiO}_2$ , MOFs, and composites

Table 4. 2: Specific Surface area of individual counterparts and composite materials

Sample	Specific surface area (m <sup>2</sup> g <sup>-1</sup> )
TiO <sub>2</sub>	300
PCN-224	1617
Cu-PCN-224	1739
PCN-224/ TiO <sub>2</sub>	370
Cu-PCN-224/ TiO <sub>2</sub>	303

### CO<sub>2</sub> uptake capacity

CO<sub>2</sub> uptake capacity is of high importance for photocatalysts used in artificial photosynthesis. An estimation of CO<sub>2</sub> absorption ability is realized by means of temperature programmed desorption. This approach, besides the quantification of the CO<sub>2</sub> absorbed by the material, permits the estimation of the type of active sites (i.e., weak, mild, strong). Herein, experiments were carried out for temperatures between 50 and 250 °C, in order to avoid the thermal decomposition of PCN materials. Namely, the MS signal of CO<sub>2</sub> (m/z=44) in function of temperature, for composite materials and the individual counterparts can be seen in Figure 4.6. TiO<sub>2</sub> presents a peak at 120 °C. This is already reported in the literature, ascribed to the surface of {001} facet with high surface energy in anatase<sup>19</sup>. TiO<sub>2</sub> is a metal oxide, on the surface of whom CO<sub>2</sub> can be adsorbed on both basic and acidic sites, depending on the mode of adsorption<sup>20</sup>. CO<sub>2</sub> can act as an acidic molecule if the carbon interacts with the oxygen of the catalyst's surface. It may also act as basic species if its oxygen atoms interact with the Ti ions<sup>21</sup>. The TPD profile of the porphyrinic MOF shows a weak peak at 120 °C and a more intense temperature higher than 240 °C. This might be attributed to NH groups of the porphyrinic ligand or to Zr clusters. The composite materials hold both types of basic sites for CO<sub>2</sub> adsorption, which align with their individual counterparts. All profiles show a peak at 100-120 °C, that is attributed to TiO<sub>2</sub> nanoparticles. The PCN-224/TiO<sub>2</sub> exhibits a weaker peak at higher temperatures, which is attributed to the presence of MOF. On the other hand, composites bearing Cu-PCN-224 present a pronounced peak at 240 °C, which is attributed to strong basic sites. With a closer inspection, we can observe that this peak is increasing with the increase of CuTCPP as organic ligand in the MOF structure. It is already reported that the unsaturated metal sites in the porphyrin linker could accept e<sup>-</sup> and improve the CO<sub>2</sub> uptake ability of the photocatalyst<sup>22</sup>. Therefore, the enhanced CO<sub>2</sub> adsorption observed is due to the interaction with the Cu<sup>2+</sup> sites. This observation is more obvious in the case of the composite material bearing MOF with CuTCPP as organic ligand.

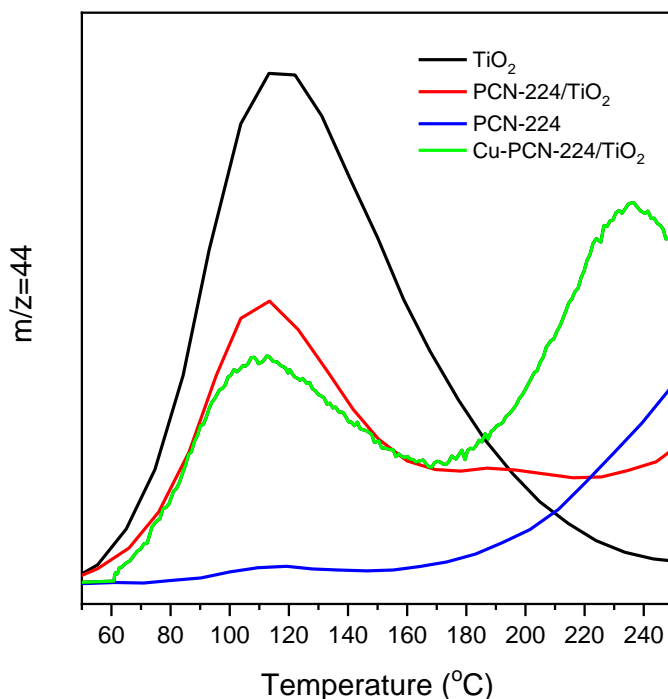


Figure 4. 6: CO<sub>2</sub> profile during temperature -programmed desorption for composite and individual materials

## 1.2. Characterization of electronic and morphological properties

### UV/Vis Spectroscopy

Prior to the synthesis of the MOF, UV/vis spectroscopy was employed to confirm the efficiency of the metalation procedure of the organic ligand. The results are presented in Figure 4.7. H<sub>2</sub>TCP is expected from the literature exhibits one Soret band at 414 nm and 4 Q bands at 517, 554, 581, and 638 nm<sup>23</sup>. After Cu<sup>2+</sup> ions are coordinated in the core of H<sub>2</sub>TCP, the number of Q bands decreases to two (i.e., 569 and 616 nm) as the molecular symmetry increases from D<sub>2h</sub> to D<sub>4h</sub> symmetry<sup>24</sup>. With a closer inspection of the CuTCP spectra, it can be observed that there is a shift of the main peak that is attributed to the  $\pi \rightarrow \pi^*$  transitions. The observed shift to higher wavelengths indicates that the incorporation of Cu in the core of the TCP induced a change in the chemical environment as already reported in the literature<sup>25</sup>.

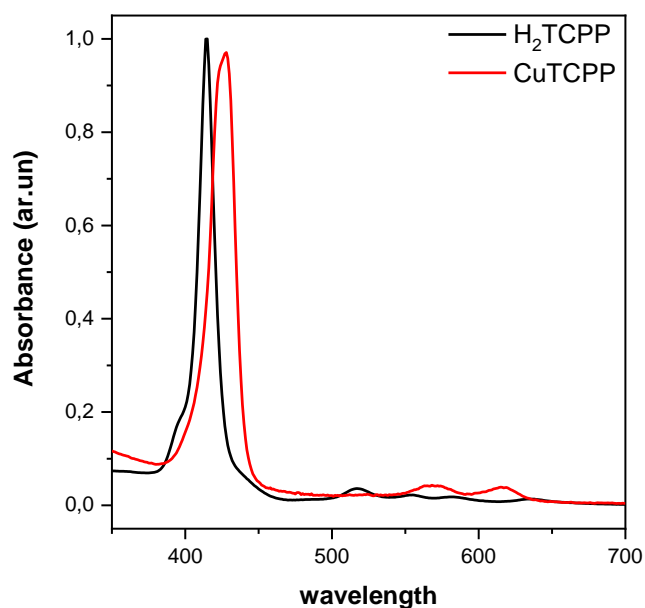


Figure 4. 7: UV/visible spectra of free-base porphyrin and metalated porphyrin

In Figure 4.8, it is shown that  $\text{TiO}_2$  exhibits absorbance peak in the UV region of light as expected from the literature for anatase polymorphs<sup>16</sup>. On the other hand, pure PCN-224 presents two major absorption edges locating at approximately 440 and 720 nm. These correspond to the absorption of the Zr-O oxo-clusters and the porphyrin ligand, respectively<sup>26,27</sup>. With a careful look we can observe that the peaks at 500, 540, 575, 630 nm are attributed to the Q bands of TCPP, that have been mentioned already in Figure 4.7<sup>28</sup>. Likewise, Cu-PCN-224 presents an absorption edge attributed to Zr-O clusters but shows two Q bands at 539 and 594 nm, similarly to CuTCPP complex. The composite material presents peaks that are attributed to both  $\text{TiO}_2$  and the MOF. In comparison to bare  $\text{TiO}_2$ , there is a bathochromic shift of the absorption edge after the formation of the composites, suggesting that PCN-224 is able to extend the light absorption of  $\text{TiO}_2$ . The presence of Cu in PCN-224 framework induces a redshift of the absorbance edge of PCN-224<sup>7</sup>. As it has been already reported for porphyrinic MOFs, porphyrin absorb visible-light and generate electrons that are then transferred to the Zr oxo clusters<sup>22</sup>. This phenomenon is so called Ligand-to-Metal-Charge-Transfer (LMCT) and it also occurs in other MOF structures<sup>29</sup>.

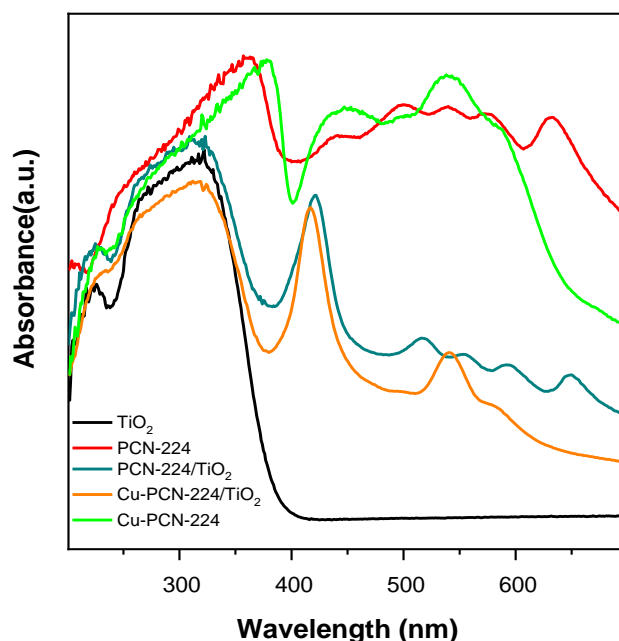


Figure 4. 8: DR-UV-vis spectra of MOFs,  $\text{TiO}_2$  and composites materials

Based on the UV-Vis spectra, the energy bandgap of the prepared materials is estimated (Table 4.3). In this direction, Kubelka-Munk function (equations shown in Chapter 2) for indirect semiconductors is used and the corresponding Tauc plots are illustrated in Figure 4.9. It is worth mentioning that there is a debate around the energy bandgap of MOF materials. As long as MOFs are comprised of organic linkers and metal nodes, the excitation of electron upon light irradiation is more complicated to predict. Contrarily to typical semiconductors, the bandgap in MOFs corresponds to the energy difference between HOMO (highest occupied molecular orbital) and LUMO (lowest unoccupied molecular orbital)<sup>30</sup>. The HOMO level energy of MOFs normally represents the organic ligands, while the relationship between the reduction potential of the metal clusters and LUMO level energy of the MOFs has been demonstrated<sup>31</sup>.

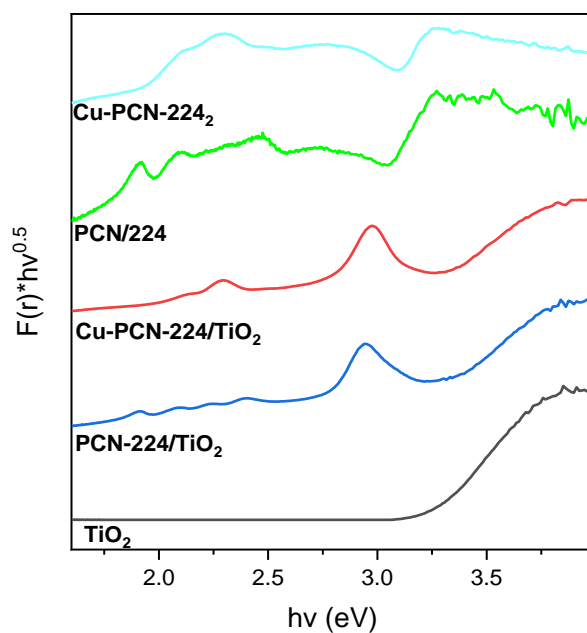


Figure 4. 9 : Tauc plots of  $\text{TiO}_2$  and composite materials

Table 4. 3: Energy bandgap and elemental quantification for  $\text{TiO}_2$ , PCN-224 and composite materials

Photocatalyst	$E_g$ (eV)	Ti (%)	O (%)	Zr (%)	N (%)	C (%)	Cu(%)
$\text{TiO}_2$	3.4	24.2	65.4	-	-	10.4	-
PCN-224	1.71	-	23.6	3.6	3.8	69.0	-
PCN-224/ $\text{TiO}_2$	3.3	19	51.1	0.8	1.4	27.7	-
Cu-PCN-224	1.69	0	23.26	3.60	3.80	68.86	0.47
Cu-PCN-224/ $\text{TiO}_2$	3.09	15.25	46.11	0.41	0.83	37.34	0.06

#### XPS

The different states of the core levels of the elements found in the composite are studied by X-ray photoelectron spectroscopy. The results show that Ti, O, C, N, Zr are observed in the overall survey spectra as seen in Fig. 4.10. The surface composition of the analyzed samples is calculated based on the Equation 2.6 given in [Chapter 2.II.4](#) and they are shown in Table 4.3.

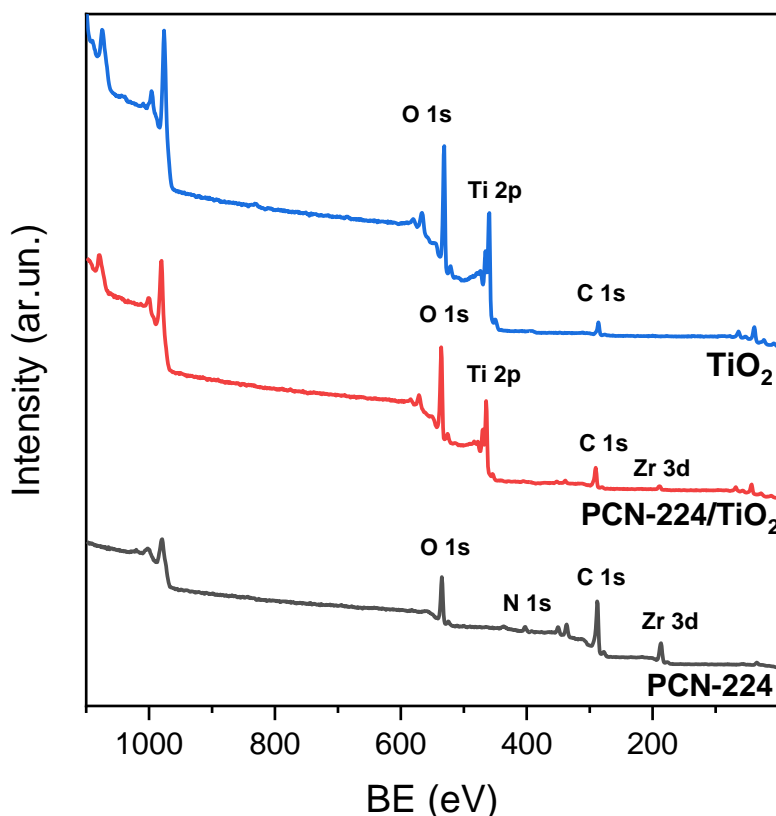


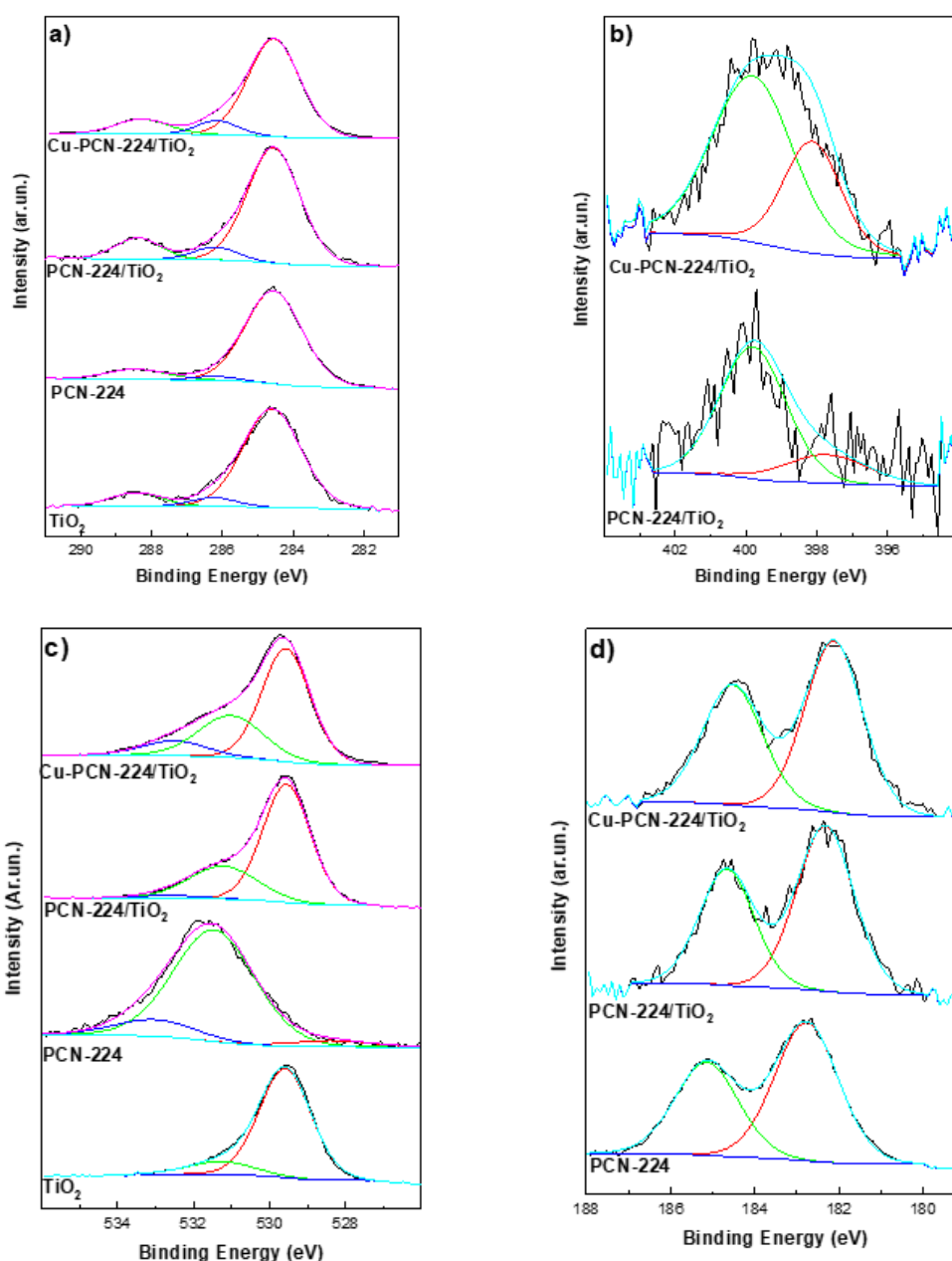
Figure 4. 10: XPS survey spectra

The C 1s signal of the composites and their individual counterparts is shown in Figure 4.11a. The carbon peak of the  $\text{TiO}_2$  sample is attributed to the adventitious carbon and impurities. For the MOFs and the composite materials, carbon signal originates from the organic ligand. In all samples containing MOF, the carbon signal can be deconvoluted in three peaks centered at 284.6, 286.2 and 288.4 eV. They are ascribed to C-C, C=O and C-N, respectively. Regarding the N 1s XPS spectra of the MOF and composite materials, it can be deconvoluted in two peaks as seen in Figure 4.11b. The peaks are located at 399.8 and 397.7 eV and they are ascribed to C-N and C-N-H groups, respectively. Both species are found in porphyrin moieties.

In figure 4.11c, O 1s XPs spectra are depicted. The oxygen signal for  $\text{TiO}_2$  is comprised of two peaks (529.6 and 531.3 eV) that are ascribed to oxygen of the lattice and to O-H species, respectively. Regarding PCN-224, the oxygen spectrum can be deconvoluted into three peaks centered at 528.3, 531.5 and 533 eV that are attributed to Zr-O, C=O, and O-H. In this case, C=O are the most abundant species, that are expected to be found in the organic ligand moieties. In the case of  $\text{TiO}_2$ , the most dominant species are Ti-O species, which is also in accordance with Ti 2p XPS

spectra (Figure 4.11f). The same observation can be made for the composite materials (PCN-224/TiO<sub>2</sub> and Cu-PCN-224/TiO<sub>2</sub>), which is expected because TiO<sub>2</sub> holds the higher percentage.

The metal center of zirconium can be confirmed by the signal in the 179-189 eV region. High resolution Zr 3d XPS spectra are shown in Figure 4.11d. Specifically, the peak at 184.7 eV is ascribed to Zr 3d<sub>3/2</sub> and the peak at 182.3 eV to Zr 3d<sub>5/2</sub>. As it is observed, Zr peaks are shifted to lower binding energies in the case of the composite materials. This observation indicates a strong interaction between the MOF and TiO<sub>2</sub>. Similarly, we can notice that the Ti 2p peak in the composite materials is decreased by 0.2 eV compared with the Ti 2p signal of the bare TiO<sub>2</sub> (Figure 4.11f). This can imply that a new bond is formed in the composite material. Specifically, the formation of Ti-O-Zr leads to an electron-deficiency tendency of Ti<sup>32</sup>.



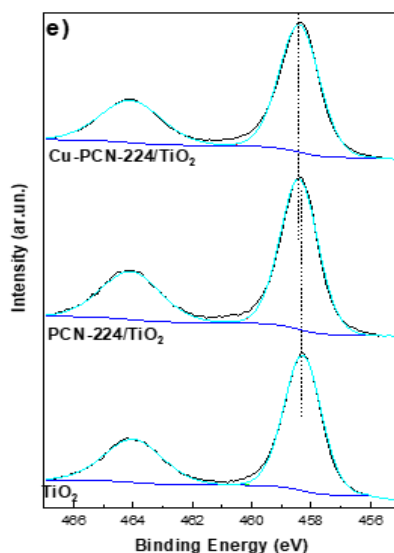


Figure 4. 11 : XPS of core levels of (a) carbon, (b) nitrogen, (c) oxygen, (d) zirconium and (e) titanium

### SEM

The successful development of PCN-224 and Cu-PCN-224 on  $\text{TiO}_2$  was demonstrated by several spectroscopies discussed above. In order to study the surface topology of the samples Scanning Electron Microscopy (SEM) is employed. SEM images are given in Figure 4.12. As we can see in Figure 4.12a, MOF PCN-224 holds a cubic morphology with truncated edges with smooth surface. The particle size varies from 5 to 8  $\mu\text{m}$ . The cubic appearance and the particle size are in accordance with previous reports <sup>6,33</sup>. Furthermore, previous studies showed that PCN-224 possesses three-dimensional (3-D) channels <sup>17</sup>. In Figure 4.12b, the developed PCN-224- $\text{TiO}_2$  composite is depicted. As expected,  $\text{TiO}_2$  particle size is significantly smaller than the MOF. This results in good dispersion of  $\text{TiO}_2$  nanoparticles on the surface of PCN-224. A fine contact between the two counterparts is observed. This implies that the protocol employed for in-situ growth of PCN-224 on  $\text{TiO}_2$  is efficient for the development of a composite. In Figure 4.12c and Figure 4.12d, SEM images of Cu-PCN-224/ $\text{TiO}_2$  are shown. It can be seen that, Cu-PCN-224 shows two different morphologies: 1) a cubic morphology with sharp edges and 2) nanorods structures. As mentioned already, nanocubes are ascribed to PCN-224, and the hexagonal nanorods are a characteristic shape of PCN-222<sup>34</sup>. It has been already reported in the literature, that PCN synthesis may produce MOFs of mixed topologies. In this case PCN-224 and PCN-222 share the same precursors (i.e.,  $\text{ZrCl}_4$ ,  $\text{H}_2\text{TCPP}$ , benzoic acid)<sup>35</sup>, and the final material may be a mix of both MOF structures. The presence of both after the synthesis of Cu-PCN-224 may be attributed to the inappropriate ratio of precursors <sup>23</sup>.

As seen in Figure 4.12d,  $\text{TiO}_2$  nanoparticles are also well dispersed around MOF particles for the case of Cu-PCN-224 composite. This minimizes the self-aggregation

of  $\text{TiO}_2$  particles, permitting a more effective interaction of Cu-PCN-224 and  $\text{TiO}_2$  nanoparticles. This has been proven previously beneficial in catalytic applications <sup>9</sup>. The presence of Cu in the structure of PCN-224 was also investigated by SEM-EDX analysis and the results are shown in Figure 4.13. We can observe that C and O from the organic ligand are the most dominant elements. This is in accordance with XPS results. It is also necessary to mention that SEM-EDX collects electrons that are emitted by a bigger volume compared to XPS which has lower operating voltage and is regarded as surface analysis technique. Therefore, the small Ti percentage observed is attributed to  $\text{TiO}_2$  nanoparticles that are in contact with Cu-PCN-224.

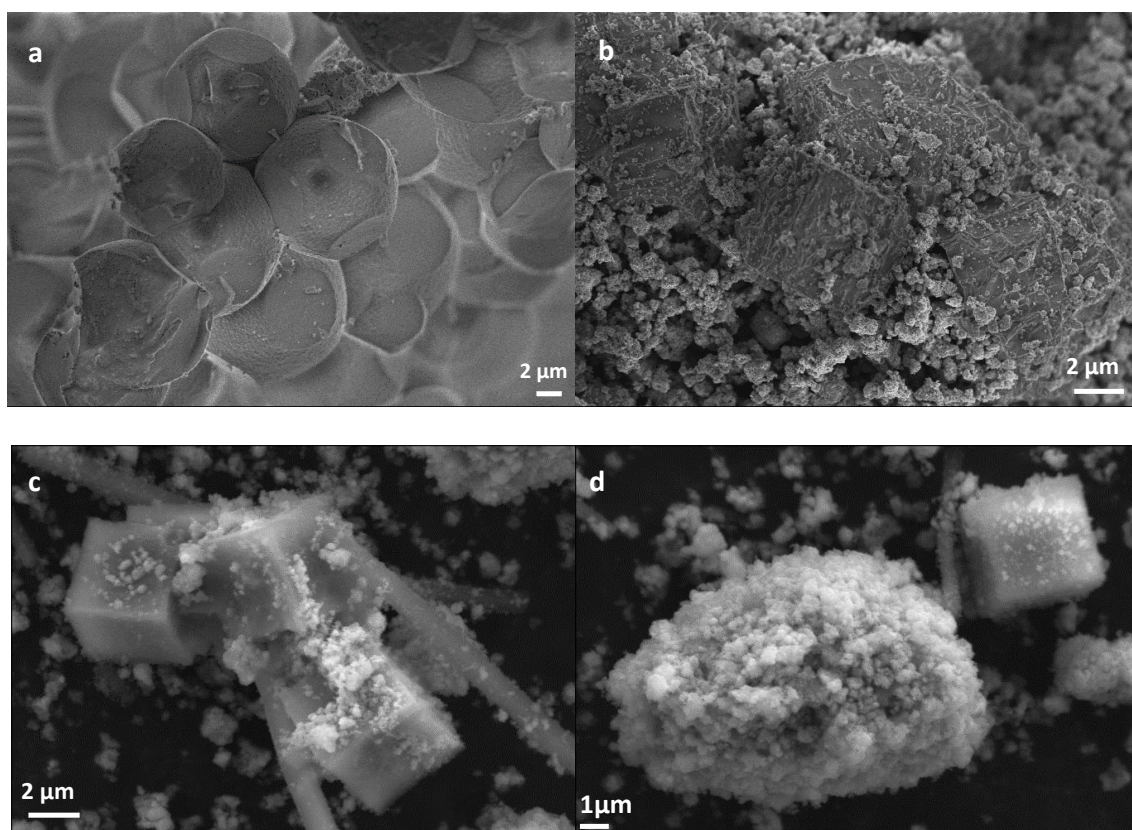


Figure 4. 12: SEM images of (a) PCN-224, (b) PCN-224/ $\text{TiO}_2$ , (c) Cu-PCN-224 and (d) Cu-PCN-224/ $\text{TiO}_2$

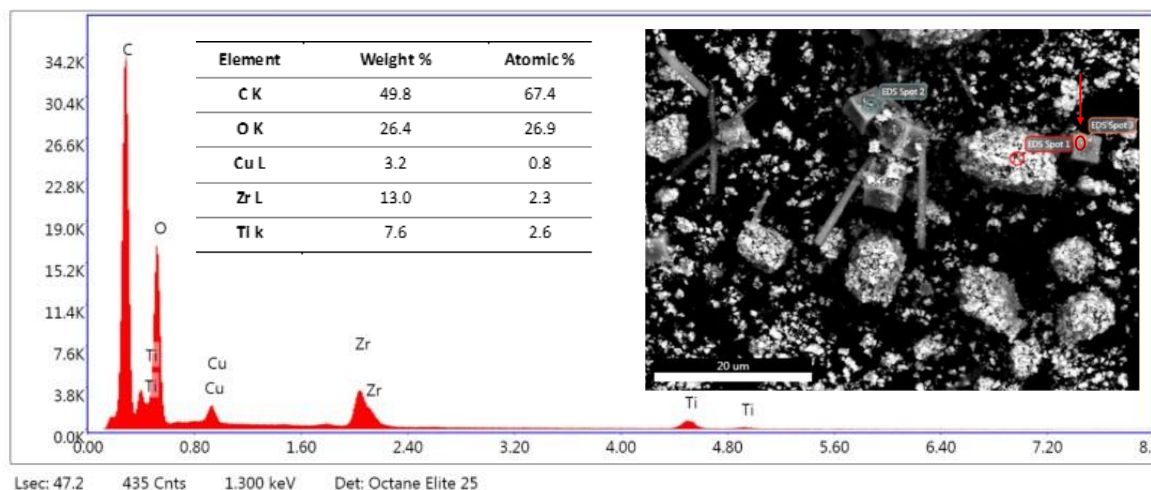


Figure 4. 13: SEM-EDX results for Cu-PCN-224

## II. Photocatalytic activity of (Me)-PCN-224/TiO<sub>2</sub>(UV-100) nanocomposites

### II.1. Photocatalytic CO<sub>2</sub> reduction results

The prepared materials were evaluated as photocatalysts towards CO<sub>2</sub> reduction under visible light, using H<sub>2</sub>O as electron donor, under the conditions that are described in Chapter 2. The products detected in the gas phase are CH<sub>4</sub>, CO and H<sub>2</sub>. The latest originates from the water splitting reaction. The results using different catalysts after 10 hours reaction-time are shown in Figure 4.14. As can be observed, all the composite materials present higher photocatalytic activity than their individual counterparts. More precisely, PCN-224 showed no photocatalytic activity under the reported experimental conditions (i.e., feed flow rate, residence time). Zr-based MOFs are reported to show moderate activity towards CO<sub>2</sub> photoreduction in liquid phase<sup>7,30</sup>. Up till now, there are not many studies using PCN materials as photocatalysts for CO<sub>2</sub> reduction in gas phase.

The coupling of MOF and TiO<sub>2</sub> resulted in interesting observations. No obvious differences are detected in the catalytic activity of TiO<sub>2</sub> compared with the PCN-224/TiO<sub>2</sub> composite. This is observed both in activity and selectivity. However, significant differences are detected in the composite material where Cu-porphyrin was used as the organic linker. The Cu-PCN-224/TiO<sub>2</sub> composite presents an impressive enhancement in H<sub>2</sub> production (ca. 3 times compared with PCN-224/TiO<sub>2</sub> composite). Regarding the C-products, an approximately 2-fold increase is observed compared with the reference TiO<sub>2</sub> and PCN-224/TiO<sub>2</sub> materials.

It is worth reminding that carbonaceous products don't require the same number of electrons. Therefore, in order to compare the overall activity of the prepared

photocatalysts, their electronic productivity is presented in Figure 4.15. As it can be seen, the insertion of Copper inside the MOF structure of the composite material, induces a 2.5-times fold increase of electronic activity.

As observed by SEM images, Cu-PCN-224/TiO<sub>2</sub> contains also PCN-222. This might influence the overall photocatalytic activity. PCN-222 and PCN-224 possess the same linkers and Zr oxo clusters and different topology. The latter is considered catalytically more active. This is attributed to the number of linkers connected to the metal oxo clusters (i.e., PCN-222 has 8-linkers connected and PCN-224 6-linkers). It is reported that low-node connected Zr-porphyrin MOFs hold higher surface area facilitating the faster transfer of absorbed CO<sub>2</sub> molecules in Zr(IV) centers<sup>37</sup>. On the other hand, PCN-222 holds more porphyrin linkers, so the unsaturated active sites (Cu<sup>2+</sup>) are more abundant, compared to PCN-224. Which can explain the 3-time fold increase of overall activity. Furthermore, a reference material is prepared in order to elucidate the influence of the porphyrin as photosensitizer. Specifically, the sample of TiO<sub>2</sub> bearing 9% H<sub>2</sub>TCP (9%) is not active towards CO<sub>2</sub> reduction. This indicates that the observed enhancement in activity of the composite materials originates from the synergistic effects of the MOF structure with the TiO<sub>2</sub>. Reference reactions under argon are carried using the most active photocatalyst sample (i.e., Cu-PCN-224/TiO<sub>2</sub>) resulting in no activity. This result implies that the C<sub>1</sub> products and H<sub>2</sub> evolution observed derive from the reduction of CO<sub>2</sub> and H<sub>2</sub>O splitting, respectively.

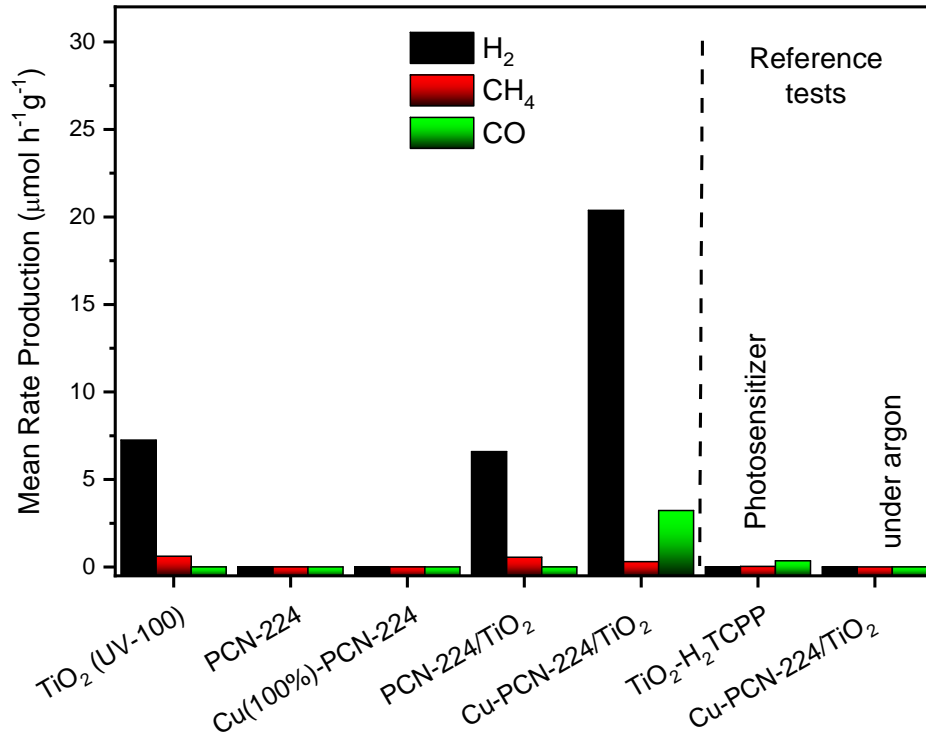


Figure 4. 14: Photocatalytic results of pristine PCN-224, Cu incorporated PCN-224, TiO<sub>2</sub> and their composite materials

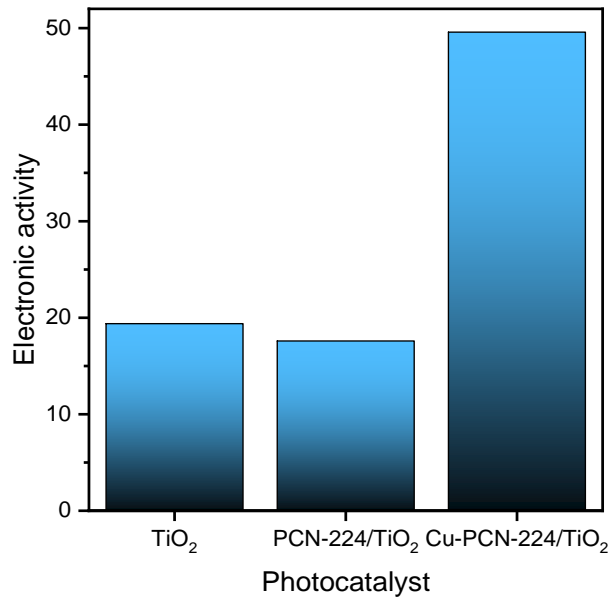


Figure 4. 15: Electronic productivity for TiO<sub>2</sub> and porphyrinic MOF composite materials

## II.2. Photocatalytic H<sub>2</sub>O Splitting results

As seen in [Section II.1](#), the prepared composite materials are much more selective to H<sub>2</sub> production during artificial photosynthesis process. Therefore, the samples are evaluated towards water splitting in the liquid phase without the use of sacrificial agent. The tests are carried out in the set-up described in detail in [Chapter 2.III.1](#). Prior to the photocatalytic test, 1% Pt is deposited on the surface of the materials as cocatalysts. The results presented in Figure 4.16 show a rapid deactivation of the photocatalyst, after a 60-minute test. This might be attributed to the blocking of micropores of MOF structure. It is obvious that the presence of Pt nanoparticles resulted in the enhancement of the activity of the composite. But the sample 1% Pt-TiO<sub>2</sub> is more active towards water splitting reaction, compared to composite materials. This observation is in contrast to the behavior of these materials observed towards CO<sub>2</sub> reduction, indicating that MOFs are acting as better catalysts in gas phase.

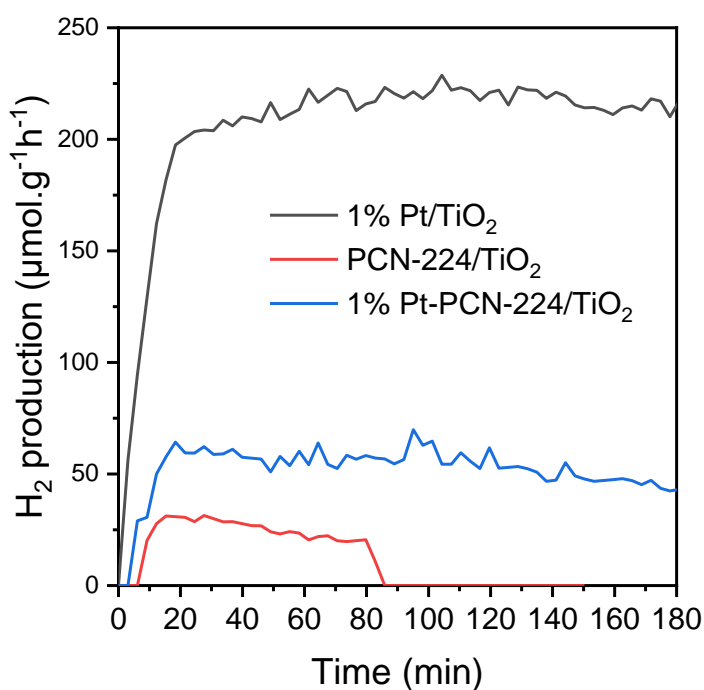


Figure 4.16 : H<sub>2</sub>O splitting results for 1%Pt-TiO<sub>2</sub>, 1%Pt-PCN-224/TiO<sub>2</sub> and PCN-224/TiO<sub>2</sub>

### III. Conclusions

Herein, we showed the successful in situ growth of the MOF PCN-224 on the TiO<sub>2</sub> nanoparticles. These MOF structures are bearing porphyrin H<sub>2</sub>TCPP as organic ligand which can act as antenna to harvest visible light, as seen by UV/Vis spectroscopy. They also possess a metalation core, that can coordinate metals as unsaturated metal sites that can enhance the properties of H<sub>2</sub>TCPP in molecular level. To this end, PCN-224 structures with incorporated Cu ions in the core of the porphyrin ligand were synthesized and coupled with TiO<sub>2</sub> via a solvothermal one-pot synthesis process.

The successful in situ growth of the MOF PCN-224 on the TiO<sub>2</sub> nanoparticles is evidenced by a plethora of spectroscopic techniques including XRD, ATR, UV/Visible Spectroscopy. Furthermore, the effective coupling between the MOF structure and TiO<sub>2</sub> nanoparticles is proved by SEM images. Also, the close interaction between the two counterparts is shown by XPS measurements, where a shift in the BE of Zr and Ti is observed. The presence of MOF in the final materials enhances not only the total available surface area of the composite material as seen by N<sub>2</sub> sorption isotherms, but also extends the response to a wider range of light as evidenced by DR-UV/Vis spectra.

Another important observation concerns the composite material that holds metalated TCPP as organic ligand. Regarding Cu-PCN-224/TiO<sub>2</sub> composite material, the incorporation of Cu ions in the framework induced a significant enhancement to the CO<sub>2</sub> uptake capacity. This is attribute to new active sites which are ascribed to the desorption peaks appearing at ca. 240°C at the TPD profiles. This might be attributed to the unsaturated metal sites introduced in the structures (i.e., Cu<sup>2+</sup>), which are considered to promote CO<sub>2</sub> adsorption ability.

The work performed herein demonstrates that MOF structures can be used to improve the overall photocatalytic efficiency of “traditional” photocatalysts (i.e., TiO<sub>2</sub>). Specifically, photocatalytic reactions performed in the gas phase in the presence of H<sub>2</sub>O as electron donor revealed that TiO<sub>2</sub>-based composite materials bearing MOF structures are more active photocatalyst than the corresponding pure anatase TiO<sub>2</sub>. Furthermore, the functionalization of the organic ligand of the MOF with Cu controlled the overall activity. Most importantly, the presence of Cu sites in the composite material enhanced the evolution towards carbonaceous products which is the most desirable, as long as they are products that require higher number of electrons for their formation. Reference experiments using TiO<sub>2</sub> and H<sub>2</sub>TCPP as photosensitizer show that observed enhanced photocatalytic activity is attributed to a synergistic effect of MOF, rather than to the presence of porphyrin as light sensitizer. Another important observation is that MOF-based photocatalysts are

## CHAPTER 4

more suitable for gas phase reactions. In the case of liquid phase, their pores might be blocked, leading to a loss of activity.

## IV. References

- (1) Ji, J.; Liu, F.; Yang, W.; Tan, M.; Luo, W.; Yin, S. Incorporation of Functional Groups in Porphyrinic Metal–Organic Frameworks by Post-modification for Highly Efficient Oxidation Catalysis. *ChemCatChem* **2020**, *12* (17), 4331–4338. <https://doi.org/10.1002/cctc.202000295>.
- (2) Javed, H. M. A.; Adnan, M.; Qureshi, A. A.; Javed, S.; Adeel, M.; Akram, M. A.; Shahid, M.; Irfan Ahmad, M.; Afzaal, M.; Abd-Rabboh, H. S. M.; Arif, M. Morphological, Structural, Thermal and Optical Properties of Zn/Mg-Doped TiO<sub>2</sub> Nanostructures for Optoelectronic Applications. *Optics & Laser Technology* **2022**, *146*, 107566. <https://doi.org/10.1016/j.optlastec.2021.107566>.
- (3) Mahlambi, M. M.; Mishra, A. K.; Mishra, S. B.; Krause, R. W.; Mamba, B. B.; Raichur, A. M. Comparison of Rhodamine B Degradation under UV Irradiation by Two Phases of Titania Nano-Photocatalyst. *J Therm Anal Calorim* **2012**, *110* (2), 847–855. <https://doi.org/10.1007/s10973-011-1852-7>.
- (4) Li, X. W.; Song, R. G.; Jiang, Y.; Wang, C.; Jiang, D. Surface Modification of TiO<sub>2</sub> Nanoparticles and Its Effect on the Properties of Fluoropolymer/TiO<sub>2</sub> Nanocomposite Coatings. *Applied Surface Science* **2013**, *276*, 761–768. <https://doi.org/10.1016/j.apsusc.2013.03.167>.
- (5) Zacher, D.; Baunemann, A.; Hermes, S.; Fischer, R. A. Deposition of Microcrystalline [Cu<sub>3</sub>(Btc)<sub>2</sub>] and [Zn<sub>2</sub>(Bdc)<sub>2</sub>(Dabco)] at Alumina and Silica Surfaces Modified with Patterned Self Assembled Organic Monolayers: Evidence of Surface Selective and Oriented Growth. *J. Mater. Chem.* **2007**, *17* (27), 2785. <https://doi.org/10.1039/b703098c>.
- (6) Liu, X.; Qi, W.; Wang, Y.; Lin, D.; Yang, X.; Su, R.; He, Z. Rational Design of Mimic Multienzyme Systems in Hierarchically Porous Biomimetic Metal–Organic Frameworks. *ACS Appl. Mater. Interfaces* **2018**, *10* (39), 33407–33415. <https://doi.org/10.1021/acsami.8b09388>.
- (7) Wang, L.; Jin, P.; Huang, J.; She, H.; Wang, Q. Integration of Copper(II)-Porphyrin Zirconium Metal–Organic Framework and Titanium Dioxide to Construct Z-Scheme System for Highly Improved Photocatalytic CO<sub>2</sub> Reduction. *ACS Sustainable Chem. Eng.* **2019**, *7* (18), 15660–15670. <https://doi.org/10.1021/acssuschemeng.9b03773>.
- (8) Ioannidou, T.; Anagnostopoulou, M.; Papoulis, D.; Christoforidis, K. C.; Vasiliadou, I. A. UiO-66/Palygorskite/TiO<sub>2</sub> Ternary Composites as Adsorbents and Photocatalysts for Methyl Orange Removal. *Applied Sciences* **2022**, *12* (16), 8223. <https://doi.org/10.3390/app12168223>.
- (9) Lei Wang; Shuhua Duan; Pengxia Jin; Houde She; Jingwei Huang; Ziqiang Lei; Tierui Zhang; Qizhao Wang. Anchored Cu(II) Tetra(4-Carboxylphenyl)Porphyrin to P25 (TiO<sub>2</sub>) for Efficient Photocatalytic Ability in CO<sub>2</sub> Reduction. *Applied Catalysis B: Environmental* **2018**, *239*, 599–608.
- (10) Wang, L.; Jin, P.; Duan, S.; She, H.; Huang, J.; Wang, Q. In-Situ Incorporation of Copper(II) Porphyrin Functionalized Zirconium MOF and TiO<sub>2</sub> for Efficient Photocatalytic CO<sub>2</sub> Reduction. *Science Bulletin* **2019**, *64* (13), 926–933. <https://doi.org/10.1016/j.scib.2019.05.012>.
- (11) Xu, J.; Liu, X.; Zhou, Z.; Xu, M. Photocatalytic CO<sub>2</sub> Reduction Catalyzed by Metalloporphyrin: Understanding of Cobalt and Nickel Sites in Activity and

- Adsorption. *Applied Surface Science* **2020**, *513*, 145801. <https://doi.org/10.1016/j.apsusc.2020.145801>.
- (12) Das, R.; Manna, S. S.; Pathak, B.; Nagaraja, C. M. Strategic Design of Mg-Centered Porphyrin Metal–Organic Framework for Efficient Visible Light-Promoted Fixation of CO<sub>2</sub> under Ambient Conditions: Combined Experimental and Theoretical Investigation. *ACS Appl. Mater. Interfaces* **2022**, *14* (29), 33285–33296. <https://doi.org/10.1021/acsami.2c07969>.
- (13) Jahan, M.; Bao, Q.; Loh, K. P. Electrocatalytically Active Graphene–Porphyrin MOF Composite for Oxygen Reduction Reaction. *J. Am. Chem. Soc.* **2012**, *134* (15), 6707–6713. <https://doi.org/10.1021/ja211433h>.
- (14) Wang, J.; Fan, Y.; Tan, Y.; Zhao, X.; Zhang, Y.; Cheng, C.; Yang, M. Porphyrinic Metal–Organic Framework PCN-224 Nanoparticles for Near-Infrared-Induced Attenuation of Aggregation and Neurotoxicity of Alzheimer’s Amyloid- $\beta$  Peptide. *ACS Appl. Mater. Interfaces* **2018**, *10* (43), 36615–36621. <https://doi.org/10.1021/acsami.8b15452>.
- (15) Zong, Y.; Ma, S.; Gao, J.; Xu, M.; Xue, J.; Wang, M. Synthesis of Porphyrin Zr-MOFs for the Adsorption and Photodegradation of Antibiotics under Visible Light. *ACS Omega* **2021**, *6* (27), 17228–17238. <https://doi.org/10.1021/acsomega.1c00919>.
- (16) Crake, A.; Christoforidis, K. C.; Godin, R.; Moss, B.; Kafizas, A.; Zafeiratos, S.; Durrant, J. R.; Petit, C. Titanium Dioxide/Carbon Nitride Nanosheet Nanocomposites for Gas Phase CO<sub>2</sub> Photoreduction under UV-Visible Irradiation. *Applied Catalysis B: Environmental* **2019**, *242*, 369–378. <https://doi.org/10.1016/j.apcatb.2018.10.023>.
- (17) Feng, D.; Chung, W.-C.; Wei, Z.; Gu, Z.-Y.; Jiang, H.-L.; Chen, Y.-P.; Darensbourg, D. J.; Zhou, H.-C. Construction of Ultrastable Porphyrin Zr Metal–Organic Frameworks through Linker Elimination. *J. Am. Chem. Soc.* **2013**, *135* (45), 17105–17110. <https://doi.org/10.1021/ja408084j>.
- (18) Yu, J.; Yu, H.; Cheng, B.; Trapalis, C. Effects of Calcination Temperature on the Microstructures and Photocatalytic Activity of Titanate Nanotubes. *Journal of Molecular Catalysis A: Chemical* **2006**, *249* (1–2), 135–142. <https://doi.org/10.1016/j.molcata.2006.01.003>.
- (19) Wei, Y.; Wu, X.; Zhao, Y.; Wang, L.; Zhao, Z.; Huang, X.; Liu, J.; Li, J. Efficient Photocatalysts of TiO<sub>2</sub> Nanocrystals-Supported PtRu Alloy Nanoparticles for CO<sub>2</sub> Reduction with H<sub>2</sub>O: Synergistic Effect of Pt-Ru. *Applied Catalysis B: Environmental* **2018**, *236*, 445–457. <https://doi.org/10.1016/j.apcatb.2018.05.043>.
- (20) Markovits, A.; Fahmi, A.; Minot, C. A Theoretical Study of CO<sub>2</sub> Adsorption on TiO<sub>2</sub>. *A. Ma* **1996**.
- (21) Morterra, C.; Chiorino, A.; Boccuzzi, F.; Fiscaro, E. A Spectroscopic Study of Anatase Properties. *Zeitschrift für Physikalische Chemie* **1981**, *124* (2), 211–222. <https://doi.org/10.1524/zpch.1981.124.2.211>.
- (22) Jin, J. Porphyrin-Based Metal–Organic Framework Catalysts for Photoreduction of CO<sub>2</sub>: Understanding the Effect of Node Connectivity and Linker Metalation on Activity. *New J. Chem.* **2020**, *44* (36), 15362–15368. <https://doi.org/10.1039/D0NJ03507F>.

- (23) Carrasco, S.; Sanz-Marco, A.; Martín-Matute, B. Fast and Robust Synthesis of Metalated PCN-222 and Their Catalytic Performance in Cycloaddition Reactions with  $\text{CO}_2$ . *Organometallics* **2019**, *38* (18), 3429–3435. <https://doi.org/10.1021/acs.organomet.9b00273>.
- (24) Zhao, L.; Zhao, Y.; Li, R.; Wu, D.; Xie, X.; Ye, H.; Zhang, Y.; Xin, Q. Insights into the Binding Mechanism of 2D Copper-Tetrakis-(4-Carboxyphenyl)-Porphyrin Metal-Organic Framework Nanosheets with Rhodamine B: Spectroscopic and Thermodynamics Studies. *Chemical Physics* **2020**, *534*, 110743. <https://doi.org/10.1016/j.chemphys.2020.110743>.
- (25) Jeong, E.-Y.; Burri, A.; Lee, S.-Y.; Park, S.-E. Synthesis and Catalytic Behavior of Tetrakis(4-Carboxyphenyl) Porphyrin-Periodic Mesoporous Organosilica. *J. Mater. Chem.* **2010**, *20* (48), 10869. <https://doi.org/10.1039/c0jm02591g>.
- (26) Lomova, T. N.; Berezin, B. D. Porphyrin Complexes with p, d, and f Metals in High Oxidation States: Structures, Electronic Absorption, and IR Spectra. **2001**, *27* (2).
- (27) Jin, P.; Wang, L.; Ma, X.; Lian, R.; Huang, J.; She, H.; Zhang, M.; Wang, Q. Construction of Hierarchical  $\text{ZnIn}_2\text{S}_4$ @PCN-224 Heterojunction for Boosting Photocatalytic Performance in Hydrogen Production and Degradation of Tetracycline Hydrochloride. *Applied Catalysis B: Environmental* **2021**, *284*, 119762. <https://doi.org/10.1016/j.apcatb.2020.119762>.
- (28) Kilian, K.; Pęgier, M.; Pyrzyńska, K. The Fast Method of Cu-Porphyrin Complex Synthesis for Potential Use in Positron Emission Tomography Imaging. *Spectrochimica Acta Part A: Molecular and Biomolecular Spectroscopy* **2016**, *159*, 123–127. <https://doi.org/10.1016/j.saa.2016.01.045>.
- (29) Johnson, J. A.; Luo, J.; Zhang, X.; Chen, Y.-S.; Morton, M. D.; Echeverría, E.; Torres, F. E.; Zhang, J. Porphyrin-Metalation-Mediated Tuning of Photoredox Catalytic Properties in Metal–Organic Frameworks. *ACS Catal.* **2015**, *5* (9), 5283–5291. <https://doi.org/10.1021/acscatal.5b00941>.
- (30) Xu, H.-Q.; Hu, J.; Wang, D.; Li, Z.; Zhang, Q.; Luo, Y.; Yu, S.-H.; Jiang, H.-L. Visible-Light Photoreduction of  $\text{CO}_2$  in a Metal–Organic Framework: Boosting Electron–Hole Separation via Electron Trap States. *J. Am. Chem. Soc.* **2015**, *137* (42), 13440–13443. <https://doi.org/10.1021/jacs.5b08773>.
- (31) Tekalgne, M. A.; Do, H. H.; Hasani, A.; Van Le, Q.; Jang, H. W.; Ahn, S. H.; Kim, S. Y. Two-Dimensional Materials and Metal-Organic Frameworks for the  $\text{CO}_2$  Reduction Reaction. *Materials Today Advances* **2020**, *5*, 100038. <https://doi.org/10.1016/j.mtadv.2019.100038>.
- (32) da Trindade, L. G.; Borba, K. M. N.; Trench, A. B.; Zanchet, L.; Teodoro, V.; Pontes, F. M. L.; Longo, E.; Mazzo, T. M. Effective Strategy to Coupling Zr-MOF/ZnO: Synthesis, Morphology and Photoelectrochemical Properties Evaluation. *Journal of Solid State Chemistry* **2021**, *293*, 121794. <https://doi.org/10.1016/j.jssc.2020.121794>.
- (33) Shi, R.; Lv, D.; Chen, Y.; Wu, H.; Liu, B.; Xia, Q.; Li, Z. Highly Selective Adsorption Separation of Light Hydrocarbons with a Porphyrinic Zirconium Metal-Organic Framework PCN-224. *Separation and Purification Technology* **2018**, *207*, 262–268. <https://doi.org/10.1016/j.seppur.2018.06.064>.
- (34) Safaei Moghaddam, Z.; Kaykhaii, M.; Khajeh, M.; Oveisi, A. R. PCN-222 Metal–Organic Framework: A Selective and Highly Efficient Sorbent for the Extraction

## CHAPTER 4

- of Aspartame from Gum, Juice, and Diet Soft Drink before Its Spectrophotometric Determination. *BMC Chemistry* **2020**, *14* (1), 19. <https://doi.org/10.1186/s13065-020-00674-6>.
- (35) Yu, K.; Won, D.-I.; Lee, W. I.; Ahn, W.-S. Porphyrinic Zirconium Metal-Organic Frameworks: Synthesis and Applications for Adsorption/Catalysis. *Korean J. Chem. Eng.* **2021**, *38* (4), 653–673. <https://doi.org/10.1007/s11814-020-0730-z>.
- (36) Zhang, H.; Wei, J.; Dong, J.; Liu, G.; Shi, L.; An, P.; Zhao, G.; Kong, J.; Wang, X.; Meng, X.; Zhang, J.; Ye, J. Efficient Visible-Light-Driven Carbon Dioxide Reduction by a Single-Atom Implanted Metal-Organic Framework. *Angew. Chem. Int. Ed.* **2016**, *55* (46), 14310–14314. <https://doi.org/10.1002/anie.201608597>.
- (37) Dissegna, S.; Epp, K.; Heinz, W. R.; Kieslich, G.; Fischer, R. A. Defective Metal-Organic Frameworks. *Adv. Mater.* **2018**, *30* (37), 1704501. <https://doi.org/10.1002/adma.201704501>.



Chapter 5:  
Nanocomposites of  
bimetallic ZIFs/TiO<sub>2</sub>

## Table of Figures

FIGURE 5. 1: XRD PATTERNS OF PRISTINE AND ETCHED ZIF-67, ZIF-8, AND ZIF-8-ON-67 .....	181
FIGURE 5. 2: XRD PATTERNS OF COMPOSITE MATERIALS AND TiO <sub>2</sub> .....	182
FIGURE 5. 3: IR SPECTRA OF ZIF-8, PRISTINE AND ETCHED ZIF-67.....	183
FIGURE 5. 4: N <sub>2</sub> ISOTHERMS FOR INDIVIDUAL COUNTERPARTS AND COMPOSITE MATERIALS.....	184
FIGURE 5. 5: XPS SURVEY SPECTRA .....	185
FIGURE 5.6 : XPS CORE LEVEL SPECTRA OF (A) C 1s, (B) O 1s, (C) Ti 2p AND (D) ZN 2p 3/2 FOR COMPOSITE MATERIALS AND BARE INDIVIDUALS .....	187
FIGURE 5. 7: SEM IMAGES OF (A) ZIF-67, (B) ZIF-67 ETCHED, (C) ZIF-8-ON-67 AND (D) COMPOSITE MATERIAL ZIF-8-ON-67/TiO <sub>2</sub> .....	188
FIGURE 5. 8: UV/VIS OF ZIF-8, PRISTINE AND ETCHED ZIF-67 .....	189
FIGURE 5. 9: UV/VIS OF TiO <sub>2</sub> AND COMPOSITE MATERIALS.....	190
FIGURE 5. 10: PL EMISSIONS AT $\lambda_{EX}=350$ NM FOR COMPOSITE MATERIALS.....	191
FIGURE 5. 11: RESULTS OF ARTIFICIAL PHOTOSYNTHESIS FOR TiO <sub>2</sub> AND COMPOSITE MATERIALS.....	192

## Introduction

In this chapter, the case of multi-layer ZIFs is discussed. ZIF-8 and ZIF-67 are MOF materials that possess the same isostructural morphology. The combination of these MOFs has been already reported in the literature. This concerns the development of MOFs materials with bimetallic metal nodes, and the same organic ligand. However, the main disadvantage of the simultaneous growth of bimetallic ZIFs is the unpredicted final  $Zn^{2+}/Co^{2+}$  ratio. Furthermore, there is an additional disadvantage related to the lack of morphology control. Sequential growth of ZIF-on-ZIF structures might address these shortcomings. Herein, these two specific MOFs are combined in a core-shell configuration followed by coupling with anatase  $TiO_2$  UV100. Details on the synthesis process are given in [Chapter 2](#). Initially, the effect of both layers of MOFs in  $TiO_2$ -based composites is investigated and composites with different MOF contents are examined as photocatalysts towards artificial photosynthesis. The present chapter is divided in two parts:

1. In the first part, the prepared materials are fully characterized, and the information obtained is used to elucidate the properties of the prepared materials. The characterization techniques used to study the photocatalyst are focusing on structural, optical, chemical, and morphological properties. Also, spectroscopic methods (PL) are employed in order to study the recombination of charge carriers for the composite materials, bearing multi- and single-MOF structures.
2. The second part presents the results of the photocatalytic activity of the prepared materials. Namely, the photocatalysts are evaluated towards  $CO_2$  reduction reaction in the gas phase using  $H_2O$  as the electron donor. At the end, the photocatalytic efficiency is correlated with the properties of the prepared materials.

The prepared materials presented in this Chapter are synthesized in collaboration with Dr. Clément Marchal at ICPEES.

## I. Characterization of multi-layer ZIFs/TiO<sub>2</sub> (UV-100) composites

### I.1. Characterization of structural properties

#### *XRD*

For the efficient development of core-shell structures, an etching process was applied on preformed ZIF-67. This etched structure was then used as seed for the development of the ZIF-8 shell. The maintenance of the crystalline structure of both ZIFs after the sequential growth is observed by XRD characterization. The results for bare ZIFs and composite materials are shown in Figure 5.1. The diffraction peaks seen for ZIF-67 are in accordance with the literature. Namely, the peaks at 7.3°, 10.4°, 12.9°, 14.8°, 18.3°, 23.6°, 26°, 24.6° are attributed to (011), (002), (112), (022),(222), (114), (233) and (131) planes <sup>1</sup>. Concerning the etched ZIF-67, we can observe differences in the relative intensities of the diffraction peaks, compared to the parent ZIF-67. This may imply that the chemical etching is performed ununiformly in the different facets of ZIF-67. It is shown by previous reports that during the etching process the external crystal surfaces that have the highest density of Co-2-MIM bonds are affected in a bigger extent <sup>2</sup>. Another important information that we can get from the XRD pattern in the etched materials is that the etching process doesn't affect the crystallinity of ZIF-67 etched particles. The XRD pattern of ZIF-8 is also in accordance with the one mentioned in the literature <sup>3</sup>. It can be observed that ZIF-8 diffracts in the same angles as expected, resulting by the matching morphology with ZIF-67. However, with a closer inspection we can observe that there is a slight shift to lower angles for ZIF-8 (reflection of (011)). This is explained by the different effective ionic (Zn<sup>2+</sup> vs. Co<sup>2+</sup>) radii of the divalent metals <sup>4</sup>. In addition, we can see that the final multilayered ZIF presents strong and sharp peaks, indicating the formation of well crystallized particles <sup>5</sup>. Overall, XRD analysis verified a) the successful formation of ZIF-67, b) that the etching process did not alter significantly the crystal structure of ZIF-67 and c) the successful formation of ZIF-8.

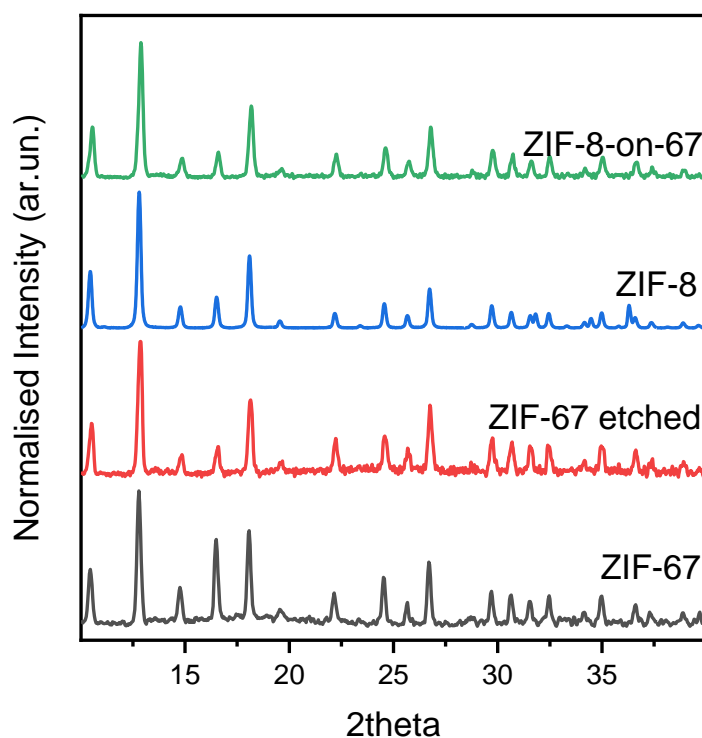


Figure 5. 1: XRD patterns of pristine and etched ZIF-67, ZIF-8, and ZIF-8-on-67

The successful formation of the MOF structures was followed by their coupling with  $\text{TiO}_2$  for the development of composites by using a simple wet impregnation process. After the development of composite materials, XRD analysis has been again employed (Figure 5.2). For MOF content below 10% it is difficult to be able to distinguish any peaks deriving from MOF structure. Therefore, more sensitive techniques focusing on the surface of the materials may give more information, such as ATR and XPS.

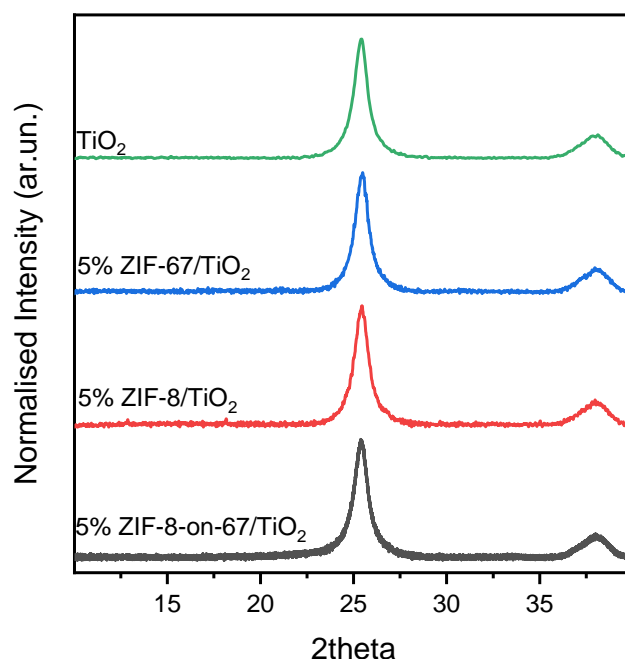


Figure 5. 2: XRD patterns of composite materials and  $\text{TiO}_2$

#### ATR spectroscopy

The surface structure of the prepared materials is also investigated by means of ATR. The IR spectra of the organic ligand and the different ZIF materials are presented in Figure 5.3. All materials present vibrational modes that are mainly attributed to the organic linker. Namely, we can observe that there is a close match in the IR spectra of the organic ligand (i.e., 2-methyl-Imidazole and the different ZIF materials). The bands in the region  $600\text{-}1500\text{ cm}^{-1}$  are attributed to the stretching and bending modes of the imidazole ring. Moreover, the peaks at  $1580$ ,  $2925$  and  $3130\text{ cm}^{-1}$  are assigned to the stretching mode of C=H bond, the C-H of the aromatic ring and the C-H of the aliphatic chain in the ligand, respectively<sup>6</sup>. The peaks centered at  $2500\text{ cm}^{-1}$  are attributed to the C=O bonds of the  $\text{CO}_2$  of the atmosphere. In accordance with the observations by XRD characterization, the IR spectra of the etched ZIF-67 indicate that the etching process doesn't affect the integrity of the organic ligand.

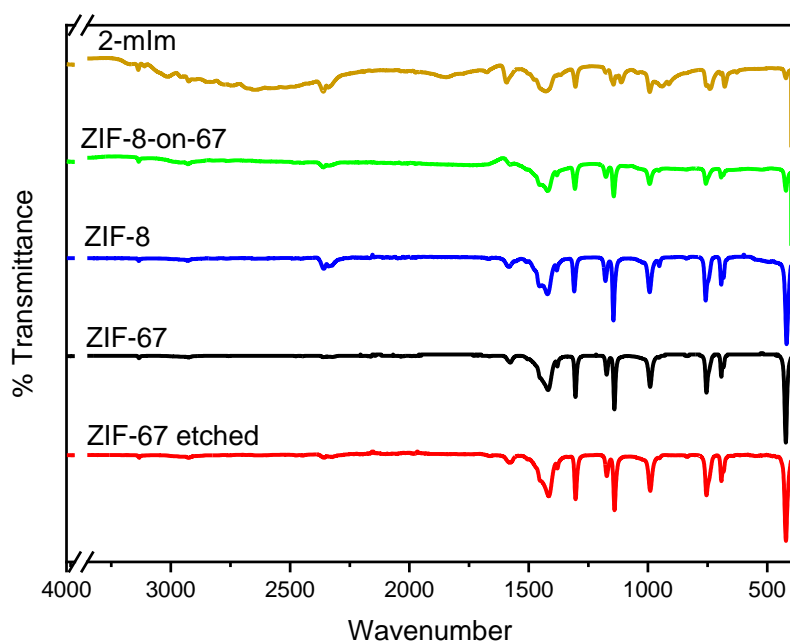


Figure 5. 3: IR spectra of ZIF-8, pristine and etched ZIF-67

#### *N<sub>2</sub> adsorption/desorption isotherms*

The textural properties of the prepared materials are investigated by N<sub>2</sub> adsorption/desorption isotherms at 77 K. The isotherms of the individual counterparts and composite materials are depicted in Figure 5.4. The BET surface area of all materials is shown in Table 5.1. The N<sub>2</sub> adsorption isotherms are of type-I in accordance with the reported microporous nature of all ZIF samples<sup>7</sup>. In the case of ZIF-8, the hysteresis loop observed at high relative pressure originates from the interparticle voids suggesting a mesoporosity, along with the existing microporosity<sup>5,8,9</sup>. A smaller hysteresis loop in lower relative pressures is observed in the case of ZIF-8-on-67 and ZIF-67. As it is observed in Table 5.1, the BET surface area of multilayer ZIF, ZIF-8-on-67 holds a specific surface area higher than ZIF-8 and less than ZIF-67. In addition, the composite materials present a surface area inferior to TiO<sub>2</sub> (ca. 300 m<sup>2</sup> g<sup>-1</sup>). This may infer to the partial blocking of porosity of TiO<sub>2</sub> induced by the presence of MOF.

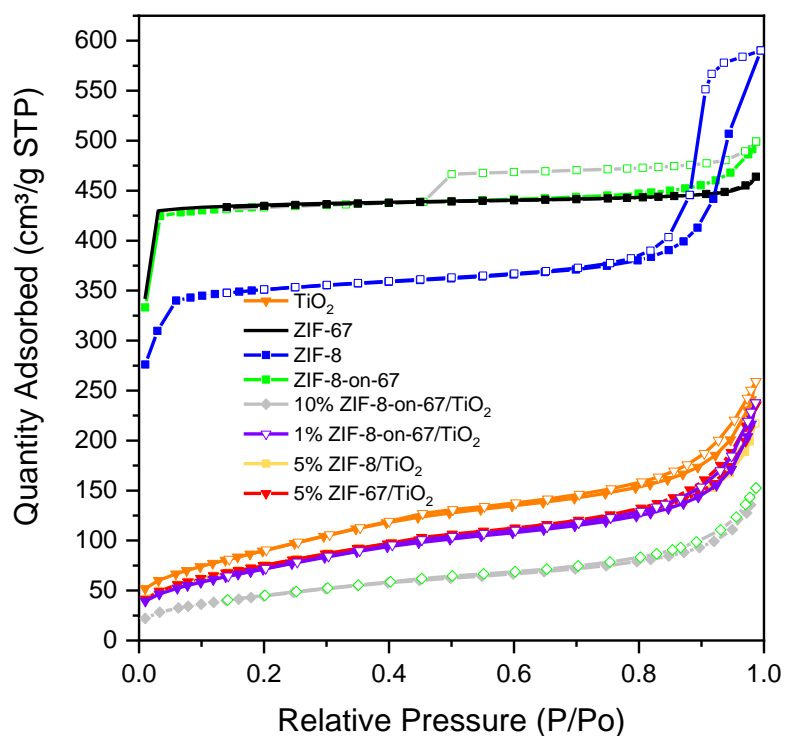


Figure 5. 4:  $N_2$  isotherms for individual counterparts and composite materials

Table 5. 1: BET surface area for individual counterparts and composite materials

Sample	SSA ( $m^2 g^{-1}$ )
TiO <sub>2</sub>	300
ZIF-8	1125
ZIF-67	1520
ZIF-8-on-67	1373
5% ZIF-8/TiO <sub>2</sub>	248
5% ZIF-67/TiO <sub>2</sub>	253
1% ZIF-8-on-67/TiO <sub>2</sub>	265
10% ZIF-8-on-67/TiO <sub>2</sub>	161

## 1.2. Characterization of chemical and morphological properties

*XPS*

The chemical species found on the surface of prepared materials is investigated by XPS analysis. The survey spectra of ZIF-8-on-67,  $\text{TiO}_2$  and their composite material is shown in Figure 5.5. As we can observe C, N, O and Zn are observed for the ZIF-on-ZIF structure, and for the case of composite material Ti is also found. The XPS core level of those elements are presented in Figure 5.6. It is also worth mentioning that XPS is a technique elucidating properties of the surface, because the penetration depth is very small. Therefore, cobalt core level could not be detected, as long as it is in the inner layer of the core-shell configuration. This observation may suggest the successful formation of a core/shell structure in the specific case of ZIF-8-on-67 material, where ZIF-67 structure containing the Co-nodes is covered with ZIF-8.

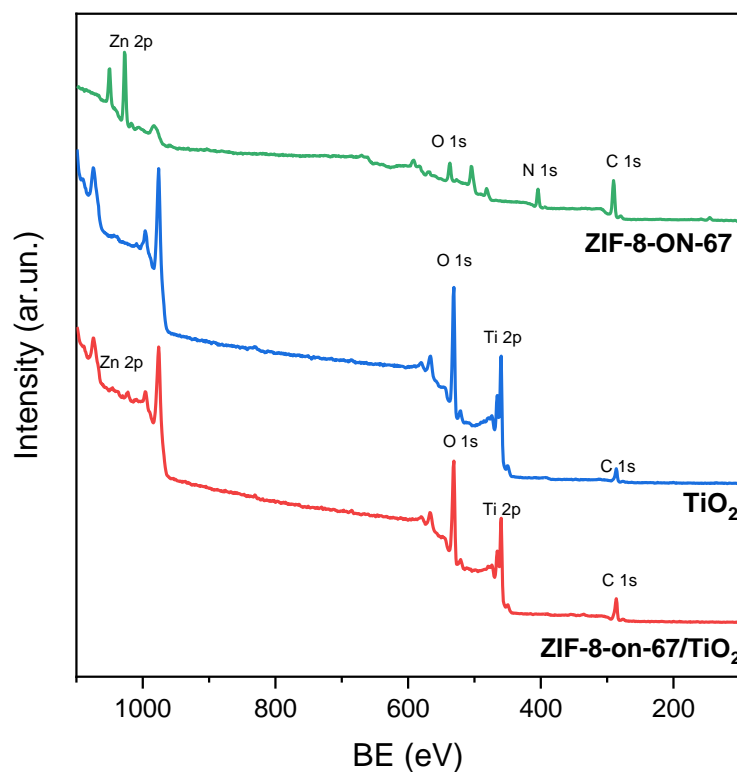


Figure 5. 5: XPS survey spectra

The C 1s core level spectra can be deconvoluted in 3 peaks centered at 284.6, 286.4 and 288.5 eV, which are attributed to C=C, C=N and C-N, respectively <sup>10</sup>. They originate from the organic ligand of the MOF for the ZIF-on-ZIF and composite spectra. Concerning the sample of bare  $\text{TiO}_2$ , the peaks are attributed to the adventitious carbon and possibly to the residual species of the titanium precursors. The deconvoluted peaks of N 1s signal of ZIF-8-on-67 and composite material are

attributed to the C=N (398.9 eV) and N-(C)<sub>3</sub> (400.4 eV) species, found in methyl-imidazole moieties.

The signal of O 1s core level spectra of ZIF-8-on-67/TiO<sub>2</sub> composite material can be deconvoluted in 3 different peaks centered at 529.5, 531.1, 533 eV. By comparing them with the O 1s spectra of TiO<sub>2</sub>, we can observe that they mainly derive from the TiO<sub>2</sub> part of the composite. Specifically, they are ascribed to Ti-O, -OH groups and H<sub>2</sub>O molecules physisorbed on the surface, respectively <sup>11,12</sup>. For the case of ZIF-8-on-67, we observe also three peaks for O 1s, corresponding to C-O, -OH and H<sub>2</sub>O molecules adsorbed. Ti 2p spectra can be deconvoluted in two peaks 458.3 and 484 eV, attributed to Ti<sup>4+</sup> ions from the metal oxide lattice in accordance to previous studies <sup>13</sup>. On the other hand, Zn 2p<sub>3/2</sub> XPS spectra is deconvoluted in a single peak located at 1021.4 eV corresponding to Zn<sup>2+</sup> ions from MOF's metal nodes <sup>14,15</sup>.

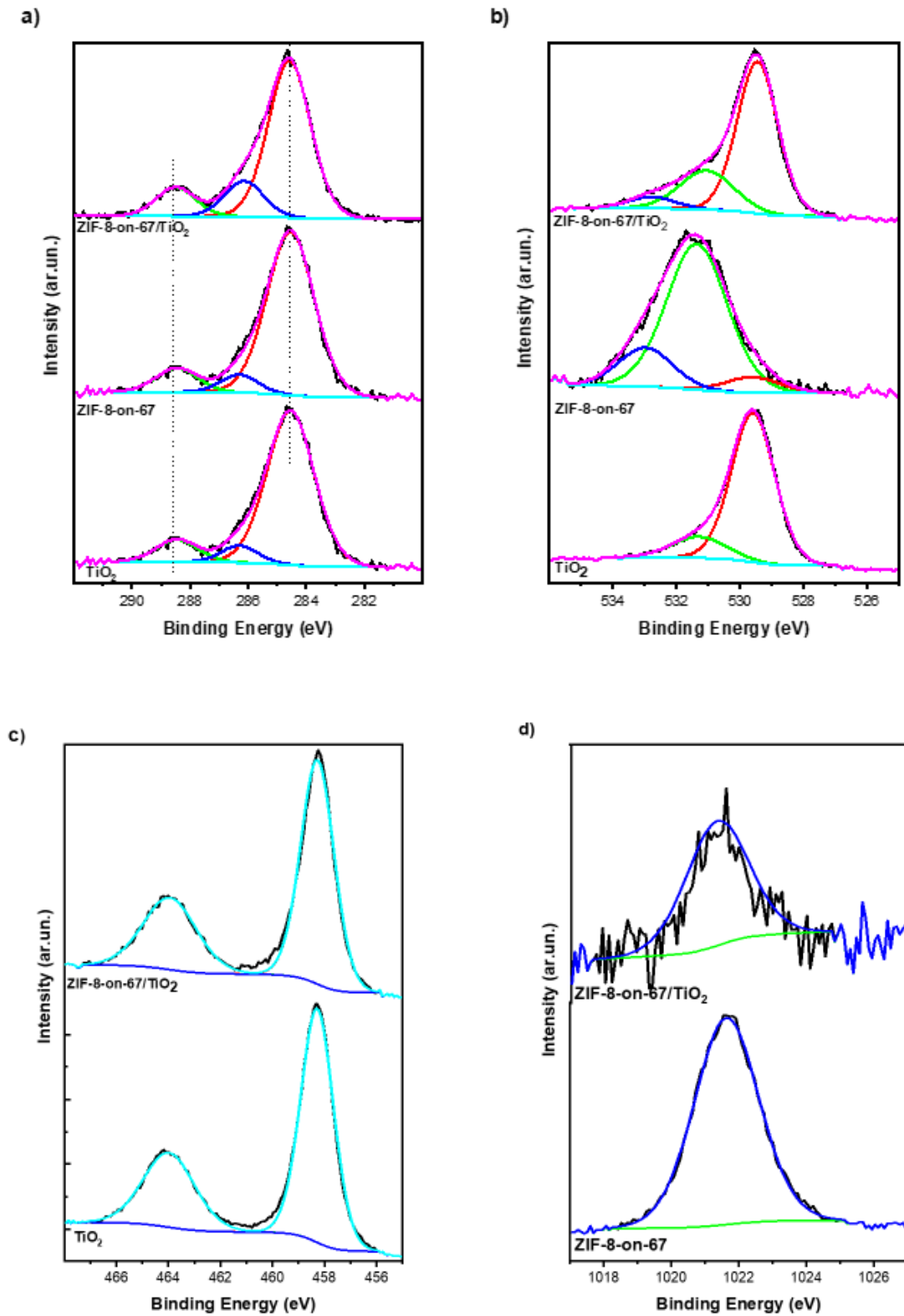


Figure 5.6 : XPS core level spectra of (a) C 1s, (b) O 1s, (c) Ti 2p and (d) Zn 2p 3/2 for composite materials and bare individuals

## SEM

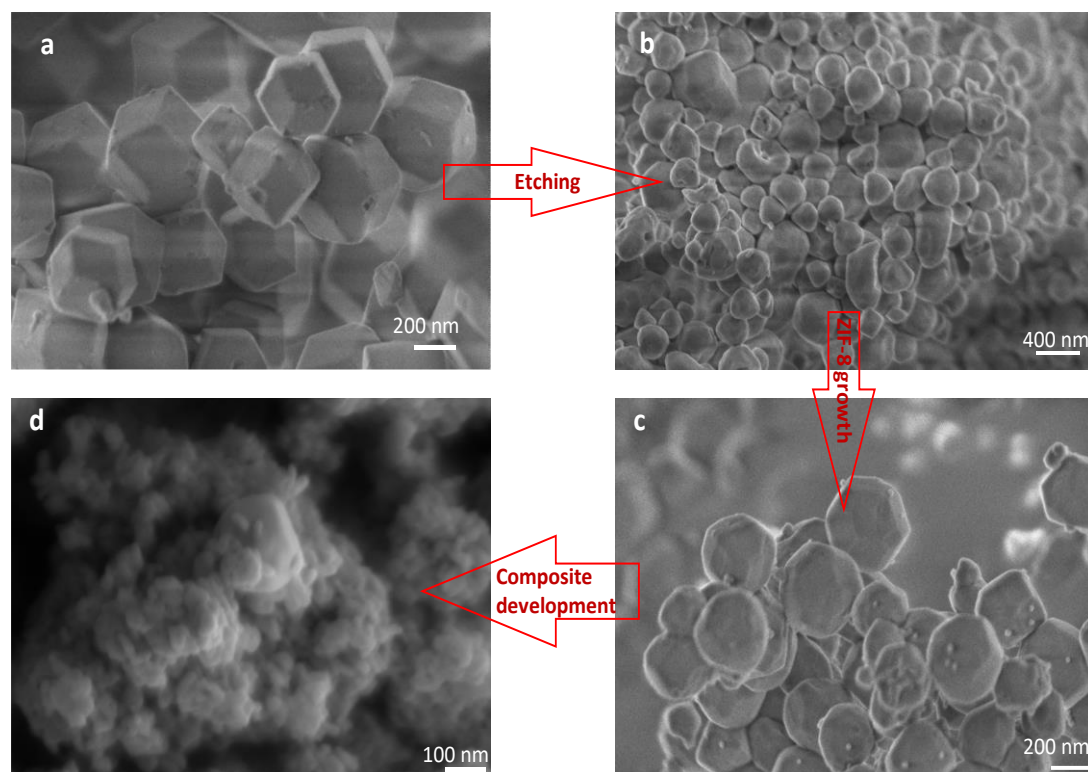


Figure 5. 7: SEM images of (a) ZIF-67, (b) ZIF-67 etched, (c) ZIF-8-on-67 and (d) composite material ZIF-8-on-67/TiO<sub>2</sub>

The morphology and the effect of chemical etching by Xylenol orange is monitored by means of scanning electron microscopy (SEM). The SEM images of ZIF-67, etched ZIF-67, ZIF-8-on-67 and the composite material of the latter is shown in Figure 5.7. It can be seen that the ZIF-67 particles hold a uniform rhombic dodecahedron morphology, with an average size of ca. 458 nm. The relatively large-particle size of ZIF-67 observed compared with that reported in the literature is attributed to the slow nucleation rate that gave rise to a smaller amount of ZIF-67 nuclei, and elongated the crystal growth stage<sup>16</sup>. Methods of synthesis with rapid mixing of the solutions, containing the MOF precursors, lead to smaller particle sizes. But herein, the ZIF-67 nanoparticles are submitted to a top-down approach, so the bigger particle size is of negligible importance. Concerning the ZIF-67 etched nanoparticles we can see that the Xylenol orange solution results in changing the crystal morphology and decreasing the crystal size<sup>17</sup>. The morphology observed is spherical rather than rhombic dodecahedron like the one held by ZIF-67. The size diminution is also confirmed by the average crystallite size of the etched nanoparticles which is calculated approximately at 365 nm. It is already reported in the literature, that chemical etching by weak acids (i.e., xylenol orange) occurs by generating protons that break the coordination interactions taking place in the framework<sup>18</sup>. The increased nanoparticle size, and the formation of polyhedron morphology observed

in Figure 5.7c, indicate the formation of ZIF-8 on the seeds of etched ZIF-67. The average particle size of the multilayer ZIF is approximately 425 nm. It can also be seen that morphology is far from the rhombic dodecahedron morphology. The close contact and the formation of a good interface between ZIF-8-ON-67 structures and TiO<sub>2</sub> nanoparticles is evidenced in Figure 5.7d.

### I. 3. Characterization of optical and electronic properties

#### *UV/Vis*

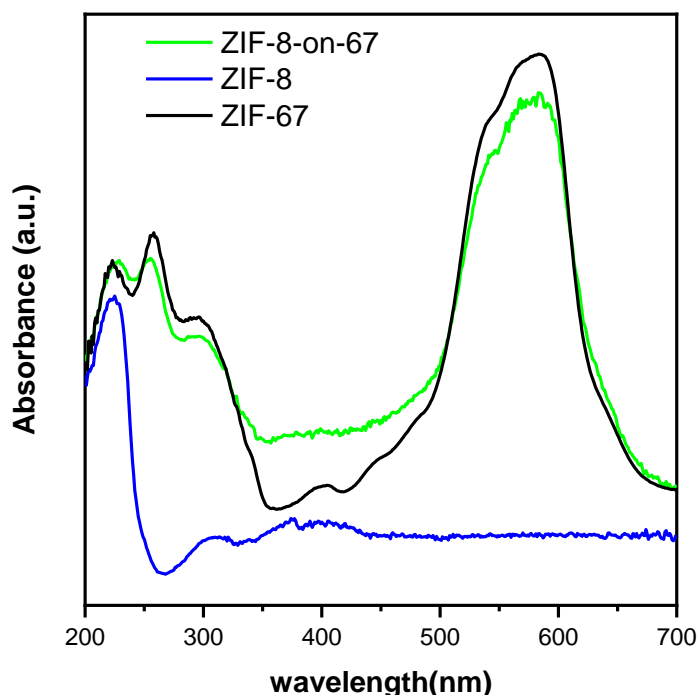


Figure 5. 8: UV/Vis of ZIF-8, pristine and etched ZIF-67

The electronic properties related to light absorption were investigated by means of DR-UV-Vis spectroscopy. The light response of the materials in the visible region is demonstrated in Figure 5.8. As we can see, ZIF-8 shows negligible visible light absorption<sup>19</sup>, specifically, it presents an absorbance edge at 220 nm which is attributed to the Zn<sup>2+</sup> nodes. On the other hand, ZIF-67 presents an absorption peak at 580 nm that could be assigned to the Co<sup>2+</sup> transitions in the tetrahedral environment<sup>17</sup>. It is worth observing that the multilayer ZIF (ZIF-8-on-67) shows characteristic peaks of both ZIF materials. This last observation further confirms the successful formation of multi-MOF structures.

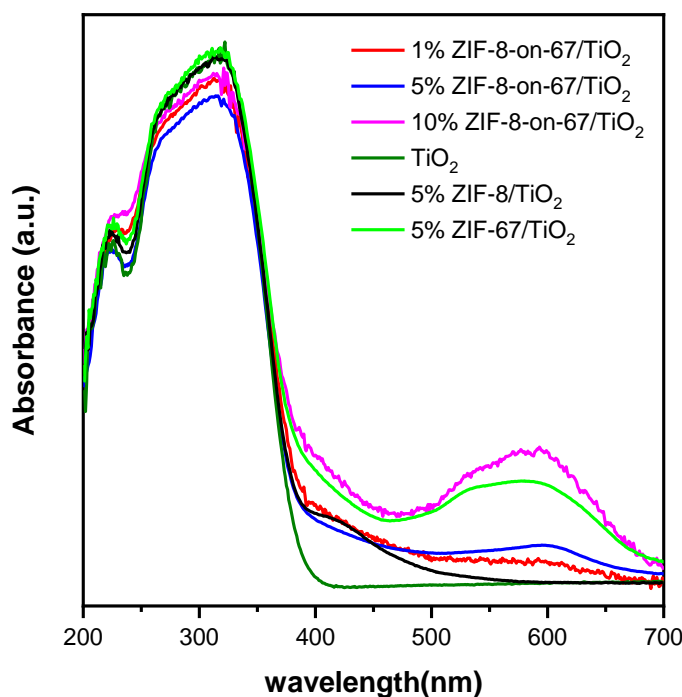


Figure 5. 9: UV/Vis of  $\text{TiO}_2$  and composite materials

On the other hand, as seen in Figure 5.9  $\text{TiO}_2$  absorbs light only in the UV region of light, as expected for the anatase polymorph. The presence of MOF in the composite materials extended light absorption to the visible region. The composite materials exhibit the characteristic peaks of both counterparts. With a closer look, light absorption of the composite materials is increasing with the increase of the MOF content. The DR-UV/Vis spectra of the reference composite materials 5% ZIF-8/ $\text{TiO}_2$  and 5% ZIF-67/ $\text{TiO}_2$  are also displayed in Figure 5.9. As expected according to the UV/Vis spectra of individual MOFs presented in Figure 5.8, the composite bearing ZIF-67 responds in a wider range of solar light compared to 5% ZIF-8/ $\text{TiO}_2$ . However, a more detailed inspection shows that the composite bearing 5% ZIF-8-on-67 is absorbing less than the 5% ZIF-67/ $\text{TiO}_2$  in the region 500-700 nm. This can be explained by the fact that in this region the absorbance peak is attributed to ZIF-67, and it is found in lower concentration when is involved in equal contents of multilayered ZIFs.

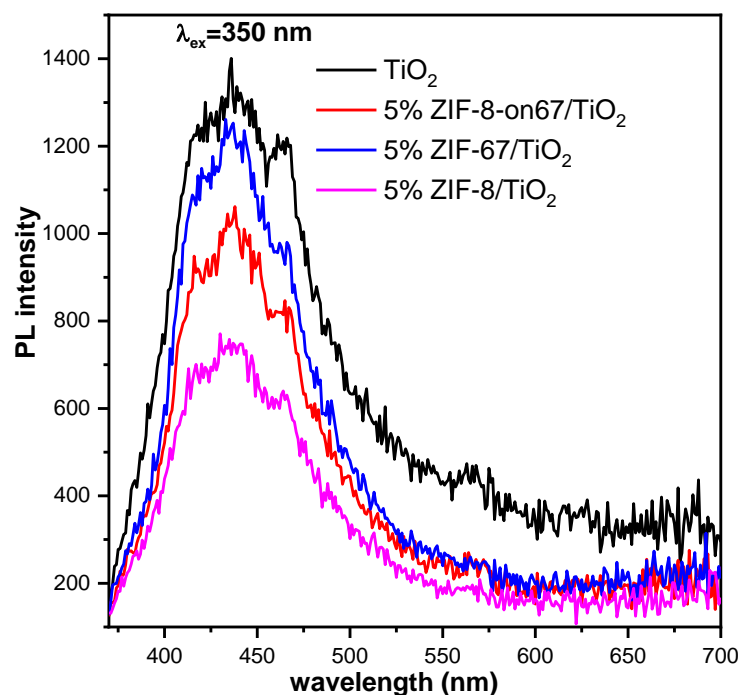
*Photoluminescence Measurements*

Figure 5. 10: PL emissions at  $\lambda_{ex}=350$  nm for composite materials

Photoluminescence spectroscopy is a technique widely applied to study recombination phenomena in photocatalysts. The charge carrier's recombination rate, resulting in radiative emissions are followed by photoluminescence spectroscopy<sup>20</sup>. The results of the PL intensity for the composite materials bearing different ZIFs are shown in Figure 5.10. At an excitation of 350 nm, the synthesized photocatalysts present emission signals at about 435 nm. Higher PL intensity is observed for TiO<sub>2</sub> caused by the rapid recombination rate of charge carriers, as a result of trap state existence. PL quenching is observed upon the coupling of TiO<sub>2</sub> with ZIF structures. This indicates a decrease of the radiative recombination rate in the case of composite materials when compared with the pure TiO<sub>2</sub> phase.

Out of all the composite materials, the composite bearing ZIF-67 exhibits PL signal comparable to TiO<sub>2</sub>. On the other hand, ZIF-8/TiO<sub>2</sub> exhibits more significant PL quenching, giving a hint that the presence of ZIF-8 can block efficiently the recombination of photogenerated electron hole pairs. This has been already seen in previous studies, indicating a special path for carrier transport between TiO<sub>2</sub> and ZIF-8<sup>21</sup>. It is already mentioned in the literature that ZIF-8 itself exhibits luminescence in higher wavelength of excitations (i.e.,  $\lambda_{ex}=396$  nm), which originates from the organic 2-methylimidazolate linkers coordinated with transition metal ions<sup>22</sup>. Therefore, we can conclude that the signal observed upon excitation at 350 nm is attributed to TiO<sub>2</sub>. The PL signal of ZIF-8-on-67/TiO<sub>2</sub> is weaker compared to the ZIF-67/TiO<sub>2</sub>

composite. This may indicate that the presence of the second layer (i.e., ZIF-8) improves the electron transfer inhibiting the charge carrier's recombination.

## II. Photocatalytic activity of bimetallic ZIFs/TiO<sub>2</sub>(UV100) composites

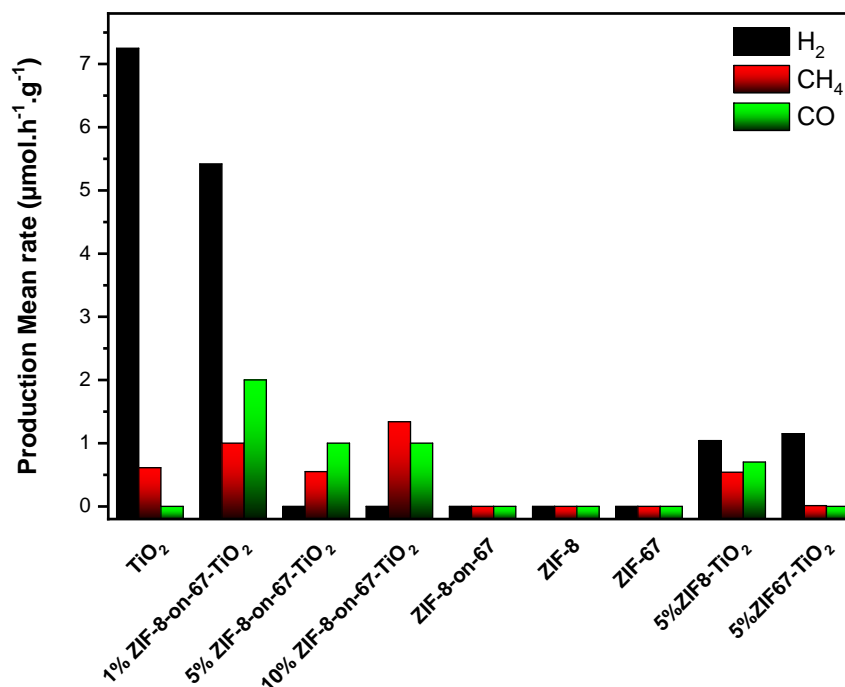


Figure 5. 11: Results of artificial photosynthesis for TiO<sub>2</sub> and composite materials

The prepared materials are evaluated for their activity towards the process of photocatalytic CO<sub>2</sub> conversion in the gas phase, in presence of water vapor as electron donor. Their photocatalytic behavior under pure visible light irradiation is shown in Figure 5.11. It can be observed that TiO<sub>2</sub> is more active towards the reduction of H<sub>2</sub>O to H<sub>2</sub>, with no production of CH<sub>4</sub>.

Although activity is an important parameter when it comes to photocatalysts, selectivity is also an important factor. In other words, it is more interesting and desirable to produce C<sub>1+</sub> products during artificial photosynthesis tests. It is shown that the presence of multi-layer ZIF on TiO<sub>2</sub> surface is beneficial towards this direction. Specifically, composites bearing multilayer MOF structures exhibited higher activity towards C<sub>1</sub> products than the composites with individual MOFs. This can be attributed to the increased light absorption properties of composites provided by the multilayered ZIFs. Different percentages of multi-layered ZIF on TiO<sub>2</sub> composites are also tested. The results obtained suggest a significant contribution of the MOF content on photoactivity. Composites with higher loading of ZIFs are less active than

the one bearing 1% ZIF-8-on-67. However, by increasing the ZIF content, higher selectivity in C products is gained. One may imply that the excess of MOFs can cause the blocking of the photocatalytically active sites of TiO<sub>2</sub>, which can be suggested also by N<sub>2</sub> isotherms.

Composites with ZIF-67 and ZIF-8, respectively, are prepared in order to elucidate the importance of multi-layers. In addition, reference tests were also carried out for bare MOFs. It is shown that the ZIF-67/TiO<sub>2</sub> composite is active only towards H<sub>2</sub> production. Whereas ZIF-8/TiO<sub>2</sub> composite shows a moderate activity towards both H<sub>2</sub> and C<sub>1+</sub> products and it remains less efficient than the multilayer ZIF-8-on-67/TiO<sub>2</sub> composite. This is a very important observation and clearly suggests that the presence of both ZIF structures is beneficial for CO<sub>2</sub> reduction. This can be ascribed to the synergistic effect of multiple layers and the presence of double metal nodes (Zn<sup>2+</sup> and Co<sup>2+</sup>). Namely, earlier studies have mentioned that metal species in ZIFs can act as Lewis's acid sites, and in combination with the basic moieties deriving from nitrogen imidazole ligands, they play a crucial role in the catalytic performance of ZIFs<sup>8</sup>. The superior performance of ZIF-8-on-67 composite, can be also attributed to the minimization of charge carriers' recombination, that was observed by Photoluminescence measurements.

It is also worth mentioning that ZIF-8, ZIF-67 and ZIF-8-on-67 show no activity under identical conditions. This infers that when they are combined with TiO<sub>2</sub> they are favoring CO<sub>2</sub> adsorption and conversion.

### III. Conclusions

Herein, we show that the isostructural ZIF-67 and ZIF-8 can be combined in a multilayer configuration, via sequential deconstruction/construction of MOF framework. This allows a controllable core/ shell morphology. Another advantage while employing this approach is the defined ratio between  $Zn^{2+}/Co^{2+}$  in the structure, over other protocols that have been already presented in the literature.

The successful synthesis and etching of the first layer (i.e., ZIF-67) has been verified by means of scanning electron microscopy and XRD. The latter showed any evident difference in the XRD patterns of the parent and etched MOF. The same characterization techniques have been repeated after the development of the second MOF is carried out, indicating that ZIF-8 has been successfully grown on top of the etched ZIF-67 nanoparticles. The existence of both ZIF-67 and ZIF-8 in the multilayer ZIF, has been also observed by UV/Vis spectra. Specifically, ZIF-8-on-67 absorbance spectra displays characteristic peaks of both metal nodes (i.e., 230 nm attributed to  $Zn^{2+}$  and 580 nm to  $Co^{2+}$  respectively).

Once the MOF is fully characterized, we couple it with  $TiO_2$  in different percentages (1%, 5% and 10%), via a wet impregnation method. The final product exhibits all characteristic IR peaks, and the SEM images show close contact between the two structures. This indicates a well development of ZIF-8-ON-67/ $TiO_2$  composites. The presence of MOFs on  $TiO_2$  extends the response to visible part of light. Interestingly, the light absorbance increases with the increase of MOF content, as shown by DR-UV/Vis spectroscopy.

ZIF structures not only result in harvesting visible light irradiation, but also improved the charge carrier's recombination phenomena as shown by PL measurements. More precisely, fast recombination of electron/hole pairs is inhibited for composite materials. Amongst them, the composite baring ZIF-67 shows the slightest PL quenching, while the composite baring multi-layered ZIF shows a superior inhibition of recombination rate. This may be attributed to the second metal nodes (i.e.,  $Zn^{2+}$ ) of ZIF-8. This observation is in line with the results of the photocatalytic experiments towards artificial photosynthesis.

All composite materials show superior photocatalytic activity towards carbonaceous products compared to bare  $TiO_2$  and composites with single ZIF structures. This may derive from a synergistic effect of ZIF-on-ZIF structure. Although the activity is not so high, it can be explained by the fact that we didn't use any noble metal as cocatalyst. However, there is a threshold of ZIF-on-ZIF content in order to achieve advantageous effect. Supplementary tests show that the increase of the MOF content in the composite does not an effect significantly the production of  $C_1$  products, however, restricts  $H_2$  evolution. In other words, the presence of the multi-layer ZIF structures

## CHAPTER 5

increases the selectivity towards CO<sub>2</sub> reduction. We show that among the prepared composite materials, the one with 1% of ZIF-8-on-67 presents the highest overall activity.

## IV. References

- (1) Sundriyal, S.; Shrivastav, V.; Kaur, H.; Mishra, S.; Deep, A. High-Performance Symmetrical Supercapacitor with a Combination of a ZIF-67/RGO Composite Electrode and a Redox Additive Electrolyte. *ACS Omega* **2018**, *3* (12), 17348–17358. <https://doi.org/10.1021/acsomega.8b02065>.
- (2) Avci, C.; Ariñez-Soriano, J.; Carné-Sánchez, A.; Guillerm, V.; Carbonell, C.; Imaz, I.; Maspoch, D. Post-Synthetic Anisotropic Wet-Chemical Etching of Colloidal Sodalite ZIF Crystals. *Angew. Chem. Int. Ed.* **2015**, *54* (48), 14417–14421. <https://doi.org/10.1002/anie.201507588>.
- (3) Schejn, A.; Aboulaich, A.; Balan, L.; Falk, V.; Lalevée, J.; Medjahdi, G.; Aranda, L.; Mozet, K.; Schneider, R. Cu<sup>2+</sup>-Doped Zeolitic Imidazolate Frameworks (ZIF-8): Efficient and Stable Catalysts for Cycloadditions and Condensation Reactions. *Catal. Sci. Technol.* **2015**, *5* (3), 1829–1839. <https://doi.org/10.1039/C4CY01505C>.
- (4) Jiang, Z.; Li, Z.; Qin, Z.; Sun, H.; Jiao, X.; Chen, D. LDH Nanocages Synthesized with MOF Templates and Their High Performance as Supercapacitors. *Nanoscale* **2013**, *5* (23), 11770. <https://doi.org/10.1039/c3nr03829g>.
- (5) Schejn, A.; Balan, L.; Falk, V.; Aranda, L.; Medjahdi, G.; Schneider, R. Controlling ZIF-8 Nano- and Microcrystal Formation and Reactivity through Zinc Salt Variations. *CrystEngComm* **2014**, *16* (21), 4493–4500. <https://doi.org/10.1039/C3CE42485E>.
- (6) Mohamed, R. M.; Shawky, A. Visible-Light-Driven Hydrogen Production over ZIF-8 Derived Co<sub>3</sub>O<sub>4</sub>/ZnO S-Scheme Based p-n Heterojunctions. *Opt. Mater.* **2022**, *124*, 112012. <https://doi.org/10.1016/j.optmat.2022.112012>.
- (7) Panchariya, D. K.; Rai, R. K.; Anil Kumar, E.; Singh, S. K. Core–Shell Zeolitic Imidazolate Frameworks for Enhanced Hydrogen Storage. *ACS Omega* **2018**, *3* (1), 167–175. <https://doi.org/10.1021/acsomega.7b01693>.
- (8) Zhou, K.; Mousavi, B.; Luo, Z.; Phatanasri, S.; Chaemchuen, S.; Verpoort, F. Characterization and Properties of Zn/Co Zeolitic Imidazolate Frameworks vs. ZIF-8 and ZIF-67. *J. Mater. Chem. A* **2017**, *5* (3), 952–957. <https://doi.org/10.1039/C6TA07860E>.
- (9) Sing, K. S. W. Reporting Physisorption Data for Gas/Solid Systems with Special Reference to the Determination of Surface Area and Porosity (Recommendations 1984). *Pure Appl. Chem.* **1985**, *57* (4), 603–619. <https://doi.org/10.1351/pac198557040603>.
- (10) Wan, M.; Shi, C.; Qian, X.; Qin, Y.; Jing, J.; Che, H. Metal-Organic Framework ZIF-67 Functionalized MXene for Enhancing the Fire Safety of Thermoplastic Polyurethanes. *Nanomaterials* **2022**, *12* (7), 1142. <https://doi.org/10.3390/nano12071142>.
- (11) McCafferty, E.; Wightman, J. P. Determination of the Concentration of Surface Hydroxyl Groups on Metal Oxide Films by a Quantitative XPS Method. *Surf. Interface Anal.* **1998**, *26* (8), 549–564. [https://doi.org/10.1002/\(SICI\)1096-9918\(199807\)26:8<549::AID-SIA396>3.0.CO;2-Q](https://doi.org/10.1002/(SICI)1096-9918(199807)26:8<549::AID-SIA396>3.0.CO;2-Q).
- (12) Fan, C.; Chen, C.; Wang, J.; Fu, X.; Ren, Z.; Qian, G.; Wang, Z. Black Hydroxylated Titanium Dioxide Prepared via Ultrasonication with Enhanced

- Photocatalytic Activity. *Sci. Rep.* **2015**, *5* (1), 11712. <https://doi.org/10.1038/srep11712>.
- (13) Marouazi, H. E.; Jiménez-Calvo, P.; Breniaux, E.; Colbeau-Justin, C.; Janowska, I.; Keller, V. Few Layer Graphene/TiO<sub>2</sub> Composites for Enhanced Solar-Driven H<sub>2</sub> Production from Methanol.
- (14) Wei, X.; Wang, Y.; Huang, Y.; Fan, C. Composite ZIF-8 with CQDs for Boosting Visible-Light-Driven Photocatalytic Removal of NO. *J. Alloys Compd.* **2019**, *802*, 467–476. <https://doi.org/10.1016/j.jallcom.2019.06.086>.
- (15) Liu, P.; Liu, S.; Bian, S.-W. Core–Shell-Structured Fe<sub>3</sub>O<sub>4</sub>/Pd@ZIF-8 Catalyst with Magnetic Recyclability and Size Selectivity for the Hydrogenation of Alkenes. *J. Mater. Sci.* **2017**, *52* (20), 12121–12130. <https://doi.org/10.1007/s10853-017-1357-2>.
- (16) Shao, J.; Wan, Z.; Liu, H.; Zheng, H.; Gao, T.; Shen, M.; Qu, Q.; Zheng, H. Metal Organic Frameworks-Derived Co<sub>3</sub>O<sub>4</sub> Hollow Dodecahedrons with Controllable Interiors as Outstanding Anodes for Li Storage. *J Mater Chem A* **2014**, *2* (31), 12194–12200. <https://doi.org/10.1039/C4TA01966K>.
- (17) Shao, W.; Chen, Y.-R.; Xie, F.; Zhang, H.; Wang, H.-T.; Chang, N. Facile Construction of a ZIF-67/AgCl/Ag Heterojunction *via* Chemical Etching and Surface Ion Exchange Strategy for Enhanced Visible Light Driven Photocatalysis. *RSC Adv.* **2020**, *10* (63), 38174–38183. <https://doi.org/10.1039/D0RA06842J>.
- (18) Lupica-Spagnolo, L.; Ward, D. J.; Marie, J.-J.; Lymperopoulou, S.; Bradshaw, D. Pollen-like ZIF-8 Colloidosomes *via* Emulsion Templating and Etching. *Chem. Commun.* **2018**, *54* (61), 8506–8509. <https://doi.org/10.1039/C8CC03511C>.
- (19) Liu, Y.; Cheng, H.; Cheng, M.; Liu, Z.; Huang, D.; Zhang, G.; Shao, B.; Liang, Q.; Luo, S.; Wu, T.; Xiao, S. The Application of Zeolitic Imidazolate Frameworks (ZIFs) and Their Derivatives Based Materials for Photocatalytic Hydrogen Evolution and Pollutants Treatment. *Chem. Eng. J.* **2021**, *417*, 127914. <https://doi.org/10.1016/j.cej.2020.127914>.
- (20) Zhao, G.; Wu, H.; Feng, R.; Wang, D.; Xu, P.; Wang, H.; Guo, Z.; Chen, Q. Bimetallic Zeolitic Imidazolate Framework as an Intrinsic Two-Photon Fluorescence and PH-Responsive MR Imaging Agent. *ACS Omega* **2018**, *3* (8), 9790–9797. <https://doi.org/10.1021/acsomega.8b00923>.
- (21) Huang, Z.; Dong, P.; Zhang, Y.; Nie, X.; Wang, X.; Zhang, X. A ZIF-8 Decorated TiO<sub>2</sub> Grid-like Film with High CO<sub>2</sub> Adsorption for CO<sub>2</sub> Photoreduction. *J. CO<sub>2</sub> Util.* **2018**, *24*, 369–375. <https://doi.org/10.1016/j.jcou.2018.01.024>.
- (22) Liu, S.; Xiang, Z.; Hu, Z.; Zheng, X.; Cao, D. Zeolitic Imidazolate Framework-8 as a Luminescent Material for the Sensing of Metal Ions and Small Molecules. *J. Mater. Chem.* **2011**, *21* (18), 6649. <https://doi.org/10.1039/c1jm10166h>.





# General Conclusions and Perspectives

## GENERAL CONCLUSIONS AND PERSPECTIVES

Over the past few years, climate crisis became more evident. Global warming and droughts are some of the examples that are attributed to the increased greenhouse gas emissions. One of them is CO<sub>2</sub>, which derives from the destabilization of carbon cycle and the anthropogenic emissions that are related to the modern lifestyle (i.e., industry, transport). Thus, legislative frameworks are suggested and implemented in order to mitigate both problems. The first aims to the energetic transition towards renewable and environmental-friendly resources, in order to decrease the CO<sub>2</sub> emissions from fossil fuels combustion. The second targets the CO<sub>2</sub> conversion to other high-added value chemicals, in the framework of circular economy and carbon sequestration.

In this context, photocatalysis is introduced as a promising and environmentally friendly pathway, reducing CO<sub>2</sub> into other chemicals, notably solar fuels. This approach allows also to tackle the energy shortage. In order to reduce CO<sub>2</sub>, the presence of photocatalysts is prerequisite and the use of electron donor is mandatory. When water is used as electron donor, the process is called artificial photosynthesis, which mimics the natural photosynthesis realized by the plants. However, the yields of the photocatalytic processes are still low, in comparison with other catalytic pathways, that have been mostly developed earlier (i.e., electrocatalysis, heterogeneous thermal catalysis). A crucial step towards improving the yield of this photocatalytic process is the development of cost-effective, efficient, and robust photocatalysts.

Firstly, the bibliographic review presented in [Chapter 1](#), permits us to introduce the context of this study. The principle of photocatalysis and the most commonly used materials, such as TiO<sub>2</sub> and g-C<sub>3</sub>N<sub>4</sub> are presented. Their interesting properties, but also their main drawbacks are discussed. Specifically, the former holds low surface area and exhibits fast charge recombination. The latter is active under ultraviolet irradiation, which represents only 4% of solar light spectra. Therefore, in the present PhD studies the development of heterostructures with MOFs is used in order to address the shortcomings previously mentioned. In this experimental work, MOFs are used either as templates for the oxide materials, or as bifunctional materials that can exhibit both enhanced CO<sub>2</sub> adsorption and photocatalytic properties.

In [Chapter 3](#), the importance of the morphology of both parts in composite materials is examined. Namely, CN holding planar morphology obtained by thermal treatment, has been functionalized with MOF-derived Co<sub>3</sub>O<sub>4</sub> in different morphologies. Herein, the advantages of using MOF as templates have been highlighted. We showed that employing the appropriate synthetical pathways the preferable morphology can be obtained. This approach permits control not only the morphological characteristics, but also the chemical species. More precisely, it is shown that this protocol not only allowed the formation of Co<sub>3</sub>O<sub>4</sub> bulk (Bk) or Co<sub>3</sub>O<sub>4</sub> nanosheets (NS), but it also introduced structural defects on Co<sub>3</sub>O<sub>4</sub>-NS. The defects are mostly referring to

## GENERAL CONCLUSIONS AND PERSPECTIVES

oxygen vacant sites which are considered advantageous for gas adsorption, as confirmed by CO<sub>2</sub> uptake capacity measurements. Simultaneously, the Co<sup>2+</sup> were formed as a result of charge neutrality species that are also considered beneficial for the catalytic mechanism of CO<sub>2</sub> reduction.

The deposition of Co<sub>3</sub>O<sub>4</sub> on the surface of CN was carried out via an easy, fast and simple procedure. The detailed study performed on the morphology of the two parts showed that the matching structure of 2D Co<sub>3</sub>O<sub>4</sub>-Ns with the planar surface of CN is beneficial for the photocatalytic activity. This was linked with the larger interface, as observed by electronic microscopies. Resulting in the formation of heterostructures with enhanced electrons and holes spatial separation, and concomitantly in higher lifetime of energy charge carriers. This was more efficient than the one observed for Co<sub>3</sub>O<sub>4</sub>-bk/CN heterojunctions as evidenced by Transient adsorption spectroscopy, EPR and photocurrent measurements. The presence of Co<sub>3</sub>O<sub>4</sub> increased the light absorption of the composite materials in the whole visible region of light. In addition, the presence of Co<sub>3</sub>O<sub>4</sub> enhanced the available total surface area as seen by N<sub>2</sub> sorption/desorption isotherms. This experimental methodology led to materials more active than their individual counterparts. With the highlight that the nanocomposites bearing Co<sub>3</sub>O<sub>4</sub>-Ns showed higher activity compared to the corresponding bulk Co<sub>3</sub>O<sub>4</sub>/CN composites. Then, the effect of Co<sub>3</sub>O<sub>4</sub> content was investigated and it is shown that the Co<sub>3</sub>O<sub>4</sub>-NS/CN composite bearing 7 wt.% Co<sub>3</sub>O<sub>4</sub> presented the highest CO yield. Another significant observation is that the prepared catalysts are more selective to CO<sub>2</sub> reduction than to the competitive H<sub>2</sub> production when H<sub>2</sub>O is used as electron donor. Furthermore, the composite materials are more active towards H<sub>2</sub>O splitting reaction in liquid phase in presence of low concentration of sacrificial agent, than the individual counterparts.

In [Chapter 4](#) another category of MOF (PCN-224) materials was presented and focused on the functionalization of MOFs with metal centers, in order to modify their properties at molecular level. The protocol used to develop PCN-224 is simple and easy to scale up. More precisely, commercial porphyrin (H<sub>2</sub>TCP) was used as organic ligand for the development of PCN-224. It has been shown that this porphyrin can be easily functionalized by metals. Specifically, in the present thesis copper has been coordinated in the core of the porphyrin (CuTCP) via a direct substitution method, which then used as organic ligand for MOF synthesis (Cu-PCN-224). The presence of copper didn't affect the morphology of the final MOF as shown by XRD characterization. The composite materials are obtained by in situ growth of MOFs, in the presence of commercial TiO<sub>2</sub> (Hombikat UV100), and the strong interface between the two phases in the final composite have been verified by XPS characterization and SEM images. All heterojunctions showed better activity towards the reaction of CO<sub>2</sub> reduction in presence of water in the gas phase, compared to bare materials.

In detail, the photocatalytic results showed that porphyrins act more beneficial as organic ligands of MOFs, rather than photosensitizers. The advantage of using

materials MOF on TiO<sub>2</sub> composites has been confirmed by characterization techniques (i.e., DRS-UV/Vis). The incorporation of copper sites in the MOF structure is of high interest because it resulted in the 3-fold increase of both H<sub>2</sub> and CO production. In other published studies, copper ions have been considered as active sites promoting CO<sub>2</sub> adsorption ability, together with Zr oxo sites. This suggestion has been confirmed here by CO<sub>2</sub>-TPD. Specifically, it is shown that under the same analysis conditions Cu-PCN-224/TiO<sub>2</sub> showed a supplementary desorption peak at high temperatures. This infers the presence of strong active compared to TPD profile of the composite bearing PCN-224.

The aforementioned observations render MOF composites a promising candidate for CO<sub>2</sub> capture and reduction in gas phase, permitting also their functionalization and tuning. However, we showed that the same MOF composite (PCN-224), when used for H<sub>2</sub>O splitting in liquid phase doesn't present an enhanced activity. On the contrary, bare MOF and MOF composite is significantly less active than bare TiO<sub>2</sub>, notably they presented fast deactivation. The loss of activity can be attributed to blocking of the micropores of MOF structures, that may inhibit the diffusion of the reactants to the active sites.

The last case of MOFs studied in this experimental work is presented in [Chapter 5](#). Specifically, we have shown the case of composite materials of TiO<sub>2</sub> and multi-layer ZIFs. In the first place, a core-shell configuration of ZIF-67 and ZIF-8 has been developed. These hold the same morphology and the same organic linker (dimethylimidazole) and Co<sup>2+</sup> and Zn<sup>2+</sup> nodes for ZIF-67 and ZIF-8, respectively. The protocol of MOF synthesis comprised of 3 steps and the order of ZIF layers has been chosen since ZIF-8 is reported to be more active as photocatalyst towards CO<sub>2</sub> reduction than ZIF-67. Firstly, the construction and chemical etching of the first layer (ZIF-67) took place and later followed the growth of ZIF-8 on ZIF-67 etched seeds. This approach is of high interest because it attempts to tackle the problems that have been reported in the literature deriving from the simultaneous one pot growth of bimetallic MOFs. These are the uncontrollable morphology and final ratio of Co<sup>2+</sup> and Zn<sup>2+</sup> species. Later, the multi-layered MOFs were coupled in different percentages with commercial TiO<sub>2</sub> (Hombikat UV100) via a wet impregnation method.

The characterization techniques (i.e., XRD) showed that the final materials were highly crystalline with matching diffraction peaks as the individual MOFs. The results of UV/Vis characterization show that the light absorbance of the final MOF material is a contribution of both ZIF structures. Specifically, Co<sup>2+</sup> and Zn<sup>2+</sup> nodes present an absorbance edge at 580 and 220 nm, respectively. It is also shown that the presence of MOF in the composite materials extended the response of TiO<sub>2</sub> from UV to visible light. Furthermore, the intensity of light absorption in the composites was found to be proportional to the content of the MOF.

The prepared multilayered composite materials showed good activity towards artificial photosynthesis process. It is important to highlight that they exhibited higher activity towards C<sub>1</sub> products than the composites with individual MOFs. This

can be attributed to the increased light absorption properties of composite materials bearing multilayered ZIFs. This observation implies that there is a synergy between the two ZIFs. For further investigation, charge carriers' recombination for the composite materials and TiO<sub>2</sub> were studied by Photoluminescence measurements (PL). It was shown that charge carrier's separation is more efficient for the composite materials with ZIF-8-on-67 compared to ZIF-67, suggesting a formation of heterojunction between the two layers. This can be attributed to the presence of double unsaturated metal sites.

However, the study of the effect of MOF content on composite materials shows that higher loading is not necessarily beneficial for the overall activity. It may lead to the blocking of the TiO<sub>2</sub> active sites preventing the adsorption of reactants. It is worth mentioning that even though TiO<sub>2</sub> remains more active towards H<sub>2</sub> evolution, compared to composite materials, herein the aim is improving the selectivity of carbonaceous products. Therefore, the competitive reaction of H<sub>2</sub>O splitting is of minor interest.

In this present study, we showed that by coupling MOF materials with commonly used semiconductors (i.e., TiO<sub>2</sub>, C<sub>3</sub>N<sub>4</sub>) we are able to enhance their photocatalytic activity. Herein three approaches for the MOF functionalities (i.e, morphology, organic ligand functionalization, morphology configuration) are presented. To summarize, the composites presented in [Chapter 3](#) have no similarities with the materials presented in [Chapter 4](#) and [Chapter 5](#). Firstly, because the semiconductors are the same, and secondly because the CO<sub>2</sub> conversion is realized in different conditions. Therefore, any comparison of these nanomaterials with the TiO<sub>2</sub> composites regarding their photocatalytic activity towards CO<sub>2</sub> reduction, will lead us to false and vague observations.

On the other hand, when comparing the porphyrinic MOF composites with the multilayered ZIF composites, we can see that the former ones exhibit a higher overall activity. The difference is bigger when the composite bears copper functionalized MOFs. It is worth reminding that PCN/TiO<sub>2</sub> composites require a 2-step synthesis that involves the copper integration and the in-situ growth of PCN-224 in presence of titania. On the contrary, the development of ZIF-8-on-67 composite materials requires 3 steps of MOF synthesis and then one-pot impregnation for the coupling process. Considering the synthesis requirements, we can suggest that the approach of metal functionalized MOFs is more favorable, in order to enhance the photocatalytic properties.

The present PhD studies is a preliminary work towards the understanding of the different functionalities of MOFs. Taking into consideration the aforementioned conclusions and bearing in mind the improvement of the materials' properties, further investigation of different parameters is necessary. The main ideas of supplementary study for future works are presented below:

## GENERAL CONCLUSIONS AND PERSPECTIVES

### 1. MOF-derived $\text{Co}_3\text{O}_4$ and CN composites

- Coupling ZIF-67 and m-ZIF-67 with ZIF-8, and annealing them in 350 °C, in order to obtain a MOF derived p-n heterojunction of  $\text{Co}_3\text{O}_4/\text{ZnO}$ .

### 2. Composites of (M)-PCN-224/ $\text{TiO}_2$ (UV100)

- A parametric study of MOF content on the composites, in order to study the effect of MOF, and find the optimal content.
- Preparation of composites bearing MOFs with different ratios of  $\text{H}_2\text{TCCP}$  and  $\text{CuTCCP}$ , in order to elucidate the role of Cu on the MOF structure. This will permit us to estimate the contribution of Cu ions to the overall electronic properties.
- Investigation of charge carriers' behavior (charge availability and lifetime) by time dependent techniques. For example, by employing the method of Time resolved microwave conductivity (TRMC) or time-resolved Photoluminescence.

### 3. Nanocomposites of bimetallic ZIFs/ $\text{TiO}_2$ (UV-100)

- Investigation of  $\text{Zn}^{2+}/\text{Co}^{2+}$  ratio for the multi-layered MOF composite materials by elemental analysis (Induced Coupled Plasma-Mass spectroscopy). In order to elucidate the role of each metal.
- Enclosure of Metal NPs (i.e., Au, Cu) between the two layers of the core shell configuration, in order to explore their influence in the photocatalytic properties. Supplementary investigation of charge carriers' lifetime, in order to verify if the electron transport between the two layers will be enhanced by the presence of enclosed NPs.

## GENERAL CONCLUSIONS AND PERSPECTIVES

Maria ANAGNOSTOPOULOU  
Nanomatériaux à base de  
MOF pour la réduction  
photocatalytique de CO<sub>2</sub> et  
la production de  
l'hydrogène

## Résumé

Au cours des dernières années, le réchauffement climatique est devenu de plus en plus évident. Les émissions excessives de gaz à effet de serre en sont la principale cause. Le CO<sub>2</sub> est l'un de ces gaz à effet de serre, dont l'augmentation dans l'atmosphère est attribuée à la déstabilisation du cycle du carbone et aux émissions anthropiques (c'est-à-dire, l'industrie, les transports). Afin de résoudre ce problème, la diminution des émissions de CO<sub>2</sub> par la transition énergétique vers des ressources respectueuses de l'environnement et la conversion du CO<sub>2</sub> en d'autres produits chimiques à valeur ajoutée, est suggérée. Dans cette direction, la photocatalyse est introduite comme une voie prometteuse et respectueuse de l'environnement, en réduisant le CO<sub>2</sub> en d'autres produits chimiques, qui peuvent être utilisés comme carburants, appelés carburants solaires (CH<sub>4</sub>, CO, H<sub>2</sub>). Outre la lumière du soleil, la présence de photocatalyseurs est également nécessaire. Les photocatalyseurs les plus couramment étudiés présentent certains désavantages. Par conséquent, cette thèse vise à coupler des matériaux MOF avec des semi-conducteurs couramment utilisés (g-C<sub>3</sub>N<sub>4</sub>, TiO<sub>2</sub>), afin d'obtenir des matériaux composites avec des propriétés photocatalytiques supérieures à leurs constituants.

**Mots-clés:** photocatalyse, réduction de CO<sub>2</sub>, production d'hydrogène, MOF, nitrure de carbone, dioxyde de titane

## Abstract

Over the past few years, global warming has become more and more evident. Excessive greenhouse gas emissions are the main cause. CO<sub>2</sub> is one of the greenhouse gases, whose increase on the atmosphere is attributed to the destabilization of carbon cycle and the anthropogenic emissions (i.e., industry, transport). In order to tackle this problem, the decrease of CO<sub>2</sub> emissions by energetic transition towards environmental-friendly resources and the CO<sub>2</sub> conversion to other high-added value chemicals, is suggested. In this direction, photocatalysis is introduced as a promising and environmentally friendly pathway, by reducing CO<sub>2</sub> into other chemicals, which can be used as fuels-so called solar fuels (CH<sub>4</sub>, CO, H<sub>2</sub>). Except for the presence of sunlight, the presence of photocatalysts is also prerequisite. Actually, the most commonly studied photocatalysts present some shortcomings. Therefore, this thesis aims to couple MOFs materials with commonly used semiconductors (g-C<sub>3</sub>N<sub>4</sub>, TiO<sub>2</sub>), aiming to obtain composite materials with photocatalytic properties superior to their bare counterparts.

**Keywords:** photocatalysis, CO<sub>2</sub> reduction, Hydrogen production, MOF-based, carbon nitride, titanium dioxide